

Broad-band study of selected Gamma-ray active blazars

INAUGURAL-DISSERTATION

zur
Erlangung des Doktorgrades
der Mathematisch-Naturwissenschaftlichen Fakultät
der Universität zu Köln



vorgelegt von

Bindu Rani

aus Mukandpur Jhajjar Haryana, India

Köln 2014

Berichterstatter: Prof. Dr. J. Anton Zensus
Prof. Dr. Andreas Eckart

Tag der letzten mündlichen Prüfung: 24.01.2014

ABSTRACT

The analysis presented in this thesis is aimed to provide a more detailed understanding of the relation between flux density outbursts seen at radio, optical, and γ -ray frequencies and the subsequent structural variability as seen by VLBI. Setting tighter observational constraints on parameters required for the synchrotron self-Compton and inverse-Compton modeling of the high-energy radiation is the prime target. A special attention is given to the parsec scale jet kinematics of the BL Lac object S5 0716+714 using mm-VLBI with an angular resolution up to $\sim 50 \mu\text{as}$. The aim of the broad-band variability study reported in this thesis is to provide a general physical scenario, which allows to put the observed variation of the source across several decades of frequencies in a coherent context.

The densely sampled multi-frequency observations of S5 0716+714 over the past 5 years allow us to study its broad-band flaring behavior from radio to γ -rays and probe into the physical processes, location and size of the emission regions for the source, which is ultra-compact and known to be one of the fastest variable blazars. The combination of the broad-band variability characteristics with the VLBI measurements provides new insights into the core region and at the jet base, a view which was not possible in earlier studies at lower VLBI observing frequencies. More explicitly, the correlation of the γ -ray flaring activity with the emission at optical to radio frequencies is investigated focusing on some prominent flares observed between April 2007 and April 2012. The time evolution of radio (cm and mm) spectra is tested in the context of a standard shock-in-jet model. The broad-band spectral energy distribution (SED) of the source is investigated using a one-zone synchrotron self-Compton (SSC) model and also with a hybrid model, which involves a SSC and an external Compton (EC) component.

The intense optical monitoring of the source reveals fast quasi-periodic variations superimposed on a long-term variability trend at a time scale of ~ 360 days. Episodes of fast variability recur on time scales of ~ 60 – 70 days. The prominent and simultaneous flaring activity at optical and γ -ray frequencies favors the SSC mechanism for the production of the high-energy emission. The high-energy (γ -ray – optical) flares propagate down to radio frequencies with a time delay of ~ 65 days following a power-law dependence in frequency with a slope ~ 0.3 . This indicates that the internal opacity effects play a key role in producing time delays among light curves at optically thin and thick wavelengths. The evolution of the radio flares agrees with the formation of

a shock and its propagation with a contribution of geometrical variation in addition to intrinsic variations in the jet.

The broad-band spectral energy distributions (SEDs) of the source during different flaring episodes can not be well described by a pure one-zone SSC model, and require an additional EC contribution from the external radiation field, which is dominated by Ly- α emission from the broad-line region (BLR). A detailed investigation of the high-energy spectrum supports the view that the BLR has a significant impact on the observed γ -ray spectral breaks at a few GeVs, due to pair production. The energy density of this external radiation field varies between 10^{-6} to 10^{-5} erg cm $^{-3}$, which is a factor of ~ 1000 lower than what is expected for a typical quasar, and is a reasonable value for a gas poor (emission line-free) BL Lac object like S5 0716+714.

High-frequency VLBI observations revealed a standing feature observed at ~ 0.1 milli-arcsecond separation from the core. Further downstream, the individual component motion indicates jet acceleration. Curved trajectories in the component motion, variations in the jet ridge line, and a position angle swing at the base of the jet are all consistent with the helical jet model, in which the ejected components transport angular momentum away from the central engine. The observed correlation of the core flux with the single dish radio flux light curves and the concurrent variations in the inner jet position angle with high-energy (optical/ γ -ray) flux suggests that the high-energy emission is coming from a region, which is located inside the mm-VLBI core, so upstream to the $\tau=1$ surface on scales < 0.27 parsec towards the central black hole.

ZUSAMMENFASSUNG

Mit der in dieser Dissertation präsentierten Analyse wird ein besseres Verständnis der Beziehung zwischen Flussdichteausbrüchen im Radio-, optischen und Gammastrahlungsbereich und den darauffolgenden, mit VLBI gesehenen, strukturellen Veränderungen angestrebt. Das Primärziel ist stärkere, durch Beobachtungen gewonnene Einschränkungen für Parameter zu setzen, die für die Synchrotron-Selbst-Compton- und die inverse Compton-Modellierung der Hochenergiestrahlung benötigt werden. Besondere Aufmerksamkeit gilt der Kinematik des Jets des BL Lac-Objekts S5 0716+714 auf Größenskalen von Parsecs unter Verwendung von mm-VLBI mit einer Winkelauflösung von bis zu $\sim 50 \mu\text{as}$. Ziel der hier präsentierten Studie der Breitbandvariabilität ist ein allgemeines physikalisches Szenario zu erhalten, in dem die beobachteten Variationen der Quelle über zahlreiche Größenordnungen von Frequenzen in einen schlüssigen Zusammenhang gebracht werden.

Die Multifrequenz-Beobachtungen von S5 0716+714 in kurzen zeitlichen Abständen über 5 Jahre ermöglichen uns den Verlauf der Breitband-Strahlungsausbrüche vom Radiobereich bis zur Gammastrahlung zu studieren. Weiterhin können damit die physikalischen Prozesse, die Position und die Größe der Emissionsregion in dieser Quelle – die ultra-kompakt und als einer der Blazare mit der schnellsten Variabilität bekannt ist – erforscht werden. Die Kombination von Eigenschaften der Breitbandvariabilität mit VLBI-Messungen liefert neue Einblicke in die Kernregion und den Entstehungsbereich des Jets; einen Einblick, der in früheren Studien bei niedrigeren Beobachtungsfrequenz nicht möglich war. Die Korrelation zwischen Gammastrahlungsausbrüchen und der Emission vom Radio- bis zum optischen Bereich wird untersucht, insbesondere die auffälligsten Ausbrüche, die zwischen April 2007 und April 2012 beobachtet wurden. Die zeitliche Entwicklung der Radiospektren (cm und mm Wellenlängen) werden im Kontext des standardmäßigen “Schock-in-Jet”-Modells getestet. Die spektrale Energieverteilung (SED) der Quelle wird mit einem Synchrotron-Selbst-Compton-Modell (SSC) mit einer Emissionszone sowie mit einem gemischten Modell, das SSC und einen externen Comptonbeitrag beinhaltet, untersucht.

Das intensive optische Beobachtungsprogramm der Quelle zeigt schnelle quasi-periodische Variationen, die mit einem Langzeit-Variabilitätstrend auf Zeitskalen von ~ 360 Tagen überlagert sind. Phasen mit schneller Variabilität wiederholen sich auf Zeitskalen von ~ 60 – 70 Tagen. Die starke und simultane Aktivität im optischen und im Gammastrahlungsbereich spricht für den SSC-Mechanismus als Quelle der Hochenergieemission.

Die Hochenergieausbrüche (Gammastrahlung – optischer Bereich) pflanzen sich mit Zeitverzögerung von ~ 65 Tagen bis in den Radiobereich fort. Die Verzögerung ist frequenzabhängig und folgt einem Potenzgesetz mit einem Exponent von ~ 0.3 . Dies deutet darauf hin, dass interne Opazitätseffekte eine Schlüsselrolle bei der Entstehung der Zeitverzögerung zwischen Lichtkurven bei verschiedenen Wellenlängen spielen. Die zeitliche Entwicklung der Ausbrüche im Radiobereich ist konsistent mit der Entstehung eines Schocks und dessen Ausbreitung mit einem Beitrag von geometrischen Veränderungen zusätzlich zu intrinsischen Variationen im Jet.

Die Breitband-SED der Quelle kann während verschiedener Zeiträumen mit Strahlungsausbrüchen nicht gut durch ein reines SSC-Modell mit nur einer Emissionszone beschrieben werden, sondern benötigt einen zusätzlichen externen Comptonbeitrag, wobei das externe Strahlungsfeld durch Ly- α -Emission der Broad-Line-Region (BLR) dominiert wird. Eine detaillierte Untersuchung des Hochenergiespektrums spricht dafür, dass die BLR, aufgrund von Paarerzeugung, einen starken Einfluss auf den beobachteten Knick im Gammastrahlenspektrum bei einigen wenigen GeV hat. Die Energiedichte dieses externen Strahlungsfelds variiert zwischen 10^{-6} und 10^{-5} erg cm $^{-3}$. Das ist um einen Faktor ~ 1000 niedriger als für einen typischen Quasar erwartet, aber es ist ein plausibler Wert für ein BL Lac-Objekt mit wenig Gas (keine Emissionslinien) wie S5 0716+714.

Hochfrequente VLBI-Beobachtungen zeigen eine stationäre Struktur bei einer Entfernung von ~ 0.1 milli-arcsecond vom Kern. Weiter stromabwärts deutet die Bewegung von individuellen Komponenten auf Beschleunigung im Jet hin. Gekrümmte Trajektorien der Komponenten, Variationen der “Ridge-Line” des Jets und eine Drehung des Positionswinkels des Jets nahe seiner Entstehungsregion sind konsistent mit helikalen Jetmodellen, in welchen ausgestossene Jetkomponenten Drehmoment vom zentralen Objekt wegtransportieren. Die beobachtete Korrelation zwischen dem Kernfluss und dem mit Einzelteleskopen gemessenen Radiofluss, sowie die gleichzeitigen Änderungen des Positionswinkels des inneren Jets und des Hochenergieflusses (optisch und Gammastrahlung) deuten darauf hin, dass die Hochenergiestrahlung ihren Ursprung in einer Region hat, die sich innerhalb des bei mm-Wellenlängen gesehenen VLBI-Kerns hat, also stromaufwärts der $\tau = 1$ Oberfläche auf Größenskalen < 0.27 parsec vom zentralen schwarzen Loch.

PREFACE

The BL Lac object S5 0716+714 is one of the fastest variable blazars with a featureless optical spectrum. It is one of the best studied source in order to search for rapid flux variability and broad-band flux correlations. During 2007-2012, the source was very bright and highly active at millimeter and optical frequencies showing multiple flares, some of which being particularly rapid. These flares are accompanied by corresponding γ -ray activity. The analysis presented in this thesis is aimed to relate the observed structural variability seen with mm-VLBI at a fine angular resolution ($\sim 50\mu\text{as}$) to the broad-band flares in the source. This thesis provide a unique framework to study the characteristics of prominent mm-/gamma-ray flares in the context of (1) the shock-in-jet model, (2) broad-band spectral modeling, (3) and jet kinematics, to probe the location and the origin of the high-energy emission region.

The combination of the broad-band variability characteristics with the VLBI measurements provides new insight into the core region and at the jet base, a view which was not possible in earlier studies due to their lower VLBI observing frequencies. A detailed investigation of temporal and spectral characteristics of the source is performed using a number of statistical analysis tools. The thesis is structured as follows:

- A brief introduction to active galaxies, relativistic jets, introducing their taxonomy, general observational properties, and the basic ideas for a physical theory of relativistic jets, discussing their formation, structure, evolution, and emission mechanisms is provided in Chapter 1.
- The target source, BL Lac object S5 0716+714 is introduced in Chapter 2.
- Chapter 3 covers the details on the multi-wavelength observations performed in the course of this dissertation and on archival data processing. It discusses the instruments used and data reduction techniques applied. A brief overview of the utilized statistical analysis tools is also given in this Chapter.
- A detailed analysis of the temporal characteristics of the broad-band flux variability is given in Chapter 4.

-
- Chapter 5 presents the results of the cross-correlation analysis of radio to γ -ray flux variability observed in the source.
 - Chapter 6 presents the spectral analysis of the radio flares and the estimation of the physical parameters of the jet. The evolution of the radio flares is tested in the context of the shock-in-jet model.
 - Chapter 7 covers the details of the broadband spectral modeling with a focus on the high-energy emission part of the spectrum.
 - Chapter 8 presents the results on the high-resolution multi-frequency VLBI kinematics study to investigate the inner jet kinematics and to explore the morphological evolution of the source and its relation with the broad-band flux variations.
 - Chapter 9 provides a summary of the results presented here and gives a future outlook.

Contents

1	Introduction	1
1.1	Historical background	1
1.2	The physical picture of AGN	2
1.3	The AGN zoo and unification model	4
1.3.1	The unification model	6
1.3.2	Blazars	8
1.4	Acceleration in jets	9
1.5	Emission mechanisms	10
1.5.1	Thermal radiation	11
1.5.2	Synchrotron radiation	12
1.5.3	Inverse-Compton scattering : SSC & EC	13
1.6	Shocks and plasma instability	15
1.7	Relativistic effects	17
1.8	Geometrical effects	19
2	The BL Lac Object S5 0716+714	20
2.1	Radio Properties	21
2.2	Optical Properties	22
2.3	High Energy Emission	23
2.4	Broadband Variability	23
3	Multi-wavelength Observations, Data Reduction and Analysis Techniques	25
3.1	Observations and data reduction	26
3.1.1	Radio observations	26
3.1.2	Optical monitoring	27

3.1.3	X-Ray data	28
3.1.4	Gamma-ray data	29
3.1.4.1	LAT	30
3.1.4.2	LAT data reduction	31
3.2	The time series analysis techniques	34
3.2.1	Statistical analysis tools	35
3.2.1.1	Structure function analysis	35
3.2.1.2	Discrete correlation function analysis	37
3.2.1.3	Lomb-Scargle periodogram	38
3.2.1.4	Power spectrum density	40
3.3	Very long baseline interferometry	42
3.3.1	Observations and data reduction	42
4	Broad-band Flux Variability	45
4.1	Radio frequencies	45
4.2	Optical frequencies	50
4.3	X-ray frequencies	54
4.4	Gamma-ray frequencies	56
4.4.1	Sky map	56
4.4.2	Light curves	57
4.4.3	Flux variations at different energy bands	59
4.4.4	Highest energy photons	62
4.4.5	Variability timescales at gamma-ray frequencies	62
4.5	Summary and discussion	63
5	Multi-wavelength Correlated Variability	65
5.1	Radio-radio correlation	66
5.2	Radio versus optical correlation	72
5.3	Radio versus gamma-ray correlation	75
5.4	Optical versus gamma-ray correlation	78
5.5	The orphan X-ray flare	79
5.6	Discussion	80
5.6.1	Origin of optical variability	80
5.6.2	Origin of gamma-rays	81
5.6.3	Opacity and delay at radio wavelengths	81

5.6.4	Origin of the X-ray flare	83
5.6.5	Broad-band correlation alignment	85
5.7	Summary	85
6	Evolution of Radio flares and physical properties of the jet	87
6.1	Evolution of radio flares in the shock-in-jet scenario	87
6.1.1	Modeling the radio spectra	88
6.1.1.1	One-component SSA model	91
6.1.1.2	Two-component SSA model	93
6.1.2	Evolution of radio flares	93
6.1.3	Breaks in the synchrotron spectrum	97
6.2	Physical parameters of the jet	99
6.2.1	Brightness temperature T_B^{app}	99
6.2.2	Doppler factor from variability timescales (δ_{var})	100
6.2.3	Size of the emission region (θ)	101
6.2.4	Inverse-Compton Doppler factor (δ_{IC})	101
6.2.5	Gamma-ray Doppler factor (δ_γ)	102
6.2.6	Magnetic field from synchrotron self-absorption	103
6.2.7	Equipartition magnetic field and Doppler factor	104
6.3	Comparison of the estimated parameters	105
7	Modeling the high-energy emission	106
7.1	Gamma-ray spectrum	106
7.1.1	Spectrum over the entire period	107
7.1.2	Spectral variations	107
7.1.3	Origin of the gamma-ray spectral break	112
7.2	The complete spectral energy distribution	115
7.2.1	SED modeling	115
7.2.2	Results	119
7.3	Conclusions	122
8	Inner jet kinematics and the origin of high-energy emission	124
8.1	Multi-frequency VLBI data	125
8.2	Jet kinematics	132
8.2.1	Evolution of the jet ridge line	132

8.2.2	Position angle variations	132
8.2.3	Component motion	133
8.2.4	Brightness temperature gradient in the jet	139
8.3	Correlation: Jet kinematics and broad-band flares	141
8.3.1	Position angle versus flux variations	141
8.3.2	Connection with broad-band flares	143
8.4	Discussion	144
9 Summary and Future Perspectives		146
References		162
Erklärung		165
Curriculum Vitae		167

List of Figures

1.1	The standard picture of AGN model	3
1.2	A schematic representation of the current understanding the AGN phenomenon in the unified scheme (graphic by Marie-Luise Menzel, MPE). The radio-loud AGN are shown in the upper part and radio-quiet in the lower part.	6
1.3	The contribution of various emission mechanisms in broadband SED of Blazars	11
1.4	A sketch of the structure and locations of emission at different wavebands in a radio-loud quasar	14
1.5	A schematic diagram of the standard shock-in-jet model	16
1.6	A sketch of shock induced flare spread over a range of frequencies	17
3.1	An artists rendering of the three scientific instruments on board Swift spacecraft	29
3.2	Schematic diagram of the <i>Fermi</i> /LAT	31
3.3	The general analysis flow of the <i>Fermi</i> /LAT data reduction tools	32
3.4	A schematic diagram showing the ideal structure function for a time series	36
4.1	Radio to mm wavelength light curves of S5 0716+714 observed over the past ~ 3 years	46
4.2	Structure function curves at radio frequencies	47
4.3	Structure function versus frequency (GHz) curve with a time binning of 50, 100, and 200 days.	48
4.4	Optical V passband light curve of S5 0716+714.	49
4.5	Structure function curve at optical frequency	50

4.6	LSP analysis curve showing a peak at a period of 63 and 359 days. The dotted line represents the white noise level.	51
4.7	Power spectrum density curve of S5 0716+714	52
4.8	Optical V passband light curve of S5 0716+714 with different time binning	52
4.9	The X-ray (0.3 – 10 KeV) light curve of S5 0716+714.	54
4.10	Soft and hard X-ray light curves of S5 0716+714	55
4.11	Sky map of γ -ray events centered on S5 0716+714	56
4.12	Gamma-ray flux and photon index light curve of S5 0716+714	57
4.13	Light curves of the source flux above 100 MeV with a time binning of 3 day	58
4.14	Photon index (Γ) versus photon flux variations at $E > 100$ MeV	60
4.15	Gamma-ray flux light curves of S5 0716+714 at different energies	61
4.16	The γ -ray structure function analysis curve at $E > 100$ MeV	63
5.1	Light curves of S5 0716+714 from γ -ray to radio wavelengths	67
5.2	The DCF curves among the different radio frequency light curves	68
5.3	The plot of time lag versus frequency, using 15 GHz as the reference frequency	70
5.4	The modeled radio flare, R6. The blue points are the observed data, while the red curve represent the fit.	71
5.5	Optical versus radio DCF analysis curves	74
5.6	Gamma-ray versus radio DCF analysis curves	76
5.7	Gamma-ray versus optical DCF analysis curves	77
5.8	The DCF curve of X-ray versus optical V passband flux using a bin size of 3 days.	80
5.9	A plot of time lag measurements versus frequency using 15 GHz as the reference frequency for the two radio flares	84
6.1	230 GHz light curve of S5 0716+714 showing the major radio flares	88
6.2	Quiescent radio spectrum.	89
6.3	Result of the spectral fitting using the synchrotron self-absorption model	90
6.4	Evolution of R6 flare in the $S_{max} - \nu_{max}$ plane	95
6.5	Evolution of R8 flare in the $S_{max} - \nu_{max}$ plane	96
6.6	Radio-IR spectrum using Spitzer observations	98

7.1	Gamma-ray spectrum of S5 0716+714	108
7.2	Gamma-ray spectrum of S5 0716+714 during different brightness phases	109
7.3	Break Energy plotted as a function of γ -ray flux for the different activity phases of the source	110
7.4	Change in $\Delta\Gamma$ plotted as a function of E_{Photon} for the different activity phases of the source	110
7.5	broad-band flux light curves of the source	116
7.6	Broad-band SED of S5 0716+714 for time Bin1	117
7.7	Broad-band SED of S5 0716+714 for time Bin2	118
7.8	Broad-band SED of S5 0716+714 for time Bin3	119
7.9	Broad-band SED of S5 0716+714 for time Bin4	120
7.10	A comparison of the broad-band SEDs of S5 0716+714 during different activity states. The solid curves represent the best fitted model.	122
8.1	7mm VLBI maps of S5 0716+714	126
8.2	3 mm VLBI maps of S5 0714+714	128
8.3	Evolution of the jet ridge line of S5 0716+714	133
8.4	Position angle variations in the central region of the jet	134
8.5	The core separation of individual components as a function of time.	135
8.6	Trajectories of the jet knots in the X-Y plane	136
8.7	Evolution of radial separation of different components from the core	138
8.8	Component brightness temperature as a function of radial separation from the core	140
8.9	Gamma-ray flux versus position angle correlation analysis plots	142
8.10	The radio (single dish) and γ -ray flux light curves superimposed on the 43 GHz VLBI core flux light curve.	144

List of Tables

3.1	Ground based radio observatories	26
4.1	Variability time scales at radio wavelengths	48
4.2	Fitted parameters of the rapid flares	59
5.1	Correlation analysis results among radio frequencies	66
5.2	Radio correlation analysis results for individual flares	69
5.3	Fitted model parameters for R6 flare	72
5.4	Optical versus radio DCF analysis results	73
5.5	Optical versus γ -ray cross-correlation analysis results	79
6.1	Best-fit spectral parameters for the evolution of radio flares using a one-component SSA model	91
6.2	The best fitted spectral parameters over the evolution of radio flares using a two component SSA model	92
6.3	Different states of spectral evolution and their characteristics	97
6.4	Variability Brightness temperatures	100
6.5	Brightness temperature	103
7.1	Parameters of fitted power laws	111
7.2	Parameters of SSC and EC fits to SED of S5 0716+714	121
8.1	Results from Gaussian Model fitting and component parameters	129
8.2	Physical parameters of the radio emission	137

Chapter 1

Introduction

The term Active Galactic Nuclei (AGN) is used for a sample of extragalactic objects, which are very unique in their emission properties and all share a striking characteristic which distinguishes them from all other objects in the Universe. The mystery of AGN is that they produce very high luminosities in a very compact volume, through accretion processes in the vicinity of super massive black holes. In the last few decades, AGN attract the attention of the astronomical community because of their extreme properties. The need to explain the very high rates of energy generation, requiring supermassive black holes powered sources, jets of relativistic particles blasting out of the nucleus of galaxies and exotic particle–radiation interactions are among the key questions which we would like to answer. Thus, AGN are the special laboratories for extreme physics which we would like to understand. They are also our principal probes of the Universe on large scales, so their study is essential to understand the formation and evolution of galaxies and even the Universe itself.

1.1 Historical background

The first AGN was discovered in 1908 by Edward A. Fath while analyzing the nuclear spectrum of the “spiral nebula” NGC 1068. Later, in 1943, Carl Seyfert discovered that these “emission line” objects constitute a small fraction of the galaxies which had a bright quasi-stellar nucleus and broad emission lines covering a wide range of ionization states. This class of AGN were named as *Seyfert galaxies* (Seyfert, 1943). Radio galaxies have been known since the mid of 1950s, when the Third Cambridge

Catalog (3C) was created; however, these sources were missing their optical counterpart until 1954 (Baade & Minkowski, 1954).

In 1962, a lunar occultation of the radio source 3C 273 allowed an accurate determination of its radio position and consequently the identification of its optical counterpart. This turned out to be of star-like appearance, but its optical spectrum contained several strong emission lines unlike stellar spectra, where only absorption lines are detected. For this reason 3C 273 and similar objects were called quasars which stands for quasi-stellar radio sources (QSR). In 1963, Maarten Schmidt interpreted quasar spectra in terms of cosmological redshift and these sources were recognized to be extragalactic in nature (Schmidt, 1963). Later on, with the discovery of many more star-like objects, which lacked strong radio emission, it was understood that not all of these sources are powerful radio emitters. This leads to a broader definition of Quasi-Stellar Objects (QSOs) as radio-loud and radio-quiet quasars.

The object BL Lacertae (or BL Lac) was at first believed to be a variable star in the constellation of ‘Lacerta’ due to its stellar appearance. ‘BL Lac’ originally represent the 89th variable star in constellation Lacerta. In 1968, its radio counterpart was found (Schmidt, 1968), and later it was identified as a new class of AGN, which shows a featureless optical continuum, rapid variability properties and a high degree of polarization. When similar sources were discovered afterwards, they inherited the name *BL Lac objects or BL Lacs* from it.

With the advent of X-ray and observation facilities at even higher energies, broad-band emission features of AGN have been studied and various sub-classes were named accordingly. The spectra of AGN over the whole electromagnetic band are essentially of non-thermal origin, contrary to normal galaxies where the spectrum is composed mainly from the integrated thermal light of stars. The broad-band features and the observational properties of AGN spectra are discussed in the following Sections.

1.2 The physical picture of AGN

There is considerable progress in our understanding of an AGN over the past two-three decades (e.g. Blandford & Königl, 1979; Meier et al., 2001; Urry & Padovani, 1995, and references therein). The center of an AGN is a supermassive black hole (SMBH, $10^6 - 10^9 M_{\odot}$) which accretes matter by its strong gravitational force. Matter pulled towards the black hole loses angular momentum through viscous or turbulent processes

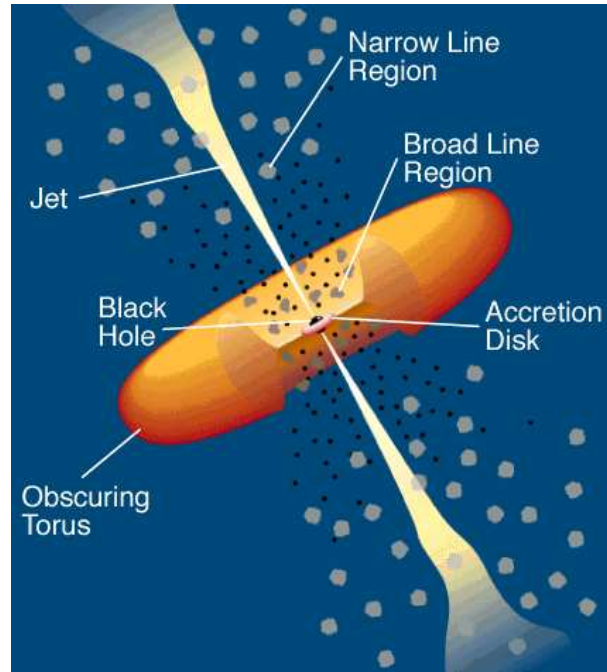


Figure 1.1: A schematic diagram of radio-loud AGN (from [Urry & Padovani, 1995](#)). The SMBH is surrounded by an accretion disk. Broad emission lines are produced by the clouds orbiting the disk. A thick and dusty torus obscures the broad-line region and the inner portion of the jet. Narrow lines are produced by the clouds much farther from the central source.

in an accretion disk. The emitted radiation outshines the disk at ultraviolet (UV) and X-ray wavelengths. One of the prominent theories of jet production asserts that the jet plasma is driven by twisted magnetic field lines threading the accretion disk or the black hole's ergosphere, with the flow collimated and accelerated along the poles ([Blandford & Königl, 1979](#); [Blandford & Payne, 1982](#); [Spruit, 2010](#)). The transfer of energy powering the outflow is thus from gravitational energy to kinetic energy of rotation, and from there via the magnetic field to an outflow, which transports kinetic energy ([Meier et al., 2001](#); [Spruit, 2010](#)). But still, how the gravitational energy is transformed into kinetic and radiative energy is poorly understood.

Strong emission lines at optical and UV wavelengths originate from clouds of gas and dust moving rapidly in the vicinity of accretion disk. The emission lines have line widths over $\sim 1000 \text{ km s}^{-1}$ (and up to $10,000 \text{ km s}^{-1}$). This region is known as broad-line region (BLR), and it is believed to be caused by photo-ionization from the hot accretion disk. The BLR region is located at up to a distance of ~ 1 parsec (pc) from

the SMBH. The torus or warped disk of gas and dust lies well outside the accretion disk and BLR region. Beyond the torus, there are clouds of slower moving gas and dust which produce narrow emission lines. The line width in this case extends only up to 1000 km s^{-1} . This emission region is known as narrow-line region (NLR) and it is believed to be located at a distance of $\sim 10 \text{ pc}$ to 1 kpc from the central engine.

The flow of radiation and energetic particles occur along the two poles of the accretion disk, forming jets and giant radio structures which extend from a few hundred of kpc to several Mpc. Jets are mainly composed of either normal plasma (electron - protons) or pair plasma (electron - positron). When the jet plough into the surrounding extragalactic medium a bow shock is formed and energy is dissipated at the working surface; lobes are formed from turbulent plasma, of which some may even form a cocoon of back-flowing material (Blandford & Königl, 1979). Twin jets fit well with the simple idea of a rotational phenomenon, in which the two poles of the rotation axis provide a natural symmetry for back-to-back jets. A schematic picture of a standard radio-loud AGN is shown in Fig. 1.1.

1.3 The AGN zoo and unification model

The full class of AGN constitute a zoo of different names, detection criteria, flux, spectral, and polarization variability characteristics. Over the years, two major classes of AGN have been established i.e. radio-loud AGN and radio-quiet AGN. The classification is often made on the basis of a parameter value called *radio-loudness factor*, defined as :

$$R_L = \log\left(\frac{f_{5\text{GHz}}}{f_B}\right) \quad (1.1)$$

where $f_{5\text{GHz}}$ is the radio flux at 5 GHz and f_B is the optical B band flux centered at the wavelength $\lambda = 4400\text{\AA}$. Roughly $\sim 10 - 15\%$ of AGN are radio-loud, meaning that they have $R_L \geq 1$, while the rest with $R_L \leq 1$ are classified as radio-quiet AGN (e.g. Kellermann et al., 1989). *However, the object which is radio-quiet is not necessarily radio-silent; it can still show a certain amount of radio emission. The relativistic jets discriminate the two type of sources; the radio emission in radio-loud AGN is dominated by powerful radio jets, which are absent in radio-quiet AGN.*

Both the radio-quiet as well as radio-loud AGN are further sub-classified into *type1* and *type2* objects depending on the strength of emission lines in their optical spectra.

The *type2* objects show only narrow emission lines (FWHM $\sim 1000 \text{ km s}^{-1}$), while the spectrum of *type1* objects is characterized by both narrow and broad emission lines. The line widths of broad emission lines in *type1* sources can extend up to $10,000 \text{ km s}^{-1}$.

The *Seyfert 2 galaxies* belong to the category of *type2* AGN. Their spectrum is characterized by narrow emission lines, and they are hosted in nearby spiral galaxies. This subclass also includes the *Narrow Emission Line Galaxies (NELGs)*, which are also called *Narrow Line X-ray Galaxies (NLXGs)*. Their optical spectra is similar to Seyfert 2 galaxies with narrow emission lines only, but their hard X-ray emission is comparatively stronger.

Seyfert 1 galaxies belong to *type1* AGN. They are similar to the Seyfert 2 galaxies with broad emission lines in their optical spectra (FWHM $\geq 1000 \text{ km s}^{-1}$) in addition to the narrow lines. Many of the Seyfert galaxies are radio-quiet in nature. Other than the types of radio-quiet galaxies defined above, *Broad Absorption Line Quasars (BAL QSOs)* and *Low Ionization Nuclear Emission Line Region galaxies (LINERs)* also belong to this category.

The radio galaxies *Fanaroff-Riley type 1 (FR I)* and *Fanaroff-Riley type 2 (FR II)* (Fanaroff & Riley, 1974) are classified as *type1* objects. The FR II galaxies have radio morphologies characterized by powerful edge-brightened double lobes with prominent hot spots and tend to be found in less dense environments (towards the edge in galactic clusters); while the FR I have radio emission peaking near the nucleus, have rather diffuse edge-darkened lobes and frequently inhabit more dense environments. The FR I galaxies often lie in the center of galactic cluster medium which on interaction with any outward flow from the central engine causes the dissipation of energy.

The radio-loud *type1* AGN are called *Broad Line Radio Galaxies (BLRGs)* at low luminosity and *radio-loud quasars* at high luminosity. The radio-loud quasars are further classified into *Steep-Spectrum Radio Quasars (SSRQs)* with radio spectral index $\alpha_r^1 \geq 0.5$ and *Flat-Spectrum Radio Quasars (FSRQs)* with $\alpha_r \leq 0.5$. The SSRQs and FSRQs are basically luminous BLRGs and both display often FR II radio morphologies with extended lobes. They have broad emission lines in their optical spectra and can thus be classified as type 1 objects, but their continuum spectrum has the peculiar properties of blazars. *Blazars* (Section 1.3.2) are a subclass of radio-loud AGN characterized by strong and rapid flux variability across the entire EM spectrum and strong polarization

¹ $F_\nu \propto \nu^{-\alpha_r}$

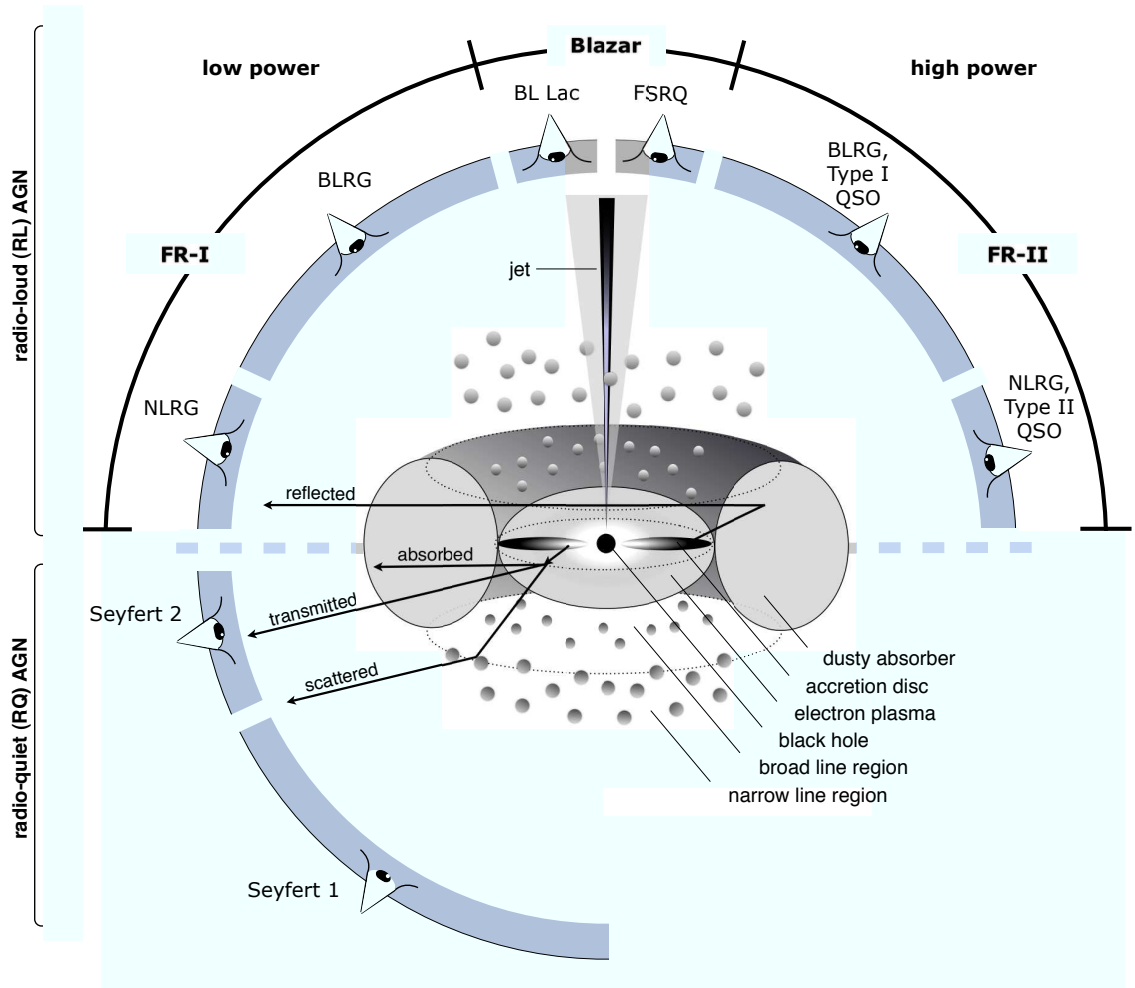


Figure 1.2: A schematic representation of the current understanding the AGN phenomenon in the unified scheme (graphic by Marie-Luise Menzel, MPE). The radio-loud AGN are shown in the upper part and radio-quiet in the lower part.

from radio to optical wavelengths.

1.3.1 The unification model

The idea of unification for different types of AGN came when it was realized that projection effects can play an important role in the interpretation of some of these sources. With the improvement in spectroscopic capabilities, Seyfert galaxies showing features of both *type1* and *type2* objects were discovered. Moreover, polarization observations revealed similar properties for the two classes of Seyfert galaxies (Smith et al., 2004). Since then numerous efforts have been made in determining to what extent different

types of AGN are simply different manifestations of the same object viewed from different angles.

Rowan-Robinson (1977) reported that the central region in many AGN is contaminated by obscuring material in the form of gas and dust (IR through UV), which prevents penetrating some lines of sight. The gas or dust is either distributed in a torus (Pier & Krolik, 1992, 1993) or in a wrapped disk (Sanders et al., 1989). Also, emission from AGN is not isotropic in nature. The radiation is strongly beamed along the jet direction. So, apart from obscuration by accretion disk and torus, there are certain other phenomena like Doppler boosting and superluminal motion (see Section 1.7) which play a key role in modifying the appearance of an AGN. All these effects cause AGN to appear markedly different from different viewing angles.

It is the orientation of the nuclear zone and torus and of the jet with respect to observer which forms the basis of the unification model. If the AGN is orientated more edge-on then the torus hides the central region, and at large angles it would hide the BLR completely. In this case the observed spectrum of an AGN is featured by narrow emission lines, while the observer who is looking face-on at the AGN, is able to see the BLR and related features of the central engine. The observed properties of radio-loud AGN are characterized by relativistic jets, which are absent in radio-quiet AGN. When the line of sight intercepts the radio jet which is then viewed along its axis, relativistic beaming strongly amplifies the luminosity and produces strong variability, polarization, superluminal motion and all the other effects described for the blazar class.

The first attempt of unification was made by Scheuer & Readhead (1979). They proposed that FSRQs were the beamed counterparts of radio-quiet quasars. Orr & Browne (1982) suggested that FSRQs are aligned versions of SSRQs. An alternative suggestion was that SSRQs and FSRQs are increasingly aligned versions of FR II galaxies (Barthel, 1989; Padovani & Urry, 1992). BL Lacs were thought to be more aligned versions of quasars since their line width of emission lines is much smaller than in FSRQs (Blandford & Rees, 1978).

The recent unification scheme is proposed by Urry & Padovani (1995). The various different types of AGN are defined according to their distinct observational properties, as given in Fig. 1.2; the radio-loud AGN are shown in the upper half and radio-quiet AGN in the lower part. According to the current unification model, NLRGs, BLRGs, radio-loud QSOs and blzars belong to the category of radio-loud AGN in which blzars are observed along the line of sight of the observer, radio-loud QSOs and BLRGs at

modest angles, while NLRGs are seen at large angles along the line of sight of the observer. Radio-quiet QSOs, Seyfert galaxies, LINERs etc. belong to radio-quiet AGN. BL Lacs are less luminous than QSOs; this suggests that the parent population of BL Lacs are FR I galaxies and of QSOs are FR II galaxies.

1.3.2 Blazars

BL Lacertae objects (BL Lacs) and flat-spectrum radio quasars (FSRQs) are now usually clubbed together and called *blazars*. In spite of the dissimilarity of their optical spectra (FSRQs show strong broad emission lines, while BL Lacs have only weak or no emission lines in their optical spectra), they share the same peculiar continuum properties (e.g. strong variability and polarization properties). Furthermore, objects such as *Optically Violently Variable Quasars (OVVs)*, *Highly Polarized Quasars (HPQs)*, and *Core Dominated Quasars (CDQs)* turned out to be different empirical definitions of the same kind of objects and are now included in the FSRQ class.

Blazars form a small subset of radio-loud AGN, which are characterized by strong and rapid flux variability across the entire electromagnetic (EM) spectrum (e.g., [Heidt & Wagner, 1996](#); [Rani et al., 2010b, 2013a](#); [Wagner et al., 1996](#), etc.). Blazars exhibit strong polarization from radio to optical wavelengths ([Fan et al., 1997](#); [Impey et al., 1982](#); [Takalo et al., 1994](#)) and usually have core-dominated radio structures. According to the orientation based unified model of radio-loud AGN, blazar jets usually are oriented at a small angle to the line of sight of the observer (e.g. [Urry & Padovani, 1995](#)).

Blazars emit radiation across the whole electromagnetic (EM) spectrum from radio to γ -rays. The EM radiation from blazars is predominantly non-thermal. The spectral energy distributions (SEDs) of blazars have a double-peaked structure (e.g. [Fossati et al., 1998](#); [Ghisellini et al., 1997](#); [Giommi et al., 1995](#)). Based on the location of the first peak of their SEDs (ν_{peak}), blazars are often sub-classified into *low-energy peaked blazars (LBLs)* and *high-energy peaked blazars (HBLs)* ([Padovani & Giommi, 1995](#)); however, it should be noted that the SED peaks can be located at intermediate frequencies as well, giving rise to the *intermediate peaked blazar (IBL)* classification (e.g. [Sambruna et al., 1996](#)). The first component peaks in the near-infrared (NIR)/optical in case of LBLs and at UV/X-rays in HBLs, while the second component usually peaks

at GeV energies in LBLs and at TeV energies in HBLs. More specifically, [Nieppola et al. \(2006\)](#) classify over 300 BL Lacs and suggest that blazars with peak frequency, $\nu_{peak} = 10^{13-14}$ Hz are LBLs, those with $\nu_{peak} = 10^{15-16}$ Hz are IBLs, and those with $\nu_{peak} = 10^{17-18}$ Hz are HBLs. The location of peaks in the SEDs of LBLs and HBLs is shown in [Fig. 1.3](#).

1.4 Acceleration in jets

The non-thermal emission in blazar jets extending from hundreds of pc to kpc scale implies that a powerful particle acceleration mechanism is at work. Particles accelerated to very high energies have been considered as a prime candidate source of extragalactic cosmic rays (e.g. [Brecher & Burbidge, 1972](#)). The AGN jets are believed to be collimated by magnetic fields and accelerated through conversion of magnetic energy to bulk kinetic energies. The jet emission can be driven by kinetic energy, e.g. the dissipation of shocks and/or by reconnection of magnetic field lines, ([Blandford & Rees, 1978](#); [Blandford & Znajek, 1977](#)). In short, the jets of AGN carry a large fraction of the accreted power off the super massive black holes.

Black holes alone are not able to form jets and therefore magnetic fields are required to form such powerful outflows. The black hole magnetosphere has to be anchored in the accretion flow, extracting angular momentum from the black hole through a Poynting flux jet ([Blandford & Znajek, 1977](#); [Meier et al., 2001](#)). The powering of a jet solely by the accretion disk (without magnetic field) is still controversial. After the formation of the plasma flow close to the central engine, it will be collimated and accelerated in the presence of strong magnetic fields. The collimation zone spans a distance scale of up to $\sim 10^3$ Schwarzschild radii, for which magnetic fields may play a dominant role. Kelvin–Helmoltz instabilities are considered as one of the reason why we see wiggly jets at a distance of hundreds of kpc from their site of origin in the nucleus. A brief review of recent developments in the area of magnetic acceleration can be found in [Komissarov \(2011\)](#).

The Kelvin–Helmoltz instabilities (due to pressure imbalance between the external medium and the jet) can lead to the development of turbulence and formation of shocks causing enhanced emission seen on parsec and kpc scales. Much of the rich structure seen in some jets may result from the presence of such instabilities ([Sikora et al., 2005](#)). The observations of synchrotron radiation from jets imply that the material in the

jet is a magnetized plasma. The content of the plasma may be electrons–protons or electrons–positrons or a mixture of these. The plasma in relativistic jets is highly hydro-magnetically turbulent. This fact is confirmed by observations of low linear polarization, lower than is expected from synchrotron radiation, which means that the magnetic field is randomly oriented in absence of self-absorption.

Turbulence causes the formation of ‘eddies’ of many different length scales. Most of the kinetic energy of the turbulent motion is contained in these ‘eddies’. The energy cascades from large to smaller scales creating smaller and smaller structures, and producing a hierarchy of ‘eddies’. Hence, the eddies are the regions of higher electron density, velocity, and magnetic field etc.. As the disturbance propagates down the jet, it brightens at sites where it encounters density and/or magnetic field enhancements and fades where it encounters diminishments. It is mainly the magnetic field fluctuations that amplify or reduce the flux density at a given location in the shock (Marscher, 1996). As a result, the interaction of shock wave and turbulent medium in a jet may explain some key characteristics of blazar emission. A brief discussion of the various emission processes is given in the next Section.

1.5 Emission mechanisms

The electromagnetic radiation from AGN is spread over a wide range of frequencies through radio to γ -rays. This is evident in the spectral energy distribution of BL Lac shown in Fig. 1.3. Such a broad spectrum occurs because AGN emit a mixture of thermal and non-thermal radiation. The low frequency radio emission is the synchrotron radiation from the kpc scale jet, while the high frequency radio to optical emission is dominated by the synchrotron mechanism from the the inner parsec scale region of the jet. The accretion disk emits thermal optical-UV radiation, and the X-rays and γ -rays are produced by inverse-Compton scattering of synchrotron photons and also of the seed photons outside the jet (e.g. photons from accretion disk, BLR region etc.). The details of thermal and non-thermal emission mechanisms are given in the following subsections.

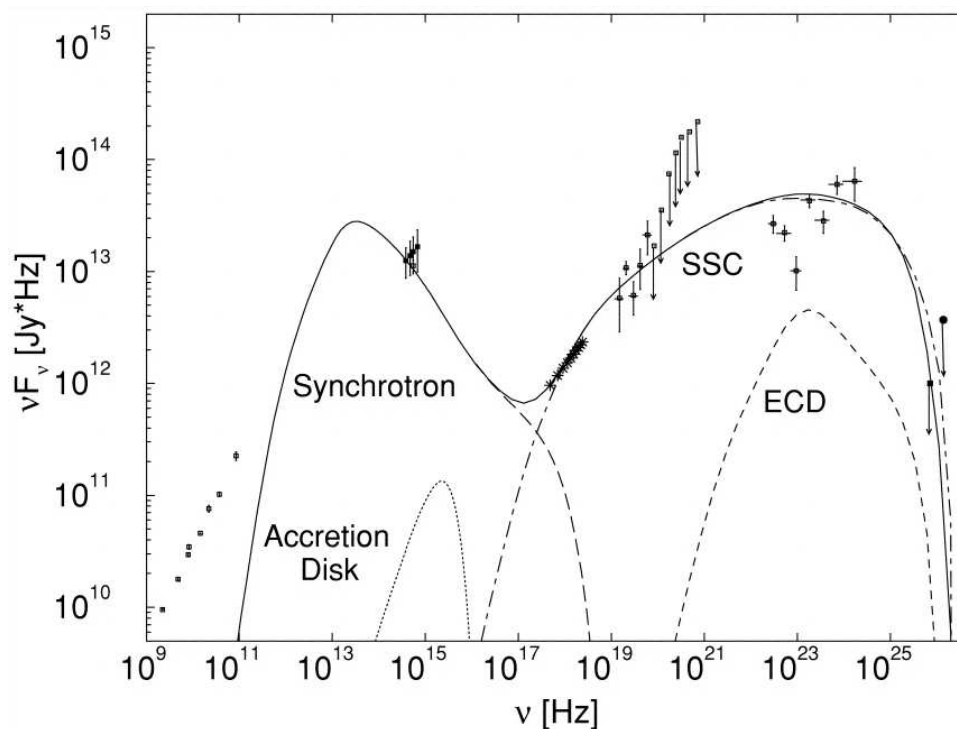


Figure 1.3: The broadband SED of BL Lac object showing the contribution of various emission mechanisms from radio to γ -rays. The low energy part of the SED is mainly dominated by non-thermal (synchrotron) emission with an additional thermal contribution from the accretion disk. However, the high-energy photons are produced either by SSC or EC. Figure courtesy : [Böttcher & Bloom \(2000\)](#).

1.5.1 Thermal radiation

The radiation emitted by a body due to its thermal energy which is a function of its temperature is known as *thermal radiation*. The emitted thermal energy is characterized by the black-body radiation and can be defined by Planck’s Law. The thermal structure of the accretion disk of an AGN follows a negative temperature gradient which means its temperature decreases as a function of radial distance from the SMBH ([Shakura & Sunyaev, 1973](#)). The overall structure of the accretion disk is governed by the accretion rate and the mass of the central engine. For standard geometrically thick and optically thin accretion disks, the temperature changes as a function of the radial distance from the center as $T \propto r^{-3/4}$ ([Shakura & Sunyaev, 1973](#)). The temperature (T) as a result depends on the mass of the central BH (M_{BH}) as $T \propto M_{BH}^{-1/4}$. Therefore, the accretion disk is a “multi-color” black body where each annulus radiates following Planck’s Law,

given by

$$F(\nu) = \frac{2h\nu^3/c^2}{\exp(h\nu/kT(r)) - 1} \quad (1.2)$$

where h , c , and k are Planck's constant, the speed of light in vacuum, and the Boltzmann's constant, respectively, and $T(r)$ is the temperature of the black body at radial distance r from SMBH. After integrating over r , the emission spectrum of the accretion disk as a whole is given by

$$F(\nu) \propto \nu^{1/3} \exp\left(-\frac{h\nu}{kT(r_{max})}\right) \quad (1.3)$$

where r_{max} is the radius at which the maximum dissipation of energy per unit area occurs, and lies somewhat outside the marginally stable orbit (Krolik, 1999). The wavelength (λ_{max}) at which the intensity peaks is determined by Wien's Displacement Law:

$$\lambda_{max}T = 0.29 \text{ cmK} \quad (1.4)$$

The temperature of the accretion disk in AGN vary between ~ 4000 to $40,000$ K, hence it emits optical-UV radiation. So, the optical-UV part of electromagnetic spectrum of AGN is significantly dominated by thermal emission from the accretion disk (Malkan & Sargent, 1982). The contribution of thermal emission in the overall SED of blazars is shown in Fig. 1.3.

1.5.2 Synchrotron radiation

When the relativistic charged particles are accelerated in the presence of a magnetic field (B), then they emit electromagnetic radiation which is known as *synchrotron radiation*. The relativistic jets of AGN containing magnetized relativistic plasma emit synchrotron radiation at radio to optical (sometimes X-ray) frequencies. So, the lower energy part of blazar SEDs is dominated by the synchrotron mechanism (Figure 1.3). The most of the synchrotron luminosity occurs at a critical frequency, ν_c which is given by

$$\nu_c = 2.8 \times 10^6 B \gamma^2 \quad (1.5)$$

where γ is the Lorentz factor ($\gamma = (1 - v^2/c^2)^{-1/2}$), B is magnetic field in Gauss, and ν_c is in Hz.

The average rate at which energy is lost is given by

$$\frac{dE}{dt} = \frac{4}{3} \sigma_T c \gamma^2 U_{mag} \quad (1.6)$$

where σ_T is the Thompson scattering cross-section and U_{mag} is the energy density in the magnetic field ($U_{mag} = B^2/8\pi$).

The spectrum of power emitted by an ensemble of electrons follows a power law given by

$$P(\nu) \propto \nu^{-\alpha}, \quad \alpha = \frac{p-1}{2} \quad (1.7)$$

where α is the spectral index of the observed power law and p is the power law index of energy distribution of emitting electrons.

The power law spectrum is naturally produced if the emitting electrons follow a power law distribution of energy ($N(E)dE \sim E^{-p}$). Such power law distribution of electrons can be produced in a variety of ways such as second order Fermi-acceleration through shocks (Blandford, 1990; Kirk et al., 2000). But, the observer will see this power law spectrum only if there is no absorption by the emitting region. In presence of magnetic field, the emitted photons can be absorbed by the emitting region itself or by some other medium in between. The absorption of emitted radiation by the emission region itself is known as *synchrotron self-absorption* at low radio frequencies, which produces an inverted power law spectrum with index, $\alpha \sim 5/2$.

1.5.3 Inverse-Compton scattering : SSC & EC

In *inverse-Compton (IC) scattering*, a (seed) photon gains energy when it is scattered off by a high-energy electron. Whenever the moving electron has sufficient kinetic energy compared to the photon, energy is transferred from the electron to the photon. This process therefore converts low energy photons (IR/optical) to high-energy photons (X-ray/ γ -ray). It is the dominating process through which electrons in the AGN jets can emit high-energy photons.

In the framework of leptonic jet models, in which the radiative signatures of the jet are dominated by the relativistic electrons (and possibly electron-positron pairs) in the jet, the high-energy emission, at X-ray and γ -ray energies, is believed to be produced through Compton up-scattering of soft seed photons by the same population of relativistic electrons which also produces the synchrotron emission at lower frequen-

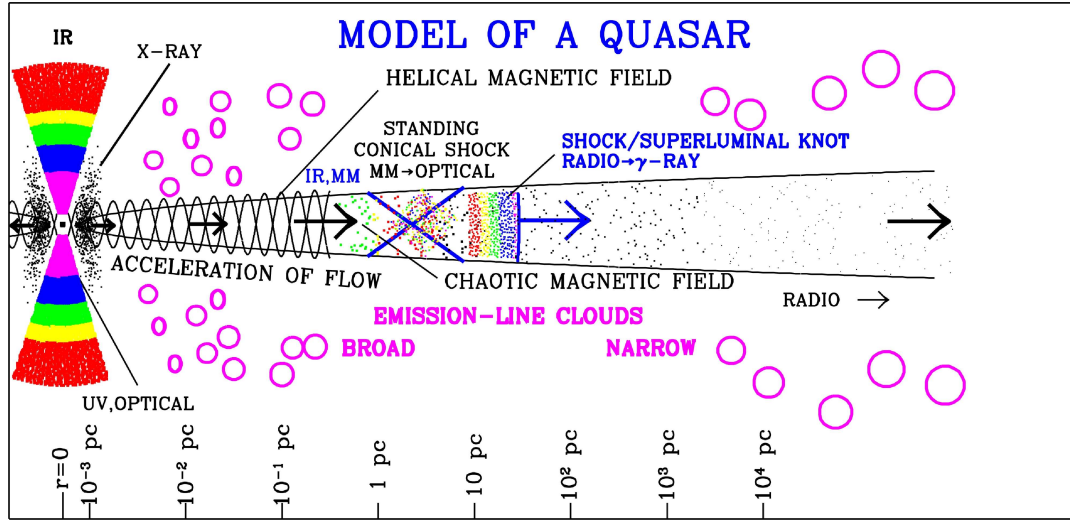


Figure 1.4: A cartoon illustrating location of different regions of a radio-loud quasar from the central engine in terms of Schwarzschild radii of the black hole and its various physical and emission components. The radiation produced in the jet is relativistically beamed along the line of sight to the observer (Figure Courtesy : Alan Marscher).

cies (e.g. Böttcher et al., 2007; Krawczynski, 2004; Sikora & Madejski, 2001). Possible sources of the target photons for Compton scattering are (a) the synchrotron photons themselves (SSC for Synchrotron Self-Compton), (b) external photons from the accretion disk entering the jet directly from behind (ECD for External Comptonization of Disk photons), (c) external photons from the broad line regions and other circumnuclear debris, which is reprocessing part of the central accretion disk luminosity, (d) jet synchrotron emission, reflected off circumnuclear debris, and/or (e) infrared emission from circumnuclear dust (IRC for Infra-Red Comptonization). The energy loss rate in IC scattering is given by

$$\frac{dE_{IC}}{dt} \propto \gamma^2 U_{ph} \quad (1.8)$$

where U_{ph} the energy density of the seed photon field. The frequency of up-scattered photons (ν_f) is approximately given by

$$\nu_f \sim \gamma^2 \nu_i \quad (1.9)$$

where ν_i is the frequency of seed photons.

The first peak in the SED of blazars is thought to originate from synchrotron emis-

sion. The high-energy part of blazar spectrum is mainly produced by the IC (SSC or EC) scattering processes (see Fig. 1.3). The optical-UV photons are up-scattered to GeV-TeV energy ranges in AGN jets by these scattering processes. In LBL and FSRQ, the second peak is situated in the hard X-ray/ γ -ray band, at lower energies with respect to the HBL. As a consequence, for blazars, the X-ray band contains contributions from both the synchrotron emission and the IC emission, giving rise to a wide range of slopes. In HBLs, the X-ray emission is the high-energy tail of the synchrotron emission and the resulting slope is steep; for LBL and FSRQ it is the rising part of the inverse-Compton bump and thus the slope is flat. The strong γ -ray emission is produced in all blazars through IC scattering.

1.6 Shocks and plasma instability

The relativistic shocks propagating down in a conical jet were proposed to explain the observed superluminal knots in AGN (Blandford & Rees, 1978). A major increase in either the bulk speed or internal energy of the jet flow will cause a shock wave to form and propagate down the jet (Marscher, 1996) (Fig. 1.4). A shock front compresses the plasma resulting into an increase in its internal energy, magnetic field (B), and velocity etc.. In this process, the energy of the particles increase because of successive shock-crossing, their velocity distribution becomes isotropic with respect to the flow due to internal scattering. By crossing the shock front multiple times, particles can be accelerated to high-energy before they leave the acceleration region (diffusive shock acceleration, Schwadron et al., 2008). The acceleration is most efficient when the magnetic field is perpendicular to the shock front, as the particles can stream more freely along the field lines. Hence, the synchrotron emission in shocks can be amplified by

1. the increase in density behind a shock front,
2. the increase in magnetic field strength,
3. the increase in internal energy, and
4. by diffusive shock acceleration.

The particles accelerated across the shock front emit radiation over a range of frequencies depending upon their energy.

For a shock induced flare, the emitted synchrotron spectrum evolves following three stages depending on the dominant emission-loss mechanism of the electrons (Fromm et al., 2011; Marscher & Gear, 1985; Türler, 2011) :

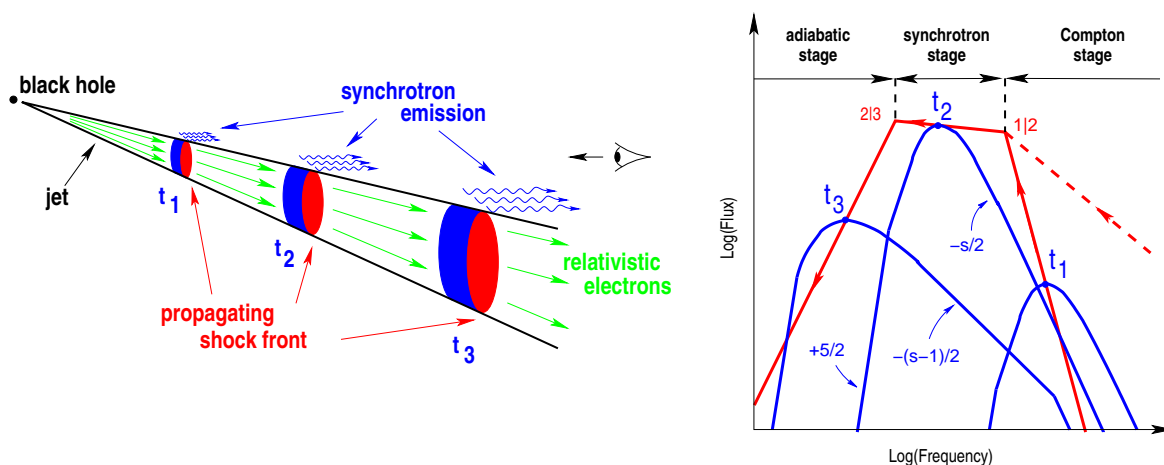


Figure 1.5: A schematic diagram of the standard shock-in-jet model (Marscher & Gear, 1985) showing a propagating shock wave in a relativistic jet (left) and the three-stage spectral evolution (right) according to the model. Figure Courtesy : Türler (2011).

1. Compton losses,
2. Synchrotron losses, and
3. Adiabatic (non-radiative) losses.

As a consequence, the flare follows a particular trend in the turnover flux density – turnover frequency ($S_m - \nu_m$) diagram as shown in Fig. 1.5. During the first stage, Compton losses are dominant and ν_m decreases with increasing jet radius, R , while S_m increases. In the second stage, where synchrotron losses are the dominating energy loss mechanism, ν_m continues to decrease, while S_m remains almost constant. Both S_m and ν_m decrease in the final, adiabatic stage. Therefore, the flare is spread over many decades of frequencies where the high-energy photons emerge sooner and within a small distance across the shock front. The thickness of this sheet increases as frequency decreases (Marscher, 1996). As a result, in a shock-induced flare, the γ -ray and X-ray flux peaks first, followed by optical, IR and then radio. The frequency stratification in a shock induced flare is shown in Fig. 1.6.

Shock-shock interaction is one of the feasible mechanism that could accelerate particles which result into broadband flares. The scenario could be explained by the interaction of a moving shock wave with a stationary shock/feature in the jet. Stationary features are a common characteristic of compact jets (Fromm et al., 2013a; Jorstad et al., 2001; Lister et al., 2009). These could be either standing re-collimation shocks

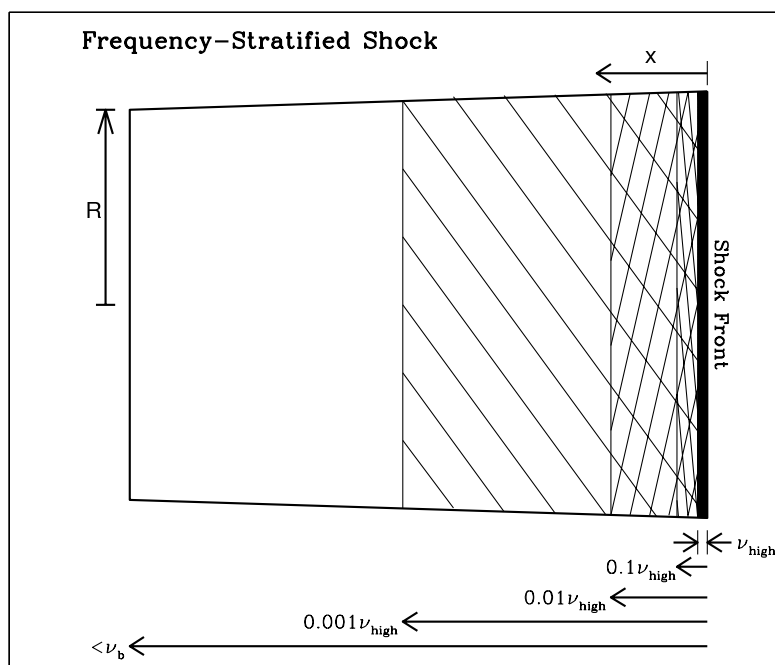


Figure 1.6: A sketch of shock propagating down a relativistic jet. The electrons are accelerated at the shock front and drift behind the shock while losing energy to radiative losses. Figure courtesy : [Marscher \(2009\)](#).

caused by pressure imbalances at the boundary between the jet fluid and the external medium (Kelvin–Helmholtz instabilities), or could be the sites of maximized Doppler beaming where a curved jet points most closely to the line of sight. Bends can also cause stationary features, either because the jet turns more into the line of sight or due to the formation of a shock ([Alberdi et al., 1993](#)). Multiple shocks propagating down the jet can also lead to shock-shock interactions. Hydrodynamic simulations of a shock front passing through a steady relativistic flow revealed formation of multiple conical shocks trailing the main shock front ([Agudo et al., 2001](#)). A detailed overview about formation of stationary features in the jet and shock-shock interaction is given in [Fromm et al. \(2013\)](#).

1.7 Relativistic effects

When a source of radiation moves with relativistic velocities towards the observer (like in blazars) a series of relativistic effects will take place. If a source is moving at a velocity close to the speed of light along a direction which forms a small angle with the

observer's line of sight, then the time intervals between the emission of two successive photons as measured in the observer's frame is reduced, and the source appears to move faster than it actually does (Blandford & Königl, 1979). This effect is known as *Superluminal motion*. The apparent velocity of the emitting material in this case is given by

$$v_{app} = \frac{\beta c \sin \theta}{1 - \beta \cos \theta} \quad (1.10)$$

where θ is the angle between the direction of motion of the emitting material and the observer line of sight and $\beta = v/c$, where v is the velocity of the plasma within the jet and c is the velocity of light in vacuum.

The emitted radiation will be collimated in the direction of motion into a cone with opening angle $\theta \sim 1/\Gamma$, where Γ is the bulk Lorentz factor, and the intensity of the radiation will be amplified by Doppler boosting in the direction of motion. These effects are all direct consequences of the Lorentz transformations of special relativity and they are known as *relativistic beaming*. The parameter which quantifies the relativistic beaming is the Doppler factor :

$$\delta = \frac{1}{\Gamma(1 - \beta \cos \theta)} \quad (1.11)$$

where Γ is the Lorentz factor of flow, given by

$$\Gamma = [1 - \beta^2]^{-1/2} \quad (1.12)$$

As a consequence of the effects discussed above, the time interval and frequency will transform as

$$\Delta t = \delta^{-1} \Delta t' \quad (1.13)$$

$$\nu = \delta \nu' \quad (1.14)$$

As a result, the observed flux density of the plasma from a moving knot is modified as

$$f(\nu) = \delta^{2+\alpha} f'(\nu') \quad (\text{steady state}), \quad (1.15)$$

$$f(\nu) = \delta^{3+\alpha} f'(\nu') \quad (\text{moving structure}). \quad (1.16)$$

where the primed quantities refer to the rest frame of the source and α is the spectral index. Before the radiation is observed by the observer it is modified due to the rela-

tivistic effects. So, what the observers see is not the same as it is emitted by the source. Hence, relativistic effects play a key role in the appearance of AGN and form the backbone of the unification model. In conclusion, the observed emission from blazars is greatly enhanced by relativistic effects in the jet.

1.8 Geometrical effects

Geometrical effects can modify the observed emission in blazars and can also introduce variations in amplitudes, time scales and/or flares in the observed flux. The curved radio structures, and moving emission regions in bent trajectories are frequently found in radio jets (ballistic motion) (Agudo et al., 2012; Lobanov & Zensus, 2001; Ly et al., 2007; Piner et al., 2009). Theoretical models for such oscillating, bent structures include helical modes in hydrodynamic jets (Hardee, 1987) or in magnetized jets (Königl & Choudhuri, 1985). When a shock moves down the jet with a helical structure, each time the shock meets the twist of the helical structure that is closest to our line of sight (say the near-side of a conical jet) then boosting will be maximum. For a conical jet the time between the shock intersections and the helical structure might change, implying a ‘quasi-periodic oscillation’ (Camenzind & Krockenberger, 1992). The quasi-periodic activity thought to be tightly connected to perturbations in the relativistic flow, either due to instabilities, or due to injection cycles at the origin of the jet, influenced by the accretion behavior of the central engine. This recurring activity in AGN jets and its connection to the central engine is however not yet well understood.

Chapter 2

The BL Lac Object S5 0716+714

In this thesis, I study the broadband variability of the γ -ray active blazar S5 0716+714, and relate the flux variations to existing VLBI observations at high frequencies. The BL Lac S5 0716+714 is an extreme blazar in terms of its variability properties with a featureless optical spectrum. This source was cataloged in the late seventies as the optical counterpart of an extra-galactic radio source (Kühr et al., 1981), and later identified as a BL Lac object due to its featureless optical spectrum and high linear polarization (Biermann et al., 1981). Various attempts to determine its redshift failed and only a lower limit of $z \geq 0.3$ was suggested from its starlike appearance and the absence of a host galaxy (Stickel et al., 1993; Wagner et al., 1996). Nilsson et al. (2008) claimed a value of $z = 0.31 \pm 0.08$ based on the photometric detection of the host galaxy. Very recently, the detection of intervening Ly α systems in the ultra-violet spectrum of the source constrains the earlier estimates into a redshift range of $0.2315 < z < 0.3407$ (Danforth et al., 2013). The source has been classified as an intermediate-peak blazar (IBL) by Giommi et al. (1999), as the turnover frequency of the first spectral energy distribution (SED) peak lies between 10^{14} and 10^{15} Hz, and thus does not fall into the wavebands specified by the usual definitions of low and high energy peak blazars (i.e. LBLs and HBLs). A concave X-ray spectrum in 0.1–10 KeV band adds another factor in support of the IBL nature of the source (Ferrero et al., 2006; Foschini et al., 2006).

2.1 Radio Properties

In the radio bands, 0716+714 is an intraday variable source (Heeschen et al., 1987; Witzel et al., 1986). Intraday variability (IDV) at radio wavelengths is likely to be a combination of intrinsic and extrinsic (due to inter-stellar scintillation) mechanisms. A significant correlation between optical-radio flux variations at day-to-day timescales has been reported by Wagner et al. (1996). The frequency dependence of the variability index at radio bands is not found to be consistent with the inter-stellar scintillation model (Fuhrmann et al., 2008), which implies the presence of very small emitting regions ($<100 \mu\text{as}$) within the source. The IDV time scale does show evidence in favor of an annual modulation, suggesting that the IDV of 0716+714 is dominated by interstellar scintillation (Liu et al., 2012). From the observed IDV at cm-wavelengths a typical brightness temperature of $T_B = 10^{15-17}$ K was derived (Kraus et al., 2003). A Doppler factor of 15 to 50 would be needed to bring these brightness temperatures down to the inverse-Compton limit of 10^{12} K.

Very Long Baseline Interferometry (VLBI) studies of the source spanning more than 20 years at cm-wavelengths show a core-dominated evolving jet extending several 10 milli-arcseconds to the north (Eckart et al., 1986, 1987; Witzel et al., 1988). On milli-arcsecond scales (VLBI observations), 0716+714 has a core-dominated structure with a bright point-like core and a faint diffuse jet pointing at the position angle of $\sim 20^\circ$. At the scale of arcseconds (VLA observations), the source structure is again core-dominated, its jet is double-sided, located along the position angle of $\sim 100^\circ$ (misaligned with the VLBI jet by $\sim 80^\circ$), and has extended diffuse lobes (Wagner et al., 1996). The long-term kinematics of the source has been extensively studied, and two mutually exclusive models have been suggested: one implies relatively fast outward motion of the superluminal components in the jet with speeds ranging from $5c$ to $16c$ (“fast scenario”, Bach et al., 2005), and the other claims the jet to be stationary, with significant non-radial (“precession”) motion of the jet as a whole (“stationary scenario” Britzen et al., 2009). Both scenarios are based on the reanalysis of historical VLBI observations that span the years 1992-2001 (“fast”) and 1992-2006 (“stationary”) at frequencies from 5 to 43 GHz.

2.2 Optical Properties

The source S5 0716+714 is a highly variable BL Lac object at optical frequencies. Optical IDV in 0716+716 was first detected by [Quirrenbach et al. \(1991\)](#), who also computed discrete autocorrelation functions to search for possible periodicities in the flux variations and found a period of 4 days. Later on also microvariability has been studied by several authors. The source is one of the brightest BL Lac objects in optical bands. Unsurprisingly, this source has been subject of many optical monitoring campaigns on intraday (IDV) timescales (e.g. [Heidt & Wagner, 1996](#); [Montagni et al., 2006](#); [Rani et al., 2010a, 2011](#); [Wagner et al., 1996](#), and references therein). The source has shown five major optical outbursts separated roughly by $\sim 3.0 \pm 0.3$ years ([Raiteri et al., 2003](#)). High optical polarization $\sim 20\% - 29\%$ have also been observed in the source ([Fan et al., 1997](#); [Takalo et al., 1994](#)). [Gupta et al. \(2009\)](#) analyzed the optical light curves of the source observed by [Montagni et al. \(2006\)](#) and reported evidence of nearly periodic oscillations ranging between 25 to 73 minutes on several different nights. Good evidence of the presence of ~ 15 -min periodic oscillation at optical frequencies has been reported by [Rani et al. \(2010a\)](#). A detailed multiband short-term optical flux and color variability study of the source is reported in [Rani et al. \(2010b\)](#).

A contemporaneous optical-radio activity has also been observed in the source ([Tornikoski et al., 1994](#); [Villata et al., 2008](#)). [Villata et al. \(2007\)](#) observed a simultaneous optical-radio outburst in the source during GASP-WEBT-AGILE campaign in 2007. [Raiteri et al. \(2003\)](#) noticed that in the 1994-2001 observing period, major optical outbursts of 0716+714 do not corresponds to bright radio flares. They found only modest radio counterparts during bright optical flares. Thus, the optical emission region of the jet is sometimes opaque and sometimes not completely opaque to the radio frequencies. This could be a signature of varying opacity in the source. From the analysis of BVRI data taken in 1994–1995, [Ghisellini et al. \(1997\)](#) found no correlation between spectral index and brightness level in the long-term trend, but were able to detect a spectral flattening when the flux was higher during rapid flares. A flattening of optical spectrum during bright phases was also observed by [Rani et al. \(2010b\)](#).

2.3 High Energy Emission

The source was first observed at X-ray frequencies in 1977 (Biermann et al., 1992). A spectral and temporal analysis was possible for the first time with ROSAT observations in March 1991 (Cappi et al., 1994; Urry et al., 1996; Wagner, 1992; Wagner et al., 1996). These studies suggest an existence of two spectral components in order to account for the X-ray spectrum in the 0.1–2.4 KeV band. These components were interpreted as synchrotron and IC emission, respectively. The shape of the X-ray spectrum within 0.5–10 KeV band was further constrained by Ferrero et al. (2006). They argued for the presence of two power laws, a steep one at soft energies plus a flat one at hard energies. The soft power law was related to synchrotron emission of the high-energy electrons, whereas the hard power law was interpreted as IC emission from the low-energy electrons. Therefore, X-ray observations provide evidence for a concave X-ray spectrum in 0.1–10 KeV band, a signature of the presence of both, the steep tail of synchrotron emission and a harder Inverse Compton (IC) component. Interestingly, no emission or absorption feature has been detected in the source at X-ray frequencies.

The source was first detected at γ -rays ($E > 100$ MeV) by EGRET on board the *Compton Gamma-ray Observatory (CGRO)* in 1991 and later several times between 1991 to 1996 (Hartman et al., 1999; Lin et al., 1995). Two strong γ -ray flares on September and October 2007 were observed by Chen et al. (2008). Recently, the MAGIC collaboration reported the first detection of very high energy (VHE) γ -rays ($E > 400$ GeV) from the source at 5.8σ significance level (Anderhub et al., 2009). The discovery of S5 0716+714 as a VHE γ -ray blazar happened during a very bright optical state, suggesting a possible correlation between VHE γ -ray and the optical emissions. The source has been detected by *Fermi*/LAT since the beginning of its observations. The source also belongs to bright blazars of the *Fermi*/LAT Bright AGN Sample (LBAS) (Abdo et al., 2010a), where the GeV spectra of the source is governed by a broken power law. The combined GeV-TeV spectra of the source displays absorption-like features in 10-100 GeV energy range (Senturk et al., 2011).

2.4 Broadband Variability

The broadband flaring behavior of the source is quite complex. The literature study reveals that the broadband flaring activity of the source is not simultaneous at all

frequencies (Chen et al., 2008; Ostorero et al., 2006; Villata et al., 2008; Vittorini et al., 2009). Also, it is hard to explain together the slow modes of variability at radio and hard X-ray bands and the rapid variability observed in the optical, soft X-ray, and γ -ray bands using a single component SSC model (see Chen et al., 2008; Giommi et al., 2008; Villata et al., 2008; Vittorini et al., 2009). The X-ray spectrum of the source is contributed by both synchrotron as well as inverse-Compton (IC) emission (Ferrero et al., 2006; Foschini et al., 2006), and the simulations optical– γ -ray variations favor a synchrotron self-Compton (SSC) emission mechanism (Chen et al., 2008; Vittorini et al., 2009). Despite of several efforts to understand the broadband flaring activity of the source, we still do not have substantial intimation of the emission mechanisms responsible for its origin.

Chapter 3

Multi-wavelength Observations, Data Reduction and Analysis Techniques

A series of multi-frequency observations covering most of the electromagnetic spectrum were carried out in the course of this thesis. From April 2007 to April 2012, the BL Lac object S5 0716+714 was observed using both ground and space based observing facilities. These multi-frequency observations extend over a frequency range between radio and γ -rays including optical and X-rays. In addition to Very Long Baseline Interferometry (VLBI) at radio wavelengths, observations were performed using several ground based telescopes covering radio and optical frequencies. The high frequency observations were carried out using the *Swift* X-ray telescope (XRT), and the *Fermi*-Large Area Telescope (LAT) aboard the *Swift* and *Fermi* satellites, respectively. This chapter is structured as follows. Section 3.1 covers the details of the broad-band observations and data reduction. A brief introduction of the statistical analysis techniques used in the thesis is given in Section 3.2. Section 3.3 provides a brief description of VLBI observations and data reduction.

Table 3.1: Ground based radio observatories

Observatory	Telescope diameter	Frequency (GHz)
Effelsberg, Germany	100 m	2.7, 4.8, 6.7 8.3, 10.7, 15, 23 32, 43
UMRAO, USA	26 m	4.8, 8, 14.5
NOTO, Italy	32 m	5, 8, 22, 43
Urumqi, China	25 m	4.8
OVRO, USA	40 m	15
Metsahovi, Finland	14 m	37
PdBI, France	6×15 m	86, 143, 230
Pico Veleta, Spain	30 m	86, 143, 230
SMA, USA	8×6 m	230, 345

3.1 Observations and data reduction

3.1.1 Radio observations

I have collected 2.7 to 230 GHz radio wavelength data of the source over a time period of April 2007 to January 2011 (JD = 2454200 to 2455600) using the 9 radio telescopes listed in Table 3.1. The cm/mm radio light curves of the source were observed as a part of observations within the framework of F-GAMMA program (*Fermi*-GST related monitoring program of γ -ray blazars, e.g. [Angelakis et al., 2008](#); [Fuhrmann et al., 2007](#)). The overall frequency range spans from 2.7 GHz to 230 GHz using the Effelsberg 100 m telescope (2.7 to 43 GHz) and the IRAM 30 m Telescope at the Pico Veleta (PV) Observatory (86 to 230 GHz). These flux measurements were performed quasi-simultaneously using the cross-scan method slewing over the source position, in azimuth and elevation direction with an adaptive number of sub-scans for gaining the desired sensitivity. Subsequently, atmospheric opacity correction, pointing off-set correction, gain correction, and sensitivity correction were applied to the data.

This source is also a part of an ongoing blazar monitoring program at 15 GHz at the Owens Valley Radio Observatory (OVRO) 40-m radio telescope which provides the radio data sampled at 15 GHz. We have also used the combined data from the University of Michigan Radio Astronomy Observatory (UMRAO; 4.8, 8 and 14.5 GHz, [Aller et al., 1985](#)) and the Metsähovi Radio Observatory (MRO; 37 GHz; [Teräsranta et al., 2004, 1998](#)), which provide us with radio light curves at 5, 8, 15, and 37 GHz. Additional flux monitoring at 5, 8, 22, and 43 GHz radio bands is obtained using the 32

m telescope at NOTO radio observatory. The Urumqi 25 m radio telescope monitors the source at 5 GHz. The 230 and 345 GHz data are provided by the Submillimeter Array (SMA) Observer Center¹ data base (Gurwell et al., 2007), complemented by some measurements from PV and the Plateau de Bure Interferometer (PdBI). The radio light curves of the source are shown in Fig. 4.1. The mm observations are closely coordinated with the other flux density monitoring programs conducted by IRAM.

3.1.2 Optical monitoring

Optical V passband data of the source were obtained from the observations at the 1.5-m Kanata Telescope located on Higashi-Hiroshima Observatory from February 14, 2009 to June 01, 2010 (JD = 2454877 to 2455349). The Triple Range Imager and SPECTrograph (TRISPEC) (Watanabe et al., 2005) was used for the observations from May 25, 2008 to January 31, 2010 (JD = 2454612 to 2455228). The HOWPol (Hiroshima One-shot Wide-field Polarimeter, Kawabata et al., 2008) was used for later observations. Exposure times for an image ranged from 10 to 80 s, depending on the magnitude of the object and sky conditions. The photometry on the CCD images was performed in a standard procedure : after bias subtraction and flat-field division, magnitudes were calculated using the aperture photometry technique. The radius of the aperture, which depended on the seeing size of each night, was 3–5 arcsec corresponding to 3–4 pixels on the optical CCD in TRISPEC and 10–17 pixels in HOWPol. No correction was performed for the contamination of the host galaxy in our observations as the source shows almost no contribution of thermal emission in the optical spectrum.

Additional optical V passband data were obtained from the 2.3 m Bok Telescope of Steward Observatory from April 28, 2009 through June 2, 2010. These data are from the public data archive that provides results of polarization and flux monitoring of bright γ -ray blazars selected from the *Fermi*/*LAT*-monitored blazar list². Optical V passband archival data extracted from the *American Association of Variable Star Observers* (AAVSO; see <http://www.aavso.org/> for more information) for a time period between September 2008 and January 2011 was also included.

¹<http://sma1.sma.hawaii.edu/callist/callist.html>

²<http://james.as.arizona.edu/~psmith/Fermi>

3.1.3 X-Ray data

The Earth’s atmosphere does not allow X-rays to penetrate through it, so X-ray observations are only possible from space. For the study presented in this thesis, X-ray data was obtained with the X-ray Telescope (XRT) on board the *Swift* satellite¹. The Swift Gamma Ray Burst Explorer (Gehrels et al., 2004) is part of NASA’s medium class “Explorer” spacecraft series (MIDEX), one of their longest running spacecraft series, with highly durable and long-lasting spacecrafts, probing a wide range of scientific areas. It was launched on November 20, 2004 from Cape Canaveral and since then it is successfully operating in a nearly circular low Earth orbit of ~ 600 km altitude. The main goal of Swift is to detect gamma-ray bursts (GRBs) and to observe their afterglows within a few seconds after the detection. The *Swift* satellite has three instruments on board :

1. Ultra-Violet Optical Telescope (UVOT) [170–650 nm],
2. X-ray Telescope (XRT) [0.2–10 KeV], and
3. Burst Alert Telescope (BAT) [15–150 KeV].

The BAT continuously scans a large fraction of the sky, watching out for sudden bursts of γ -ray radiation. During the times at which Swift is not detecting or following up on GRBs, the XRT and UVOT instruments are used to observe interesting targets, which can be proposed via a Target of Opportunity or through regular science proposals. This provides an excellent opportunity for AGN science to obtain simultaneous observations in the spectral region where the synchrotron branch connects to the inverse-Compton branch.

XRT

The XRT (Burrows et al., 2000) uses a Wolter Type I X-ray telescope with 12 nested mirrors, focused onto a single MOS charge-coupled device (CCD) similar to those used by the XMM-Newton EPIC MOS cameras. The CCD consists of an array of 600×600 pixels and can be used in image, photodiode, window timing, and photon counting mode. A sensitivity of 2×10^{-14} erg cm⁻² s⁻¹ in the observations is achieved within 10 ks (Burrows et al., 2005). On-board software allows fully automated observations, with the instrument selecting an appropriate observing mode for each object, based on its measured count rate. In this thesis, the X-ray data are included for a time period between August 2008 and January 2011. The XRT data were processed with standard

¹<http://www.swift.psu.edu/>

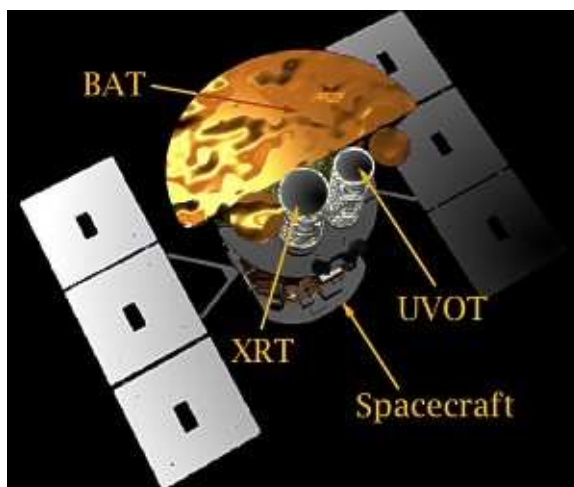


Figure 3.1: An artists rendering of the three scientific instruments on board Swift spacecraft. Credit: NASA/GSFC.

procedures by means of the FTOOLS in the Heasoft package version 6.8¹. The details of the analysis tools and data reduction can be found in [Stroh & Falcone \(2013\)](#).

All of the observations were obtained in photon counting (PC) mode. Circular and annular regions are used to describe the source and background areas respectively, and the radii of both regions depend on the measured count rate using the FTOOLS script *xrtgrblc*. Spectral fitting was done with an absorbed power law with the hydrogen column density $N_H = 0.31 \times 10^{21} \text{ cm}^{-2}$ set to the Galactic value found by [Kalberla et al. \(2005\)](#). One sigma errors in the de-absorbed flux were calculated assuming that they share the same percentage errors as the absorbed flux for the same time and energy range.

3.1.4 Gamma-ray data

The Fermi Gamma-ray Space Telescope (Fermi), formerly known as the Gamma-ray Large Area Space Telescope (GLAST) was launched by NASA on June 11, 2008 on a Delta II Heavy launch vehicle. Its orbit is similar to that of *Swift*, with a low Earth orbit at an altitude of ~ 550 km. The Fermi spacecraft orbits the earth in about 96 minutes. This space observatory covers photon energy range of 8 KeV to greater than

¹xrtpipeline and FTOOLS are part of the Heasoft software package: <http://heasarc.gsfc.nasa.gov/lheasoft/>; a detailed discussion on XRT data analysis can be found in the XRT User's Guide: http://heasarc.gsfc.nasa.gov/docs/swift/analysis/xrt_swguide_v1_2.pdf

300 GeV. *Fermi* carries two instruments:

1. GLAST Burst Monitor (GBM) and
2. Large Area Telescope (LAT).

The LAT is *Fermi*'s primary instrument, and the GBM is the complementary instrument. The GBM (Meegan et al., 2007) detects sudden flares of γ -rays produced by gamma-ray bursts and solar flares. Recently, it has also been used to detect terrestrial γ -ray flashes produced in thunderstorms. The scintillators of the instrument are mounted on the sides of the spacecraft to view all of the sky which is not blocked by the earth. The design is optimized for good resolution in time and photon energy. The GBM includes two sets of detectors: twelve Sodium Iodide (NaI) scintillators, and two cylindrical Bismuth Germanate (BGO) scintillators. The NaI detectors are sensitive in the lower end of the energy range, from a few KeV to about 1 MeV, while the BGO detectors cover the energy range between 150 KeV to 30 MeV.

3.1.4.1 LAT

The LAT measures tracks of the electron-positron (e^-e^+) pairs produced by an incident γ -ray, and it also measures direction and energy of the incident photon. The instrument is designed to cover the energy band from 20 MeV to greater than 300 GeV. It is the product of an international collaboration between NASA and Department of Energy (DOE) in the U.S. and many scientific institutions from France, Italy, Japan, Sweden, and Germany. LAT has a good angular resolution for source localization, high sensitivity over a broad field of view (FoV) to monitor variability and detect transients, good calorimetry over an extended energy band to study spectral breaks and cutoffs, and good calibration and stability for absolute, long term flux measurements (Atwood et al., 2009). The general layout of LAT is depicted in Fig. 3.2.

LAT is a pair-conversion telescope with a precise converter-tracker and calorimeter, each consisting of a 4×4 array of 16 modules supported by a low-mass aluminum grid structure. A segmented anti-coincidence detector (ACD) covers the tracker array, and a programmable trigger and data acquisition system (DAQ) utilizes prompt signals available from the tracker, calorimeter, and ACD subsystems to form a trigger. To avoid measuring back-scattering events or to reject other back-ground particles, an anti-coincidence detector made of plastic scintillators is fixed all around LAT, enabling the detection of stray charged particles, in order to reject measurements with which they could interfere (Atwood et al., 2009). The overall aspect ratio of the LAT tracker

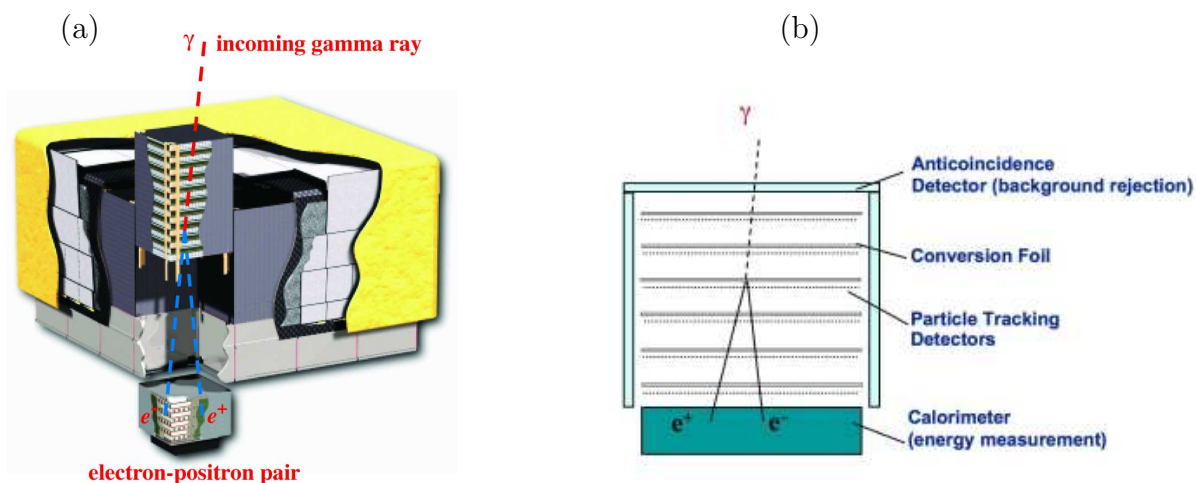


Figure 3.2: (a) Schematic diagram of the *Fermi*/LAT cut-away showing the instrument with the dimensions $1.8 \text{ m} \times 1.8 \text{ m} \times 0.72 \text{ m}$ (Atwood et al., 2009). (b) The LAT design showing its various parts.

(height/width) is 0.4, allowing a large field of view of 2.4 steradian which corresponds to $\sim 20\%$ of the sky. To take full advantage of the LAT's large FoV, the primary observing mode of *Fermi* is the so-called survey mode (Atwood et al., 2009). In default operating mode it continuously observes the entire sky every 3 hours (~ 2 orbits).

3.1.4.2 LAT data reduction

In the following the typical analysis procedure of *Fermi*/LAT data is described. The *Fermi*/LAT team provides software (*Fermi*/LAT ScienceTools) for the standard analysis based on the maximum likelihood method. Detailed information on the ScienceTools and their application is provided online at <http://fermi.gsfc.nasa.gov/ssc/data/analysis/>. The analysis methods are also described on the basis of individual studies of sources (see, Abdo et al., 2010b, for details). The general analysis strategy is illustrated as a flow chart in Fig. 3.3.

The γ -ray data (100 MeV – 300 GeV) used for this study are observed over a time period between JD = 2454686 (August 08, 2008) to JD = 2456022 (April 04, 2012) in survey mode by the *Fermi*/LAT instrument. The LAT data are analyzed using the standard ScienceTools (software version v9.23.1) and the instrument response function

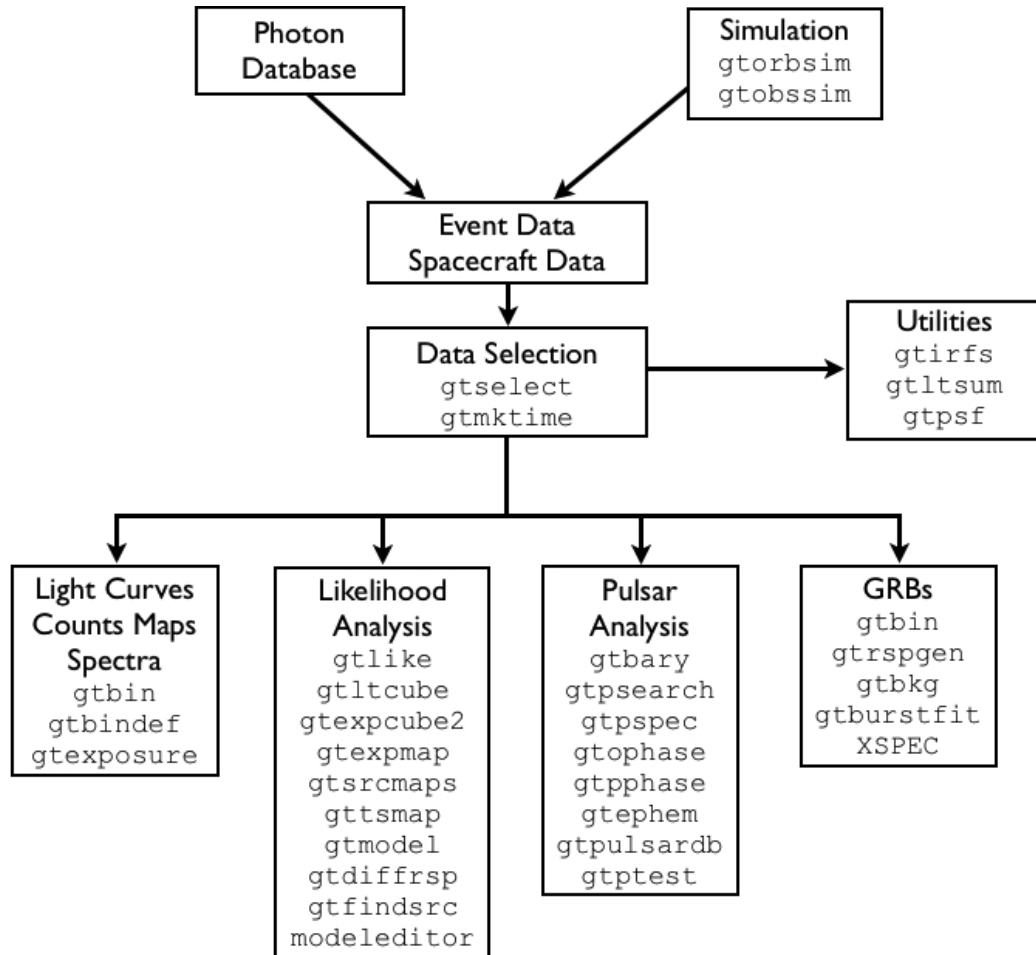


Figure 3.3: The general analysis flow of the *Fermi*/LAT data reduction tools. The details of the analysis threads are provided online at <http://fermi.gsfc.nasa.gov/ssc/data/analysis/documentation/Cicerone/>.

P7V6¹. The first step of the analysis is selection and filtering of data. Photons in the event class 2 are recommended for the analysis of point sources because of their reduced charged-particle background contamination and a good angular reconstruction. Event classification aims at selecting the best estimates of the event direction and energy among those available for the event and determining their accuracy, as well as reducing the backgrounds in the final data sample. A zenith angle $< 100^\circ$ cut in the instrument coordinates is used to avoid γ -rays from the Earth's limb. This analysis was performed with the standard analysis algorithm *gtselect*.

¹<http://fermi.gsfc.nasa.gov/ssc/data/analysis/scitools/overview.html>

In addition to the selection of the total time range for data, good time intervals within that specified time range have to be determined. The *gtmktime* algorithm tool was used for the selection of Good Time Intervals and to make cuts based on spacecraft parameters contained in the pointing and live-time history (spacecraft) FITS file. This allow us to exclude the time intervals where the zenith cut intersects the region of interest (ROI). The integrated live-time (exposure cube) of the ROI as a function of sky position and off-axis angle is calculated using *gtlucube* algorithm. The exposure map of the ROI is generated using the *gtexpmap* algorithm. The exposure map is required to compute the predicted number of photons within a given ROI for the diffuse components in the source model. The next step is to model the observed events using the expose map and the exposure cube obtained in the previous steps. The source model is created using the *make2FGLxml* algorithm provided with the analysis tools. The source model contains various sources of the 2FGL catalog ([Ackermann et al., 2011](#)) and their model parameters to be fitted using the *gtlike* tool.

The data analysis is performed with an unbinned maximum likelihood technique using the likelihood analysis software developed by the LAT team. Unbinned likelihood analysis is the preferred for time series analysis of the LAT data, where the number of events in each time bin is expected to be small. The model fitting procedure involves finding the set of parameters that maximizes the log-likelihood to get the best match of the model to the data. In the ROI model, the diffuse emission from our Galaxy is modeled using a spatial model (*gal_2yearp7v6_v0.fits*). The extragalactic diffuse and residual instrumental backgrounds are modeled as an isotropic component (*isotropic_p7v6source.txt*), which is provided with the data analysis tools. The LAT science tools offer several spectral functions with *gtlike*. For the light curve and the spectral analysis, the following functions are used :

1. Power Law (PL) :

$$N(E) = N_0(E)^\Gamma \tag{3.1}$$

where N_0 is prefactor and Γ is the photon index.

2. Broken power law (BPL) :

$$N(E) = N_0(E/E_{break})^{-\Gamma_i}, i = 1 \text{ if } E < E_{break}, \text{ and} \tag{3.2}$$

$$i = 2 \text{ if } E > E_{break}.$$

where Γ_1, Γ_2 are the two photon indices and E_{break} is the break energy.

I have analyzed a RoI of 10° in radius centered at the position of the γ -ray source associated with S5 0716+714, using the maximum-likelihood algorithm implemented in *gtlike* (Mattox et al., 1996). In the RoI model, all the 24 sources within 10° are included with their model parameters fixed to their catalog values except for 4C +71.07 (2FGLJ0841.6+7052), as none of the other sources were reported as variable in the 2FGL catalog (see Ackermann et al., 2011, for details). The source 4C +71.07 was reported as a variable source in the 2FGL catalog (see Nolan et al., 2012, for details); hence, all the model parameters are kept free for it. It is important to note that the contribution of the other 23 sources within the RoI model to the observed variability of the source is negligible as they are very faint compared to 0716+714. The LAT instrument-induced variability is tested with bright pulsars and is found to be much smaller than the statistical errors reported for the source (Ackermann et al., 2012).

The source variability is investigated by producing light curves by likelihood analysis with different time binnings (1 day, 1 week and 1 month) and over different energy ranges ($E > 100$ MeV, $E > 248$ MeV, $E = 0.1-1$ GeV and $E > 1$ GeV). The light curves are produced by modeling the spectra over each bin using a simple power law which can provide a good fit over these small time bins, since the statistical uncertainties on the power law (PL) indices are smaller than those obtained from the broken-power law (BPL) fits.

The spectral analysis is performed by fitting the GeV spectra with multiple models over the whole energy range covered by *Fermi/LAT* above 100 MeV. The simple power law and the broken power law models are used to investigate the γ -ray spectrum. The spectral behavior of the source over the whole energy range is also examined with a power-law model fitting over equally spaced logarithmic energy bins with Γ kept constant and equal to the value fitted over the whole range.

3.2 The time series analysis techniques

This thesis presents a detailed analysis of the time variable emission of the BL Lac object S5 0716+714, which can be helpful in establishing a model of AGN activity by constraining the physical parameters of the emission region, the physics of relativistic jets, the dominating emission mechanisms across the broad-band spectra, etc. To investigate the time variability properties of AGN, a set of robust and objective

tools is required so that the deduced results are statistically significant. A suite of statistical analysis techniques was used to extract the physical information from the observed data. A detailed description of each statistical analysis method is provided in the following subsections. All of these statistical tools have been developed using the statistical analysis package R¹.

3.2.1 Statistical analysis tools

3.2.1.1 Structure function analysis

The Structure Function (SF) analysis method is a very useful tool to search for timescales of variability and periodicity in non-uniformly sampled light curves, for which ordinary Fourier transform methods fail to provide useful results. Nor can simple periodograms give useful results. Under these circumstances, the structure function method is the best way to quantitatively determine the time scale of variation in unevenly sampled data sets, as this is the case in most of the astronomical observations. The first order SF represents a measure of the mean squared of the flux differences ($F_i - F_{i+\Delta t}$) of N pairs with a common time separation/lag Δt (e.g. [Simonetti et al., 1985](#), and references therein) defined as,

$$\text{SF}(\Delta t) = \frac{1}{N} \sum_{i=1}^N [F_i - F_{i+\Delta t}]^2 \quad (3.3)$$

The error of the SF value at a given time lag is given by the standard deviation of the squared flux differences at that time lag. [Figure 3.4](#) shows the SF curve of a typical measured process, which consists of two plateaus and a slope between them. For shorter time lags, the plateau is twice the variance of the measurement noise. At longer time lags, the plateau corresponds to twice the variance of the signal. The slope of the region between the two plateaus depends on the nature of intrinsic variation of the source ([Hovatta et al., 2007](#); [Hughes et al., 1992](#); [Rani et al., 2009](#)). The variability timescale is given by the maximum in the rising part of the SF curve as shown in [Fig. 3.4](#). Following this rising portion, the structure function will then fall into one of the following classes:

- (i) if no plateau exists, the time scale of variability exceeds the length of the data train,
- (ii) if there are one or more plateaus, each one indicates a time scale of variability, and

¹R: A language and environment for statistical computing. R Foundation for Statistical Computing, Vienna, Austria. ISBN 3-900051-07-0, URL <http://www.R-project.org>.

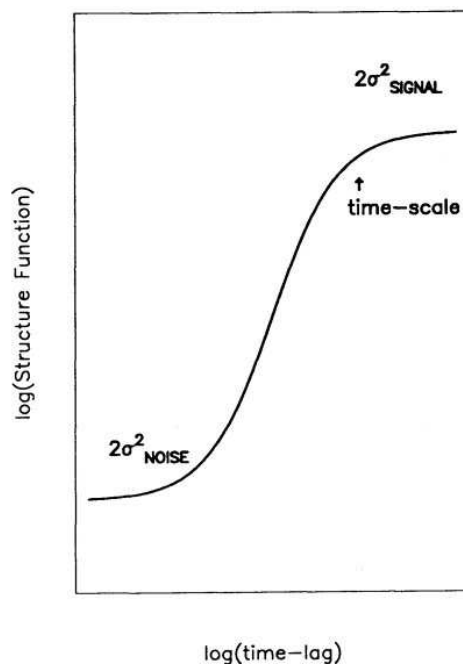


Figure 3.4: A schematic diagram showing the ideal structure function for a time series (Figure courtesy : [Hughes et al. \(1992\)](#)).

- (iii) if that plateau is followed by a dip in the SF curve, the timescale corresponding to the minimum of that dip, indicates a possible periodic cycle.
- (iv) Uncorrelated data produce a ‘white noise’ behavior with a slope close to zero ([Ciprini et al., 2003](#)). The details of the SF slope dependence on different underlying processes can be found in [Hughes et al. \(1992\)](#).

The Structure function analysis method has been employed for quite some time in examining the nature of AGN variability. For example, using long term radio observations of a sample of over 50 radio loud AGN, [Hughes et al. \(1992\)](#) reported that most of them showed some plateau in their SF curves; the mean time scale they found for BL Lac objects was 1.95 yr, while that for quasars was 2.35 yr. A recent extension of this analysis using SFs and other techniques also examined high-frequency radio data and found that small flux density variations were often present on 1 to 2 year time scales but larger outbursts were much rarer; however, a significant difference between AGN classes was not detected ([Hovatta et al., 2007](#)).

3.2.1.2 Discrete correlation function analysis

The Discrete Correlation function (DCF), a method to deal with unevenly sample data, was first introduced by [Edelson & Krolik \(1988\)](#), and it was later generalized to provide better error estimates ([Hufnagel & Bregman, 1992](#)). The DCF analysis is frequently used for finding the correlation and possible time lags between multi-frequency AGN light curves where different data trains are used in the calculation (e.g., [Hovatta et al., 2007](#); [Raiteri et al., 2003](#); [Villata et al., 2004](#), and references therein). The first step is to calculate the unbinned discrete cross-correlation function (UDCF) using the given time series through (e.g. [Hovatta et al., 2007](#))

$$\text{UDCF}_{ij} = \frac{(a(i) - \bar{a})(b(j) - \bar{b})}{\sqrt{(\sigma_a^2 - e_{a,i}^2)(\sigma_b^2 - e_{b,j}^2)}} \quad (3.4)$$

where $a(i)$ and $b(j)$ are the individual points in the time series a and b , respectively, \bar{a} and \bar{b} are respectively the means of the time series, σ_a^2 and σ_b^2 are their variances and $e_{a,i}$, $e_{b,j}$ are the corresponding measurement error associated with data set a , b .

UDCF $_{ij}$ is calculated for each possible pair of time lag defined as

$$\Delta t_{ij} = t_j - t_i \quad (3.5)$$

The correlation function is binned in time after calculation of the UDCF. The DCF method does not automatically define a bin size. The size of the bin size has to include a large enough number of data points so that the data averaging in each bin leads to statistically meaningful results. If the bin size is too big, useful information is lost, but if the bin size is too small, a spurious correlation can be found. Taking τ as the center of time bin and n is the number of points in each bin, the DCF is calculated from the UDCF via

$$\text{DCF}(\tau) = \frac{1}{n} \sum \text{UDCF}_{ij}(\tau) \quad (3.6)$$

The error for each bin can be calculated using

$$\sigma_{def}(\tau) = \frac{1}{n-1} \sqrt{\left\{ \sum [\text{UDCF}_{ij} - \text{DCF}(\tau)]^2 \right\}} \quad (3.7)$$

DCFs can be used to compare flux variations at multiple wavelengths and to determine the inter-wavelength time delay. A comparison of flux variations at different

wavelengths is important for distinguishing between possible models of variability. The cross-frequency time lag relates to the relative locations of the emission regions at the different wavebands, which in turn depend on the physics of the jet and the emission mechanism.

The DCF analysis is mostly used for finding the correlation and possible lags between multi-frequency AGN data, but can be applied on the same data train as well, which is called as auto-correlation function (ACF). In this case, there is obviously a peak at zero, indicating that there is no time lag between the two data trains, but any other strong peaks in the ACF curve give the indication of variability timescales (Hovatta et al., 2007). A disadvantage of this method is that it does not give any exact probability value for the calculated results. The only way to check and test the reliability of the results is to use Monte Carlo simulations.

3.2.1.3 Lomb-Scargle periodogram

The Lomb-Scargle periodogram (LSP) is a very useful technique for the search of periodic patterns in time series. This method has a good tolerance for missing values (e.g., Glynn et al., 2006), so it does not require any special treatment for gaps in the data, and is thus suitable for non-uniformly sampled data trains. The LSP method is frequently used by astronomers and in other fields also (e.g., Glynn et al., 2006). It also has the advantage of providing a p -value¹, which specifies the significance of a peak.

The LSP was first introduced by Lomb (1976) and later extended by Scargle (1982); somewhat later a more practical mathematical formulation was provided by Press & Rybicki (1989). For a series of observations $a(t_i)$ ($i = 1, 2, \dots, N$), the LSP is defined at a frequency ω_j as (Press & Rybicki, 1989)

$$P(\omega_j) = \frac{1}{2\sigma^2} \left\{ \frac{(\sum_{i=1}^N [a(t_i) - \bar{a}] \cos[\omega_j(t_i - \tau)])^2}{\sum_{i=1}^N \cos^2[\omega_j(t_i - \tau)]} + \frac{(\sum_{i=1}^N [a(t_i) - \bar{a}] \sin[\omega_j(t_i - \tau)])^2}{\sum_{i=1}^N \sin^2[\omega_j(t_i - \tau)]} \right\} \quad (3.8)$$

¹The p -value is the probability of obtaining a test statistic assuming that the null hypothesis is true. The null hypothesis is rejected when the p -value turns out to be less than a certain significance level, often 0.05 corresponding to a confidence level of 95 %.

Here $j = 1 \dots M$, where τ is defined by

$$\tan(2\omega_j\tau) = \frac{\sum_{i=1}^N \sin(2\omega_j t_i)}{\sum_{i=1}^N \cos(2\omega_j t_i)} \quad (3.9)$$

and M depends on the number of independent frequencies (N_0) and the total number of observations (N), through $M = N_0 \approx -6.363 + 1.193N + 0.00098N^2$ (Press & Rybicki, 1989).

The significance is tested using the null hypothesis or false-alarm probability. If the probability that the peak value of the LSP is smaller than x , the p -value, or probability of the null hypothesis that the observed peak in an LSP was found by chance, is

$$p = 1 - (1 - e^{-x})^M \quad (3.10)$$

The smaller the p -value for a given peak, the higher its significance; the maximum limit that can be reasonably specified for a p -value is 0.05 (equivalent to 95% confidence level), i.e., any peaks having p -values smaller than 0.05 are considered as significant.

Two difficulties usually arise while using this method as is discussed in Scargle (1982); the first is statistical and the other is spectral leakage. The main statistical problem is that the function $P(\omega_j)$ is very noisy even if the data are not very noisy. However, if a large sample of data is used, even though the size of noise remains large, the signal-to-noise (S/N) ratio of the function $P(\omega_j)$ increases. The S/N ratio (Scargle, 1982) is given as

$$P_{S/N} = N_0(X_0/2\sigma_0)^2 \quad (3.11)$$

where N_0 is the number of data points or sample size, X_0 is the amplitude of observed periodic process and σ_0 represents the observational error. The power per unit bandwidth increases as the bandwidth decreases (which is a decreasing function of N_0), whereas the noise power is a constant function of bandwidth. So, the S/N ratio of $P(\omega_j)$ increases with an increase in N_0 (Scargle, 1982).

Spectral leakage or aliasing means that the power in the periodogram not only appears at the frequencies which are actually present in the data, but can also leak to other frequencies. The leakage to nearby frequencies is due to the finite length of the data. The leakage to more distant frequencies is caused by the finite sampling interval. A small presence of unevenness in the data spacing substantially reduces

aliasing. However, if the sampling is semi-regular (intermediate between randomly and evenly spaced) significant leakage of periodogram power to the side-lobes can occur. The details of regular and semi-regular aliasing effects are described in [Scargle \(1982\)](#). The usual way to minimize both statistical and leakage problems is to window or taper the data by smoothing in the spectral domain. But the disadvantage of smoothing is that the spectral values at different frequencies are no longer independent and hence, the joint statistical properties become more complicated.

3.2.1.4 Power spectrum density

Many astrophysical sources, galactic as well as extra-galactic show erratic, aperiodic brightness fluctuations with steep power spectra. This type of variability is known as red noise. In this context, ‘noise’ is defined as the intrinsic variations in the source brightness being random. The power spectral density (PSD) is a powerful tool to search for periodic signals in time series, including those contaminated by white noise and/or red noise ([Vaughan, 2005](#)). The PSD defines the amount of variability ‘power’ as a function of temporal frequency. For an evenly sampled light curve (with a sampling period ΔT) the periodogram is the modulus-squared of the Discrete Fourier Transform (DFT) of the data ([Press & Rybicki, 1989](#); [Vaughan et al., 2003](#)). For a light curve comprising a series of fluxes x_i measured at discrete times t_i ($i = 1, 2, \dots, N$):

$$|\text{DFT}(f_j)|^2 = \left| \sum_{i=1}^N x_i e^{2\pi i f_j t_i} \right|^2 \quad (3.12)$$

at $N/2$ evenly spaced frequencies $f_j = j/N\Delta T$ (where $j = 1, 2, \dots, N/2$), $f_{N/2} = 1/2\Delta T$ is the Nyquist frequency, f_{Nyq} . The periodogram, $P(f_j)$, is

$$P(f_j) = A |\text{DFT}(f_j)|^2 = \frac{2\Delta T}{N} |\text{DFT}(f_j)|^2 \quad (3.13)$$

The calculated PSD at a given frequency, $I(f_j)$, is scattered around the true power spectrum, $\mathcal{P}(f_j)$, following a χ^2 distribution with two degrees of freedom :

$$I(f_j) = \mathcal{P}(f_j) \chi_2^2 / 2, \quad (3.14)$$

where χ_2^2 is a random variable distributed as χ^2 with two degrees of freedom. The PSD follows this distribution because the real and imaginary parts of the DFT are normally

distributed for a stochastic process and the sum of two squared normally distributed variables is a χ_2^2 - distributed variable (Scargle, 1982; Vaughan, 2005).

The underlying power spectrum can be described by a power law with slope α and normalization constant N . One of the simplest methods to estimate these parameters from the calculated PSD is to fit it with a model of the form $\mathcal{P}(f) = Nf^{-\alpha}$. A least-square (LS) fitting procedure can be used to get a reasonable estimate of the power spectral slope α and normalization N by fitting a linear function $y = mx + c$ to the plot of $\log[I(f_j)]$ versus $\log[f_j]$. The slope of the linear fit gives $\alpha = -m$ and the y -intercept gives $\log(N) = c + 0.25068$. However, it is important to note that the data point at the Nyquist frequency ($j = n$) should be ignored in the LS fitting, because the distribution of the periodogram ordinate at this frequency is not identical to that at other frequencies, which means that the LS fit should be performed on the $n' = n - 1$ lowest frequencies (Vaughan, 2005).

The uncertainties on α and N values are estimated using the standard theory of linear regression (Vaughan, 2005) which can be used to drive the uncertainty of the fitted power law to the calculated PSD. The confidence limit on $\gamma_j \equiv 2I(f_j)/\mathcal{P}(f_j)$ can be derived using the null hypothesis. For a given probability ϵ , γ_ϵ is defined such that $\Pr(\gamma_j > \gamma_\epsilon) = \epsilon$, i.e.

$$\gamma_\epsilon = -2 \ln[\epsilon] \tag{3.15}$$

For a significance level of 95%, the value of ϵ is 0.05 which yield a value of $\gamma_\epsilon = 5.99$. This implies that if the null hypothesis is true, then γ_j should be higher than 5.99 for a significance level of 95%. The significance is searched over a range of frequencies, so the confidence level detection criteria is modified accordingly. As a result, for $n' = n - 1$ (ignoring Nyquist frequency) independent trials γ_ϵ is given as (Vaughan, 2005) :

$$\gamma_\epsilon = -2 \ln[1 - (1 - \epsilon_{n'})^{1/n'}] \tag{3.16}$$

The PSD method is therefore a very promising tool to differentiate the random fluctuations from the real variations in the light curves of AGNs. It is widely accepted and used to search for periodic variations in multi-frequency light curves of AGNs (e.g., Gierliński et al., 2008; Rani et al., 2010b; Vaughan, 2005, and references therein). However, this method is only suitable for evenly sampled data. Since most of the astronomical data carries gaps, so one should apply the SF or DCF or LSP methods which are better suited for unevenly sampled data.

3.3 Very long baseline interferometry

The technique of interferometry is driven by the aim for highest possible angular resolution in astronomical observations. In the early days of radio interferometry, the baseline length and thus the resolution of observations was limited to a few hundred kilometers, with angular resolutions at a few arcsecond scale (Anderson et al., 1965). However, this angular resolution was not sufficient to resolve the fine-scale structures in case of bright quasars. This led to the development of very long baselines (thousands of kilometers), with angular resolutions at milli-arcsecond (mas) scales. A good review about the efforts and developments in the early days of VLBI can be found in Porcas (2010).

The very high angular resolution in radio interferometry is increased further in two ways, (1) either by using longer baselines or/and (2) by observing at shorter wavelengths. The first approach leads to “space-VLBI” (VLBI with one or more orbiting antennas), and the second to “millimeter-VLBI” (mm-VLBI). The advent of radio interferometry and technological advances thereafter offer a much higher angular resolution up to 50 μ mas at 3 mm wavelengths (see, Krichbaum et al., 2013, for details). In the quest for even greater angular resolution, dedicated VLBI satellites have been placed in Earth orbit to provide greatly extended baselines. A detailed review about space-VLBI can be found in Andreyanov (1999) and Sokolovsky (2013).

The Very Long Baseline Interferometry (VLBI) imaging with the highest possible angular (and spatial) resolution shed light on the physical processes acting within the centers of blazars, in regions where jets are forming and γ -rays are produced. In addition, at mm-wavelengths, we can probe the regions of the jet which are self-absorbed at longer wavelengths.

3.3.1 Observations and data reduction

For the jet kinematics study of the BL Lac S5 0716+714, the high frequency VLBI (43 and 86 GHz) data were employed for a time period between December 2008 to October 2010. The source is monitored by the Boston University group at 43 GHz within a program of monthly monitoring of bright γ -ray blazars¹. The 86 GHz observations were performed using the Global mm VLBI Array (GMVA²) (project codes : GM063A/B/C,

¹<http://www.bu.edu/blazars>

²<http://www3.mpifr-bonn.mpg.de/div/vlbi/globalmm/index.html>

GM065A/B, and GM065C; P. I. : A. Marscher). The GMVA is currently an array consisting of 14 antennas in Europe and the United States including the 8 VLBA stations equipped with 3 mm receivers, the Effelsberg 100 m dish, Onsala, Metsähove, Pico Valeta, Plateau de Bure and the new Yebes 30 m antenna in Spain. A good review about the GMVA monitoring and future developments of mm-VLBI can be found in [Krichbaum et al. \(2006\)](#) and [Krichbaum et al. \(2008\)](#).

The data reduction is performed using the standard tasks of the Astronomical Image Processing System (AIPS) and DIFMAP ([Shepherd et al., 1994](#)). In the following, the main steps adopted for the data reduction are summarized. Further details can be found in [Krichbaum et al. \(1992\)](#) and [Jorstad et al. \(2001\)](#). Further information about VLBI data reduction in AIPS is available at <http://www.aips.nrao.edu/cook.html>. A cookbook for Difmap can be found at <ftp://ftp.astro.caltech.edu/pub/difmap/difmap.html>.

The VLBI data were calibrated using the standard tasks in AIPS package. The imaging of the source (including amplitude and phase self-calibration) was done using the *CLEAN* algorithm ([Högbom, 1974](#)) and *SELFCAL* procedures in Difmap package ([Shepherd et al., 1994](#)). The first step in imaging is to flag the outliers or “bad” data, due to glitches in the observations and/or bad weather. After this, the data were averaged and statistical weights were calculated for each complex visibility. Images of the source structure were reconstructed using the deconvolution method ([Högbom, 1974](#)) following the “clean” algorithm. Detailed discussions of the clean algorithm can be found in [Taylor et al. \(1999\)](#) and references therein. The self-calibration process requires several iterations of phase calibration followed by amplitude self-calibration. Finally, one obtains the self-calibrated data, a model, and a map of the source.

After imaging the observed brightness distribution of the radio emission, it is modeled by multiple circular Gaussian components providing positions, flux densities, and sizes of the distinct bright features in the jet. The model fits were also carried out using the DIFMAP package starting with a point-like model for all the epochs. For all model fits, the brightest component is used as a reference with its position being fixed to (0, 0). The final number of jet components necessary to fit the data was adequately achieved when the addition of extra components did not lead to a significant improvement in the quality of fit, as measured by the reduced χ^2 value. The uncertainties of the model component parameters were determined by comparing the parameter ranges obtained by performing model fits using different number of model components.

Component identification was carried out on the basis of the assumption that

changes in flux density, core separation, and position angle of the modeled jet components should be small on time scales between adjacent epochs. The identification across the epochs has to take differences in the number of data points, UV-coverage, data quality and resolution of the data sets into account. Therefore in order to prevent a potentially large systematic error arising from the incorrect cross-identification of moving features from epoch to epoch, the simplest scheme is adopted while identifying the jet-features in the jet of 0716+714. A self-consistent cross-identification scenario is proposed using all available model-fit parameters (flux-density, core separation, position angle, size of axis). Therefore, the results presented in this thesis are meant to provide the most robust and simplest identification based on the available data set.

Chapter 4

Broad-band Flux Variability

The study of flux density variability is one of the most powerful tool for revealing the nature of the emission mechanism in blazars and probing the various processes occurring in them. Over the last two decades, the broad-band flux variability of blazars has been extensively studied from days to years timescales (e.g. [Carini & Miller, 1992](#); [Miller et al., 1989](#); [Rani et al., 2013a,b, 2009](#); [Takalo et al., 1996](#); [Teräsranta et al., 2004](#), and references therein). Despite of the extensive broad-band variability study, the detailed physical understanding of its origin is not yet clear. A comparison of multi-frequency features of the observed variability is required to put tight constraints on emission mechanisms and the size of emission regions. This chapter presents results of the broad-band (radio to γ -ray) flux variability study of the BL Lac object S5 0716+714 observed between April 2007 and April 2012. Section [4.1](#) presents a detailed investigation of flux variations at cm and mm radio bands. Section [4.2](#) provides results of the flux variability at optical frequencies. The investigation of the flux variability at X-ray and γ -ray frequencies is given in Section [4.3](#) and [4.4](#), respectively.

4.1 Radio frequencies

The radio frequency light curves of S5 0716+714 are displayed in Fig. [4.1](#). The flux monitoring covers several radio bands between 2.7 to 230 GHz over the past ~ 3 years (April 2007 to January 2011). The source exhibits significant variability, being more rapid and

¹Work presented in this chapter has already published in [Rani et al. 2013a,b](#).

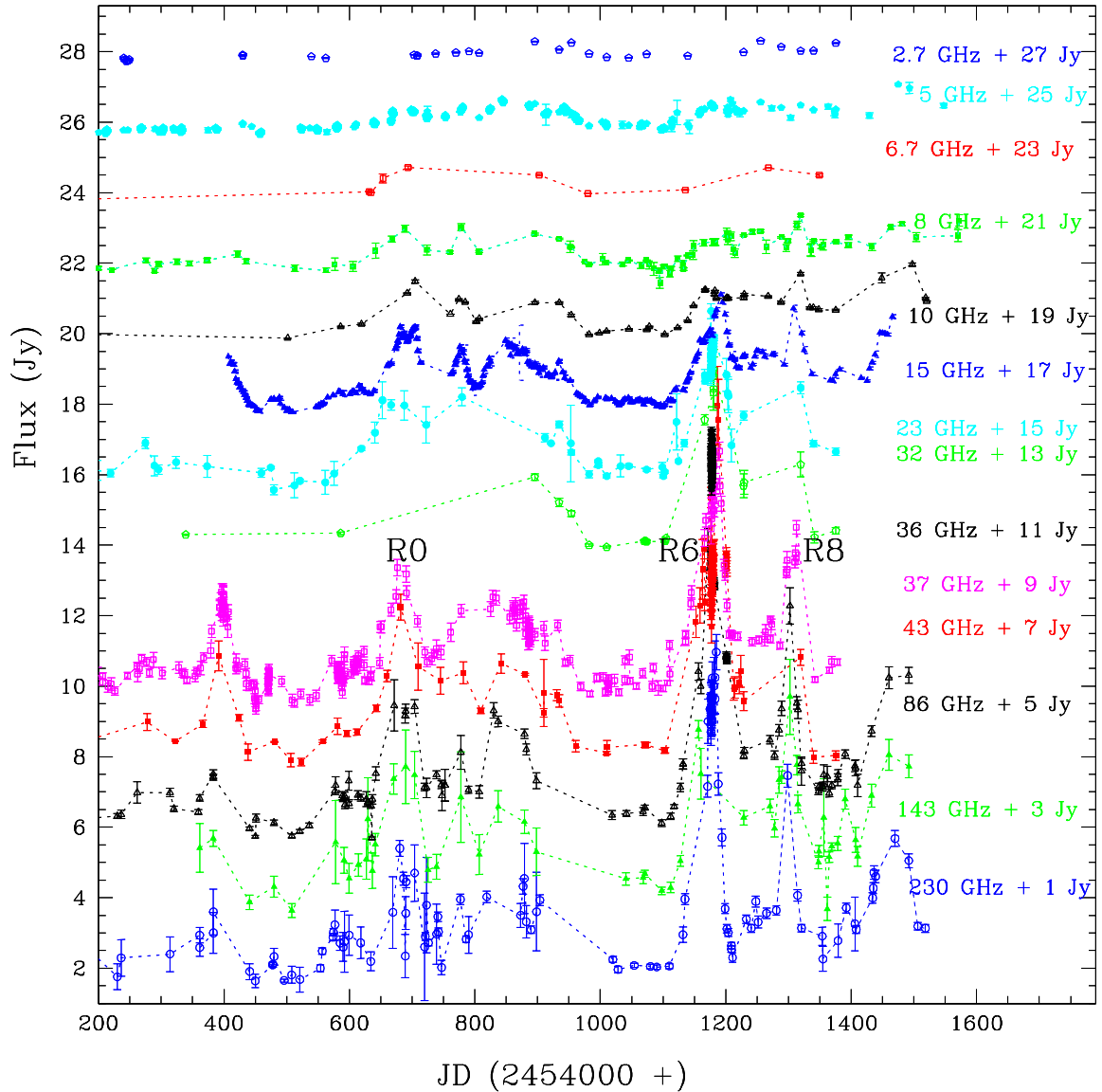


Figure 4.1: Radio to mm wavelength light curves of S5 0716+714 observed over the past ~ 3 years. For clarity, the light curves at different frequencies are shown with arbitrary offsets (indicated by a “Frequency + x Jy” label). The major radio flares are labeled as “R0”, “R6”, and “R8” (see Fig. 5.1 for the details of labeling).

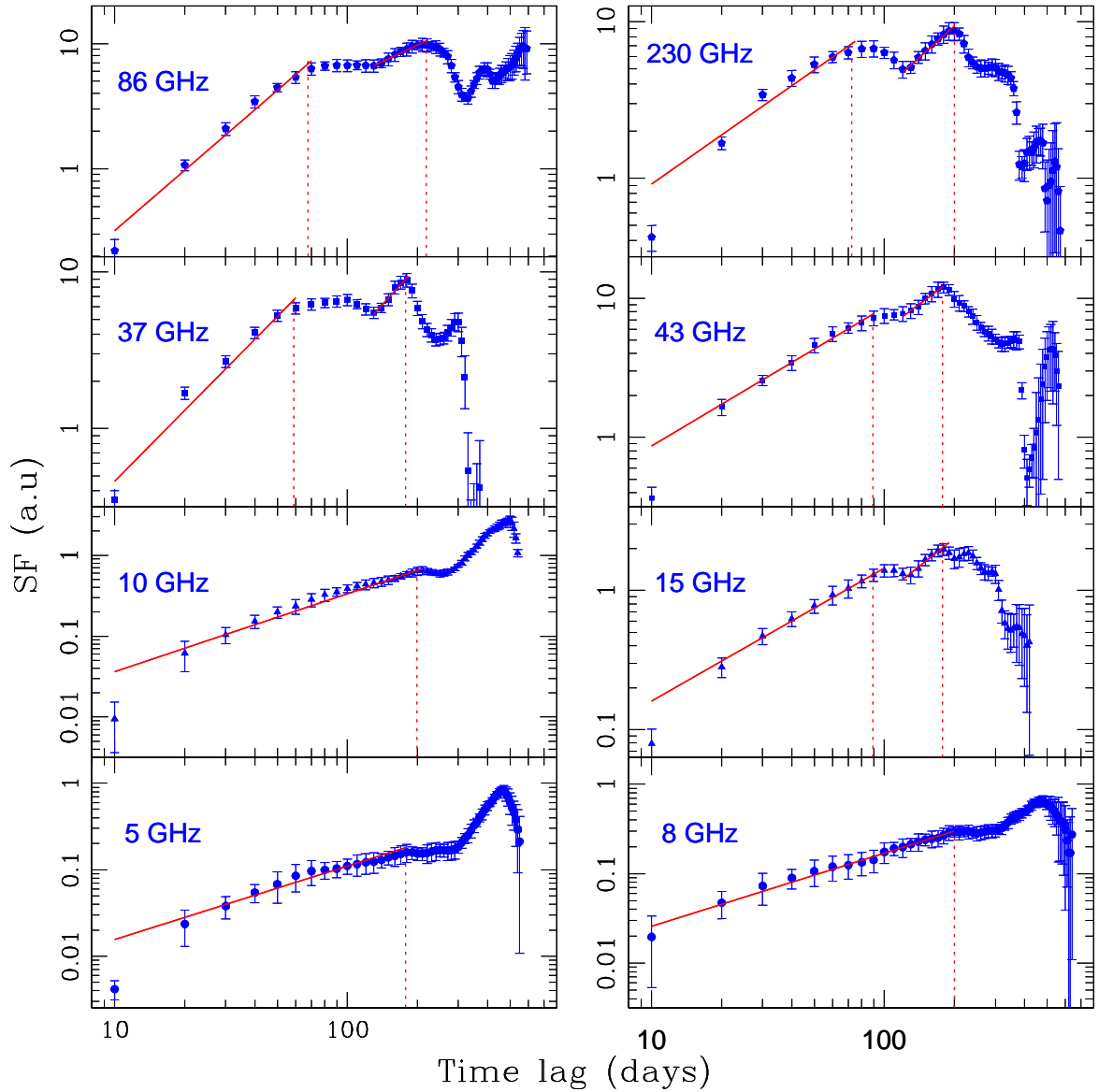


Figure 4.2: Top: Structure function curves at radio frequencies. The solid curves represent the best fitted power laws. The dotted lines in each plot indicate the timescale of variability (t_{var}).

Table 4.1: Variability time scales at radio wavelengths

Frequency	β_1^*	$t_{var,1}$ (days)	β_2	$t_{var,2}$ (days)
15 GHz	0.95 ± 0.03	100 ± 5	1.32 ± 0.04	195 ± 5
37 GHz	1.50 ± 0.13	100 ± 5	1.64 ± 0.10	200 ± 5
43 GHz	0.99 ± 0.02	90 ± 5	1.23 ± 0.04	180 ± 5
86 GHz	1.60 ± 0.10	90 ± 5	0.89 ± 0.02	180 ± 5
230 GHz	1.04 ± 0.03	90 ± 5	1.31 ± 0.03	180 ± 5

* : $P(f) \sim f^\beta$, β is the slope of the power law fit.

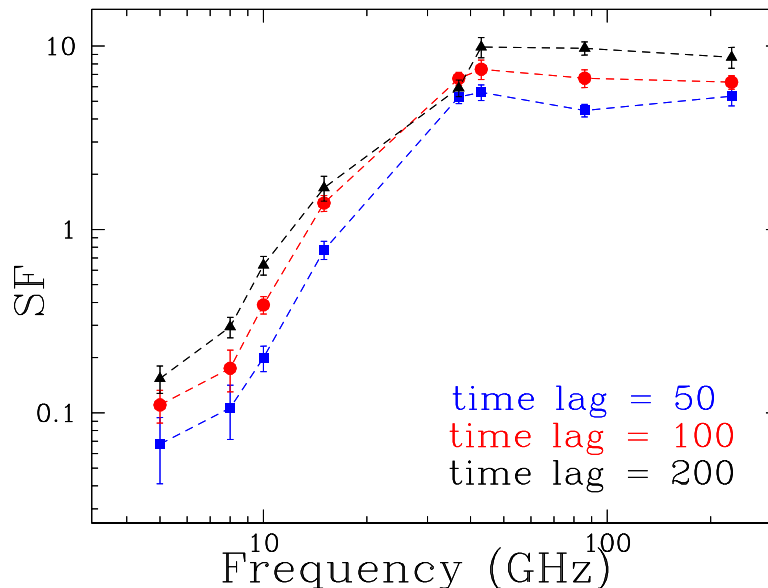


Figure 4.3: Structure function versus frequency (GHz) curve with a time binning of 50, 100, and 200 days.

pronounced towards higher frequencies over this period with two major outbursts. Towards lower frequencies (<10 GHz), the individual flares appear less pronounced and broaden in time.

To quantify the strength of variability at different radio frequencies and to extract the time scale of variability (t_{var}) from the observed light curves, the structure function analysis method is used. The details of the method are given in Section 3.2.1.1. The radio structure function curves are shown in Fig. 4.2.

At 15 GHz and higher radio frequencies, the structure function curves exhibit a continuous rising trend showing a peak at $t_{var,1}$, following a plateau and again reaching a maximum at $t_{var,2}$. However, the structure function curves at 10 GHz and lower

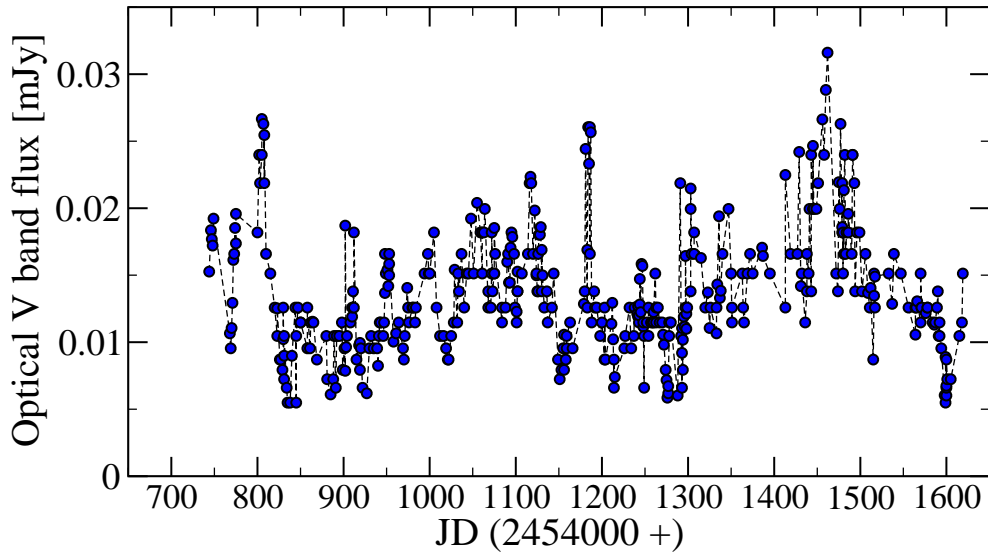


Figure 4.4: Optical V passband light curve of S5 0716+714.

frequencies do not reveal a sharp break in the slope, as the variability features seem to be smeared out at these frequencies. The variability features at time lags longer than half of the length of the observations are not considered due to the increasing statistical uncertainty of the structure function values in this region.

To extract the variability timescales, a power law ($P(f) \sim f^\beta$) is fitted to the two rising parts of the structure function curves. The variability timescale is given by a break in the slope of the power law fits. In Fig. 4.2, the red curves represent the fitted power laws to the rising trend of the structure function curves, and the two vertical dotted lines stand for the variability timescales, $t_{var,1}$ and $t_{var,2}$. The best fitted values of the power law slopes and the estimated timescale of variability are given in Table 4.1. Thus, the structure function curves reveal two different variability time scales, one which reflects the short-term variability ($t_{var,1}$), while the other one refers to the long-term variability ($t_{var,2}$).

The structure function value is proportional to the square of the amplitude of variability, so to compare the strength of the variability at different frequencies, structure function versus frequency plots are produced at different time lags. Figure 4.3 shows the structure function versus frequency plot at a time binning of 50, 100, and 200 days. The source displays more pronounced and faster variability at higher radio frequencies compared to lower ones, peaking at a frequency of 43 GHz, and have similar amplitude at higher frequencies. It seems that the radio flux variability saturates above 43 GHz.

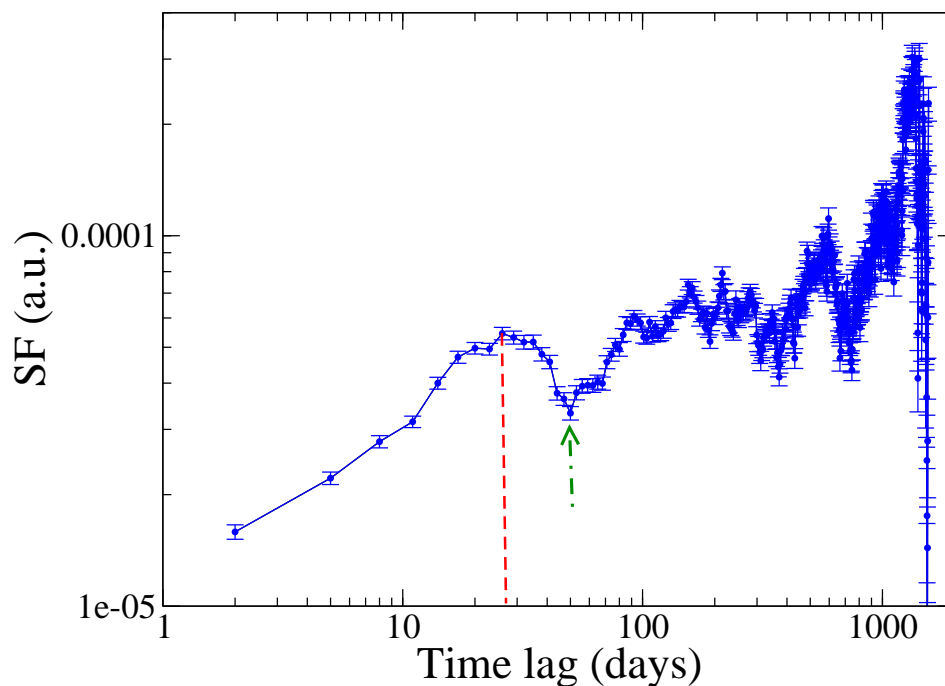


Figure 4.5: Structure function curve at optical frequency. The dotted lines indicate the shortest timescale of variability (t_{var}) and the arrow indicate the time scale of repetitive flux variations.

It is evident in Fig. 4.3 that the result does not change if different time binnings are used.

4.2 Optical frequencies

In contrast to radio wavelengths, the source exhibits more rapid variability and multi-flaring behavior at optical frequencies, with each flare roughly separated by 60 – 70 days (see Fig. 4.4). The optical V band structure function curve in Fig. 4.5 shows rapid variability with multiple cycles of rises and declines. The first peak in the structure function curve appears at a timescale $t_{var} \sim 30$ days which is followed by a dip at ~ 60 days (see red and green lines in Fig. 4.5). This peak corresponds to the fastest variability timescale. The other peaks in the structure function curve represent the long-term variability timescales. This indicates a possible superposition of a short 30 – 40 day time scale variability with the long-term variability trend.

Multiple cycles in the optical structure function curve suggest the nearly periodic

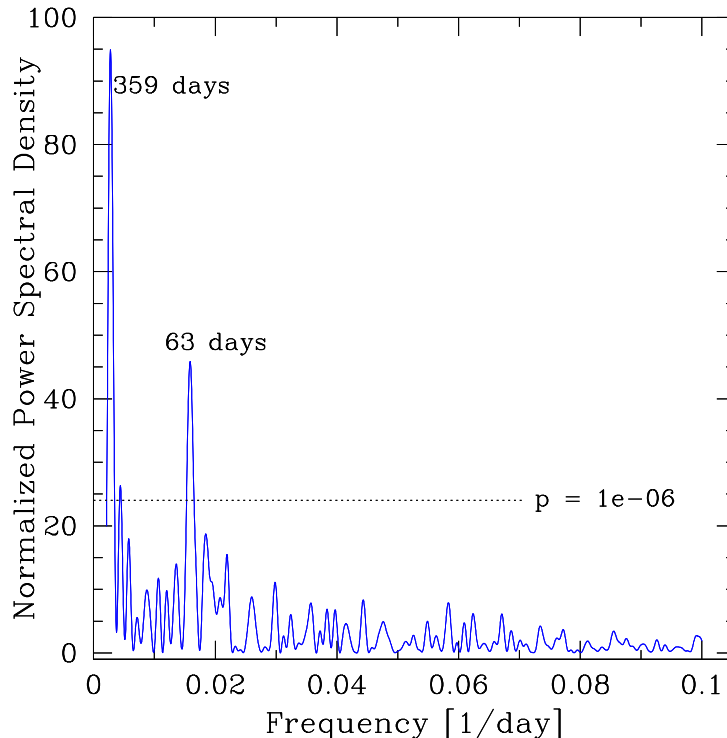


Figure 4.6: LSP analysis curve showing a peak at a period of 63 and 359 days. The dotted line represents the white noise level.

variations at ~ 60 days timescale. In the following, I will discuss in detail about the optical variability in the context of harmonics. The Lomb-Scargle Periodogram (LSP) (Section 3.2.1.3) method is used to test the presence of these harmonics. The LSP analysis of the optical data set is displayed in Fig. 4.6. The LSP analysis reveals two significant ($>99.9999\%$ significance) peaks at 359 and 63 days. The peak at 359 days is close to half of the duration of observations, so it is hard to claim this frequency as real due to the limited duration of observations. The periodicity of ~ 360 days could also be due to an annual observing cycle.

A visual inspection of the light curve indicates a total of 7 rapid flares separated by 60 – 70 days. Also, the LSP method is only sensitive for a dominant white-noise process ($P_N(f) \propto f^0$). It is for this reason that the significance of this frequency is further inspected with the Power Spectral Density (PSD) analysis method (Section 3.2.1.4), which is a powerful tool to search for periodic signals in time series, including those contaminated by white noise and/or red noise. To achieve a uniform sampling

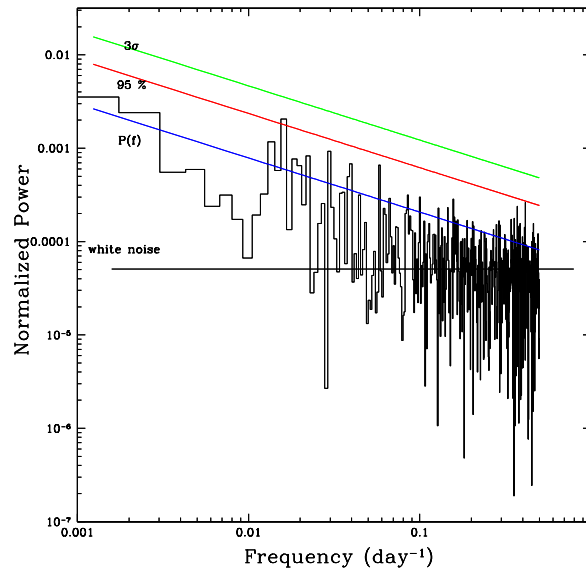


Figure 4.7: PSD of S5 0716+714. $P(f)$ is the best power law fit with a slope = 0.62 ± 0.09 ($P(f) \propto f^{-\alpha}$). The confidence limits and the white-noise level are shown.

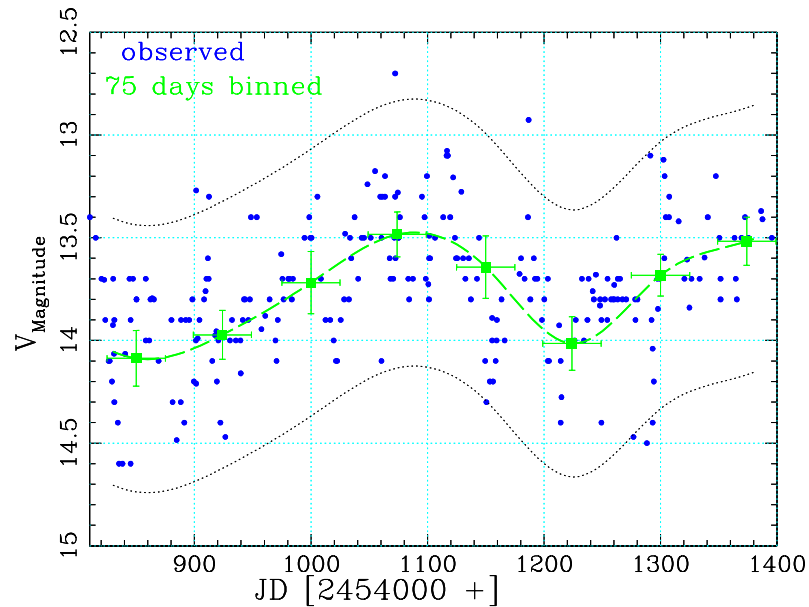


Figure 4.8: Optical V passband light curve of S5 0716+714 with different time binning. The light curve appears as a superposition of fast flares on a modulated base level varying on a (350 ± 9) day timescale. These slower variations can be clearly seen in 75 days binned light curve (error bar represents variations in flux over the binned period). The dashed line represents a spline interpolation through the 75 day binned light curve. Dotted lines are obtained by shifting the spline by ± 0.65 mag.

in the optical data, a time-average binning of 3 days is applied. First, as shown in Fig. 4.7, a single power law is fitted to the calculated PSD, assuming a form of $P(f) \propto f^{-\alpha}$ at low frequencies. Then I examined the significance of the frequency peak using the power spectral density method. It is found that the significance of the period at ~ 60 days is 95%.

During the course of the optical monitoring of the source, it was also notice that that the peak-to-peak amplitude of the short-term variations remains almost constant, ~ 1.3 magnitudes. Hence, the variability trend traced by the upper envelope is very similar to that by the lower envelope of the light curve during the course of ~ 2 years of our monitoring. The constant variability trend is displayed in Fig. 4.8. In this figure, the dashed line denotes a spline through the 75-days binned light curve, and the dotted lines are obtained by shifting the spline by ± 0.65 mag. So, the observed variations fall within an area of constant variation. A constant variability amplitude in magnitudes implies that the flux variation amplitude is proportional to the flux level itself (following $m_1 - m_2 \propto \log_{10}(f_1/f_2)$). This can be easily interpreted in terms of variations of the Doppler boosting factor, $\delta = [\Gamma(1 - \beta \cos \theta)]^{-1}$ (Raiteri et al., 2003). In such a scenario, the observed flux is relativistically boosted by a factor of δ^3 and requires a variation in δ by a factor of ~ 1.2 . Such a change in δ can be due to either a viewing angle (θ) variation or a change of the bulk Lorentz factor (Γ) or may be a combination of both. A change in δ by a factor of 1.2 can be easily interpreted by a variation of θ by few degrees, while it requires a more noticeable change of the bulk Lorentz factor. Therefore, it is more likely that the long-term flux base-level modulations are dominated by a geometrical effect than by an energetic one.

In summary, the flux variability amplitude remains almost constant during the course of optical observations. A similar variability trend was also observed in this source by Raiteri et al. (2003). The optical light curve of the source also displays fast flares with a rising timescale of ~ 30 days, which are much faster than the flux variations at radio wavelengths and therefore set tighter constrains on the size of the emission region.

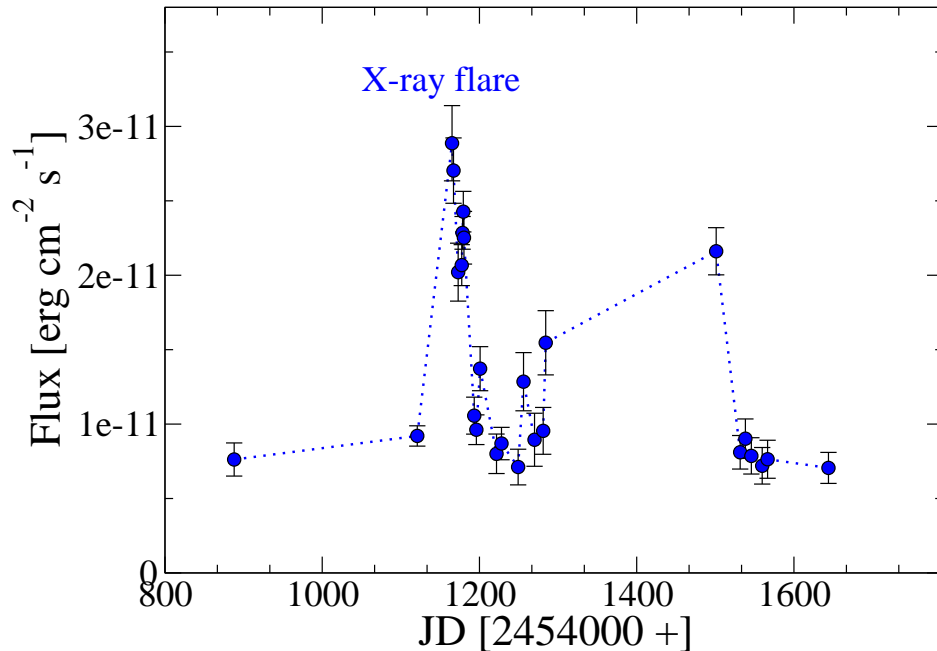


Figure 4.9: The X-ray (0.3 – 10 KeV) light curve of S5 0716+714.

4.3 X-ray frequencies

The X-ray (0.3–10 KeV) data were obtained by Swift/XRT over a time period of September 2008 to January 2011. Figure 4.9 displays the 0.3 – 10 KeV light curve of S5 0716+714. Although the X-ray light curve is not as well sampled as those at other frequencies, the data indicate occurrence of a flare at KeV energies between MJD = 55122 to 55165. However, due to large gap in the data train, it is not possible to locate the exact peak time of this flare.

In order to investigate the origin of the X-ray flare (JD' = 1120-1210, Fig. 4.9), the correlation between X-ray photon index and flux is investigated. No systematic change in the X-ray photon index (Γ_{X-ray}) is found with respect to a change in the flux. The X-ray photon index versus flux plot over the flaring period is shown in Fig. 4.10 (bottom) and the estimated correlation coefficient r_P is 0.25 with a confidence level of 69 %. Thus, as per correlation statistics, the X-ray photon index and flux are not significantly correlated with each other. It is worth pointing out that the flaring amplitude is similar at soft and hard X-ray bands as shown in Fig. 4.10 (top). The fractional variability is 22.5% and 25% in the soft and hard X-ray bands, respectively. The comparable fractional variability implies that the X-ray flare has equal contributions from the soft

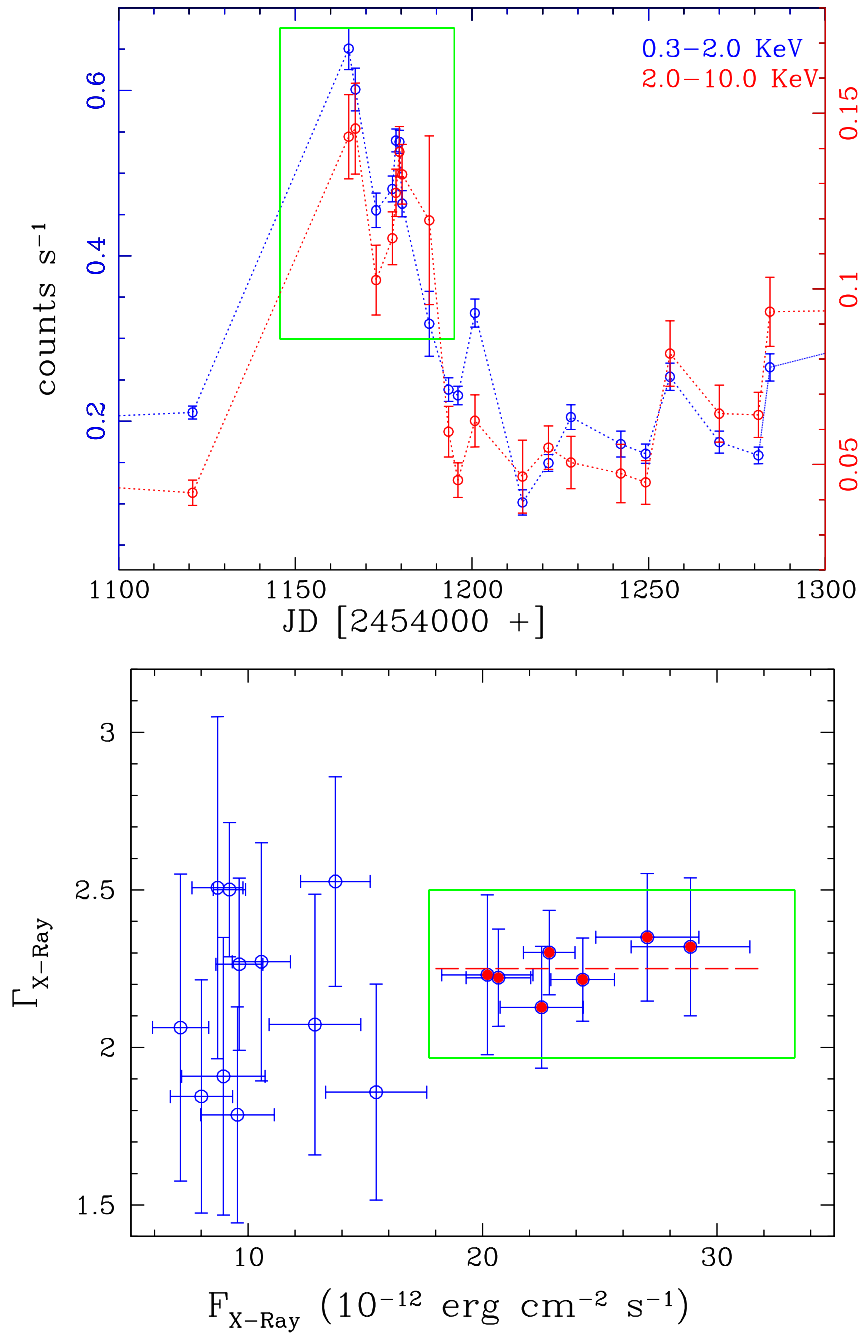


Figure 4.10: Top: Soft and hard X-ray light curves of the source over the period of high X-ray activity. The flaring activity is similar in the two X-ray bands. Bottom: X-ray photon index versus flux at 0.3 – 10 KeV. The data points in the box belong to a phase of brightening shown in the top figure. The X-ray photon index of the source is almost constant at 2.25 ± 0.25 (shown by a dashed line) over the flaring period.

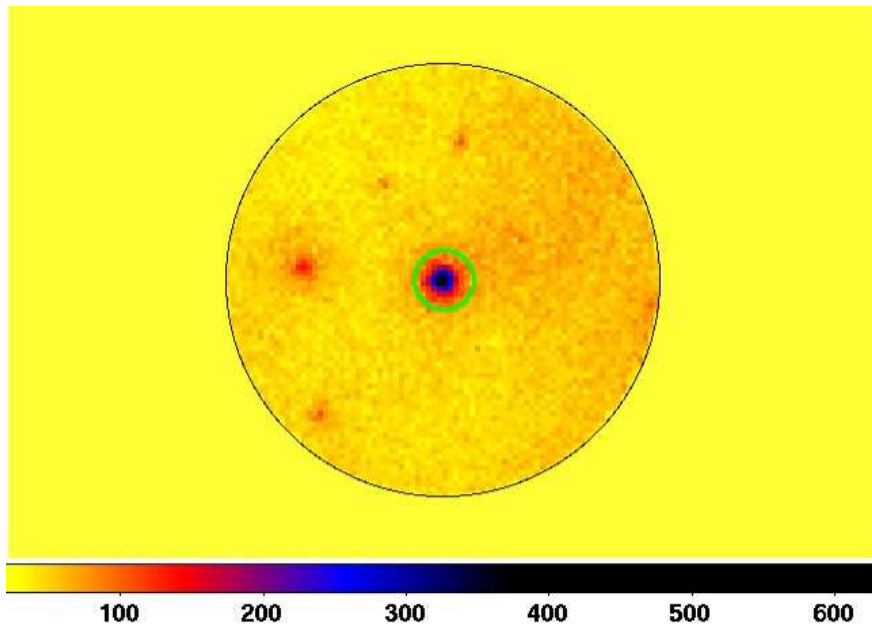


Figure 4.11: Sky map of γ -ray events centered on S5 0716+714 (image radius of 10°) above 100 MeV as measured by *Fermi-LAT* over the past > 3 years. The brightness scale at the bottom represents the number of observed photons.

and the hard X-ray bands. The concave shape of the X-ray spectrum (see Section 7.2), suggests that the X-ray emission shows a combination of synchrotron and inverse-Compton mechanisms which could prevent the source from exhibiting any steepening or hardening trend during the flare.

4.4 Gamma-ray frequencies

4.4.1 Sky map

Figure 4.11 shows the *Fermi-LAT* count map of the γ -ray events above 100 MeV centered on the position of S5 0716+714 with an image radius of 10° . There is no source as bright as 0716+714 within 10° of region of interest (RoI). The nominal position of 0716+714 is marked by a green circle. A total of 14,657 γ -ray photons associated with 0716+714 were detected during ~ 3.8 years of observations within the 68% containment radius of the LAT point spread function (PSF) above 100 MeV.

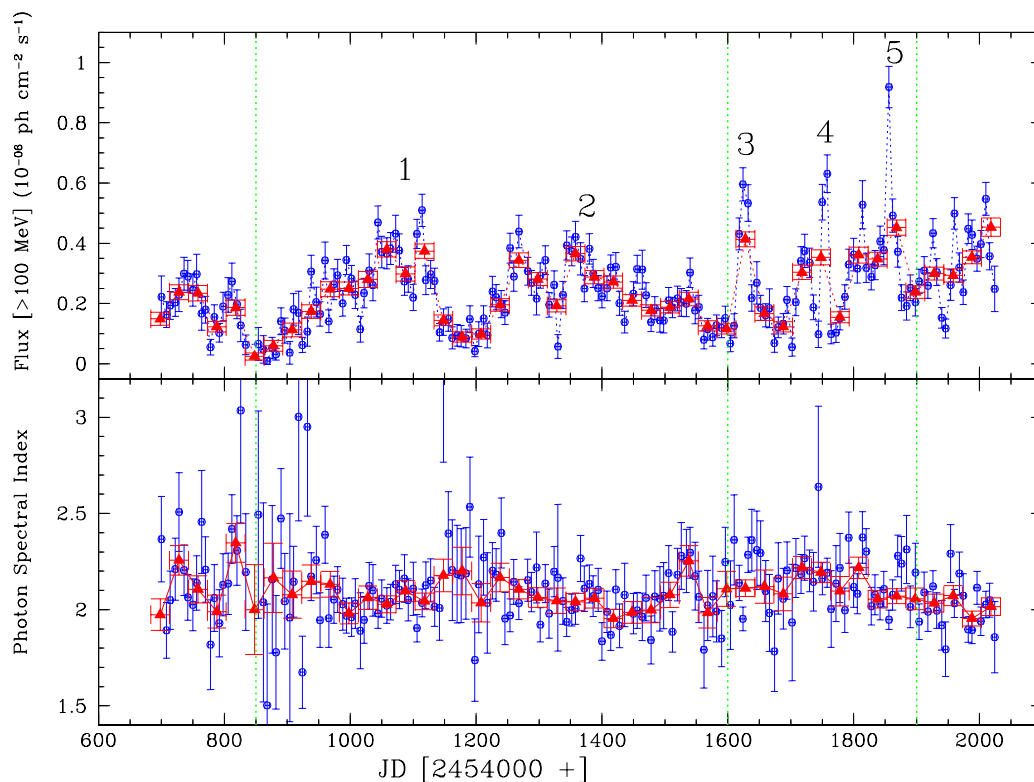


Figure 4.12: Gamma-ray flux and photon index light curve of S5 0716+714 measured with the *Fermi-LAT* since launch till April 04, 2012. The blue symbols show weekly averaged flux, while monthly averaged are in red. The green lines separate the two different modes of variability observed in the source (see text for details).

4.4.2 Light curves

The γ -ray flux variability of the source is investigated over a time period between August 04, 2008 to April 04, 2012. Figure 4.12 shows the weekly and monthly averaged γ -ray light curves extracted over an energy range from 100 MeV to 300 GeV. The source displays substantial flux variability during the past ~ 3.8 years of LAT monitoring with five major flares labeled as “1” to “5”. Apparently, some individual flares consist of a number of sub-flares.

There is a significant enhancement in the weekly averaged γ -ray flux over a time period between $\text{JD}'^1 = 900$ to 1110 (flare 1), peaking at $\text{JD}' \sim 1110$, with peak flux equal to $(0.57 \pm 0.05) \times 10^{-6} \text{ ph cm}^{-2} \text{ s}^{-1}$, which is ~ 6 times brighter than its minimum value and ~ 3 times brighter than its average value. Later it decays reaching a minimum

¹JD' = JD-2454000

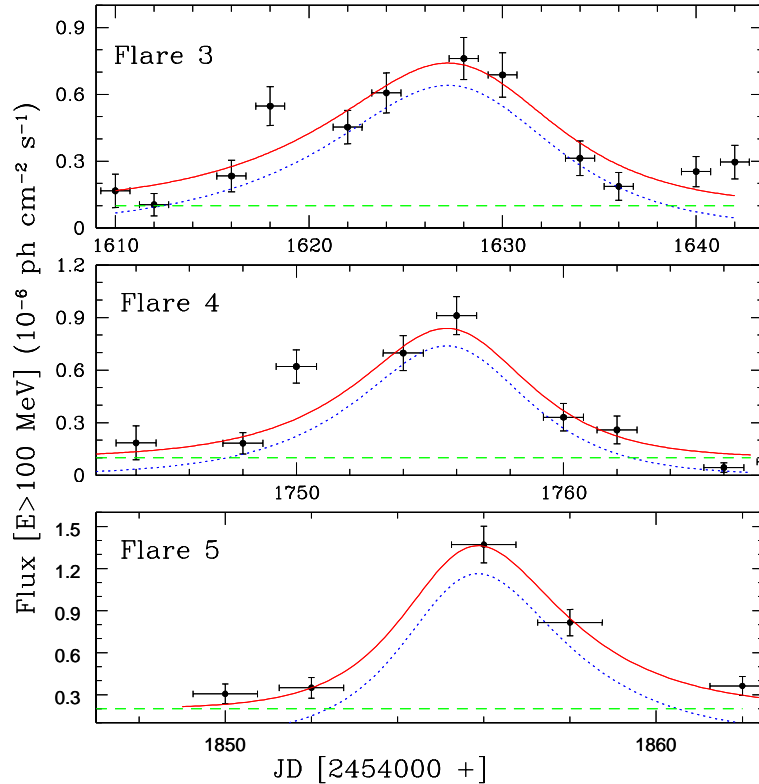


Figure 4.13: Light curves of the source flux above 100 MeV with a time binning of 3 day. The lines correspond to the results of fitted components using equation 4.1. The dotted curve is the flaring component. The dashed line is the background flux level and the solid curve is the total of the two components.

at $JD' = 1150$ followed by a quiescent state until $JD' = 1220$. The quiescent state is followed by a low amplitude flux variability (flare 2) and later by a sequence of rapid flares (flare 3 to 5).

The high photon statistics during the rapid flares allows us to investigate their evolution with finer time resolution. The light curves for F_{100} ($F[E > 100 \text{ MeV}]$ in units of $10^{-6} \text{ ph cm}^{-2} \text{ s}^{-1}$) with a 3 day time binning for the individual flares are shown in Fig. 4.13. A fit consisting of a nearly constant background and sub-flaring components is performed for each individual flare. The background is roughly approximated by a constant photon flux value = $0.40 \times 10^{-7} \text{ ph cm}^{-2} \text{ s}^{-1}$. Each component is fitted by a function of the form :

$$F(t) = 2 F_0 [e^{(t_0-t)/T_r} + e^{(t-t_0)/T_f}]^{-1} \quad (4.1)$$

Table 4.2: Fitted parameters of the rapid flares

Flare	T_r (days)	T_f (days)	t_0 JD'	F_0 10^{-6} ph cm $^{-2}$ s $^{-1}$	Doubling Time (days)*
3	6.22±1.02	4.14±0.86	1628.2±0.2	0.63±0.11	4.31
4	4.21±0.66	2.44±0.34	1756.0±0.1	0.73±0.12	2.91
5	1.29±0.12	2.05±0.18	1855.5±0.1	1.13±0.03	0.89

doubling timescale = $T_r \times \ln 2$

where T_r and T_f are the rising and decay times, respectively, and F_0 is the flux at t_0 representing approximately the flare amplitude. The solid curves in Fig. 4.13 represent the fitted flare components, and the fitted parameters for each flare are given in Table 4.2.

Flare 3 lasts for a duration of ~ 12 days ($JD' = 1610-1638$). The source reaches a peak flux value $F_{E>100MeV} = (0.63 \pm 0.11) \times 10^{-6}$ ph cm $^{-2}$ s $^{-1}$ during this flare with a doubling timescale of 4.3 days. This flare is followed by another rapid flare (flare 4) which has a duration of ~ 10 days. During this flare, the source reaches a peak flux value = $(0.73 \pm 0.12) \times 10^{-6}$ ph cm $^{-2}$ s $^{-1}$ above 100 MeV. Flare 5 is the brightest γ -ray flare observed in the source with a peak flux value = $(1.13 \pm 0.03) \times 10^{-6}$ ph cm $^{-2}$ s $^{-1}$ at $E > 100$ MeV with a doubling timescale of less than a day. So far, this is the fastest recorded γ -ray flare in the source.

In comparison to the substantial flux variations, the photon index (Γ) remains almost constant during the different modes of flux activity (see Fig. 4.14). A marginal steepening of the spectrum was noticed in the monthly averaged light curves during the flaring epochs. As shown in Fig. 4.14, the photon flux variations are characterized by a weak spectral hardening. For monthly averaged statistics, Γ changes from (2.20 ± 0.01) to (2.00 ± 0.04) for a flux variation of (0.10 ± 0.02) to $(0.50 \pm 0.01) \times 10^{-6}$ ph cm $^{-2}$ s $^{-1}$.

4.4.3 Flux variations at different energy bands

The temporal characteristics of the source were also investigated at different energy bands. Fig. 4.15 shows a comparison of the flux variability at different energies. Figures 4.15 (b) & (c) show the GeV flux variations above and below 1 GeV, respectively. No substantial difference is found in the flux variability at $E < 1$ GeV and $E > 1$ GeV. Such a behavior is obvious because of the marginal variation in Γ . I also do not find any time lag between the two light curves (at E below and above 1 GeV) for the weekly averaged

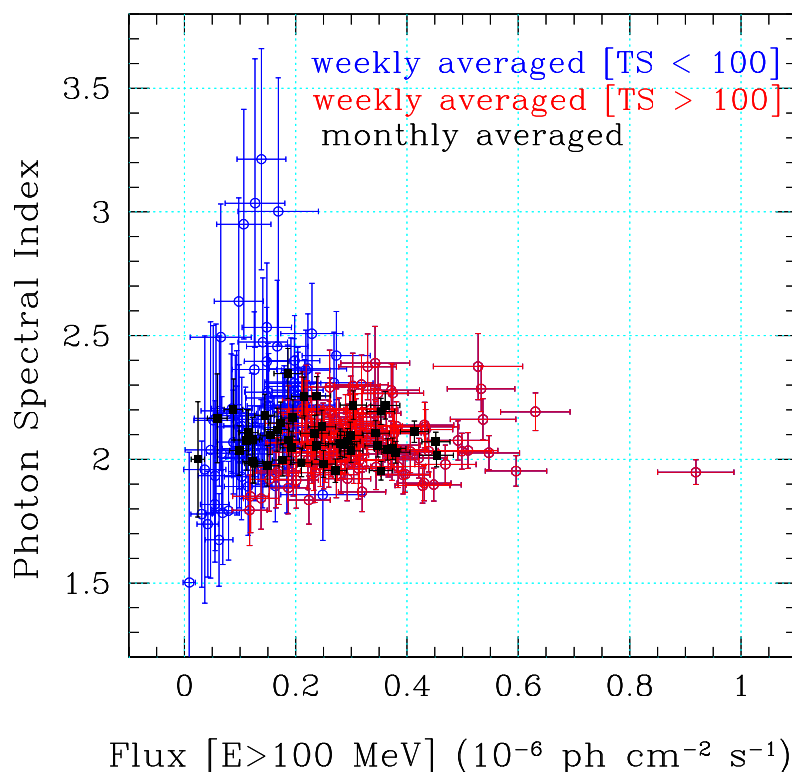


Figure 4.14: Photon index (Γ) versus photon flux variations at $E > 100$ MeV. The blue ($TS < 100$) and the red ($TS > 100$) symbols represent the weekly averaged values, while the monthly averaged are in black.

light curves. Due to a limited statistics for the finer binned light curves, any time lag shorter than our binning interval of 7 days can not be claimed.

I have also investigated photon fluxes variations above the de-correlation energy E_0 (Lott et al., 2012), the energy which minimizes the spurious correlations between integrated photon flux and photon index (Γ). Over the course of 3.8 years of observations, E_0 is found to be 248 MeV. Figure 4.15 (d) shows the flux variations above the de-correlation energy, $E_0 = 248$ MeV. The constant uncertainty (15%) light curve (red symbols) is obtained through the adaptive binning analysis method following Lott et al. (2012). An advantage of using this method is to avoid upper limits and to obtain better characteristics of the flares. The estimated systematic uncertainty on the flux using this method is 10% at 100 MeV, 5% at 500 MeV, and 20% at 10 GeV. The weekly averaged light curve below E_0 is shown in part (e) of the Fig. 4.15. The variability features are not clearly visible below E_0 due to large uncertainty and scattering of individual data

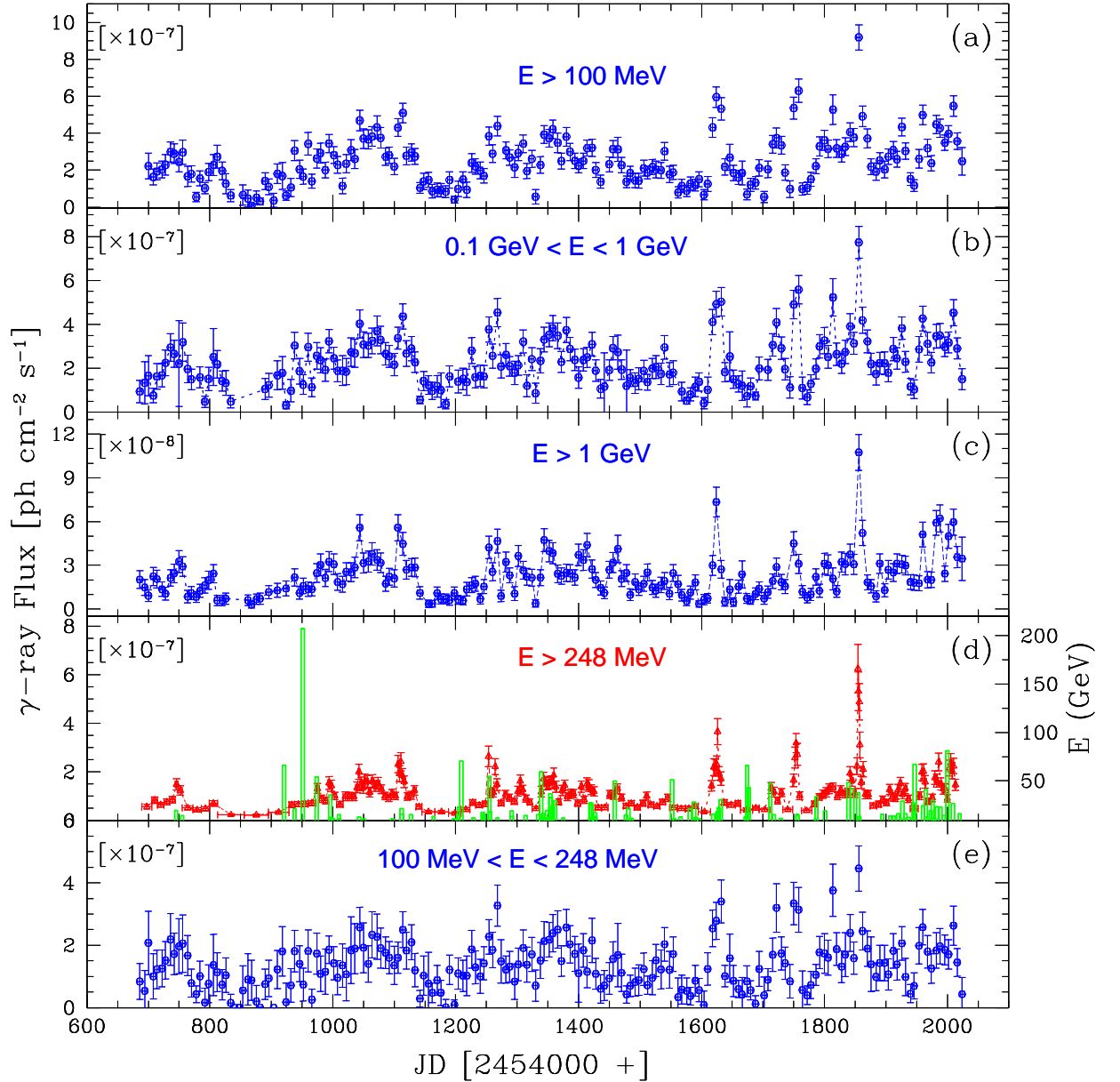


Figure 4.15: Gamma-ray flux light curves of S5 0716+714 during the first 3.8 years of the *Fermi-LAT* observations from August 2008 to April 2012; (a) weekly averaged light curve sampled above 100 MeV, (b) weekly averaged light curve sampled at 0.1–1 GeV, (c) weekly averaged light curve above 1 GeV, (d) the constant uncertainty (15%) light curve above de-correlation energy, $E_0 > 248\text{MeV}$ obtained through adaptive binning analysis method. The green histogram represents the arrival time distribution of $E > 10\text{GeV}$ photons associated with S5 0716+714, and (e) weekly averaged light curve below $E_0 = 248\text{MeV}$.

points.

4.4.4 Highest energy photons

During the 3.8 years of observations, the highest energy photon associated with 0716+714 was detected at $JD = 2454951$ with an estimated energy of 207 GeV. This photon is observed as a front event of the LAT detector. The reconstructed arrival direction of the photon is 0.05° away from S5 0716+714, and is within the 68% containment radius of the LAT PSF at 207 GeV. Based on our model fit of the epoch which contains that highest-energy photon, the estimated probability that the photon was associated with S5 0716+714 (as opposed to all other sources in the model including the diffuse emission and nearby point sources) is 99.96% which corresponds to 3.56σ .

In total, 107 events were found with estimated energies higher than 10 GeV centered at S5 0716+714 within the 68% confinement radius of the LAT PSF and a total of 10 events above 50 GeV. Figure 4.15 (d) plots the arrival time distribution of photons above 10 GeV. Interestingly, the highest energy photon arrived during the rising part of flare 1. In fact, a number of several high-energy photons were observed during this period. But during the peak and decay of flare 1, the number of events associated with the arrival of high-energy photons is very small. For the other four flares “2”-“5”, the arrival time distribution of the high-energy photons does not follow any systematic trend with respect to the photon flux variations (see Fig. 4.15 (d)).

4.4.5 Variability timescales at gamma-ray frequencies

In order to extract the characteristic time scale of variability (t_{var}) from the γ -ray light curves, the structure function analysis method is used. The weekly binned γ -ray light curve at $E > 100$ MeV is used for the structure function analysis. The γ -ray structure function curve is shown in Fig. 4.16. The structure function curve follows a continuous rising trend showing a peak at ~ 30 days followed by another peak in the range of 150–180 days. The 30 day timescale peak however is within the uncertainties, and that makes it marginally significant. In summary, the γ -ray structure function analysis reveals variability at a timescale of $t_{var} \sim 180$ days and a hint of short-term variability at t_{var} equals to ~ 30 days.

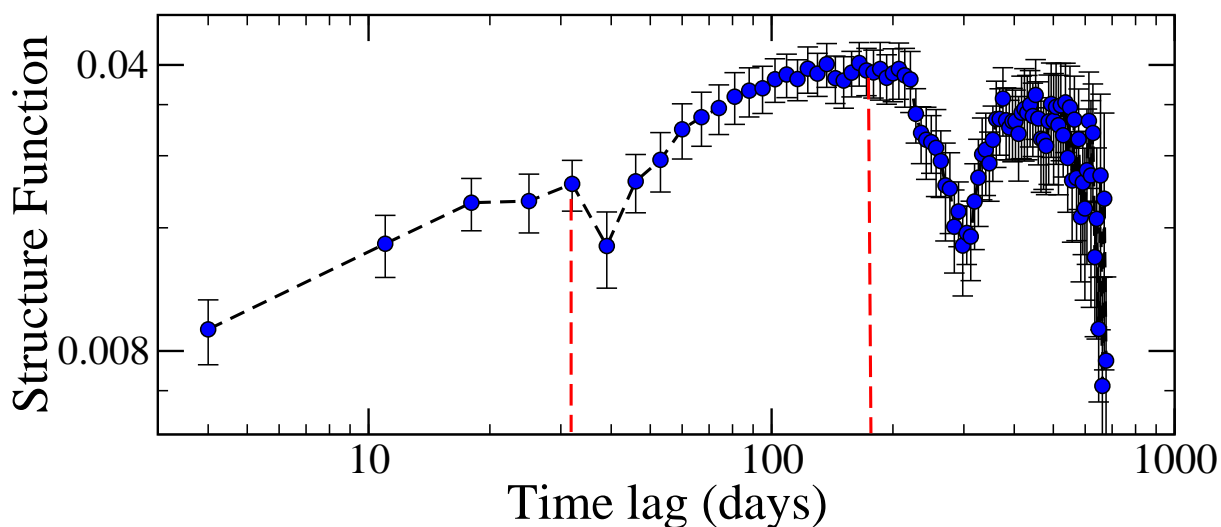


Figure 4.16: The γ -ray structure function analysis curve at E above 100 MeV with a bin size of 7 days. The vertical dashed lines indicate the characteristic variability timescales.

4.5 Summary and discussion

This chapter presents the analysis and results of the radio to γ -ray monitoring of S5 0716+714 from April 2007 to April 2012. The source was very active at optical and higher frequencies during the course of our observations. Two major radio outbursts were observed during this high activity period.

A long-term variability trend (~ 350 days timescale) is visible in the optical light curves which is superimposed with repetitive flux variations on shorter time scales (~ 60 day). The periodogram analysis reveals two significant peaks at ~ 60 and 360 day timescales. A more robust analysis using the power spectrum density method implies that the significance of a detection of a quasi-periodic signal at the frequency corresponding to these timescales is 95%. It is important to note that periodic variations at a year timescale have also been observed earlier in the source (Raiteri et al., 2003).

During the five years of the observations, I found that the long-term variability amplitude of the source remains almost constant at about 1.3 magnitudes. A constant variability amplitude can be interpreted in terms of variations of the Doppler boosting factor (Raiteri et al., 2003). The change in Doppler factor (δ) can be due to either a viewing angle (θ) variation or a change of the bulk Lorentz factor (Γ) or maybe a combination of both. I notice that a change in δ by a factor of 1.2 can be easily

interpreted as a few degree variation in θ , while it requires a more noticeable change of the bulk Lorentz factor. It is likely that the geometry significantly affects the long-term flux base-level modulations. Such variations are very likely originating as a relativistic shock traces a spiral path through the jet (Marscher, 1996).

The source displays substantial activity at γ -rays during the high optical activity period. A similar flaring behavior is observed at γ -ray and optical frequencies. This is to be expected in leptonic models, as the same electrons radiating the optical synchrotron photons would emit γ -rays through the inverse-Compton scattering process.

I notice that the long-term variability feature at $t_{var} \sim 180$ days is observed at all frequencies i.e. radio, optical, and γ -rays. However, the faster variability ($t_{var} \sim 30$ days) observed at optical and γ -ray frequencies does not extend to radio wavelengths. A similar long-term variability timescale at γ -ray, optical, and radio frequencies may suggest a co-spatial origin. In the next chapter, I present and discuss possible correlations between different observing bands (radio (cm and mm), optical, X-ray, and γ -ray).

Chapter 5

Multi-wavelength Correlated Variability

The previous chapter presented the temporal characteristics of the broad-band flux variability of S5 0716+714. The analysis suggests that the broad-band flaring behavior of the source is very complex. A sequence of flares were observed in the source at optical and higher frequencies. Two major radio outbursts followed this sequence. The multi-frequency light curves of S5 0716+714 are presented in Fig. 5.1. The source showed multiple flares across the whole electromagnetic spectrum over this period, which I label as follows. I draw the vertical lines with respect to the well defined peaks in the optical V-band light curve. The broad-band flares are labeled as “G” for γ -rays, “X” for X-rays, “O” for optical and “R” for radio followed by the number adjacent to them. For example, the optical flares should be read as “O1” to “O9”.

In order to search for possible time lags and to quantify the correlation among the multi-frequency light curves of the source, discrete cross-correlation functions (DCFs) are computed. The details of this method are given in Section 3.2.1.2. This chapter presents the details of the cross-correlation analysis between the observed light curves. The analysis presented in this chapter is focused on a time period from JD = 2454800 to 2455400 (April 2007 to January 2011), which covers the two major radio flares and the respective optical-to- γ -ray flaring activity. This chapter is structured as follows. A detailed correlation analysis of radio flux variability is provided in Section 5.1. Section 5.2 presents the correlation of radio flux variability with respect to optical, and Section

¹Work presented in this chapter is partially published in Rani et al. 2013a.

Table 5.1: Correlation analysis results among radio frequencies

Frequency (GHz)	a	b (days)	c (days)
230 vs. 15	1.56 ± 0.15	7.96 ± 2.23	19.81 ± 2.24
86 vs. 15	0.94 ± 0.13	6.65 ± 3.28	25.80 ± 4.28
43 vs. 15	1.04 ± 0.11	5.95 ± 2.08	23.86 ± 3.09
37 vs. 15	1.13 ± 0.09	4.95 ± 2.21	29.39 ± 2.81
23 vs. 15	1.17 ± 0.10	3.74 ± 1.50	25.00 ± 2.50
10 vs. 15	0.89 ± 0.09	-1.01 ± 1.09	35.07 ± 4.49
8 vs. 15	0.84 ± 0.08	-1.09 ± 1.01	35.96 ± 4.10
5 vs. 15	0.84 ± 0.10	-1.23 ± 1.25	33.13 ± 4.15
2.72 vs. 15	0.59 ± 0.12	-78.75 ± 12.39	53.54 ± 13.86

a : peak value of the DCF,

b : time lag at which the DCF peaks, and

c : width of the Gaussian function (see text for details)

5.3 with respect to γ -rays. The γ -ray versus optical correlation analysis is presented in Section 5.4. The correlation of the X-ray flare with broad-band flares is given in Section 5.5. In Section 5.6, an interpretation scheme is proposed that is able to establish a one-to-one connection of the broad-band flares based on the correlation analysis. Finally, the analysis results are summarized in Section 5.7.

5.1 Radio-radio correlation

At radio wavelengths, the source exhibits significant flux variability, being more rapid and pronounced towards higher frequencies. The two major outbursts are labeled as “R6” and “R8” (see Fig. 5.1). Apparently, the mm flares peak a few days earlier than the cm flares. The dense frequency coverage facilitates a cross-correlation analysis between the different observing bands. Owing to its better time sampling, the 15 GHz light curve was chosen as a reference. Figure 5.2 shows the DCF curves adopting a binning of 10 days.

A Gaussian profile fitting technique is used to estimate the time lag and respective cross-correlation coefficient value for the DCF curves. Around the peak, the DCF curve as a function of time lag t can be well described by a Gaussian function of the form :

$$\text{DCF}(t) = a \times \exp \left[\frac{-(t - b)^2}{2c^2} \right] \quad (5.1)$$

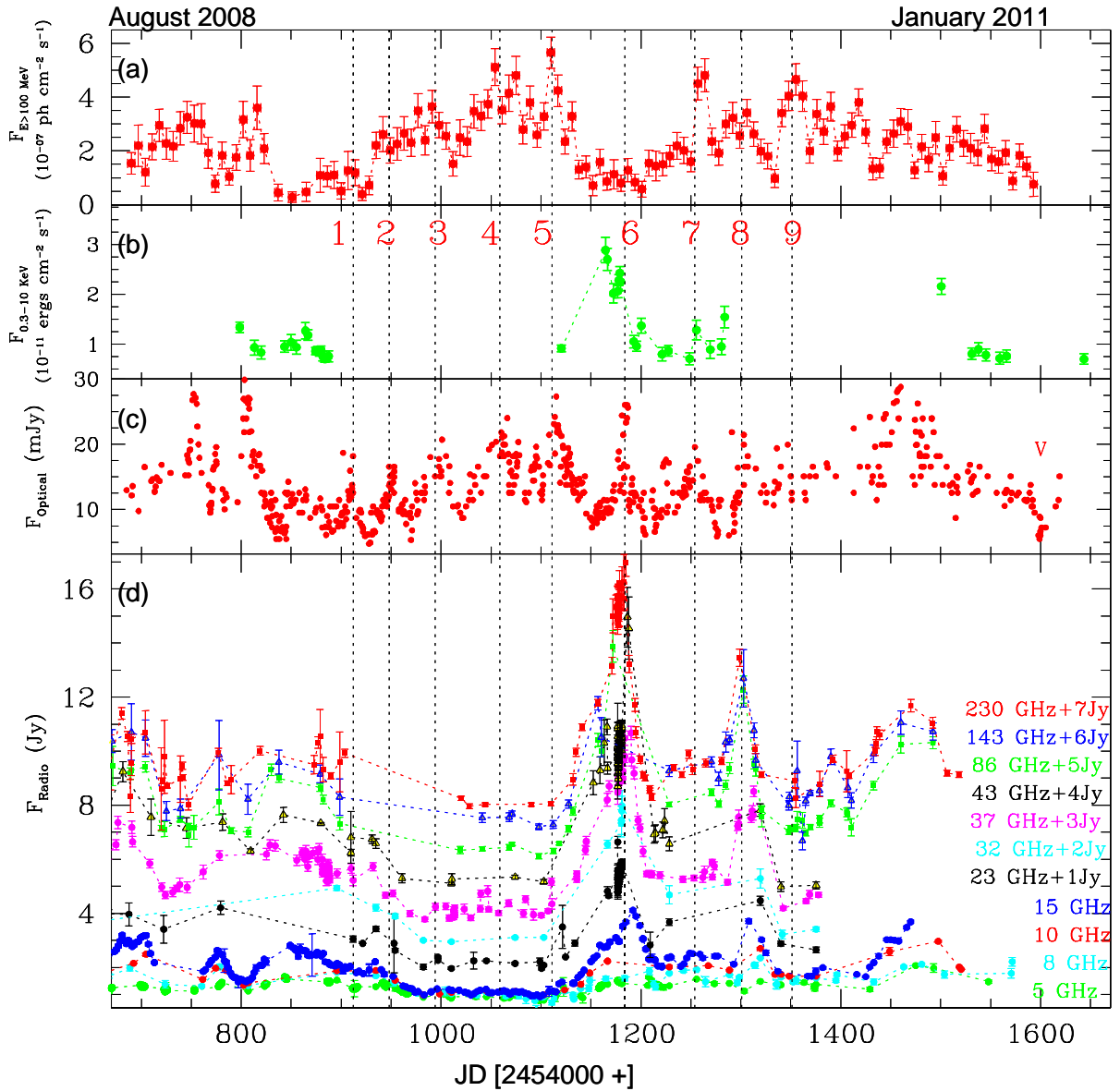


Figure 5.1: Light curves of 0716+714 from γ -ray to radio wavelengths (a): γ -ray light curve at $E > 100$ MeV, (b): X-ray light curve at 0.3–10 KeV, (c): optical V passband light curve and (d) : 5 to 230 GHz radio light curves. Vertical dotted lines are marked with respect to different optical flares labeling the broad-band flares as “G” for γ -rays, “X” for X-rays, “O” for optical and “R” for radio followed by the number close to flare.

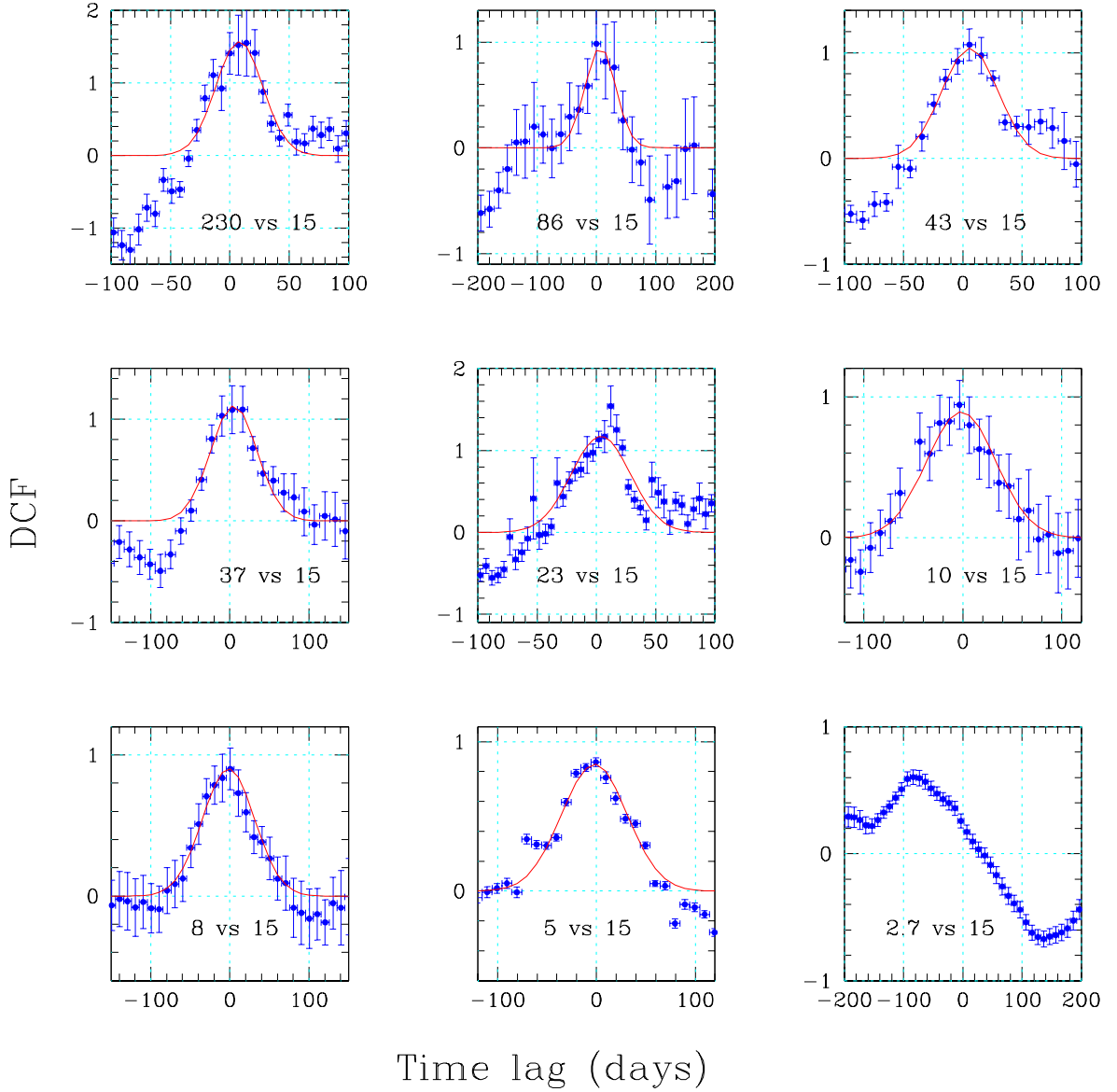


Figure 5.2: The DCF curves among the different radio frequency light curves. The solid curves represent the best-fit Gaussian function. The 2.7 versus 15 GHz DCF curve is not fitted with the Gaussian function because of weak correlation.

Table 5.2: Radio correlation analysis results for individual flares

Frequency (GHz)	Time lag* (days)		
	R0 Flare	R6 Flare	R8 Flare
23	2.9±1.4	4.06±1.6	—
33	2.1±1.0	5.88±2.1	—
37	4.2±2.6	3.15±2.1	4.0±1.0
86	4.2±1.0	6.15±2.6	5.0±1.8
143	5.8±1.8	6.82±2.5	7.0±1.5
230	6.0±2.4	8.54±1.9	9.0±2.0

* : relative to the respective flares at 15 GHz

where a is the peak value of the DCF, b is the time lag at which the DCF peaks, and c characterizes the width of the Gaussian function. The calculated parameter values (a , b , and c) for each frequency are listed in Table 5.1. The solid curve in Fig. 5.2 represents the fitted Gaussian function.

The cross-correlation analysis confirms the existence of a significant correlation across all observed radio-band light curves with formal delays listed in Table 5.1 (parameter b). However, below 10 GHz and lower frequencies, the correlation became weaker and almost vanished. The flux variations at 2.7 GHz seem to be less correlated with those at 15 GHz, which is obvious as the flaring behavior is not clearly visible below 15 GHz.

The long term radio light curves show three major radio flares, labeled as R0, R6 and R8 in Fig. 4.1. In the correlation analysis of the entire light curves, these flares are blended and folded into a single DCF. In order to separate the flares from each other, a correlation analysis over three different time bins is performed, which cover the time ranges of the individual radio flares: JD = 2454500 to 2454750 (R0 flare), JD = 2455000 to 2455210 (R6 flare), and JD = 2455210 to 2455400 (R8 flare). The time lags of these flares with respect to the 15 GHz data are estimated as above. However, due to sparse data sampling did not allow to estimate the time lags for R8 directly using the DCF method. For this flare, the data was interpolated first through a spline function, and then the DCF analysis was performed. The 23 GHz and 33 GHz radio band light curves were not included for this flare due to long data gaps. The calculated time lags of each flare are given in Table 5.2.

Figure 5.3 shows the calculated time lags as a function of frequency with 15 GHz as the reference frequency. The estimated time lag using the entire light curves are shown

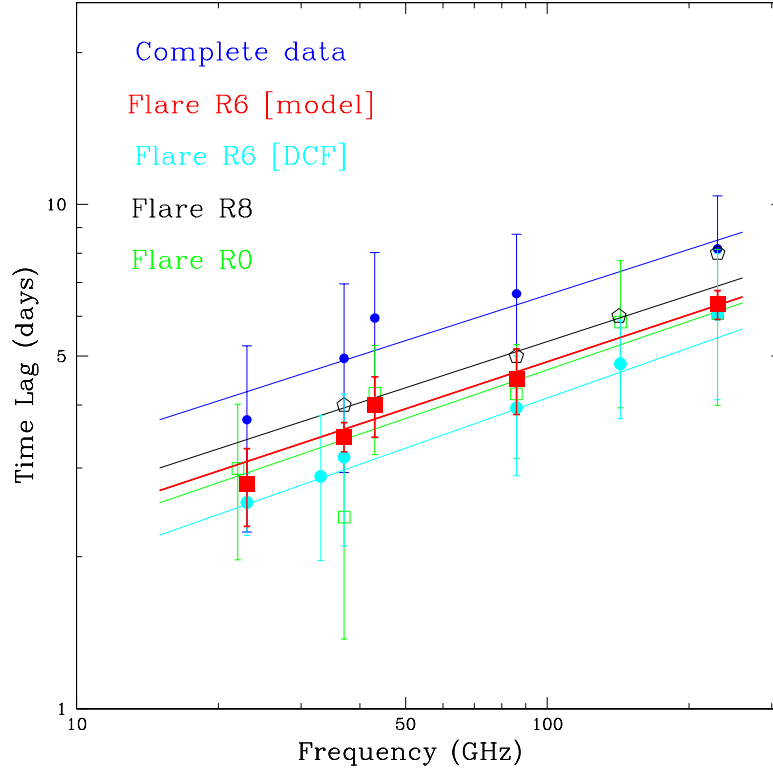


Figure 5.3: The plot of time lag versus frequency, using 15 GHz as the reference frequency. Time lag versus frequency curves for individual flares are shown with different colors. The solid lines represent the best fitted power law in each case.

with blue circles. Apparently the estimated time lag increases with an increase in frequency and seems to follow a power law. Such a power law dependence is expected due to the internal opacity effects (see Section 5.6.3 for details). Consequently, a power law, $P(f) = Nf^\alpha$ is fitted to the time lag versus frequency curve. The best-fit parameters are : $N = 1.71 \pm 0.43$, $\alpha = 0.30 \pm 0.08$. For the individual flares, the best-fit parameters are : $N = 1.07 \pm 0.06$, $\alpha = 0.32 \pm 0.01$ for the R0, $N = 1.45 \pm 0.61$, $\alpha = 0.32 \pm 0.08$ for R6, and $N = 1.33 \pm 0.01$, $\alpha = 0.29 \pm 0.03$ for R8. In conclusion, a common trend in the time lag (with 15 GHz as the reference frequency) versus frequency curve is seen for all the three radio flares (R0, R6 and R8) with an average slope of 0.30.

An alternative approach is followed to estimate the time shift of the radio flares at each frequency with respect to 15 GHz. The flares at each frequency are modeled with

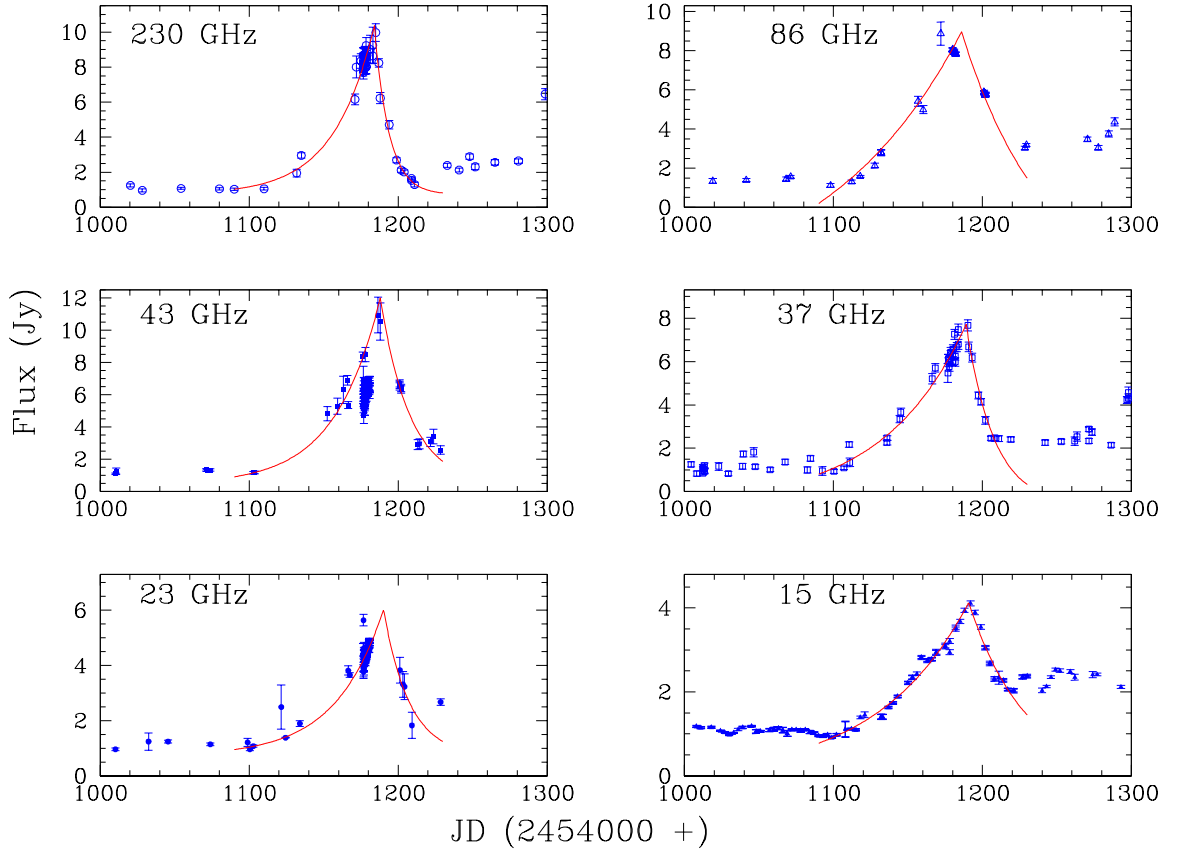


Figure 5.4: The modeled radio flare, R6. The blue points are the observed data, while the red curve represent the fit.

an exponential rise and decay of the form :

$$\begin{aligned}
 f(t) &= f_0 + f_{\max} \exp[(t - t_0)/t_r], & \text{for } t < t_0, \text{ and} & & (5.2) \\
 &= f_0 + f_{\max} \exp[-(t - t_0)/t_d] & \text{for } t > t_0
 \end{aligned}$$

where f_0 is the background flux level that stays constant over the corresponding interval, f_{\max} is the amplitude of the flare, t_0 is the epoch of the peak, and t_r and t_d are the rise and decay time scales, respectively. Since R6 is the most pronounced and best sampled flare, this flare is fitted with the above mentioned function in order to cross-check the frequency versus time lags results obtained by the DCF method. As the flaring behavior is not clearly visible below 15 GHz, I restrict this analysis to frequencies above 15 GHz.

Table 5.3: Fitted model parameters for R6 flare

Frequency GHz	f_0^* Jy	f_{max} Jy	t_r days	t_d days	t_0 JD [2454000+]
15	0.02 ± 0.07	4.15 ± 0.14	61.4 ± 6.2	37.9 ± 3.5	1191.4 ± 0.9
23	0.71 ± 0.23	5.30 ± 0.15	32.3 ± 4.8	17.3 ± 2.1	1190.2 ± 0.1
37	0.58 ± 0.11	8.20 ± 0.59	55.5 ± 11.0	18.6 ± 3.2	1189.1 ± 0.7
43	0.45 ± 0.35	9.50 ± 0.62	60.5 ± 9.4	20.1 ± 2.9	1188.0 ± 0.8
86	0.64 ± 0.18	10.6 ± 2.48	60.9 ± 28.8	25.1 ± 25.6	1186.0 ± 0.5
230	0.72 ± 0.11	12.64 ± 0.29	50.3 ± 2.4	9.9 ± 0.6	1184.2 ± 0.4

* : see text for the extension of labels.

As there is no observation available during the flaring epoch at 23 and 86 GHz, t_r and t_d at these frequencies are fixed using the fitted parameters from the adjacent frequencies. The best fit of the function $f(t)$ for the R6 flare is shown in Fig. 5.4, and the parameters are given in Table 5.3. The estimated time shift around the R6 flare at each frequency with respect to 15 GHz are shown in Fig. 5.3 (red symbols), and the fitted power law parameters are $N = 1.17 \pm 0.13$, $\alpha = -0.31 \pm 0.03$. Thus, this alternative estimate of the power law slope using the model fitting technique confirms the results obtained by the DCF analysis. *A systematic shift of the flare peaks with higher frequencies peaking earlier is expected due to internal opacity effects, as expected from synchrotron theory.* In Section 5.6.3, I will discuss about it in details.

5.2 Radio versus optical correlation

The source S5 0716+714 exhibits multiple flares at optical frequencies. The flares are roughly separated by 60–70 days. The different optical flares are labeled as O1–O9 as shown in Fig. 5.1. During this multi-flaring activity period two major flares are observed at radio wavelengths. The radio flare R6 apparently coincides in time with O6 and R8 with O8. To investigate the possible correlation among the flux variations at optical and radio frequencies, the DCF analysis is performed using the 2-year-long simultaneous optical and radio data trains from JD = 2454680 to 2455600 (see Fig. 5.1). Note that the strength of flux variability increases towards higher frequencies, peaking at 43 GHz (see Fig. 4.2). Therefore, two radio frequencies, 37 GHz and 230 GHz, are chosen in order to compare the strength of radio – optical correlation above and below the turnover frequency (43 GHz). The optical versus radio DCF analysis curves

Table 5.4: Optical versus radio DCF analysis results

V versus 230 GHz		V versus 37 GHz	
lag (days)	DCF Peak value	lag (days)	DCF Peak value
-4 ± 2.5	0.43 ± 0.10	-2 ± 2.5	0.28 ± 0.11
63 ± 2.5	0.83 ± 0.11	66 ± 2.5	0.76 ± 0.08
120 ± 2.5	0.60 ± 0.08	124 ± 2.5	0.60 ± 0.09
181 ± 2.5	0.51 ± 0.07	183 ± 2.5	0.49 ± 0.08

are shown in Fig. 5.5 (a). Multiple peaks in the DCF may reflect a quasi periodic oscillation or QPO behavior at optical frequencies. Half of the binning time is used as the formal errors for the measured time lags. The optical versus 230 GHz and 37 GHz DCF analysis results are summarized in Table 5.4.

The maximum correlation of the optical V passband with the 230 GHz light curve occurs at a 65 day time lag. However a second peak with lower peak coefficient also occurs close to zero time lag (see Fig. 5.5). The analysis shows that the cross-correlation coefficient of the simultaneous radio – optical flare peaks O6-R6 and O8-R8 is lower than the cross-correlation coefficient of the O5-R6 and O7-R8 flare peaks. In both cases, the optical flares O5 and O7 are observed ~ 65 days earlier than the radio flares R6 and R8, respectively.

In order to further quantify the correlation among optical and radio data, flux – flux plots are generated (see Fig. 5.5). For the following analysis a 1-day time binning is used. Figure 5.5 (b) shows the time shifted 230 GHz (t-63) and 37 GHz (t-66) flux plotted versus the optical V-band flux. The time-shifted radio and optical V-band fluxes fall on a straight line, indicating a strong correlation. A Pearson correlation analysis reveals a significant correlation between the two data trains. The following values are obtained : $r_P = 0.59$ and 99.93 % significance for 230 GHz (t-65) versus V-band and $r_P = 0.43$ and 99.3 % significance for 37 GHz (t-65) versus V-band, where r_P is the linear Pearson correlation coefficient. Thus, a significant correlation among the time shifted radio versus optical V-band flux is found with a confidence level > 99.99 % ($> 3\sigma$).

In contrast to this, the radio (with no time shift) versus optical V-band correlations are not found to be significant. Figure 5.5 (c) shows 230 GHz and 37 GHz versus V-band flux-flux plots, and the correlation statistics are: 230 GHz versus V-band: $r_P = 0.40$, 91 % significance and 37 GHz versus V-band: $r_P = 0.15$, 74 % significance. Thus, the significance of the correlations is lower than 95 % in these cases. The significance of

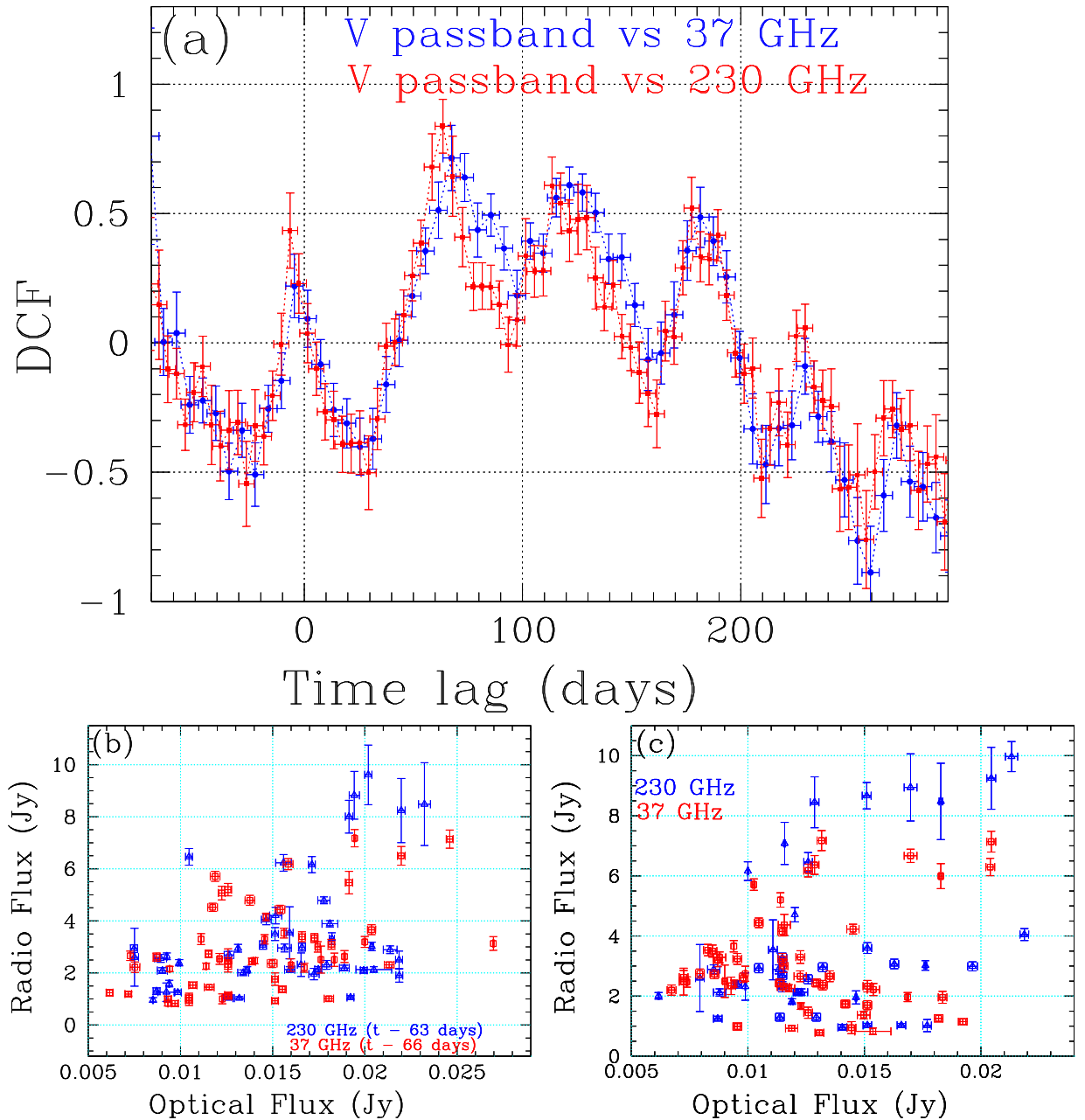


Figure 5.5: (a) The DCF curve for optical V passband versus 37 GHz (in blue) and 230 GHz (in red) flux with a bin size of 5 days. (b) Time shifted radio flux versus optical V-band flux. The blue symbols show the time shifted 230 GHz ($t - 63$ days) data while 37 GHz ($t - 66$ days) data are shown in red. (c) Radio flux versus optical V-band flux.

the correlation statistics with a time shift of ~ 120 and 180 days is also checked in the same manner. The analysis do not reveal a correlation to have a significance greater than 95 % in any case.

Hence, the DCF and linear Pearson correlation statistics reveal a significant correlation among the flux variations at optical and radio frequencies with the optical V-band leading the radio fluxes at 230 and 37 GHz by ~ 63 and ~ 66 days, respectively. *In conclusion, the flux variations at optical and radio frequencies are correlated such that the optical variability is leading the radio with a time lag of about two months.*

5.3 Radio versus gamma-ray correlation

The DCF analysis method is employed to investigate a possible correlation among flux variations at radio and γ -ray frequencies. The adequately sampled highest frequency (230 GHz) light curve is chosen for the DCF analysis. Figure 5.6 shows the DCF analysis results of the weekly averaged γ -ray light curve with the 230 GHz radio data with a time bin size of 9 days. To estimate the possible peak DCF value and respective time lag, a Gaussian function is fitted to the DCF curve with a bin size of 11 days. The best-fit function is shown in Fig. 5.6, and the fit parameters are $a = 0.94 \pm 0.30$, $b = (67 \pm 3)$ days, and $c = (7 \pm 2)$ days. This indicates a clear correlation between the γ -ray and 230 GHz radio light curves of the source with the γ -ray flare leading the radio flare by (67 ± 3) days.

To check the significance of the γ -ray versus radio correlation, flux-flux plots of the time shifted radio versus γ -ray flux are produced. Since the γ -ray flux is weekly averaged, a time binning equals to seven days is used for the flux-flux plots. The weekly averaged flux-flux plots of the time shifted 230 GHz ($t + 67$ days) and 37 GHz ($t + 70$ days) versus γ -ray are shown in Fig. 5.6 (bottom), and the correlation statistics are: 230 GHz ($t + 67$ days) versus γ -ray: $r_P = 0.37$, 97.7 % significance and 37 GHz ($t + 70$ days) versus γ -ray: $r_P = 0.33$, 97.3 % significance. Thus, in each case the significance of the correlation is higher than 95 %. This supports a possible correlation among the flux variations at γ -ray and radio frequencies with γ -rays leading the radio emission by ~ 67 days. It is also important to note that the time shifts are very similar to the time shifts observed between radio and optical bands (see Section 5.2). Therefore a very short or no time delay is expected between the flux variations at optical and γ -ray frequencies. This will be investigated in the next section.

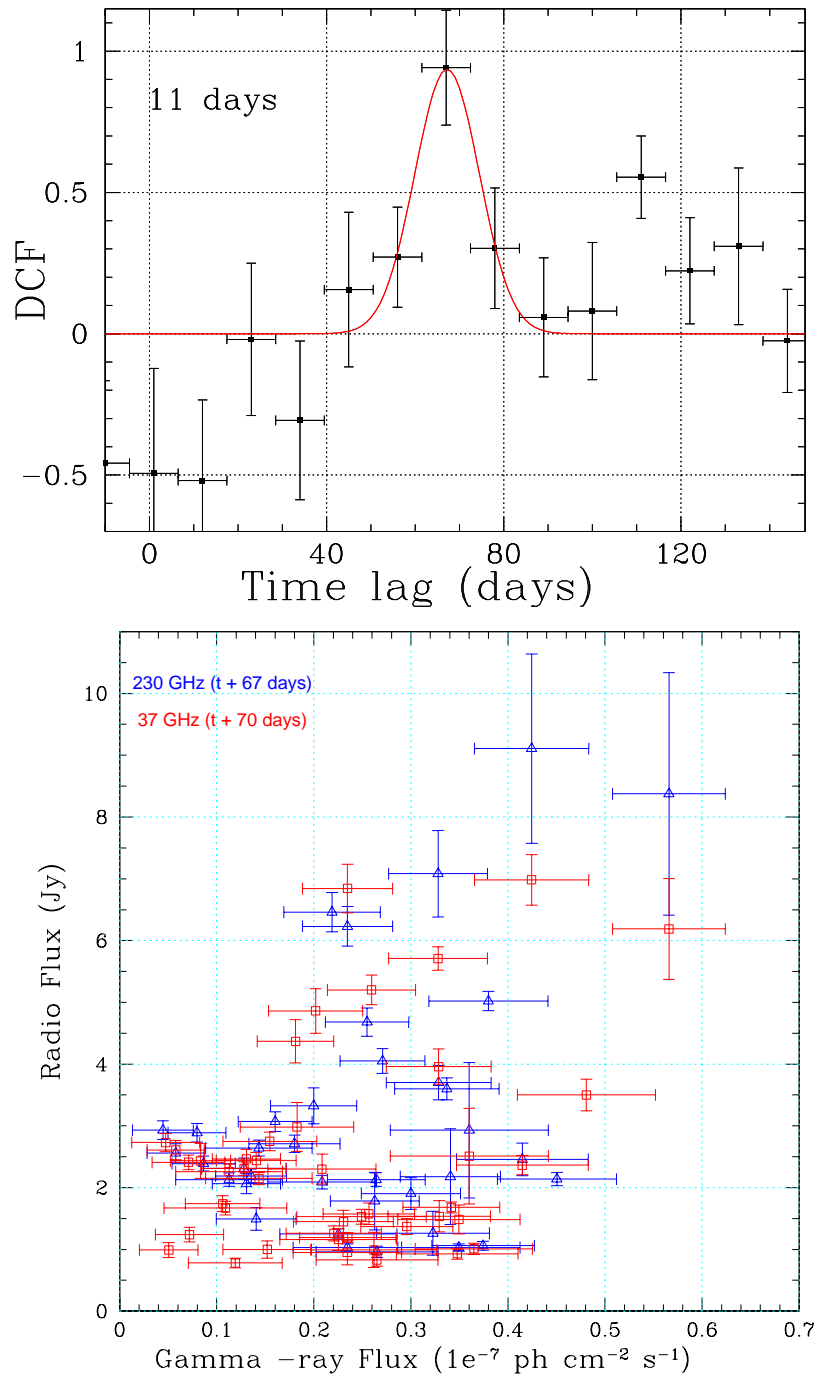


Figure 5.6: Top: DCF curve of the γ -ray light curve with respect to the 230 GHz radio light curve. The solid curve is the best fitted Gaussian function to the 11 day binned DCF curve. Bottom: Flux-flux plot of the shifted radio versus γ -ray data. The blue symbols show the time shifted 230 GHz data, while 37 GHz data are shown in red.

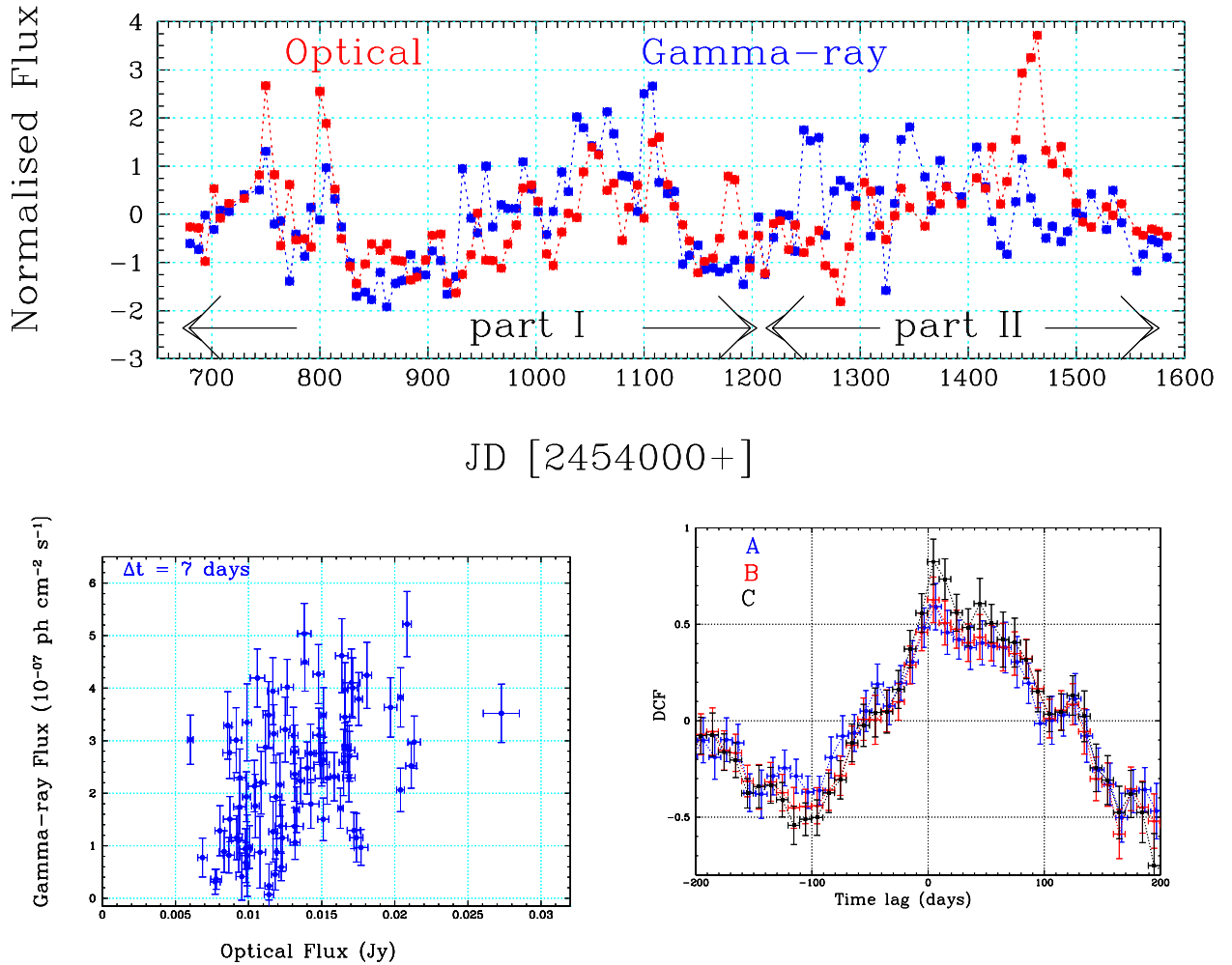


Figure 5.7: Top: The weekly averaged normalized flux at γ -ray and optical V band frequencies plotted versus time. The flux variations at these two frequencies seem to have a one-to-one correlation with each other. Bottom left : Weekly averaged γ -ray versus optical flux (all data). Bottom right: The DCF curve of γ -ray versus optical V passband flux using a bin size of 10 days in each case. A: using the complete data as shown in Fig. 5.1; B: after removing the data covering the duration of the optical flare O6; C: using the data before flare O6 (see text for details).

5.4 Optical versus gamma-ray correlation

Visual inspection of variability curves in Fig. 5.1 shows an apparent correlation between the various flux density peaks of the γ -ray light curve and the optical peaks (O1 to O9, except O6). The flaring pattern at γ -rays is similar to the QPO-like behavior observed at optical frequencies. In addition, the long-term variability features are also simultaneous at the two frequencies. To compare the flaring behavior of the source at optical and γ -ray frequencies, the normalized weekly averaged optical and γ -ray light curves are plotted on top of each other (see Fig. 5.7 top). A consistent and simultaneous flaring behavior can be seen from JD = 2454680 to 2455200 (part I); however, the γ -ray and optical variability is less correlated later (part II). Therefore, I subdivide the light curve in part I and part II as shown in Fig. 5.7 (top). Figure 5.7 (bottom left) shows a flux-flux plot of the weekly averaged γ -ray versus optical V-band data for both parts together. The weekly averaged optical flux are used for the above analysis. The uncertainty represents variation of the optical flux over a week period. A clear correlation among the two can be seen, which is confirmed by a linear correlation analysis, yielding $r_P = 0.36$ and 99.996 % confidence level. The correlation is even stronger in part I, the correlation statistics are : $r_P = 0.66$ and 99.9999 % confidence level ($>3 \sigma$).

The cross-correlation analysis results of the γ -ray and optical data trains are shown in Fig. 5.7 (bottom right). The following three cases are considered for the cross-correlation analysis :

Case A : DCF using the complete data as shown in Fig. 5.1 (both part I and part II). The γ -ray and optical flux are found to be weakly correlated with each other with DCF peak value = 0.50 ± 0.04 with a time lag = (0 ± 5) days (the error represents half of binning size used).

Case B : DCF after removing the optical flare O6 between JD = 2455150 and 2455220. The γ -ray and optical flux are found to be well correlated with each other with DCF value = 0.72 ± 0.03 with a possible time lag = (0 ± 5) days.

Case C : DCF using the data until flare O5 (part I only).

The γ -ray and optical flux are strongly correlated with each other with DCF value = 0.78 ± 0.04 with a possible time lag = (2 ± 5) days.

The optical versus γ -ray analysis results are summarized in Table 5.5. This analysis

Table 5.5: Optical versus γ -ray cross-correlation analysis results

Case	Time duration JD [2454000+]	Peak DCF value	Time lag days
A	total (840 - 1350)	0.50 ± 0.04	0 ± 5
B	removing R6 (1150 - 1220) flare	0.61 ± 0.04	1 ± 5
C	before R6 flare (840 - 1150)	0.80 ± 0.08	3 ± 5

reveals that the two-year-long γ -ray and optical data trains are strongly correlated with each other with no time lag longer than one week. It is also important to note that the strength of correlation is higher before the end of the O5/G5 flares than after those flares (see Fig. 5.7). *A one-to-one correlation between the optical and γ -ray flux variations can be expected in leptonic models, where the same electrons radiating the optical synchrotron photons would emit γ -rays through the inverse-Compton scattering process.* A detailed discussion about the origin of γ -ray emission is given in Section 5.6.2.

5.5 The orphan X-ray flare

Although the X-ray light curve of the source is the least sampled one among all the multi-frequency light curves, but it shows a flare peaking at a time between flare “5” and “6” [JD = 2455000 to 2455200] (see Fig. 5.1). However, due to the gap in the observations it is hard to determine the exact peak time of the flare. Considering that the maximum in the X-ray light curve (say X6) is close to the peak of the flare, this epoch coincides with a minimum in the optical/ γ -ray flux, and it is observed ~ 50 days after the major optical/ γ -ray flares (O5/G5) (see Fig. 5.1).

The DCFs of the X-ray light curve with γ -ray and radio frequency light curves do not follow any particular trend, as there are very few observations available in the X-ray band. A formal X-ray versus optical DCF curve (Fig. 5.8) shows a peak at a time lag = $-(60 \pm 3)$ days and another peak at (15 ± 3) days. The large DCF error bars are due to sparse data sampling of the X-ray light curve. In the former case, a negative time lag means that optical variations lead the X-ray ones, while in the other case the opposite occurs. An overall inspection of the light curves in Fig. 5.1 reveals that the optical flare (O5) is observed ~ 55 days earlier than the X-ray flare X6, and O6 appears ~ 12 days later. This indicates that the X-ray variability is governed by some other process/effect

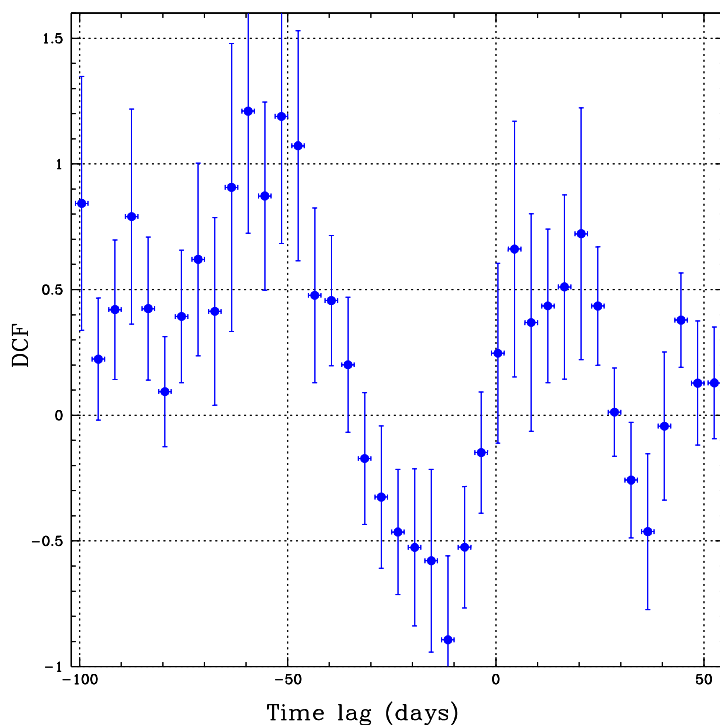


Figure 5.8: The DCF curve of X-ray versus optical V passband flux using a bin size of 3 days.

than the major optical/ γ -ray flares (O5/G5), which appear strongly correlated.

5.6 Discussion

5.6.1 Origin of optical variability

During the observations, the source was highly active at optical frequencies showing multiple flares roughly separated from each other by $\sim(60 - 70)$ days, superimposed on a long-term variability trend at a ~ 350 day timescale. The periodogram analysis reveals two significant peaks at ~ 60 and 360 day timescales. A more robust analysis using the power spectrum density method implies that the significance of a detection of a quasi-periodic signal at the frequency corresponding to a timescale of 60 days is 95 %. The periodic variations at a year timescale have been also observed earlier in the source (Raiteri et al., 2003). However, due to limited time coverage here, it remains uncertain.

During the two years of observations, the long-term variability amplitude of the source remains almost constant at about 1.3 magnitudes (see Section 4.2 for details). A constant variability amplitude can be interpreted in terms of variations of the Doppler boosting factor (Raiteri et al., 2003). The change in δ can be due to either a viewing angle (θ) variation or a change of the bulk Lorentz factor (Γ), or maybe a combination of both. I notice that a change in δ by a factor of 1.2 can be easily interpreted as a few degree variation in θ , while it requires a more noticeable change of the bulk Lorentz factor. Therefore, it would not be unreasonable to propose that the geometry significantly affects the long-term flux base-level modulations. Such variations are very likely originating as a relativistic shock traces a spiral path through the jet (Marscher, 1996).

5.6.2 Origin of gamma-rays

The source displays substantial activity at γ -rays during the high optical activity period. This is expected in leptonic models, as the same electrons radiating the optical synchrotron photons would emit γ -rays through the inverse-Compton scattering process (SSC). A similar flaring behavior is observed at the two frequencies. It is also found that the flux variations at optical and γ -ray frequencies are significantly correlated with each other (on weekly timescales) and corresponding to each optical flare “O1” to “O9” (except O6) there is a local maximum “G1” to “G9” at γ -ray frequencies. In addition, the variability timescales (both short and long) are also comparable at the two frequencies. The estimated ratio between the high and low γ -ray flux levels is about 15, while in the optical band the same ratio is of the order of 3.7. Thus, the γ -ray flux density appears to vary as the square of change in the optical flux density. This reflects a quadratic dependence of the γ -ray flux variations compared to optical variability. This favors a SSC interpretation (Chiaberge & Ghisellini, 1999; Chen et al., 2008). However, I would also like point out that a weak external-Compton contribution is also required in order to model the γ -ray spectrum of the source. The details of the spectral modeling are given in chapter 7.

5.6.3 Opacity and delay at radio wavelengths

Flares which are delayed and appear late at lower frequencies are a clear indication of opacity effects due to synchrotron self-absorption. The observed time delays can be

easily explained in terms of a shift in the absolute position of the jet base, where the optical depth $\tau = 1$ (Königl, 1981). As a result, in a shock-induced flare, the high-frequency flares are followed by those at low frequencies. This is measured as time lags among multi-frequency light curves (Kudryavtseva et al., 2011). The details of frequency-stratification in a shock-induced flare are given in Section 1.6.

Most of the earlier studies on radio-optical correlations have shown that the radio events lag behind the optical ones by several weeks or months (e.g. Agudo et al., 2011; Clements et al., 1995; Jorstad et al., 2010; Raiteri et al., 2003; Tornikoski et al., 1994; Villata et al., 2007, and references therein). Occasionally contemporaneous optical-radio activity has also been observed in the source (Quirrenbach et al., 1991; Villata et al., 2008). Raiteri et al. (2003) noticed that in the 1994-2001 observing period, major optical outbursts of 0716+714 do not correspond to bright radio flares. They only found modest radio counterparts during bright optical flares. Villata et al. (2007) observed contemporaneous optical-radio outburst in the source during a GASP-WEBT-AGILE campaign in 2007. Thus, the optical emission region of the jet is sometimes opaque and sometimes not completely opaque to the radio frequencies. Such a correlated optical-radio variability feature can be easily explained in terms of a generalized shock model e.g. as proposed by Marscher & Gear (1985).

The flux behavior i.e. time delays or lack of them can be interpreted by opacity effects in the context of the shock-in-jet model (Marscher & Gear, 1985; Valtaoja et al., 1992). In the high-peaking flares, the shock reaches its maximal development above the observing frequency and the flare becomes optically thin at the observed burst maximum and then the lower frequency flares follow the higher ones. While for the low-peaking flares, the shock reaches its maximal development below the observing frequency, the flare become optically thin near the beginning of the outburst. In this case, time delays between different frequencies are very small or non-existent. Alternatively, some optical flares may have a different origin with the optical flux coming from regions close to the core. In this case, the optical flares are the precursors of the radio flares (Valtaoja et al., 1992). Therefore, for low-peaking flares, the long time delays between optical-radio outbursts suggest that the optical activity is the precursor of that at radio wavelength.

As per cross-correlation analysis, the optical-radio variability is found to be significantly correlated, with the flux variations at optical frequencies leading those at radio bands by ~ 60 days (see Section 5.2). It is worth pointing out that the long term vari-

ability timescales are common at optical (and also at γ -rays) and radio frequencies. However, the fast repetitive optical/ γ -ray flares are not observed at radio wavelengths. Therefore, it is not unreasonable to suggest that the long term variability features observed at optical/ γ -ray frequencies propagate down to radio frequencies with a time lag of ~ 60 days. As discussed in Section 6.1.1, the two radio outbursts are low-peaking flares. Therefore, a 60 day time delay between the optical-radio activity strengthen the interpretation in the sense that the optical flares being the precursor of the radio flares.

5.6.4 Origin of the X-ray flare

The source was in a quiescent phase at X-rays during the major optical/ γ -ray flares. Although it is hard to locate the exact peak time of the X-ray flare, it is obvious that the maximum of the X-ray flux peaks ~ 50 days later than the major optical/ γ -ray flares (O5-G5) (see Fig. 5.1). At this epoch, the source was in a relatively steady state at optical/ γ -ray frequencies, while there is another bright optical flare lagging the X-ray maximum by ~ 10 days. The fractional variability of the source is comparable at soft (22.5 %) and hard (25 %) X-ray bands. Interestingly, no significant correlation is found among the X-ray spectral index and flux. This may be due to the poor data sampling or may be intrinsic to the source. The concave shape of the X-ray spectrum (see Section 7.2), suggests that the X-ray emission shows a combination of synchrotron and inverse-Compton mechanisms, which could prevent the source from exhibiting any steepening or hardening trend during the flare.

A similar orphan X-ray flare was also observed in the blazar 3C 279 by [Abdo et al. \(2010c\)](#) with X-ray flaring activity lagging optical/ γ -ray flares by 60 days. The authors argued that the X-ray photons are produced further down to the jet compared to optical/ γ -ray photons. [Hayashida et al. \(2012\)](#) argued in the context of a two component model; the X-ray flare is produced by the low-frequency component, which is less variable compared to the high-frequency component. Although the origin of the orphan X-ray flare in S5 0716+714 is not completely understood, it could be possible that the X-ray emission is not co-spatial with the optical/ γ -ray emission in this event. A low level flux activity is observed (mini-flare, say R7) in between the two major radio flares (“R6” and “R8”, see Fig. 5.1). While modeling the radio spectra of the source, it is found that a two-component model better describes the synchrotron spectra of the source during this period. This indicates that either multiple shocks are hitting the

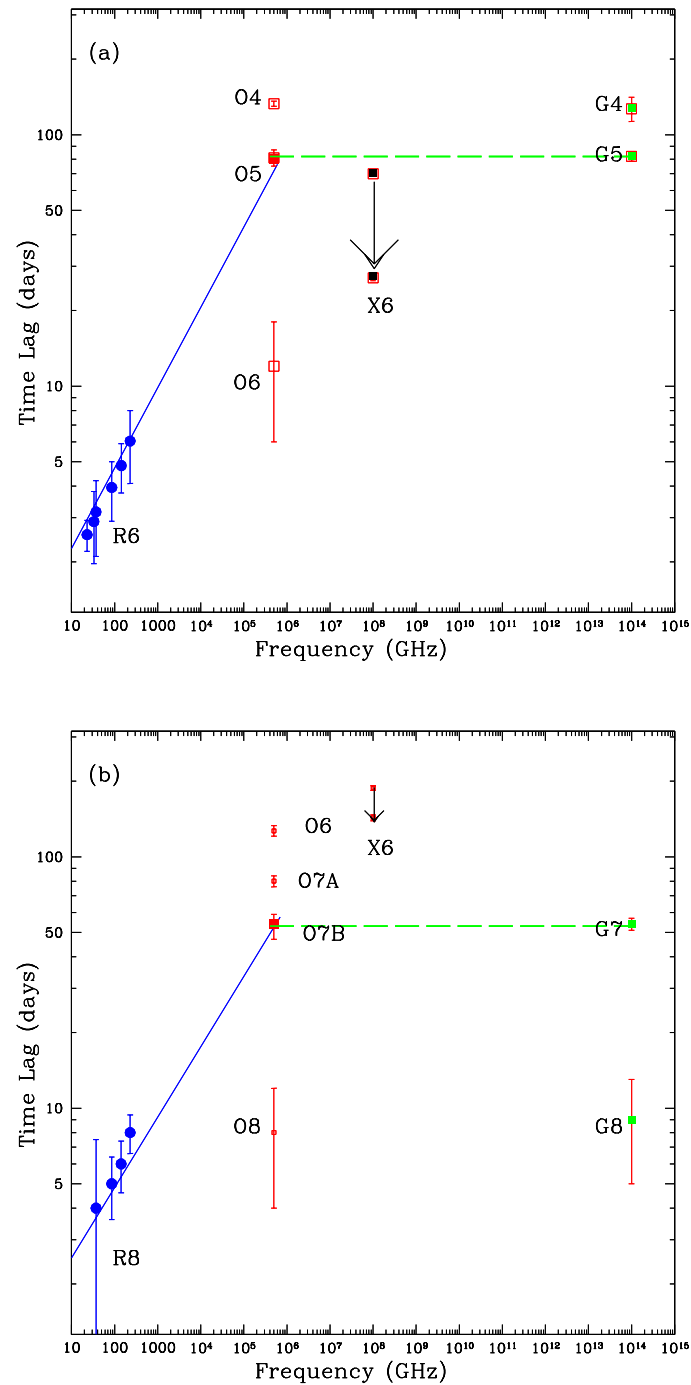


Figure 5.9: (a) A plot of time lag measurements versus frequency using 15 GHz as the reference frequency for the radio flare R6. The best fitted power law at radio and mm frequencies is extended up to the optical wavelengths. The near by optical, X-ray and γ -ray flares are shown with their possible time lags with respect to R6. (b) A similar plot for the R8 flare (see Fig. 5.1 for flare labeling) In both plots, the dashed lines indicate the SSC process with simultaneous optical- γ -ray events (see text for details).

emission region, which at first produces the major flare “O5/G5-R6”, then “X6/O6-R7” and later “O7/G7-R8”, or the radiation is contributed by two synchrotron components with the low-frequency component producing the X-ray flare.

5.6.5 Broad-band correlation alignment

Following the broad-band cross-correlation analysis, the estimated time lag is plotted as a function of frequency in Fig. 5.9. Figure 5.9 (a) shows the plot of the time lag measurements at different frequencies for the R6 flare using 15 GHz as the reference frequency (see Fig. 5.1). It has become evident in Section 5.1 that the time lags (with respect to 15 GHz) increase with frequency and follow a power law as a function of frequency with a slope ~ 0.3 . If the fitted power law is extended from radio to optical frequencies, then the R6 flare meets the O5 flare, which is observed ~ 60 days earlier than the R6 flare. *Such a power law dependence is expected in synchrotron theory due to synchrotron self-absorption.* The opacity-delay argument is strengthened by a formal cross-correlation between optical and radio frequency with a delay of ~ 60 days at radio wavelengths. The solid lines in Fig. 5.9 connects the corresponding optical and radio flares.

The dashed line in Fig. 5.9 (a) connects the simultaneous optical- γ -ray flares. *Such simultaneity is expected within the standard synchrotron self-Compton (SSC) scenario, with small or no time lag between optical and inverse-Compton scattered γ -ray photons.* The optical- γ -ray correlation shows no time lag among the flares at the two frequencies, i.e. O5 correlates with G5 and O4 with G4; but, there is no respective γ -ray flare for O6. The nearby optical, X-ray, and γ -ray flares are shown with their possible time lags with respect to R6. The allowed time range of the peak of the X-ray flare is marked by an arrow. In Fig. 5.9 (b), a similar plot is shown for the R8 flare. Both of these figures provide a one-to-one connection of the broad-band flares based on our correlation analysis.

5.7 Summary

In this chapter, I presented the cross-correlation analysis and results of the radio to γ -ray flux variability of the BL Lac S5 0716+714 from April 2007 to January 2011. A direct correlation is found between γ -ray and optical flares. The major optical- γ -ray

flares propagate down to radio wavelengths with a time lag of ~ 60 days. The radio outbursts seem to be smeared out at 10 GHz and lower frequencies. An orphan X-ray flare lags the major optical- γ -ray flare (O5-G5) by ~ 55 days. It seems that the interaction of shocks with the underlying jet structure might be responsible for optical and high energy emission, and opacity plays a key role in the time-delayed emission at radio wavelengths. To probe the mechanism of underlying radiation processes, a broad-band spectral modeling of the source needs to be performed. The details of the broad-band spectral modeling are given in the the next chapter.

Chapter 6

Evolution of Radio flares and physical properties of the jet

In this chapter, the multi-band radio frequency observations of S5 0716+714 are used to study the evolution of radio flares in the context of the standard shock-in-jet model (Marscher & Gear, 1985). The analysis is focused on the two major radio flares observed between August 2008 and December 2010. The radio flux variability is also used to constrain the size of the emission region using the causality argument, and to estimate the physical parameters like magnetic field, brightness temperature, electron density and Doppler factor etc.. This chapter is divided into two sections. The details of the evolution of radio (cm and mm) flares in the context of the standard shock-in-jet model are given in Section 6.1. Section 6.2 uses the results from Section 6.1 to estimate the physical parameters of the jet.

6.1 Evolution of radio flares in the shock-in-jet scenario

As discussed in Section 1.6, a shock induced flare follows a particular trend in the turnover flux density – turnover frequency ($S_m - \nu_m$) diagram. Therefore, the evolution of the major radio (cm and mm) flares is tested in the context of the standard shock-in-jet model. The following sections cover the details of the spectral variability study of S5 0716+714 during different phases of flaring periods as labeled in Fig. 6.1. The

¹ Work presented in this chapter has already published in Rani et al. 2013a.

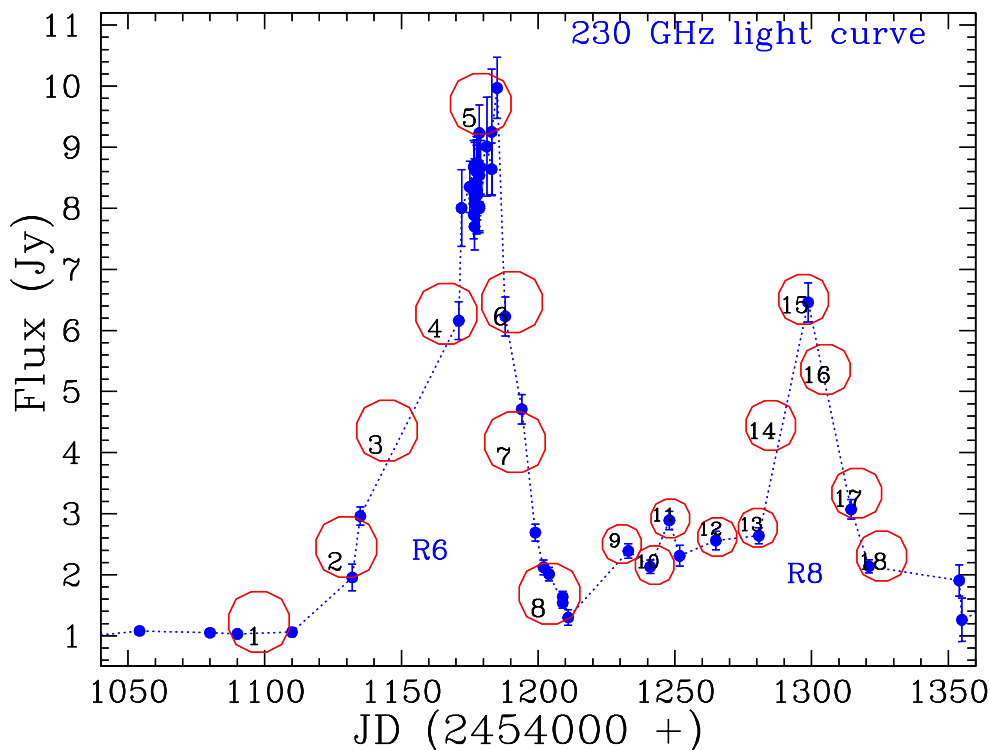


Figure 6.1: 230 GHz light curve showing different periods (labeled with numbers) over which the radio spectra are constructed.

labels in the figure represent the different periods over which the radio spectra are constructed.

6.1.1 Modeling the radio spectra

The multi-frequency radio data allow a detailed study of the spectral evolution of the two major radio flares, R6 and R8. The quasi-simultaneous radio spectra are constructed using the 2.7 to 230 GHz data as shown in Fig. 4.1. To perform a spectral analysis of the light curves, quasi-simultaneous data points are needed. Since the observed light curves are irregularly sampled, an interpolation is required to obtain quasi-simultaneous data. This is achieved by performing a linear interpolation between the flux density values from observations. A time sampling $\Delta t = 5$ days is selected for the interpolation. I interpolate the data between the two adjacent observations to predict the flux if the data gap is not longer than 5 days; for longer gaps the data points were dropped.

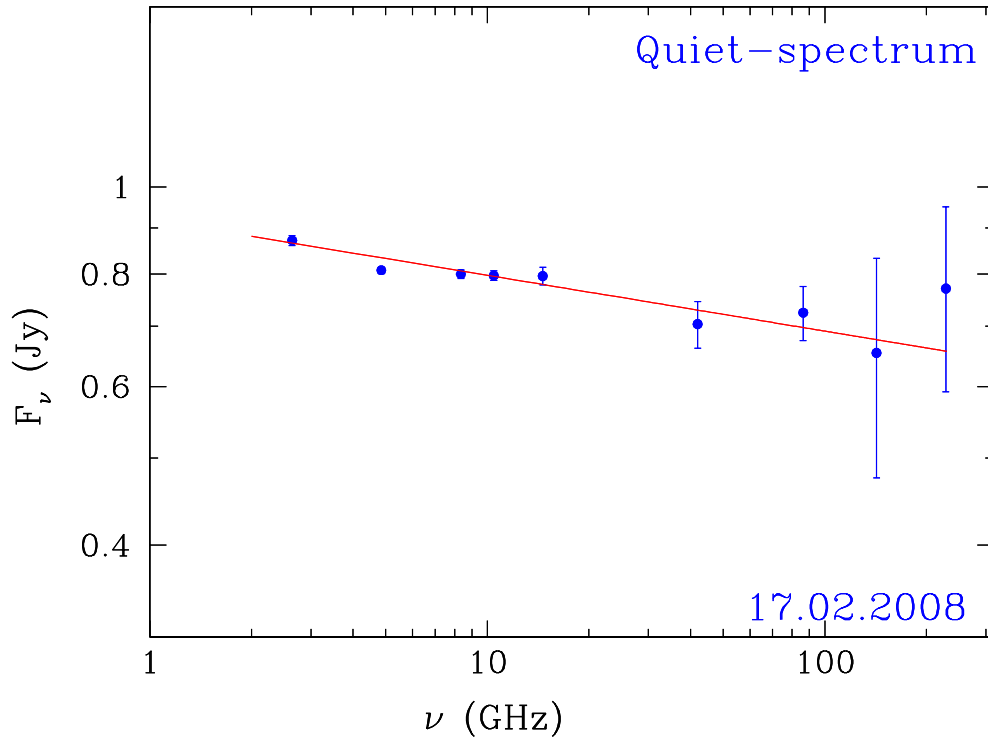


Figure 6.2: Quiescent radio spectrum.

The observed radio spectrum is thought to result from the superposition of emission from the steady state (unperturbed region) and the perturbed (shocked) regions of the jet. The quiescent spectrum is constructed using the lowest flux level during the course of our observations. Emission from a steady jet is better characterized by a steep power law spectrum. For this I have chosen the steepest spectrum during the time interval of interest, which is from February 17, 2008. The quiescent spectrum is shown in Fig. 6.2. The flux densities were fitted by a power law $F(\nu) = C_q(\nu/\text{GHz})^{\alpha_q}$ with $C_q = (0.92 \pm 0.02)$ Jy and the spectral index, $\alpha_q = -(0.06 \pm 0.01)$.

After subtraction the residual radio spectra are fitted using a synchrotron self-absorbed spectrum. A synchrotron self-absorbed (SSA) model can be described as (see: Fromm et al., 2011; Türler et al., 2000, for details) :

$$S_\nu = S_m \left(\frac{\nu}{\nu_m} \right)^{\alpha_t} \frac{1 - \exp(-\tau_m (\nu/\nu_m)^{\alpha_0 - \alpha_t})}{1 - \exp(-\tau_m)} \quad (6.1)$$

where $\tau_m \approx 3/2 \left(\sqrt{1 - \frac{8\alpha_0}{3\alpha_t}} - 1 \right)$ is the optical depth at the turnover frequency, S_m is

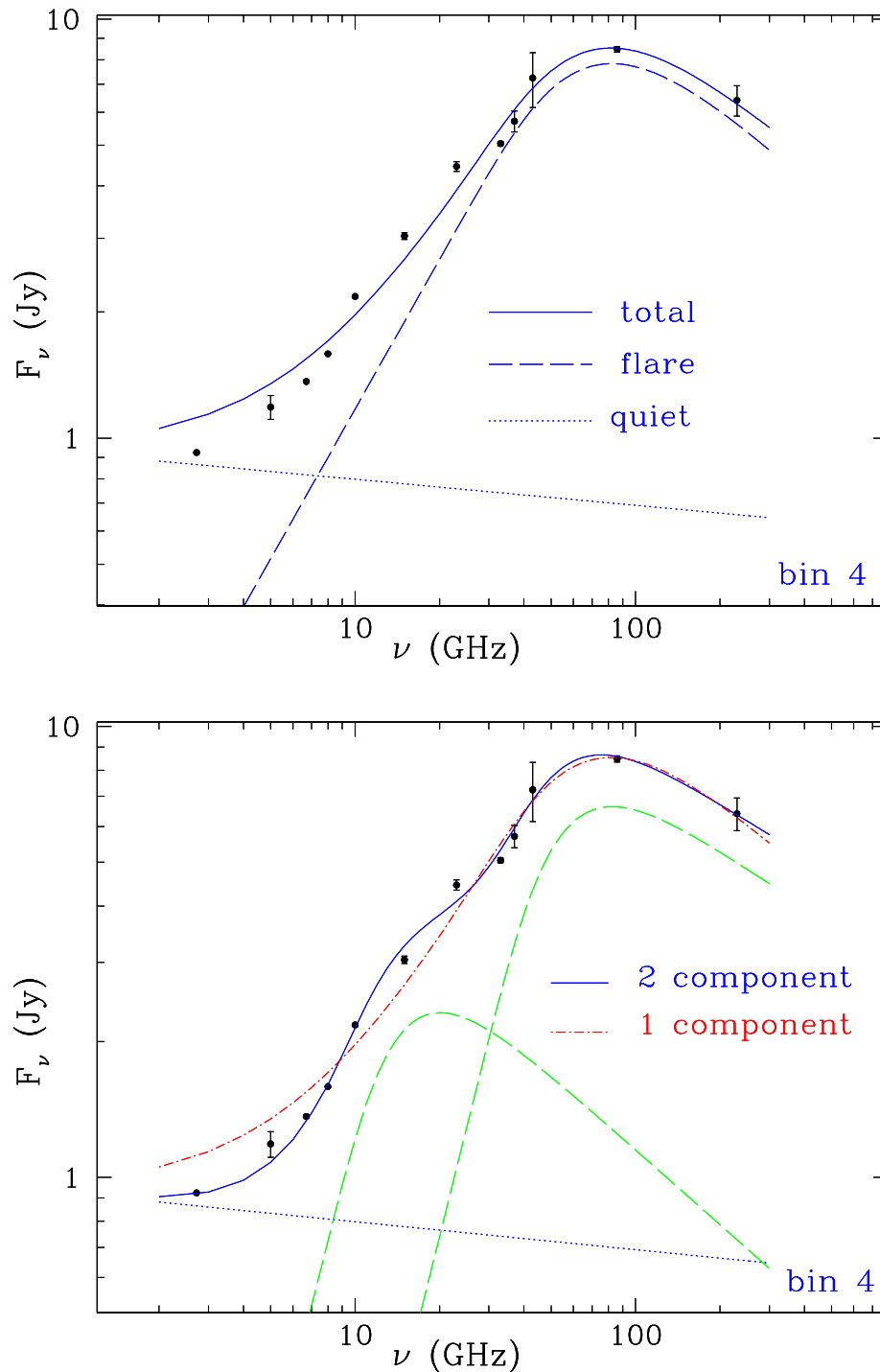


Figure 6.3: Top : Results of a single component spectral fitting at time bin “4”, the dotted line corresponds to the quiescent spectrum, the dashed one to the flaring spectrum and the solid line to the total spectrum. Bottom : The same spectrum fitted by a two-component synchrotron self-absorbed model, with the green dashed line showing the individual components and the blue solid line showing the sum of the two.

6.1 Evolution of radio flares in the shock-in-jet scenario

Table 6.1: Best-fit spectral parameters for the evolution of radio flares using a one-component SSA model

bin	Time JD [2454000+]	S_m [Jy]	ν_m [GHz]	α_t	α_0
1	1096-1101	0.58±0.09	95.05±21.78	0.70±0.26	-1.15±0.61
2	1130-1135	2.45±0.11	87.26±7.92	1.26±0.18	-0.37±0.13
3	1150-1155	4.64±0.14	84.92±5.27	1.15±0.11	-0.40±0.09
4	1173-1178	7.83±0.34	80.52±4.59	1.12±0.11	-0.62±0.12
5	1189-1194	7.57±0.84	58.96±8.05	1.37±0.41	-0.61±0.30
6	1197-1201	6.42±0.45	55.78±2.90	1.06±0.12	-1.48±0.26
7	1204-1209	5.13±0.24	60.49±2.22	0.97±0.08	-1.56±0.18
8	1216-1221	2.52±0.20	57.39±6.03	0.70±0.10	-1.24±0.33
9	1226-1230	3.23±0.17	97.03±12.60	0.39±0.08	-1.14±0.71
10	1238-1242	3.39±0.20	106.80±17.90	0.32±0.05	-1.30±0.69
11	1267-1272	3.57±0.13	92.24±7.94	0.43±0.07	-0.94±0.43
12	1273-1278	3.21±0.15	87.92±14.80	0.58±0.44	-0.31±0.12
13	1283-1288	3.42±0.11	130.70±32.50	0.67±0.09	-0.35±0.17
14	1290-1295	4.32±0.13	115.30±8.14	0.69±0.05	-0.71±0.18
15	1298-1303	6.04±0.20	74.81±4.44	1.07±0.10	-0.47±0.09
16	1309-1313	4.48±0.31	62.35±9.09	1.07±0.26	-0.33±0.17
17	1318-1323	2.77±0.08	45.66±3.06	1.56±0.29	-0.29±0.06
18	1340-1345	1.55±0.06	40.00±5.22	1.07±0.27	-0.18±0.09

the turnover flux density, ν_m is the turnover frequency, and α_t and α_0 are the spectral indices for the optically thick and optically thin parts of the spectrum, respectively ($S \sim \nu^\alpha$).

For the spectral analysis, at first the contribution of the quiescent spectrum is subtracted from the data and then equation 6.1 was used for fitting. The uncertainties of the remaining flaring spectrum are calculated taking into account the errors of the interpolated data points and the uncertainties of the quiescent spectrum. Two independent approaches are adopted to model the radio spectra : (i) a one-component synchrotron self-absorption (SSA) model, (ii) a two-component SSA model.

6.1.1.1 One-component SSA model

During the fitting process all four parameters (S_m , ν_m , α_t , α_0) (see eq. 6.1) are allowed to vary. Figure 6.1 (a) shows the 230 GHz light curve with labels (“numbers”), marking the time of best spectral coverage, for which spectra can be calculated. A typical

6.1 Evolution of radio flares in the shock-in-jet scenario

Table 6.2: The best fitted spectral parameters over the evolution of radio flares using a two component SSA model

bin	Time JD [2454000+]	$\nu_m l^*$ GHz	$S_m l$ Jy	$\alpha_0 l$	$\nu_m h^*$ GHz	$S_m h$ Jy	$\alpha_0 h$
1	1096-1101	20±0	0.26±0.10	-0.47±0.59	98.52±32.74	0.43±0.13	-0.51±0.59
2	1130-1135	20±0	0.41±0.16	-0.12±0.13	90.00±15.25	1.98±0.11	-0.12±0.03
3	1150-1155	20±0	1.37±0.14	-0.32±0.08	86.95±6.14	3.70±0.13	-0.23±0.05
4	1173-1178	20±0	2.31±0.29	-0.55±0.20	82.41±4.79	6.63±0.39	-0.41±0.08
5	1189-1194	20±0	2.17±1.00	-0.40±0.47	59.90±8.55	6.33±1.05	-0.62±0.31
6	1197-1201	20±0	2.17±0.24	-0.39±0.12	57.01±1.62	5.57±0.50	-0.72±0.31
7	1204-1209	20±0	1.46±0.26	-0.21±0.11	58.66±2.18	4.55±0.55	-0.68±0.38
8	1216-1221	20±0	1.13±0.13	-0.13±0.05	57.88±3.02	2.09±0.60	-0.91±1.50
9	1226-1230	18±1	0.95±0.29	-1.06±0.69	128.20±7.33	3.34±0.10	-0.46±0.11
10	1238-1242	18±1	1.20±0.41	-0.76±0.38	126.10±8.48	3.40±0.13	-0.55±0.17
11	1267-1272	22±1	0.76±0.13	-1.52±0.67	124.40±4.18	3.60±0.07	-0.38±0.03
12	1273-1278	23±1	0.94±0.19	-1.83±0.98	129.90±8.47	3.29±0.12	-0.33±0.04
13	1283-1288	20±0	1.55±0.18	-0.16±0.06	116.30±12.20	2.24±0.17	-0.20±0.02
14	1290-1295	20±0	1.65±0.17	-0.11±0.03	113.70±15.64	2.82±0.18	-0.28±0.13
15	1298-1303	20±0	2.42±0.16	-0.19±0.03	75.51±3.52	4.10±0.17	-0.41±0.06
16	1309-1313	20±0	2.61±0.41	-0.47±0.75	80.93±9.89	3.27±1.88	-0.40±0.28
17	1318-1323	20±0	1.82±1.07	-0.33±0.40	50.10±5.70	1.27±1.51	-0.21±0.27
18	1340-1345	20±0	0.87±0.05	-0.05±0.01	55.70±7.80	0.77±0.05	-0.26±0.08

* : Index l is for low-frequency component and h is for high-frequency component.

spectrum (for time bin “4”) is shown in Fig. 6.3. The spectral parameters of the one-component SSA fit for all spectral epochs (bin 1 to 18) are listed in Table 6.1. In a homogeneous emission region, the spectrum is described by characteristic shapes $S_\nu \propto \nu^{5/2}$ and $S_\nu \propto \nu^{-(s-1)/2}$ for the optically thick and thin domain (s is the power law index of the relativistic electrons), respectively. The theoretically expected value of the optically thick spectral index, α_t is 2.5 (Kembhavi & Narlikar, 1999). While fitting the spectra with a single-component SSA model, it is noticed that α_t varies between 0.32 to 1.56. This deviation of α_t from 2.5 indicates that the emission region is not homogeneous, and it may be composed of more than one homogeneous components. It is also found that the radio spectra over the period between the two radio flares R6 and R8 (from bin9 to bin12) can not be described by the one-component spectral model at all. Apparently, these spectra seem to be composed of two different components, one peaking near 30 GHz (low-frequency component) and the other one at ~ 100 GHz (high-frequency component). Consequently, I consider a two-component model.

6.1.1.2 Two-component SSA model

Since the flux densities at cm wavelengths are much higher than the extrapolation of the mm-flux with a spectral index $\alpha_t = 2.5$ for the optically thick branch of a homogeneous synchrotron source, it may not be unreasonable to suggest that besides the mm-submm emitting component, there is an additional spectral component which is responsible for the cm emission. Therefore the radio spectra are fitted with a two-component model. This allows to fix α_t , and set it to 2.5 for both of the components. I also fix the peak frequency of the lower frequency component to 20 GHz, as the low-frequency ν_m varies between 18 – 25 GHz and the fitting improves only marginally if it is allowed to vary. Hence, the spectral evolution of the radio spectra is studied by fixing $\alpha_t(l)^1 = \alpha_t(h) = 2.5$ and $\nu_{ml} = 20$ GHz. Such a scenario appears reasonable and is motivated by the idea of a synchrotron self-absorbed “Blandford-Königl” jet (Blandford & Königl, 1979) and a more variable core or shock component. The fitted spectrum using this restricted two-component model is shown in Fig. 6.3 (right) and the best fit parameters are given in Table 6.2. A variable low-frequency component provides a better fit over bin 9 – 12. Therefore, it is considered that both the low- and high- frequency components are varying over the time period between the two flares. The two-component SSA model describes the radio spectra much better than a single-component model. Therefore, it is concluded that the radio spectra are at least composed of two components, one peaking at cm wavelengths and the other at mm-submm wavelengths.

6.1.2 Evolution of radio flares

In the following, I adopt a model of spectral evolution as described by Marscher & Gear (1985), which considers the evolution of a traveling shock wave in a steady state jet. The typical evolution of a flare in the turnover flux density – turnover frequency ($S_m - \nu_m$) plane can be obtained by inspecting the R (radius of jet)-dependence of the turnover frequency, ν_m , and the turnover flux density, S_m (see Section 1.6 for details). During the first stage, Compton losses are dominant and ν_m decreases with increasing radius R , while S_m increases. In the second stage, where synchrotron losses are the dominating energy loss mechanism, the turnover frequency continues to decrease while the turnover flux density remains roughly constant. Both the turnover frequency and turnover flux density decrease in the final, adiabatic stage. The evolution of the radio

¹l: low-frequency component, h: high-frequency component

flares is studied using the results obtained from both the one- and two-component SSA models and in each case, the results are similar. The evolution of the R6 and R8 flares in $S_m - \nu_m$ plane are shown in Figs. 6.4 – 6.5.

In a standard shock-in-jet model, $S_m \propto \nu_m^{\epsilon_i}$ (Fromm et al., 2011; Marscher & Gear, 1985) where ϵ_i depends upon the variation of physical quantities i.e. magnetic field (B), Doppler factor (δ) and energy of relativistic electrons ($N(\gamma)$) (see Fromm et al., 2011; Marscher & Gear, 1985, for details). The estimated ϵ_i values for both the one- and two-component SSA models are given in Table 6.3. The spectral evolution of the R6 flare follows the exponential relation between S_m and ν_m with $\epsilon \sim -7$ (1-component SSA) and $\epsilon \sim -8$ (2-component SSA) over bin 1 to 4. Since S_m increases with decreasing ν_m over this period, this corresponds to the Compton stage. S_m increases with almost no change in ν_m over bin 4 to 5, as expected during the synchrotron-loss stage. $S_m - \nu_m$ variations again follow an exponential relation over bin 5 to 8 with $\epsilon \sim 10$ (1-component SSA) and $\epsilon \sim 11$ (2-component SSA). As both S_m and ν_m decreases this stage could be referred to the adiabatic phase; however, the ϵ value is much larger than what is normally expected in adiabatic decay ($\epsilon \sim 0.7$, Marscher & Gear, 1985). The typical signature of the synchrotron stage is not found in between the Compton and the adiabatic stages of the R8 flare. The exponential relation between $S_m - \nu_m$ for the R8 flare gives $\epsilon_{Compton} \sim -0.9$ (1-component SSA) and -1.2 (2-component SSA), while $\epsilon_{adiabatic} \sim 1.8$ (1-component SSA) and 2.5 (2-component SSA).

Marscher & Gear (1985) predicted a value of $\epsilon_{Compton} = -2.5$ and Fromm et al. (2011) obtain -1.21, whereas Björnsson & Aslaksen (2000) obtained $\epsilon_{Compton} = -0.43$ using a modified expression for the shock width. The estimated $\epsilon_{Compton}$ value for the R8 flare lies between these values, while for the R6 flare it is too high to be explained by the simple assumptions of a standard shock-in-jet model (see Table 6.3). For the adiabatic stage Marscher & Gear (1985) derived an exponent $\epsilon_{adiabatic} = 0.69$ (assuming $s = 3$) and Fromm et al. (2011) found $\epsilon_{adiabatic} = 0.77$. I obtained $\epsilon_{adiabatic} \sim 2$ for the R8 flare and ~ 10 for the R6 flare which is again too steep. The spectral evolution of the R8 radio flare can be well interpreted in terms of a standard shock-in-jet model based on intrinsic effects. However, the rapid rise and decay of S_m with respect to ν_m in the case of the R6 (see Fig. 6.4) flare rule out these simple assumptions of a standard shock-in-jet model considered by Marscher & Gear (1985) with a constant Doppler factor (δ).

It is worth arguing that the spectral evolution of the radio flare, R6 (in $S_m - \nu_m$ plane) needs to be investigated by considering both the intrinsic variation and the

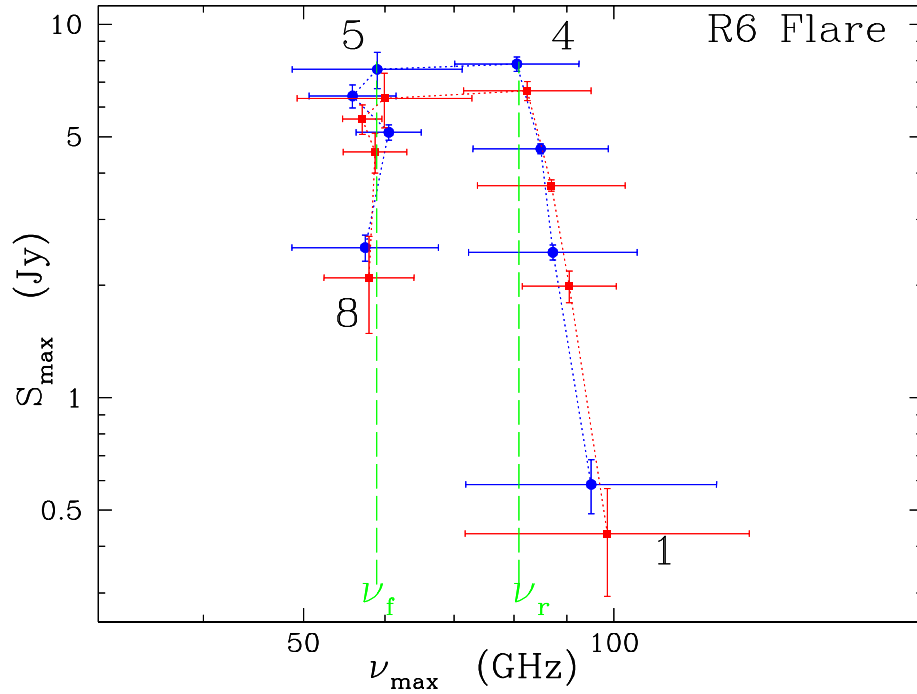


Figure 6.4: The time evolution of S_{max} versus ν_{max} for the R6 radio flare. The spectral evolution extracted using a single-component model is shown by blue symbols and the red symbols denote a two-component model.

variation in the Doppler factor (δ) of the emitting region. Qian et al. (1996) studied the intrinsic evolution of the superluminal components in 3C 345 with Doppler beaming factor variations being taken into account with a typical variation of the viewing angle by $2 - 8^\circ$. In the study of the spectral evolution of the IR-mm flare in 3C 273, Qian et al. (1999) found that the bulk acceleration of the flaring component improves the fit of the spectral evolution at lower frequencies. Therefore, it is justified to include a variation of δ along the jet axis in our model, which can be parametrized as $\delta \propto R^b$. Such an approach could easily explain the large variation in the observed turnover flux density, while the observed turnover frequency kept a nearly constant value or changed only slightly (Fromm et al., 2011). Adopting this additional parametrization, the evolution of radio flares is now studied in the framework of dependencies of physical parameters a , s , and d . Following Lobanov & Zensus (1999), ϵ is defined for the three stages as :

$$\epsilon_{Compton} = \frac{(a - 11)(s + 5) - 20b(s + 3)}{2(s + 5)(a + 1) - 8b(s + 3)} \quad (6.2)$$

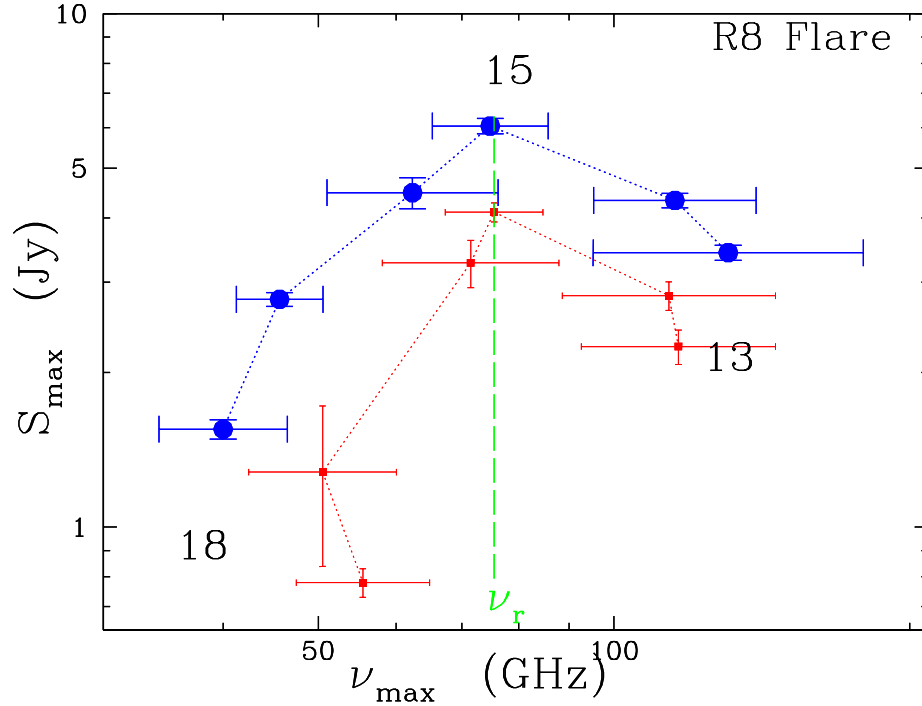


Figure 6.5: The time evolution of S_{max} versus ν_{max} for the R8 radio flare. The spectral evolution extracted using a single-component model is shown by blue symbols and the red symbols denote a two-component model.

$$\epsilon_{Synchrotron} = \frac{3b(3s + 10) - (3a + 2)(2s - 5)}{3b(s + 3) - 3a(s - 1) - 4(s + 2)} \quad (6.3)$$

$$\epsilon_{Adiabatic} = \frac{(19 - 4s) - 3a(2s + 3) + 3b(3s + 7)}{3(b - a)(s + 2) - 2(2s + 1)} \quad (6.4)$$

Here, a , s , and d parametrize the variations of $\delta \propto R^b$, $B \propto R^{-a}$, and $N(\gamma) \propto \gamma^{-s}$ along jet radius. Since it is evident that ϵ values do not differ much for different choices of a and s (Lobanov & Zensus, 1999), it is assumed for simplicity that $s \approx \text{constant}$ and for two extreme values of $a = 1$ and 2 , and the variations in b are investigated. The calculated values of b for different stages of evolution of radio flares are given in Table 6.3. Therefore, with this additional parametrization, the extreme values of ϵ become more physical. *It is important to note that the Doppler factor varies significantly along jet radius during the evolution of the two radio flares.*

Moreover, the turnover frequency between the Compton and synchrotron stages (ν_r)

6.1 Evolution of radio flares in the shock-in-jet scenario

Table 6.3: Different states of spectral evolution and their characteristics

Flare	Time	bin	ϵ	ϵ	b <i>s=2.2, a=1-2</i>	Stage
	JD [2454000+]		(1 component SSA)	(2 component SSA)		
R6	1096-1178	1-4	-7 ± 3	-8 ± 3	0.7	Compton
	1178-1194	4-5	0	0	-0.07	Synchrotron
	1194-1221	5-8	10 ± 2	11 ± 3	2.6	Adiabatic
R8	1283-1303	13-15	-0.9 ± 0.1	-1.2 ± 0.2	0.4	Compton
	1298-1345	15-18	1.8 ± 0.2	2.5 ± 0.5	-2	Adiabatic

$$\delta \propto R^b, B \propto R^{-a} \text{ and } N(\gamma) \propto \gamma^{-s}$$

and the synchrotron and adiabatic stages (ν_f) in the $S_m - \nu_m$ plane characterize the observed behavior of the radio outbursts (Valtaoja et al., 1992). In a shock induced flare, the shock strength reaches its maximal development at ν_r and the decay stage starts at ν_f . In Fig. 6.4 – 6.5, the dashed lines represent the frequencies ν_r and ν_f . The shock reaches its maximal development at 80 GHz for the R6 flare and at 74 GHz for the R8 flare. The observed behavior of the outburst depends on ν_r . In a shock induced flare, the observed frequency (ν_{obs}) is less than ν_r in the case of low-peaking flares, while $\nu_{obs} > \nu_r$ for high-peaking flares (Valtaoja et al., 1992).

In conclusion, the radio outbursts R6 and R8 are low-peaking radio flares and are in quantitative agreement with the formation of a shock and its evolution with an important addition that the Doppler factor is not constant along the jet. Such a change in the Doppler factor can be due to either a viewing angle variation or a change of the bulk Lorentz factor or may be a combination of both. A correlation of the high-energy flux with the inner jet position angle variations argues in favor of a geometric origin (see chapter 8 for details).

6.1.3 Breaks in the synchrotron spectrum

The source was observed at IR frequencies with the Spitzer Space Telescope on December 06, 2007. The IRAC+MIPS photometric measurements at 5 – 40 μm are obtained from the Spitzer archive¹. Since the source has been observed at radio wavelengths over this period, I combine the cm – mm and IR observations to construct a more complete broad-band synchrotron spectrum. The combined radio – IR spectrum is shown in Fig. 6.6. The red curve represents the best fitted synchrotron self-absorbed spectrum with a break at a frequency of $\nu_b = (1.3 \pm 0.1) \times 10^4$ GHz. The best-fit parameters are: $S_m = (1.03 \pm 0.02)$ Jy, $\nu_m = (45.74 \pm 3.12)$ GHz, $\alpha_t = (0.33 \pm 0.01)$ and the spectral

¹<http://sha.ipac.caltech.edu/applications/Spitzer/SHA/>

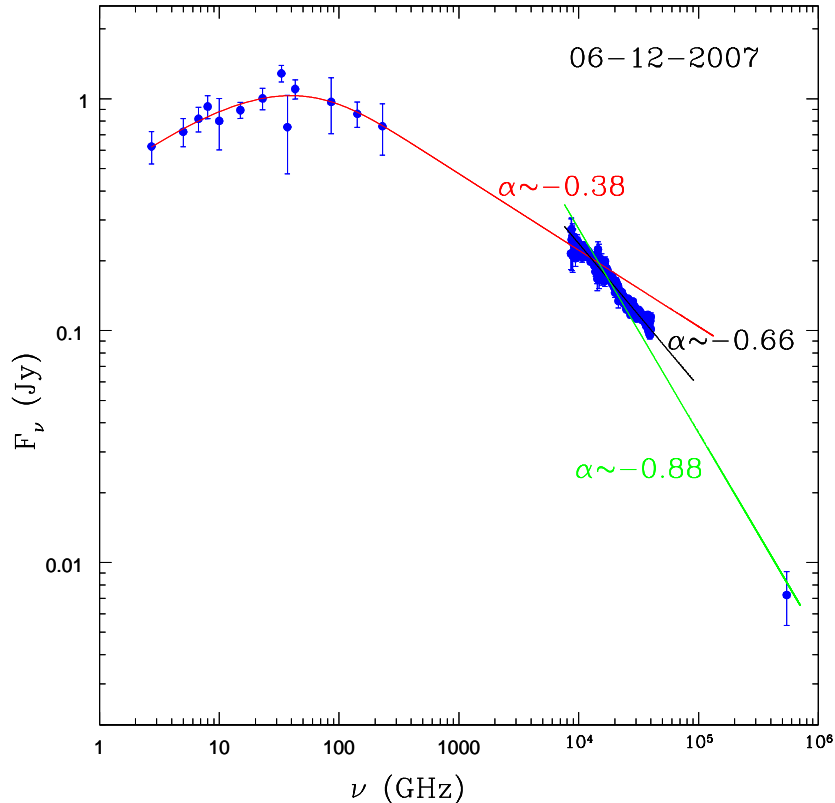


Figure 6.6: Radio-IR spectrum using Spitzer observations. The red curve is the best fitted synchrotron self-absorbed spectrum with a break at $(1.3 \pm 0.1) \times 10^4$ GHz with a spectral break $\Delta\alpha_{IR} = 0.28 \pm 0.1$. The green line represents the spectral fitting including optical data point, and this leads to spectral break $\Delta\alpha_{IR/opt} = 0.51 \pm 0.09$.

indices of the optically thin part are $\alpha_{radio/IR} = -(0.38 \pm 0.09)$ and $\alpha_{IR} = -(0.66 \pm 0.07)$ above and below the break, respectively. Hence, modeling of the radio – IR spectrum provides strong evidence for a break in the synchrotron spectrum at $\nu_b \sim 1.3 \times 10^4$ GHz with a spectral break $\Delta\alpha_{radio/IR} = 0.28 \pm 0.1$. A combined spectrum including the optical V passband flux leads to a steeper spectral index with $\alpha_{IR/opt} = -0.88 \pm 0.03$ and a break $\Delta\alpha_{IR/opt} = 0.51 \pm 0.09$.

The spectral break could be attributed to synchrotron losses of the high-energy electrons. It is widely accepted that synchrotron losses result in a steepening of the particle spectrum by one power and a steepening of the emitted synchrotron spectrum by a half-power (Kardashev, 1962; Reynolds, 2009). Also, synchrotron-loss spectral breaks differing from 0.5 could be produced naturally in an inhomogeneous source

(Reynolds, 2009). As ν_b is mainly determined by synchrotron loss, it depends on the magnetic field strength. One can estimate the minimum-energy magnetic field strength using the following relation given by Heavens & Meisenheimer (1987):

$$B_{break} = 2.5 \times 10^{-3} \beta_1^{2/3} L^{-2/3} \nu_b^{-1/3} \text{ G} \quad (6.5)$$

where $\beta_{1,c}$ is the speed of the upstream gas related to the shock, L is the length of the emission region in kpc (at $\nu < \nu_b$), and ν_b is the break frequency in GHz. For relativistic shocks β_1 is close to 1. The length of the emission region L is constrained using the variability timescales at 230 GHz as this is the closest radio frequency to ν_b . Using $L \leq 0.02 \times 10^{-3}$ kpc (see Section 6.2.3), the estimated B_{break} value is ≥ 0.23 G. The minimum energy condition implies equipartition of energy, which means $B_{break} \sim B_{eq}$ (equipartition magnetic field).

6.2 Physical parameters of the jet

6.2.1 Brightness temperature T_B^{app}

The observed rapid variability implies a very compact emission region and hence a high brightness temperature if the variations are intrinsic to the source. Assuming a spherical brightness distribution for the variable source and that the triggered flux variations propagate isotropically through the source, then the light travel time argument implies a radius $d \leq c\Delta t$ for the emission region where Δt is the time interval of expansion. So, the flux variability observed in radio bands allows us to estimate the brightness temperature of the source using the relation (see Fuhrmann et al., 2008; Ostorero et al., 2006, for details).

$$T_B^{app} = 3.47 \times 10^5 \cdot \Delta S_\lambda \left(\frac{\lambda d_L}{t_{var,\lambda} (1+z)^2} \right)^2 \text{ K} \quad (6.6)$$

where ΔS_λ is the change in flux density (Jy) over time $t_{var,\lambda}$ (years), d_L is the luminosity distance in Mpc, λ is wavelength in cm and z is the redshift of the source. Here and in the following calculations I will use $z = 0.31$ (Nilsson et al., 2008), which yields a luminosity distance, $d_L = 1600$ Mpc for a Λ CDM cosmology with $\Omega_m = 0.27$, $\Omega_\lambda = 0.73$, and $H_0 = 71 \text{ km s}^{-1} \text{ Mpc}^{-1}$ (Spergel et al., 2003).

Table 6.4: Variability Brightness temperatures

R6 flare					
Frequency (GHz)	t_{var}^a (days)	T_B^{app} (10^{12} K)	δ_{var}	θ (mas)	R (10^{17} cm)
15	61	154	>10	<0.091	<12.12
37	65	62	>7	<0.068	<9.04
86	60	13	>3	<0.027	<3.57
230	50	3	>2	<0.015	<1.98
R8 Flare					
15	37	307	>14	<0.077	<10.29
37	18	109	>9	<0.025	<3.22
86	25	55	>7	<0.021	<3.47
230	10	5	>3	<0.004	<0.59

a: t_{var} corresponds to the rising time of the flares.

Two major outbursts (R6 and R8) are observed in the source at 15 GHz and at higher radio frequencies. The rising time of the flares is used to calculate the brightness temperature (see Table 5.3) separately for the two flares at 15, 37, 86, and 230 GHz, as these are the best sampled light curves. The radio flares follow a slow rising and fast decaying trend. The calculated t_{var} for the two radio flares are listed in column 2 of Table 6.4 and the apparent brightness temperatures (T_B^{app}) are in column 3.

6.2.2 Doppler factor from variability timescales (δ_{var})

The calculated apparent brightness temperature T_B^{app} is one to two orders of magnitude higher than the IC-limit $T_{B,IC}^{limit}$ of $T_B \sim 10^{12}$ K (Kellermann & Pauliny-Toth, 1969) at all frequencies up to 230 GHz. It is noticed that T_B^{app} exceeds $T_{B,IC}^{limit}$ even at short-mm bands. The excessive brightness temperature can be interpreted by relativistic boosting of the radiation, which gives to a lower limit of the Doppler factor of the emitting region

$$\delta_{var} = (1+z) \left[\frac{T_B^{app}}{10^{12}} \right]^{\frac{1}{3+\alpha}} \quad (6.7)$$

Here α is the spectral index of the optically thin part of the radio spectrum. I obtained $\alpha_{thin} = -0.23$ to -0.91 for the R6 radio flare and $\alpha_{thin} = -0.20$ to -0.41 for the R8 flare (see Section 4.1 for details). The calculated δ_{var} values are listed in column 4 of Table 6.4. For the two flare δ_{var} is found to be ≥ 10 for R6 flare and ≥ 14 for R8 flare.

In addition, the intrinsic brightness temperature limit based on the equipartition between particle energy and field energy can also be used to calculate the Doppler factor. The intrinsic brightness temperature limit based on the equipartition between particle energy and field energy (Scott & Readhead, 1977) is defined as $T_{B,eq} \sim 5 \times 10^{10}$ K which is derived on the basis of an argument that this limit better reflects the stationary state of a synchrotron source which for many sources yields $T_B \lesssim 10^{11}$ K (Readhead, 1994, e.g.). In this case, the calculated Doppler factor values using the equipartition limit, $\delta_{var,eq} = (1+z)^{3+\alpha} \sqrt{T_B^{app}/5 \times 10^{10}}$, become higher by a factor of 4.47 i.e. $\delta_{var,eq} = 4.47 \times \delta_{var}$.

6.2.3 Size of the emission region (θ)

One can obtain the size of the emission region using the calculated Doppler factors (δ_{var}) and variability time scales (t_{var}) :

$$\theta = 0.173 \frac{t_{var}}{d_L} \delta_{var} (1+z) \text{ mas} \quad (6.8)$$

The angular size θ calculated using δ_{var} are listed column 5 of Table 6.4. The estimated value of the angular dimension θ lies between 0.004 – 0.09 mas. Again, θ will be a factor of 4.47 higher if $\delta_{var,eq}$ is used for calculation. In linear dimensions, the size of the emission region can be approximated using $R \leq c t_{var} \delta_{\gamma}/(1+z)$ (Rani et al., 2013a). The calculated R values for the flares are given in the sixth column of Table 6.4. A lower limit of the estimated Doppler factor gives $R \leq (0.6 - 12.1) \times 10^{17}$ cm.

6.2.4 Inverse-Compton Doppler factor (δ_{IC})

One can constrain the inverse-Compton Doppler factor (δ_{IC}) by comparing the expected and observed fluxes at high energies (see Ghisellini et al., 1993, for details). The IC Doppler factor is defined as

$$\delta_{IC} = [f(\alpha) S_m (1+z)]^{(4-2\alpha)/(10-6\alpha)} \left(\frac{\ln(\nu_c/\nu_m) \nu_{\gamma}^{\alpha}}{S_{\gamma} \theta^{(6-4\alpha)} \nu_m^{(5-3\alpha)}} \right)^{1/(10-6\alpha)} \quad (6.9)$$

where ν_c is the synchrotron high frequency cut-off in GHz, S_m the flux density in Jy at the synchrotron turnover frequency ν_m , S_{IC} the observed γ -ray flux in Jy (assumed

to arise from the IC process) at ν_γ in KeV, α is the spectral index of the optically thin part of the spectrum, θ_ν the source's angular size in mas and $f(\alpha) \simeq 0.14 - 0.08\alpha$. The apparent variability size is calculated using eq. 6.8. For the high-energy cut-off (asymptotic break in synchrotron spectrum), $\nu_c \sim 5.5 \times 10^5$ GHz is used from [Fuhrmann et al. \(2008\)](#).

For these calculations, I have used t_{var} equals to 9 days, which is the fastest variability timescale for the R6 flare at 86 GHz. The spectral index α is obtained from the SSA modeling (see Section 6.1.1) and the estimated values are given in Table 6.5. The inverse-Compton Doppler factor (δ_{IC}) is calculated for the same four time bins that are used to model the broad-band SEDs of the source (see Section 7.2). The estimated values for δ_{IC} are given in Table 6.5. It is found that during the four different activity states of the source $\delta_{IC} \geq 20$.

6.2.5 Gamma-ray Doppler factor (δ_γ)

It is also possible to obtain a limit on the Doppler factor δ by considering that the high-energy γ -ray photons can collide with the softer radiation to produce e^\pm pairs with the assumption that the bulk of the high-energy emission (γ -rays and X-rays) is produced in the same emission region. The cross-section of this process is maximized at $\sim \sigma_T/5$ (see [Svensson, 1987](#), for details), where σ_T is the Thomson scattering cross-section. This leads to a lower limit on δ with the requirement that $\tau_{\gamma\gamma}(\nu) < 1$ ([Dondi & Ghisellini, 1995](#); [Finke et al., 2008](#)):

$$\delta_\gamma > \left[\frac{2^{a-1}(1+z)^{2-2a}\sigma_T D_L^2}{m_e c^4 t_{var}} \epsilon f_{\epsilon^{-1}}^{syn} \right]^{\frac{1}{6-2a}} \quad (6.10)$$

where a is the power law index of the synchrotron spectrum i.e. $f_\epsilon^{syn} \propto \epsilon^a$, σ_T is the scattering Thomson cross-section, m_e is the electron mass, $\epsilon_1 = E/(m_e c^2)$ is the dimensionless energy of a γ -ray photon with energy E for which the optical depth of the emitting region $\tau_{\gamma\gamma} = 1$. For the highest energy GeV (207 GeV) photon observed in the source (Section 4.4.4), I obtain $\epsilon = 207 \text{ GeV}/(5.11 \times 10^{-4} \text{ GeV}) = 4 \times 10^4$ and $\epsilon^{-1} = 2.4 \times 10^{-6}$. Using $f_{\epsilon^{-1}}^{syn} = 3.88 \times 10^{-11} \text{ ergs cm}^{-2} \text{ s}^{-1}$, the estimated value of δ_γ is ≥ 9.1 . The detection of the source at above 400 GeV ([Anderhub et al., 2009](#)) constrains $\delta_\gamma \geq 9.8$

Table 6.5: Brightness temperature

Time bin	δ_{IC}	Used parameters
Bin1	$\delta_{IC,0.5KeV} > 11$	$S_{70} = 3.71$ Jy, $\alpha = -0.74$, $S_{0.5KeV} = 2.97 \times 10^{-6}$ Jy
	$\delta_{IC,7.5KeV} > 20$	$S_{80} = 3.71$ Jy, $\alpha = -0.74$, $S_{70.5KeV} = 8.27 \times 10^{-8}$ Jy
	$\delta_{IC,100MeV} > 14$	$S_{80} = 3.71$ Jy, $\alpha = -0.74$, $S_{100MeV} = 1.17 \times 10^{-11}$ Jy
Bin2	$\delta_{IC,0.5KeV} > 11$	$S_{40} = 1.68$ Jy, $\alpha = -0.52$, $S_{0.5KeV} = 2.97 \times 10^{-6}$ Jy
	$\delta_{IC,7.5KeV} > 14$	$S_{40} = 1.68$ Jy, $\alpha = -0.52$, $S_{7.5KeV} = 4.57 \times 10^{-8}$ Jy
	$\delta_{IC,100MeV} > 14$	$S_{40} = 1.68$ Jy, $\alpha = -0.52$, $S_{100MeV} = 1.50 \times 10^{-10}$ Jy
Bin3	$\delta_{IC,0.5KeV} > 14$	$S_{82} = 9.89$ Jy, $\alpha = -0.76$, $S_{0.5KeV} = 3.85 \times 10^{-6}$ Jy
	$\delta_{IC,7.5KeV} > 15$	$S_{82} = 9.89$ Jy, $\alpha = -0.76$, $S_{7.5KeV} = 2.97 \times 10^{-7}$ Jy
	$\delta_{IC,100MeV} > 17$	$S_{82} = 9.89$ Jy, $\alpha = -0.76$, $S_{100MeV} = 2.94 \times 10^{-11}$ Jy
Bin4	$\delta_{IC,0.5KeV} > 12$	$S_{78} = 3.85$ Jy, $\alpha = -0.78$, $S_{0.5KeV} = 2.97 \times 10^{-6}$ Jy
	$\delta_{IC,7.5KeV} > 12$	$S_{78} = 3.85$ Jy, $\alpha = -0.78$, $S_{7.5KeV} = 2.97 \times 10^{-6}$ Jy
	$\delta_{IC,100MeV} > 12$	$S_{78} = 3.85$ Jy, $\alpha = -0.78$, $S_{100MeV} = 2.08 \times 10^{-11}$ Jy

6.2.6 Magnetic field from synchrotron self-absorption

It is also possible to constrain the magnetic field using the standard synchrotron self-absorption expressions. Following Marscher (1987), an expression for the magnetic field in a homogeneous synchrotron self-absorbed region is given by:

$$B_{SA} [G] = 10^{-5} b(\alpha) \theta^4 \nu_m^5 S_m^{-2} \left(\frac{\delta}{1+z} \right), \quad (6.11)$$

where $b(\alpha)$ depends on the optically thin spectral index α_{thin} (see Table 1 in Marscher, 1987), S_m is the flux density, θ is the source's angular size at the synchrotron turnover frequency ν_m , and δ is the Doppler factor. The size of the emitting region responsible for the observed variations can be constrained using mm-VLBI measurements of the

core region of S5 0716+714 by Bach et al. (2006): $\theta < 0.04$ mas. Using $b(\alpha) = 3.13$, $S_m = 3.89$ Jy, $\nu_m = 80$ GHz, a lower limit of the magnetic field B_{SA} is found in the range of $(0.0078\text{--}0.0198)\delta$ mG. Using $\delta \geq 7$ at $\nu_m \sim 80$ GHz (peak frequency, see Table 6.4), I obtained $B_{SA} \geq 0.02$ to 0.14 G. The size of the emission region constrained using the causality arguments, $\theta \sim 0.0027$ mas at $\nu_m \sim 80$ GHz (see Table 6.4), gives $B_{SA} \geq 0.03$ G. Together, these calculations constrain $B_{SA} \geq 0.02 - 0.14$ G

6.2.7 Equipartition magnetic field and Doppler factor

The equipartition magnetic field B_{eq} , which minimizes the total energy $E_{tot} = (1 + k)E_e + E_B$ (with relativistic particle energy $E_e \sim B^{-1.5}$ and energy of the magnetic field $E_B \sim B^2$), is given by the following expression (e.g. Bach et al., 2005; Fuhrmann et al., 2008):

$$B_{eq} = (4.5 \cdot (1 + k) f(\alpha, \nu_a, \nu_b) L R^3)^{2/7} \quad (6.12)$$

here k is the energy ratio between electrons and heavy particles, L is the synchrotron luminosity of the source given by $L = 4\pi d_L^2 (1 + z) \int_{\nu_b}^{\nu_a} S d\nu$, R is the size of the component in cm, S_m is the synchrotron peak flux in Jy, ν_m is the synchrotron peak frequency in GHz, and $f(\alpha, \nu_a, \nu_b)$ is a tabulated function depending on the upper and lower synchrotron frequency cutoffs ν_a, ν_b . Using $\nu_a = 10^7$ Hz, $\nu_b = 5.5 \cdot 10^{14}$ Hz, and $f(-0.5, 10^7, 10^{11}) = 1.6 \times 10^7$, B_{eq} is given by

$$B_{eq} = 5.37 \times 10^{12} (k S_m \nu_m d_L^2 R^{-3})^{2/7} \text{ G} \quad (6.13)$$

Using $B_{eq} \geq 0.23$ G (see Section 6.1.3), $S_m = 3.89$ Jy, $\nu_m = 80$ GHz, $R = 2.90 \times 10^{16} - 1.2 \times 10^{18}$ cm (estimated using $t_{var} = 25$ days at $\nu_m = 86$ GHz), the above expression yields $k \sim 5$. A small value of k implies that the jet is mainly composed of electron-positron plasma. The Doppler factor dependence of the parameters in equation 6.13 i.e. $S_m \propto \delta^{3+\alpha}$, $\mu_m \propto \delta$, and $\mu_m \propto \delta^{-1}$, gives $B_{eq} \sim \delta^{(2 + 2\alpha/7)}$. As a result, the estimated value of k also depends the Doppler factor in the sense that for larger Doppler factor values k will be smaller.

Equations 6.11 and 6.13 give different dependencies of the magnetic field on δ , i.e. $B_{SA} \sim \delta$ and $B_{eq} \sim \delta^{(2 + 2\alpha/7)}$. This yields $B_{eq}/B_{SA} = \delta_{eq}^{(1 + 2\alpha/7)}$. Adopting the above numbers, I obtain Doppler factors $\delta_{eq,B}$ in the range of $12 - 15$ (for $\alpha = -(0.35 \text{ to } 0.7)$).

6.3 Comparison of the estimated parameters

The apparent brightness temperature T_B obtained from the day-to-day variations exceeds the theoretical limits by several orders of magnitude. Although T_B decreases towards the mm-bands, it is still higher than the IC-limit (10^{12} K). T_B exceeds 10^{14} K at 15 GHz and 10^{12} K at 230 GHz. Lower limits to the Doppler factor of the source are obtained using different methods as discussed in the earlier sections. These methods reveal a range of consistent lower limits to the Doppler factor with $\delta_{var} \geq 14$, $\delta_{IC} \geq 20$, $\delta_\gamma \geq 10$, and $\delta_{eq,B} \geq 15$. Comparing the Doppler factor estimates obtained with different methods seems to suggest that $\delta \geq 20$. An independent approach to estimate δ is spectral modeling of the broad-band SEDs, and this gives $\delta = 25$ (see Section 7.2), which is in agreement with the former values. These limits are in good agreement with the estimates based on the recent kinematical VLBI studies of the source (Bach et al., 2006) and the IC Doppler factor limits obtained by Fuhrmann et al. (2008). As $\delta_{eq,B}$ agrees fairly well with the δ values derived from the other methods, it can be concluded that the emission region is in a state of equilibrium.

The estimated magnetic field value from the broad-band spectral modeling lies between 0.05 and 1 G. A break in the optically thin power-law slope at a wavelength of $\sim 23 \mu\text{m}$ constrains the equipartition magnetic field to $B_{eq} \geq 0.23$ G. From the synchrotron self-absorption calculation B_{SA} is found to be ≥ 0.02 G. The size of the emission region (θ) derived on the basis of causality arguments lies between $\leq (0.004 - 0.091)$ mas, which agrees fairly well with the size of the emission region constrained using mm-VLBI measurements ($\theta_{VLBI} \leq 0.04$ mas, see chapter 8 for details).

Chapter 7

Modeling the high-energy emission

The spectral modeling of the continuum emission allows us to probe the spatially unresolved emission from the highly relativistic core of blazars. Constraining the spectral energy distribution (SED) of blazars requires simultaneous observations with a multitude of observatories to cover the broad-band spectrum. The synthesis of observations and modeling can significantly contribute to our understanding of accretion processes and particle acceleration at the base of jets. This chapter covers details of the broad-band spectral modeling with a focus on the high-energy emission part of the spectrum. A detailed investigation of the γ -ray spectrum is presented in Section 7.1. Section 7.2 presents the broad-band SED modeling of the BL Lac object S5 0716+714.

7.1 Gamma-ray spectrum

The acceleration mechanism responsible for the origin of high-energy photons has always been a key question in AGN physics. A detailed investigation of the high-energy (MeV – GeV) spectrum can constrain the location of the emission regions and acceleration processes close to the central engine. The γ -ray observations by *Fermi*-LAT give us the opportunity to study and characterize the high-energy (100 MeV – 300 GeV) spectral properties of the BL Lac object S5 0716+714. The details of observations and data reduction can be found in Section 3.1.4. In the following sub-sections, I will discuss the γ -ray spectral properties of the source.

¹Work presented in this chapter is partially published in Rani et al. 2013a,b.

7.1.1 Spectrum over the entire period

The γ -ray spectrum is extracted using data for the entire 3.8 year period of *Fermi* observations. Figure 7.1 shows the GeV spectrum of the source with blue symbols as spectral measurements over equally spaced logarithmic energy bins in the energy range between 100 MeV to 300 GeV. The solid curves represent the best fitting power laws, simple power law (SPL in red) and broken power law (BPL in green). The best-fit model parameters calculated by the fitting procedure are summarized in Table 7.1. A broken power law model is favored to describe the γ -ray spectral shape over the simple power law model with a difference of the logarithm of likelihood, $-2\Delta L = 73.8$, which corresponds to a significance of the order of 10σ (see Table 7.1). Therefore, it is concluded that the GeV spectrum of the source is governed by a broken power law with a break energy, $E_{\text{break}} = 3.5 \pm 0.05$ GeV with power law indices, $\Gamma_1 = 2.02 \pm 0.01$ and $\Gamma_2 = 2.40 \pm 0.04$, respectively, below and above the break energy. The change in power law index ($\Delta\Gamma$) defined as $\Gamma_2 - \Gamma_1$ is 0.38 ± 0.04 .

7.1.2 Spectral variations

It is very likely that the physical condition within the emission region changes during different activity states. This motivates us to investigate the γ -ray spectrum for individual flares. Therefore, a comparison of the GeV spectra of the source is done during different activity states. Depending on the flux variability state and the distribution of high-energy photons ($E > 20$ GeV), I construct the GeV spectrum of the source over seven different periods shown in the top panel of Fig. 7.2. It is important to note that the spectra are not equally binned in time. The following periods are considered :

Bin1 [$\text{JD}'^1 = 911-1000$] : Flux is rising and a bunch of high-energy ($E > 20$ GeV) photons are detected during this period.

Bin2 [$\text{JD}' = 1000-1100$] : Flux level is high, but only few high-energy photons are observed during this period.

Bin3 [$\text{JD}' = 1150-1200$] : Flux level is very low and very few high-energy ($E > 15$ GeV) photons arrive during this period.

Bin4 [$\text{JD}' = 1200-1550$] : The source exhibits moderate level flux activity with a random distribution of arrival times of high-energy photons.

Bin5 [$\text{JD}' = 1610-1638$] : A rapid flare with fewer high-energy photons.

¹JD' = JD -2454000

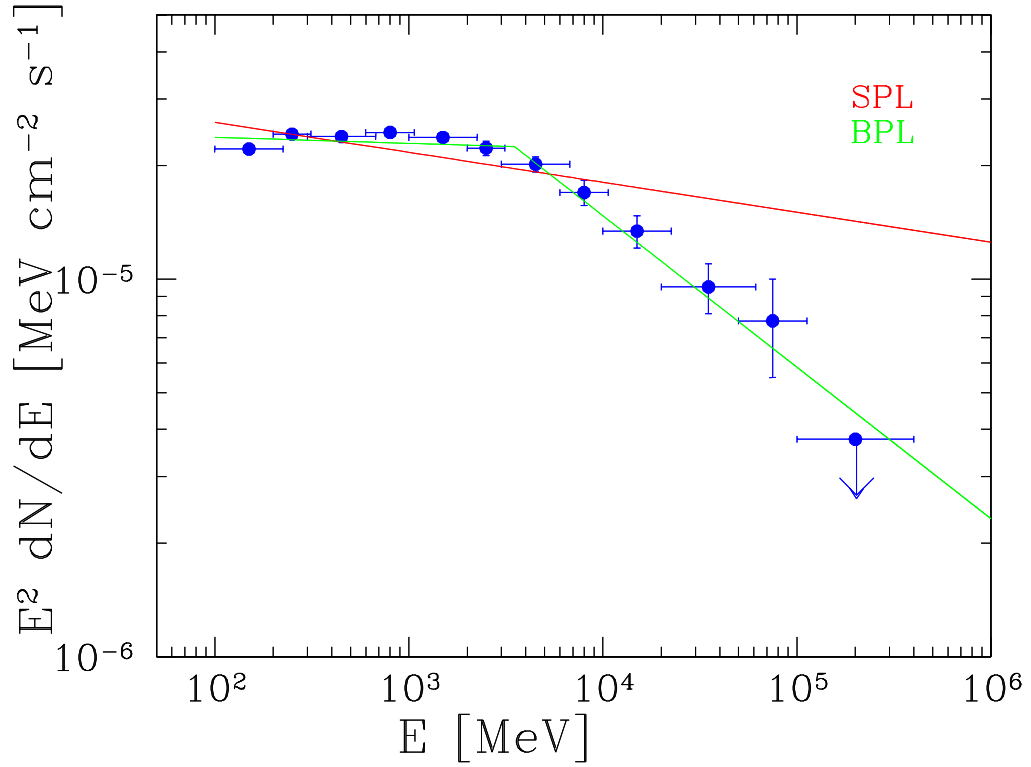


Figure 7.1: Spectral energy distribution (SED) of S5 0716+714 during the last 3.8 years of LAT monitoring. The red curve represents the best fitting simple power law (SPL), while the broken power law (BPL) is shown in green.

Bin6 [JD' = 1735-1764] : A rapid flare with very few high-energy photons.

Bin7 [JD' = 1840:1884] : The highest peaking flare with fewer high-energy photons.

Figures 7.2 (a)-(g) shows the individual GeV spectra of the source over these time bins. Here, the blue symbols represent the spectral points constructed through a PL fit over the equally spaced logarithmic energy bins and the solid curves show the best fitting power law distributions. The obtained best fit parameters of the SPL and BPL models are given in Table 7.1. The difference of the logarithm of likelihood $-2\Delta L$ is given in the second last column of Table 7.1 with a significance level by which the BPL model is preferred over the SPL model in the last column. It is found that a broken power law model is favored to describe the γ -ray spectral shape over the simple PL model for all the time bins except Bin1. For this bin, the estimated value of $2\Delta L = 0.46$, which corresponds to a significance level lower than 1σ . Thus, the broken power law model is not a better fit to the data than the simple power law. For that reason, no clear break is found in the GeV spectrum of the source for Bin1. It is noticed

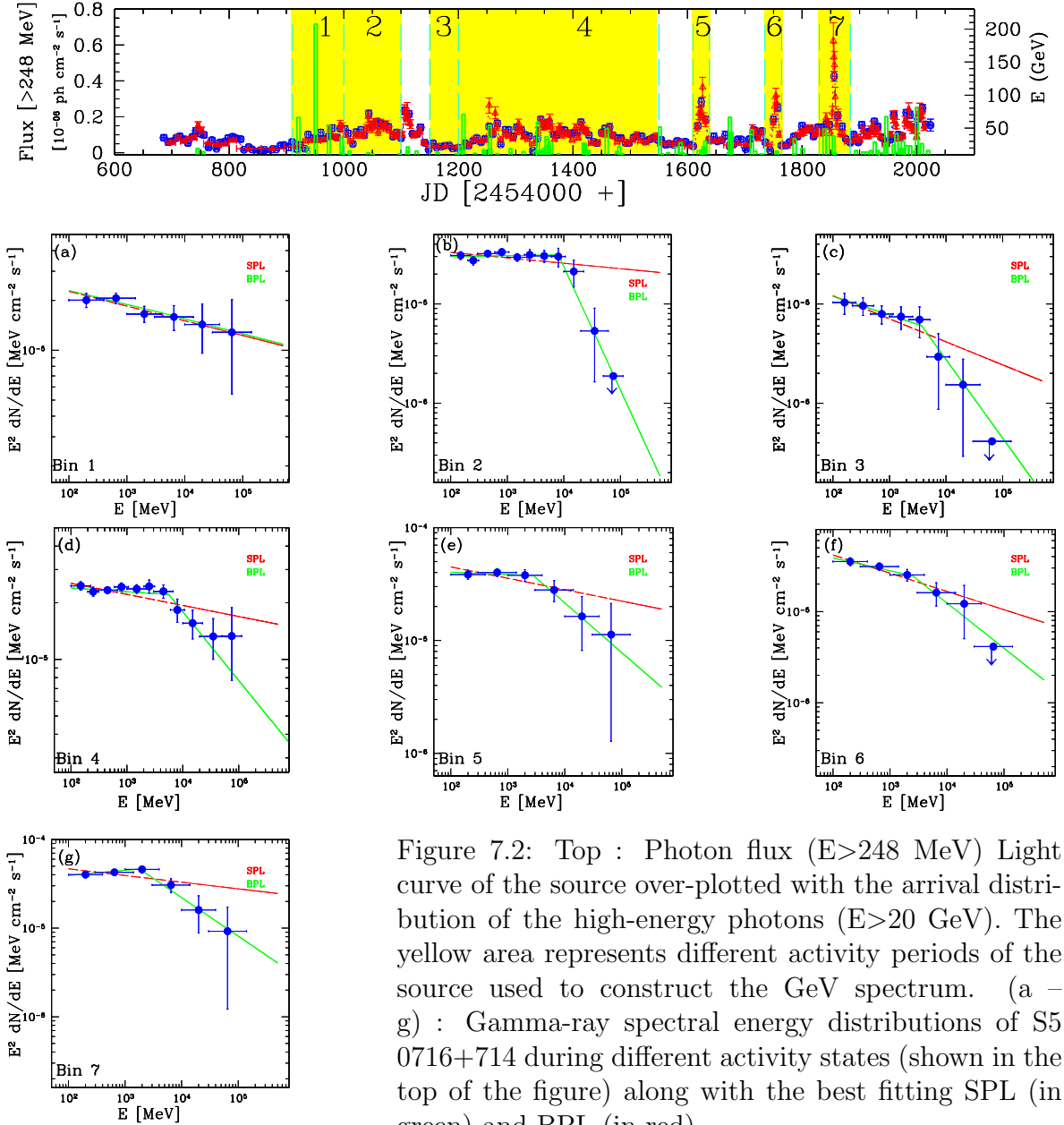


Figure 7.2: Top : Photon flux ($E > 248$ MeV) Light curve of the source over-plotted with the arrival distribution of the high-energy photons ($E > 20$ GeV). The yellow area represents different activity periods of the source used to construct the GeV spectrum. (a – g) : Gamma-ray spectral energy distributions of S5 0716+714 during different activity states (shown in the top of the figure) along with the best fitting SPL (in green) and BPL (in red).

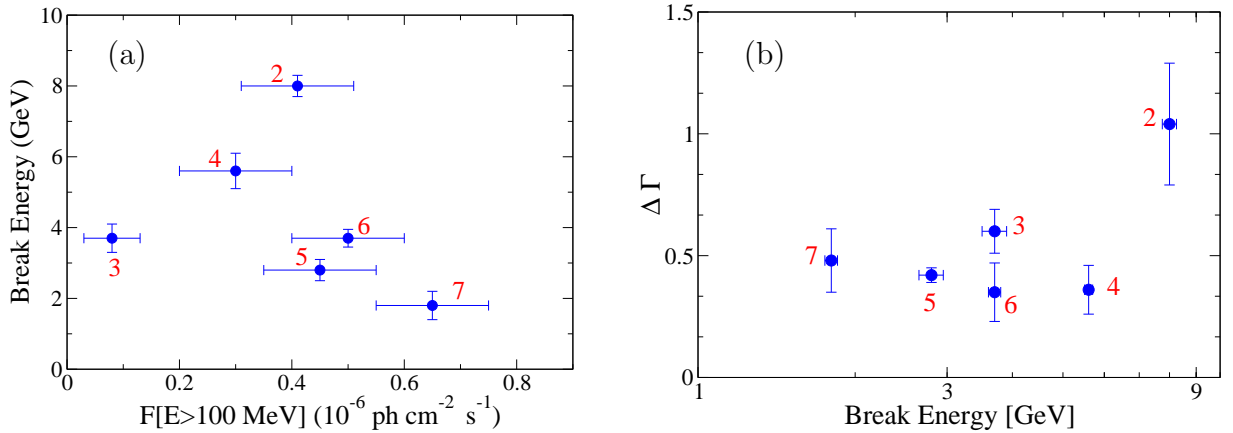


Figure 7.3: (a) : Break Energy (E_{break}) plotted as a function of flux for the different activity periods considered in Fig. 7.2 (a) to (g). (b) : Change of the spectral slope $\Delta\Gamma$ as a function of the break energy in the spectrum.

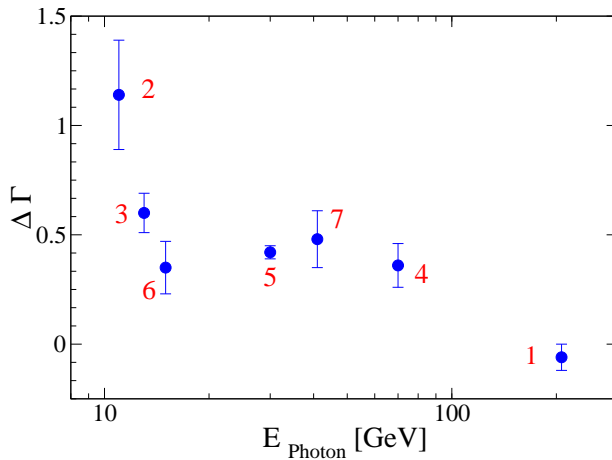


Figure 7.4: Change in $\Delta\Gamma$ plotted as a function of E_{Photon} for the different activity periods (see Fig. 7.2 a – g). E_{Photon} is the highest energy at which a photon was detected for a given bin.

that a simple power law (SPL) model better describes the spectrum (see Fig. 7.2 a). Interestingly, the γ -ray flux of the source is rising and several high-energy photons are observed during this period. In fact, the highest energy photon (207 GeV, see Section 4.4.4 for details) was also detected during this period. For the remaining time bins, the change in spectral index ($\Delta\Gamma$) below and above the break energy is listed in the column 8 of Table 7.1. I found that $\Delta\Gamma$ varies between 0.38 ± 0.02 to 1.14 ± 0.40 over the different activity states of the source.

The variation of the break energy, E_{break} with flux during the different activity states is displayed in Fig. 7.3 (a), which does not show any systematic evolution of the break energy as a function of the flux variations. The formal correlation statistics also does not

Table 7.1: Parameters of fitted power laws

Bin	JD' [JD-2454000]	F_{100} ($10^{-6}\text{ph cm}^{-2}\text{s}^{-1}$)	Model	Γ/Γ_1	Γ_2	E_{break} (GeV)	$\Delta\Gamma$	$-2\Delta L$	Significance
total	680-2022		SPL	2.09±0.01					
			BPL	2.02±0.01	2.40±0.04	3.50±0.05	0.38±0.04	73.80	$> 10\sigma$
1	911-1000	0.21±0.10	SPL	2.08±0.04					
			BPL	2.11±0.05	2.05±0.04	3.00±0.25	-0.06±0.06	0.46	$< 1\sigma$
2	1000-1100	0.41±0.11	SPL	2.05±0.02					
			BPL	1.99±0.03	3.13±0.40	8.00±0.25	1.14±0.40	16.90	$> 3\sigma$
3	1150-1200	0.08±0.04	SPL	2.23±0.09					
			BPL	2.19±0.08	2.79±0.50	3.70±0.20	0.60±0.09	13.22	$> 3\sigma$
4	1200-1550	0.27±0.10	SPL	2.05±0.01					
			BPL	2.01±0.03	2.37±0.01	5.6±0.10	0.36±0.10	11.90	$> 3\sigma$
5	1610-1638	0.45±0.12	SPL	2.10±0.04					
			BPL	2.02±0.02	2.44±0.03	2.80±0.15	0.42±0.03	11.72	3σ
6	1735-1764	0.51±0.11	SPL	2.19±0.05					
			BPL	2.14±0.07	2.49±0.14	3.70±0.10	0.35±0.12	9.80	$> 3\sigma$
7	1840-1884	0.68±0.15	SPL	2.07±0.03					
			BPL	1.94±0.05	2.42±0.13	1.80±0.05	0.48±0.13	10.52	$> 3\sigma$

reveal a significant correlation of the break energy with respect to the flux variations. Formally, the following correlation coefficient and significance are obtained : $r_P = -0.34$ and 55% confidence level (r_P being the linear Pearson correlation coefficient). Similar to other Fermi blazars, no systematic variation of E_{break} as a function of the photon flux variations is found in S5 0716+714.

The variation of change in spectral slope ($\Delta\Gamma$) as a function of the break energy (E_{Break}) is shown in Fig. 7.3 (b). Again, I do not see any systematic variation in $\Delta\Gamma$ with respect to E_{Break} . Although, $\Delta\Gamma (>1)$ is larger for the higher break energy (~ 8 GeV), but, for the rest, $\Delta\Gamma$ remains almost constant with a decrease in E_{Break} .

As shown in Fig. 7.2, no spectral break is observed during the arrival period of the highest energy photon (Bin 1). Likewise, $\Delta\Gamma$ is maximum for Bin 2 (no high-energy photons detected during this period). This indicates a possible connection between the energy of highest detected GeV photon, E_{Photon} and the spectral break parameters. Figure 7.4 shows the variation of $\Delta\Gamma$ as a function of E_{Photon} . A clear decrease in $\Delta\Gamma$ with an increase in E_{Photon} can be seen here. The correlation statistics reveal a significant correlation of $\Delta\Gamma$ with respect to E_{Photon} . Formally, I obtain the following correlation coefficient and confidence level, for $\Delta\Gamma$ versus E_{Photon} : $r_P = -0.74$ and 95% confidence level. In conclusion, the detection of the high-energy photons with energy E_{Photon} is found to be correlated with the spectral break parameter, $\Delta\Gamma$.

7.1.3 Origin of the gamma-ray spectral break

The γ -ray spectral breaks seen in many bright Fermi blazars lie within a few GeVs (Finke & Dermer, 2010; Poutanen & Stern, 2010; Rani et al., 2013b,c; Tanaka et al., 2011). The origin of these spectral breaks has generated considerable theoretical interest, and is still controversial. Among the most likely scenarios, the absorption of γ -rays via photon-photon pair production on He II Lyman recombination continuum and lines within the broad-line region (e.g. Poutanen & Stern, 2010; Tanaka et al., 2011, and references therein) is regarded as a possible explanation for the observed breaks. Spectral breaks in the bright Fermi FSRQs like 3C 454.3, 3C 279, PKS 1510-089, 4C +21.35 etc. were interpreted using this scenario. Gamma-gamma absorption by full BLR is also proposed as a reasonable possibility (Senturk et al., 2011). The γ -ray emitting region must be located deep within the BLR for this model to work.

Alternatively, the γ -ray spectral breaks could also be explained by a combination

of two Compton-scattered components, for example, by Compton scattering of the disk and BLR radiation as proposed by [Finke & Dermer \(2010\)](#). They explore this possibility to model the spectral breaks in FSRQ 3C 454.3. The combined external Compton and synchrotron self-Compton components may also explain these spectral breaks. A further explanation invokes an intrinsic origin of the spectral breaks. The change in spectral index below and above the break of order 0.5 is expected from the typical “cooling break” associated with radiative losses ([Abdo et al., 2009](#)). The observed softening may instead be due to an intrinsic decline or break in the particle distribution as well. In the following, I will investigate the observed γ -ray spectral breaks in S5 0716+714 in the context of aforementioned scenarios.

Radiative cooling :

The change in spectral slope ($\Delta\Gamma$) above and below the break energy varies between 0.4 to 1.14. The estimated $\Delta\Gamma$ values for S5 0716+714 do not favor the standard radiative cooling models that predict a spectral break of 0.5 units. It is also difficult to reconcile the constancy of the break energy with respect to the flux variations within the “cooling break” scenario. Furthermore, this scenario failed to explain the absence of spectral break for Bin 1. From this I conclude that the observed spectral breaks in 0716+714 are unlikely to have an intrinsic origin associated with the radiative cooling.

Two component model :

The spectral breaks in FSRQ 3C 454.3 were reproduced by a combination of two components, namely, the Compton-scattered disk and BLR radiations ([Finke & Dermer, 2010](#)). But, as for BL Lacs, the jet radiation completely outshines the disk emission. Therefore, the disk emission contribution seems to be negligible in the observed spectrum; although, it can not be excluded completely. A further possibility is the combination of SSC and EC components. Modeling the broad-band SEDs of the source over different time bins during the course of the *Fermi/LAT* observations (see Section 7.2 for details), it is found that a model including an external Compton component generally does a better job in reproducing the entire SED with an external radiation field dominated by Ly- α from a putative broad-line region. The estimated radiation field energy density of this external field was found to vary between 10^{-6} and 10^{-5} ergs cm $^{-3}$. But, the non-existence of a spectral break for Bin 1 is again difficult to explain with this scenario.

Absorption via pair production :

The spectral breaks within few GeVs are well described by γ -ray absorption within the broad-line region. In this scenario, the observed spectral breaks constrain the location of the γ -ray emission region. It implies that γ -rays are produced within the BLR region, i.e., within a distance of few parsecs from the central engine. The γ -ray photons originating outside of the BLR region are unlikely to be absorbed as a result of $\gamma\gamma$ absorption, and hence do not show any break in the GeV spectrum. Likewise the chances of detection of high-energy photons will also be higher. Therefore, it can be convincingly argued that the detection of many high-energy photons and the absence of a spectral break for Bin1 is due to lower absorption via pair-production ($\gamma\gamma$ absorption).

Alternatively, external Compton scattering of IR photons from a dusty torus offers an alternative explanation for the observed spectral breaks. Given the fact that 0716+714 is also detected at TeV energies by MAGIC (Anderhub et al., 2009), the frequency of the target photons for the inverse-Compton up-scattering in the Thompson regime should be less than 10^{14} Hz (Sahayanathan & Godambe, 2012). If the scattering would be in the Klein-Nishina (KN) regime, a steeper photon index should be seen, which is in disagreement of the observed hard TeV spectra. However, the lack of any excess IR detection expected from a torus, does not necessarily rule out its existence, owing to the large amount of relativistic Doppler-boosting of the core region and the resulting strong dominance of the non-thermal emission. In this context the physical nature of the observed spectral break in the GeV/TeV spectrum still remains open and poses a challenge for future theoretical modeling.

The impact of the geometry of the broad-line region on the expected absorption, through the $\gamma\gamma$ process was recently discussed by Tavecchio & Ghisellini (2012). They argued that a correlated variation in $\Delta\Gamma$ and E_{break} is expected for an “open” geometry of the BLR. However, if the BLR is “closed” the break energy does not change as long as the emission occurs within the BLR, but $\Delta\Gamma$ decreases as the emission region moves away from the central engine. For 0716+714, no correlation is found between $\Delta\Gamma$ and E_{break} ; although, both changes from state to state. This rules out the possibility of an “open” BLR geometry. Most probably the emission region in the source is not located at a fixed distance from the black hole. It is also noticed that the GeV spectrum constructed during the period of detection of the highest energy (207 GeV) photon does not show any spectral break, while the spectral break parameters ($\Delta\Gamma$ and E_{break}) are maximum for the spectrum constructed over the period where the detection of high-

energy ($E > 20$ GeV) photons is low. A significant correlation between $\Delta\Gamma$ and E_{photon} with a decreasing $\Delta\Gamma$ for an increasing E_{photon} is a signature of varying opacity.

7.2 The complete spectral energy distribution

The broad-band monitoring of the source over several decades of frequencies allows us to construct multiple quasi-simultaneous SEDs. The SEDs of the source constructed over 4 different periods of time are shown in Fig. 7.5. These time bins reflect different brightness states of the source and each time bin has a width of 10 days. The SED plots are shown in Figs. 7.6 – 7.9. The variation in flux over the bin width is shown as error bars in the SED plots. The broad-band SEDs are constructed for the following activity periods :

Bin1 : Radio-mm(steady), optical(high), X-ray(steady), GeV(low) (Fig. 7.6)

Bin2 : Radio-mm(low), optical(flaring), X-ray(low), GeV(flaring) (Fig. 7.7)

Bin3 : Radio-mm(flaring), optical(flaring), X-ray(flaring), GeV(low) (Fig. 7.8)

Bin4 : Radio-mm(steady), optical(low), X-ray(steady), GeV(steady) (Fig. 7.9)

7.2.1 SED modeling

The double-humped structures of the broad-band SEDs can usually be modeled by both leptonic and hadronic models (e.g. Böttcher et al., 2012). The broad-band SED modeling is done with the help of M. Böttcher and is published in Rani et al. (2013a). A quasi-equilibrium version of a leptonic one-zone jet model (Böttcher et al., 2012) is used for fitting. In this model, the observed radiation is assumed to be originating from ultra-relativistic electrons (and/or positrons) in a spherical emission region of co-moving radius R_b propagating with relativistic speed $\beta_{\Gamma}c$ (Γ is bulk Lorentz factor) along the jet, which is offset by an angle θ w.r.t the line-of-sight. The value of θ is fixed such that the bulk Lorentz factor, Γ equals the Doppler factor, δ , which, for highly relativistic motion ($\Gamma \gg 1$) implies $\theta = 1/\Gamma$. The emitting electrons are assumed to be instantaneously accelerated into a power-law distribution of electron energy, $E_e = \gamma m_e c^2$, of the form $Q(\gamma) = Q_0 \gamma^{-q}$ with q being the injection electron spectral index between the low- and high-energy cutoffs (γ_1 and γ_2).

An equilibrium in the emission region between particle injection, radiative cooling, and escape of particles from the emission region yields a temporary quasi-equilibrium

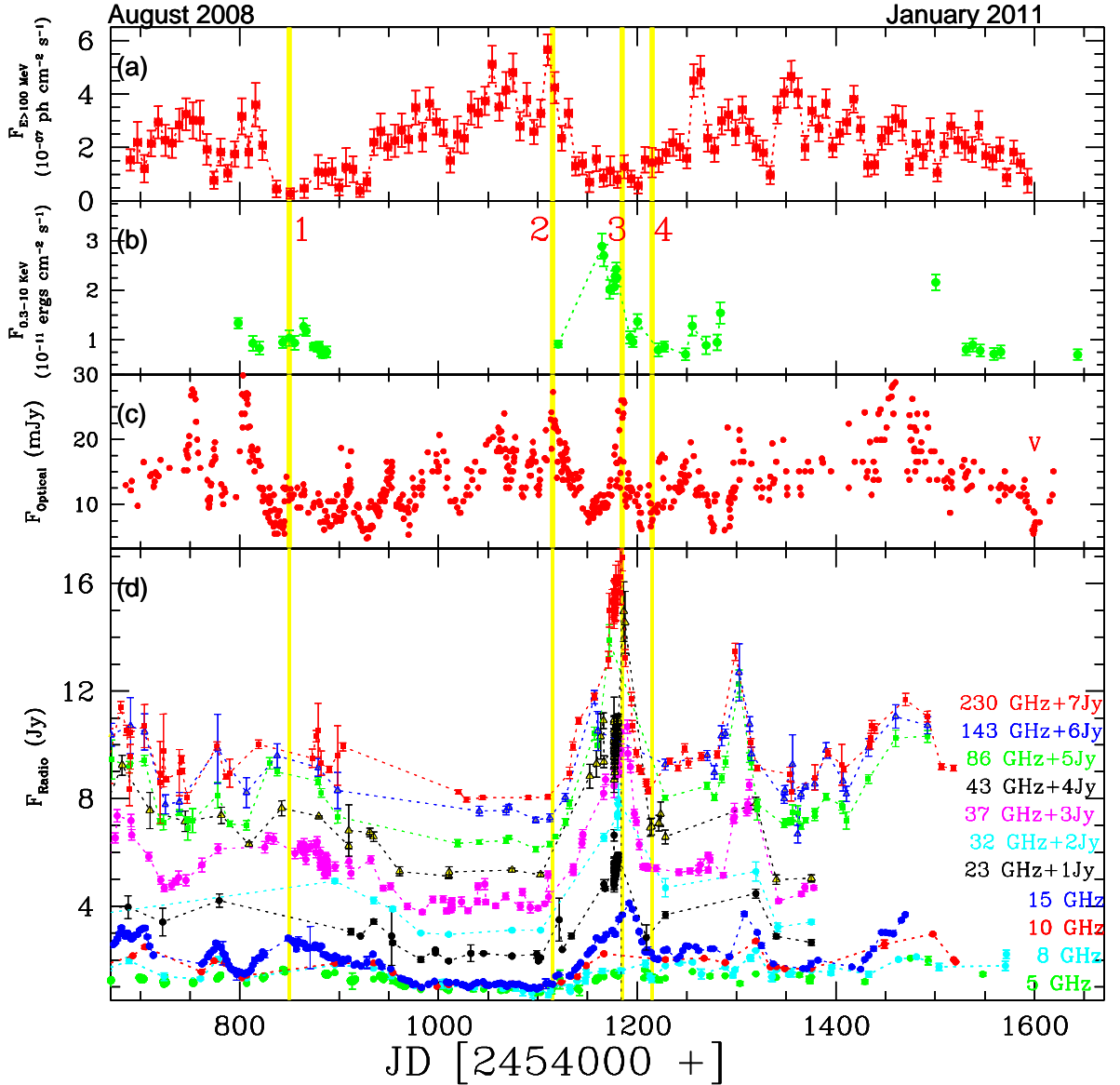


Figure 7.5: Light curves of 0716+714 from γ -ray to radio wavelengths (a): GeV light curve at $E > 100$ MeV, (b): X-ray light curve at 0.3–10 KeV, (c): optical V passband light curve, and (d) 5 to 230 GHz radio light curves. The yellow lines represent the periods (labeled as “1” to “4”) for which I construct the broad-band SEDs of the source (see text for details).

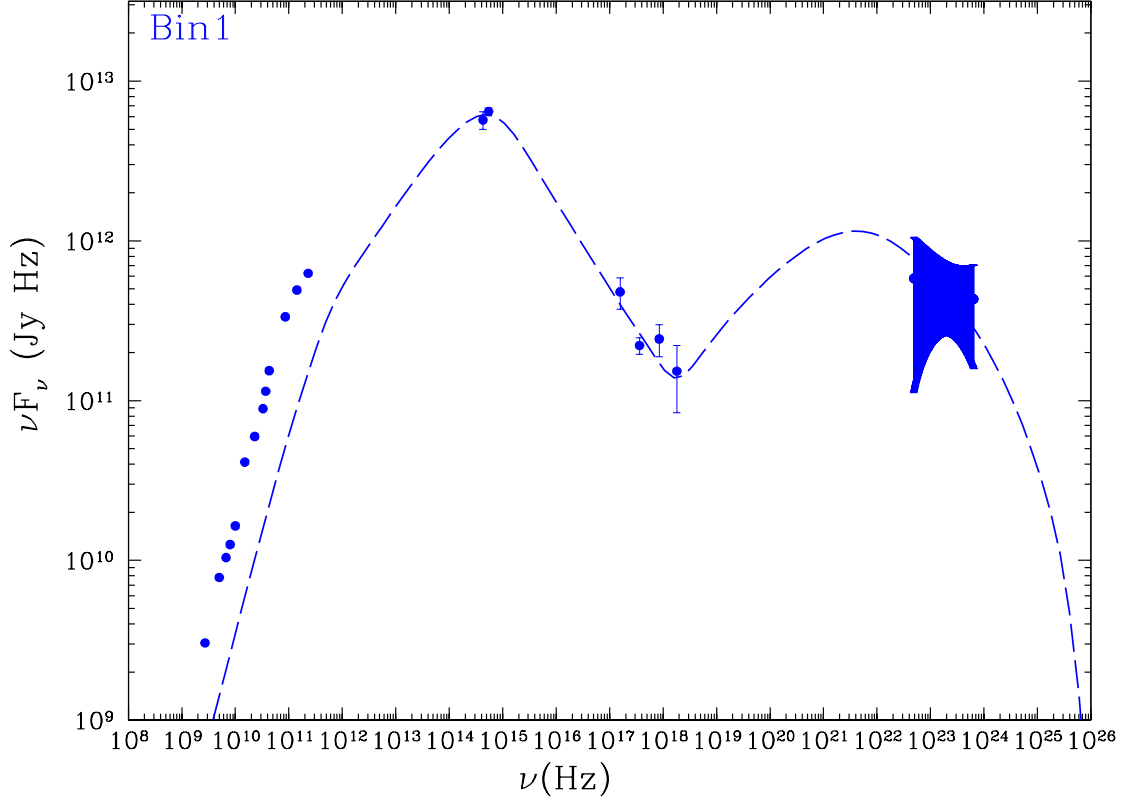


Figure 7.6: Broad-band SED of S5 0716+714 for time Bin1. The SED is constructed using 10-day averaged multi-frequency data. The error bars represent the variation of flux over 10 days. A pure SSC model is shown as dotted-dashed curve.

state described by a broken power law distribution of the electrons. The particle escape is parametrized through an escape timescale parameter $\eta > 1$ so that $t_{esc} = \eta R/c$. The balance between the particle escape and radiative cooling will lead to a break in the equilibrium particle distribution at a break Lorentz factor γ_b , where $t_{esc} = t_{cool}(\gamma)$. The cooling timescale is calculated self-consistently taking into account synchrotron, SSC and EC cooling. Depending on whether γ_b is greater than or less than γ_1 , the system will be in the slow cooling or fast cooling regime, respectively, leading to different spectral indices of the equilibrium electron distribution [Böttcher & Chiang \(2002\)](#).

In this model, the number density of injected particles is normalized to the resulting power in ultra-relativistic electrons propagating along the jet given by,

$$L_e = \pi R_e^2 \Gamma^2 \beta_\Gamma c m_e c^2 \int_1^\infty \gamma n(\gamma) d\gamma \quad (7.1)$$

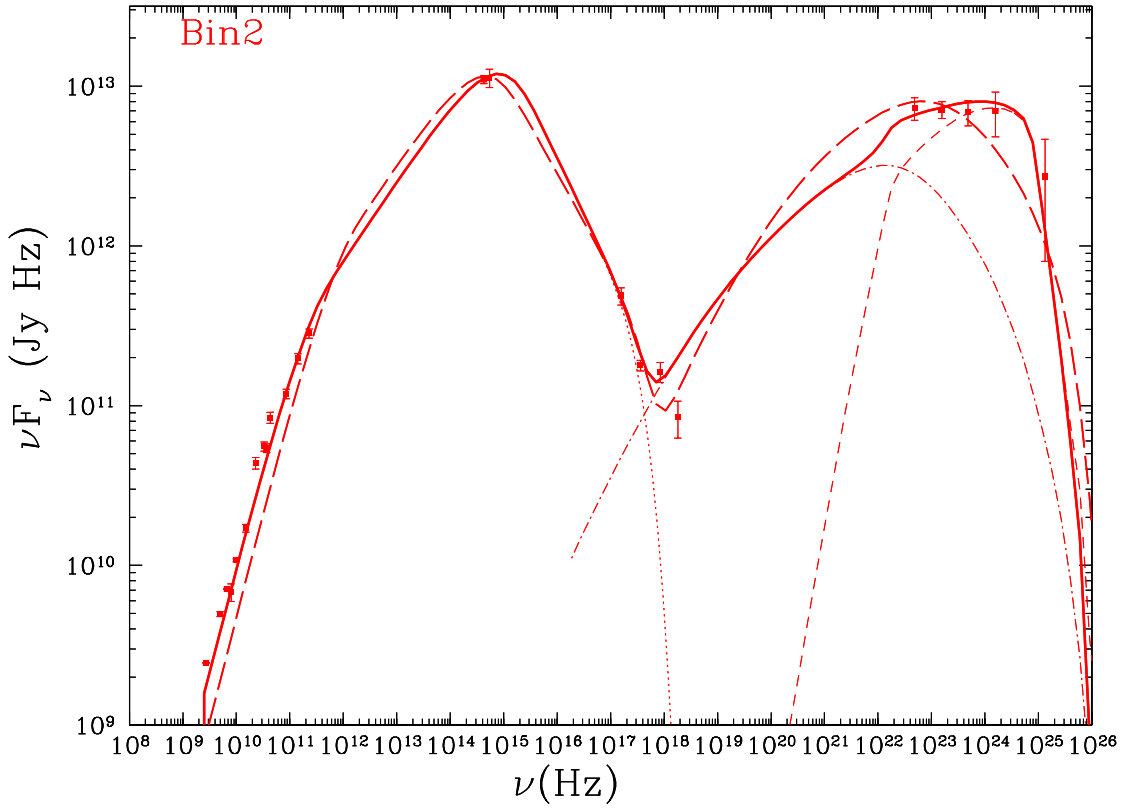


Figure 7.7: Broad-band SED of S5 0716+714 for time Bin2. The SED is constructed using 10-day averaged multi-frequency data. The error bars represent the variation of flux over 10 days. A pure SSC model is shown as thick dashed curve. For EC fit, the solid curve is the total modeled SED; the dotted curve is the synchrotron component, the SSC component is the dot-dashed curve, and the EC component is the thin dashed curve.

The magnetic field is considered as a free parameter in the emission region. The Poynting flux along the jet is $L_B = \pi R_e^2 \Gamma^2 \beta_{\Gamma} c u_B$, where $u_B = B^2 / (8\pi)$ is the magnetic field energy density. The equipartition parameter $e_B = L_B / L_e$ is calculated for each fitted model.

After evaluation of the quasi-equilibrium particle distribution in the emission region, the code calculates the radiative output from the synchrotron, SSC, and EC emissions self-consistently with the radiative cooling rates. The external radiation field, which serves as seed photons for EC scattering, is assumed to be isotropic in the stationary AGN rest frame. Its spectrum can be either chosen to be a thermal blackbody with temperature T_{ext} and radiation energy density u_{ext} , or a line-dominated spectrum (or

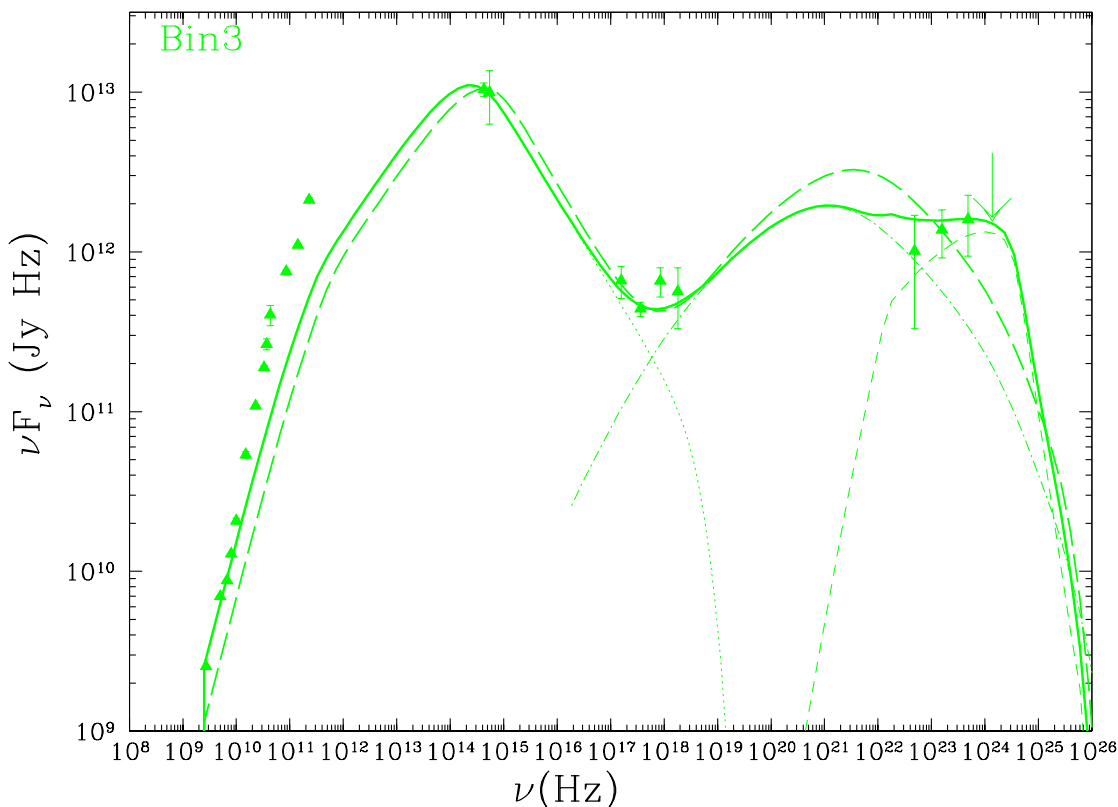


Figure 7.8: As in Fig. 7.7 for time Bin3.

a combination of the two). The direct emission from this external radiation field is added to the emission from the jet to yield the total SED model, which is fitted to the observations.

7.2.2 Results

At first the observed SEDs are tried to be fitted using a pure SSC model, as this has fewer free parameters than the EC version of the model. However, except for the SED of Bin1 (see Fig. 7.6), pure SSC models typically fail to reproduce the *Fermi/LAT* spectra of the SEDs. Therefore, an external radiation component, as outlined above, is included to produce SSC+EC fits.

The fitted models are shown in Figs. 7.6 – 7.9 and the best-fit parameters are given in Table 7.2. The pure SSC model does a moderately good job in describing the SEDs of the low states; although, the γ -ray spectra appear systematically too steep (see Fig.

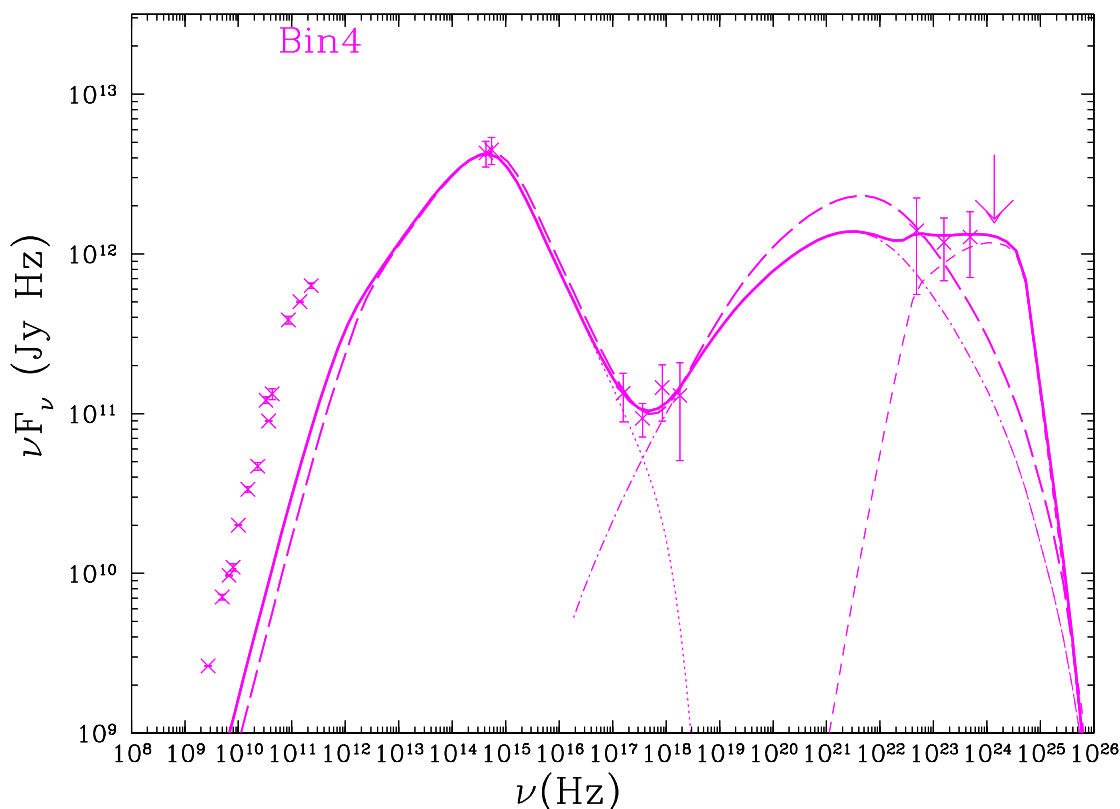


Figure 7.9: As in Fig. 7.7 for time Bin4.

7.10). The SED of Bin1 is well fitted with the SSC model, while for the other time bins an EC component is required to fit the GeV spectra. The high-state is very problematic for the SSC model as it would require a much lower magnetic field ($B = 0.05$ G, see Table 7.2). Also, in the case of Bin 2 – a very large emission region size, is in conflict with the often observed intraday optical variability. All the low-state fits are possible with parameters close to equipartition between relativistic electrons and the magnetic field.

A model including external Compton component generally does a better job in reproducing the entire SEDs (including the γ -ray spectrum), if one uses an external radiation field dominated by Ly- α emission from a putative broad-line region (BLR). The radiation field energy density of this external field varies between 10^{-6} to 10^{-5} erg cm^{-3} , which is a factor of ~ 1000 lower than expected for a typical quasar. However, this is a reasonable value for a BL Lac like S5 0716+714, which is known to have a featureless spectrum (no prominent BLR). Furthermore, this low BLR energy density

7.2 The complete spectral energy distribution

Table 7.2: Parameters of SSC and EC fits to SED of S5 0716+714

Parameters	Bin1	Bin2		Bin3		Bin4	
	SSC	SSC	EC	SSC	EC	SSC	EC
γ_1	2.5×10^3	1.1×10^3	4.0×10^3	2.5×10^3	1.8×10^3	3.0×10^3	2.5×10^3
γ_2	1.0×10^5	2.6×10^5	6.5×10^5	2.0×10^3	2.0×10^5	1.0×10^5	1.0×10^5
q	3.10	3.20	3.40	3.15	3.10	3.45	3.45
η	25	100	25	25	25	25	25
B (G)	1	0.05	0.7	0.9	0.95	0.8	1
Γ	25	25	25	25	25	25	25
R_b (cm)	1.25×10^{16}	1.7×10^{17}	2.0×10^{16}	1.4×10^{16}	2.0×10^{16}	7.5×10^{15}	7.5×10^{15}
θ (degree)	2.29	2.29	2.29	2.29	2.29	2.29	2.29
$L_e [10^{44}]$	1.33	26.99	4.15	4.298	4.31	3.09	2.48
e_B	1.61	0.063	1.11	0.87	1.59	0.27	0.53
T_{ext} K	–	–	Ly- α	–	Ly- α	–	Ly- α
E_{ext}	–	–	1.7×10^{-5}	–	3.0×10^{-6}	–	1.0×10^{-5}

γ_1, γ_2 : Low- and High-energy cutoff

q : Injection electron spectral index

η : Electron escape timescale parameter

B (G) : Magnetic field at $z=0$

Γ : Bulk Lorentz factor

R_b (cm) : Blob radius

θ (degree) : Observing angle

$L_e [10^{44}]$: Electron power in units of erg s^{-1}

e_B : Magnetic field equi-partition parameter

T_{ext} : External radiation peak photon energy

E_{ext} : External radiation field energy density in units of erg cm^{-3}

value explains the origin of γ -ray spectral breaks observed in the source. Moreover, the low BLR energy density is consistent with the non-detection of emission lines. Parameters close to equipartition can be used for all time bins, including the high states.

At first glance the fits look good, but in more detail the fit to the radio data for some bins is still relatively poor. In the EC model, the model fits the cm-radio data quite well, but is much below the mm data for Bin3. The model for Bin4 does not fit the radio data at all (see Fig. 7.10). In general, the model under-predicts the radio flux at mm and cm bands. This indicates the possibility of a missing spectral component at cm-mm wavelengths. As mentioned in Section 6.1.1.2, a two-component model better describes the radio spectra. Therefore, I conclude that an additional synchrotron component may better explain the broad-band SED particularly at mm to cm wavelengths.

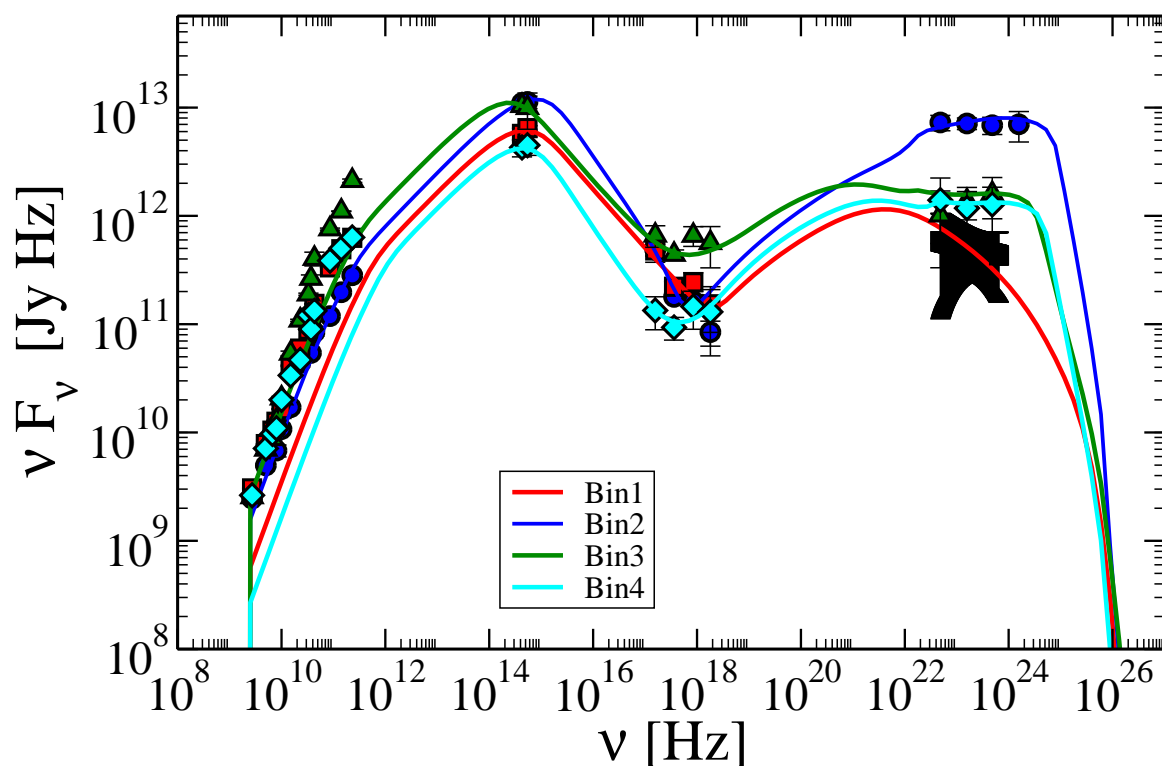


Figure 7.10: A comparison of the broad-band SEDs of S5 0716+714 during different activity states. The solid curves represent the best fitted model.

7.3 Conclusions

The 3.8 year averaged γ -ray spectral shape above 100 MeV clearly deviates from a single power law. A broken-power law model yields a break energy within a few GeV range. During different activity states of the source, the spectral break energy does not follow any systematic trend with respect to the photon flux variations. Such a behavior is similar to that observed in other bright Fermi blazars (Poutanen & Stern, 2010; Rani et al., 2013c; Tanaka et al., 2011). The combination of non-simultaneous GeV-TeV spectrum of the source shows absorption-like features between 10-100 GeV (Senturk et al., 2011). More simultaneous GeV-TeV observations are required to check this. A continuous TeV monitoring of the source will shed more light on it. This study has highlighted some possible explanations for the origin of γ -ray spectral breaks in the BL Lac object S5 0716+714.

The broad-band SEDs of the source are modeled using two different versions of leptonic models : a pure SSC and SSC+EC. It is found that the low activity states of the

source are well described by a pure SSC model, while an EC contribution is required to reproduce the SEDs for high states. The SSC+EC model returns magnetic field parameter value closer to equipartition, providing a satisfactory description of the broad-band SEDs. I found that satisfactory model fits can be achieved if the external radiation field is dominated by Ly- α emission from the broad-line region. This model nicely describes the broad-band SEDs of the source at optical and higher frequencies, but under-predicts the cm–mm spectra at least for few time periods. A separate synchrotron component seems required to fit the cm–mm radio fluxes.

Chapter 8

Inner jet kinematics and the origin of high-energy emission

A combination of high-resolution Very Long Baseline Interferometry (VLBI) images with the broad-band flux variability is a unique way to probe the emission mechanisms at the base of AGN jets. High-resolution mm-VLBI observations offer a unique possibility of studying the structural evolution in the innermost parsec to sub-parsec scale jets, which are proposed to be the sites of the high-energy emission region (Marscher et al., 2008; Rani et al., 2013c; Schinzel et al., 2012). Therefore, these VLBI observations can provide new constraints on the physical parameters of the emission regions i.e. sizes, brightness temperature, and relative motion of the bright features in the jet.

This chapter presents multi-frequency VLBI observations of the source to investigate the inner jet kinematics for a time period between September 2008 and October 2010. The focus of this study is to explore the morphological evolution of the source and to search for a possible relation with the broad-band flux variations, in particular the high-energy emission. The chapter is structured as follows. Section 8.1 provides a brief description of the VLBI data analysis. In Section 8.2, the kinematics of the pc-scale radio jet and its flux density evolution are presented. A possible relation of the jet kinematics with the high-energy (γ -ray) emission is discussed in Section 8.3. An interpretation scheme to explain the origin of broad-band emission is proposed in Section 8.4.

8.1 Multi-frequency VLBI data

For the study of the jet kinematics, I employed here the mm-VLBI data of the source for a time period between September 2008 and October 2010. The details of observations and data reduction are given in Section 3.3. The observed brightness distribution of the radio emission is modeled by multiple circular Gaussian components providing positions, flux densities, and sizes of the distinct bright features in the jet. The final number of jet components necessary to fit the data was adequately achieved when adding an extra component did not lead to a significant improvement of the fit. The formal uncertainties of the model component parameters were determined by comparing the parameter ranges obtained by performing model fits using different number of model components. I used at least four different model fits for each epoch to obtain the parameter uncertainties. However, the uncertainties depend also on the ‘self-calibration’ and on the details of editing. In addition to that, the uncertainties increase with increasing distance from the core. This is accounted by following Krichbaum et al. (1992) as an independent approach for the error estimation. The fitted model parameters for all the epochs are listed in Table 8.1, and here I just list the formal errors (obtained via comparison of fits using different number of model components). Figures 8.1 – 8.2 show the clean maps superimposed with the Gaussian components.

To investigate the kinematics in the jet of S5 0716+714, the individual model components are identified following an assumption that the changes of the flux density, distance from the VLBI core, position angle, and their sizes should be small for the time period between adjacent epochs. In order to prevent a potentially large systematic error arising from the incorrect cross-identification of moving features from epoch to epoch, the simplest scheme is adopted while identifying the jet-features. A self-consistent cross-identification is proposed using all available model-fit parameters. Therefore, the results presented here are meant to provide a robust and simple cross-identification based on the available data set, which of course could change if “non-linear” effects would be allowed.

The following sub-sections present the flux and spatial evolution of the bright radio emission in the jet of S5 0716+714. Special attention is given to the evolution of the inner jet (≤ 1 mas) kinematics. In addition to tracing the jet component motion during different epochs, I have also investigated the evolution of the jet ridge line, which is

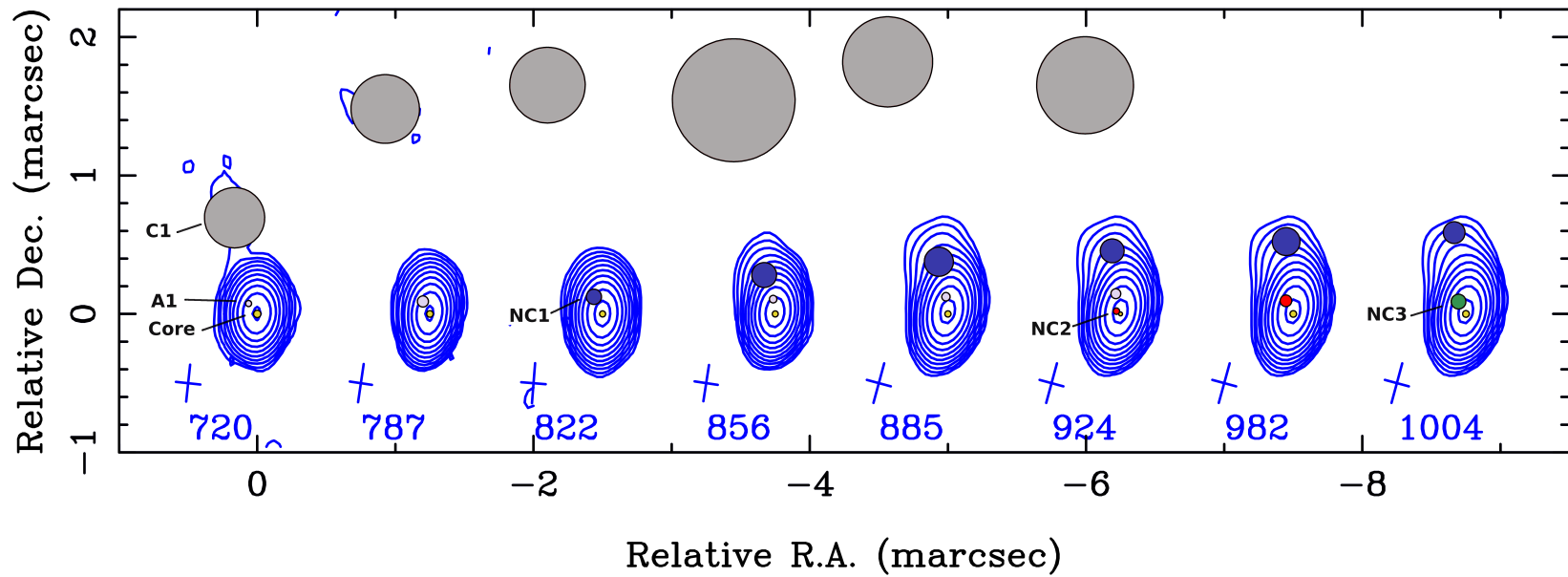
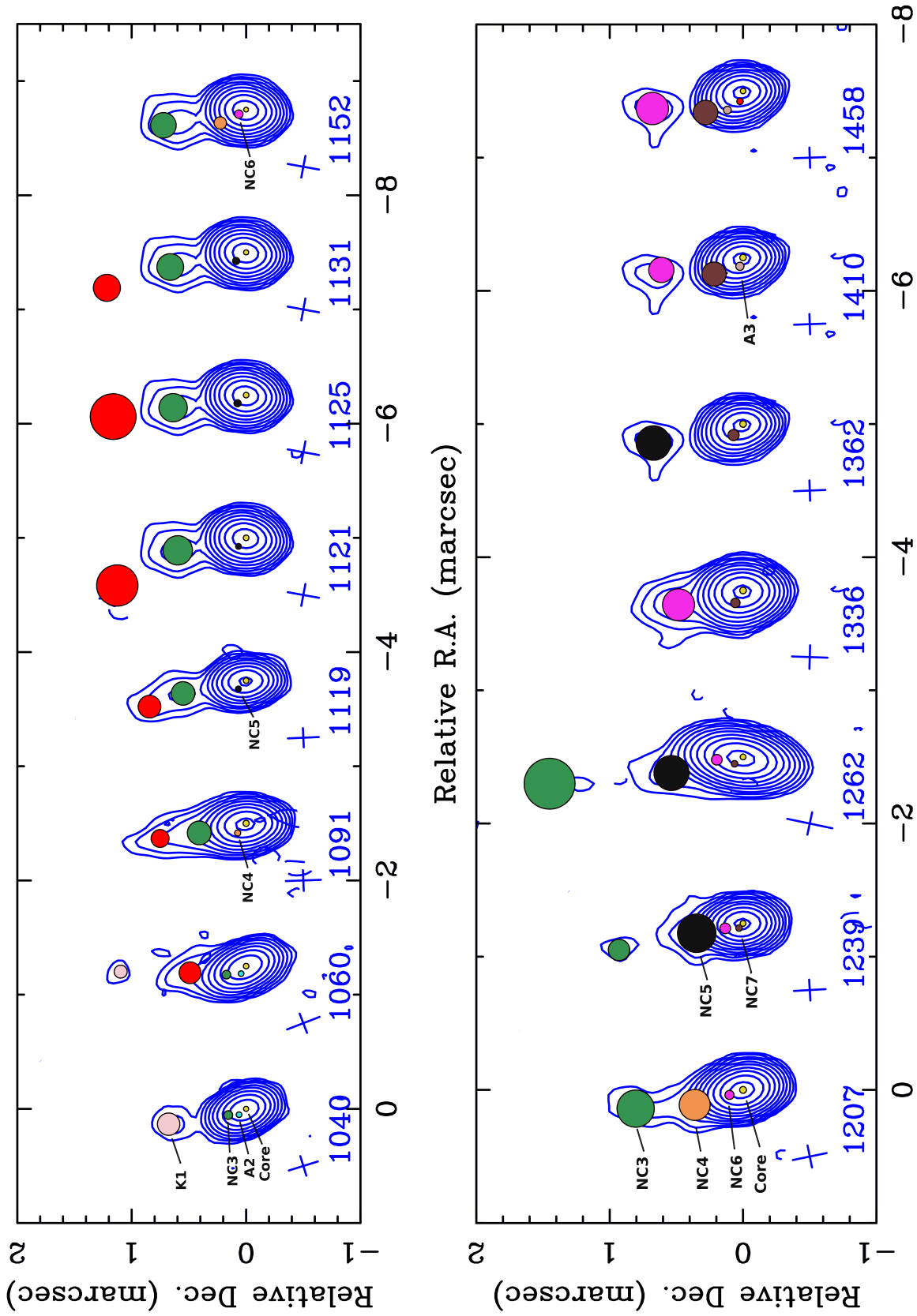


Figure 8.1: 43 GHz VLBI contour maps and Gaussian components of S5 0716+714 during different epochs. The date of observation is mentioned at the bottom of each map as the shifted Julian day (JD - 2454000). The fitted model parameters for each epoch are given in Table 8.1. The cross at the bottom of each map represents the FWHM of the restoring beam (0.25×0.18 (mas)). Contour levels are -0.003 0.003 0.006 0.012 0.024 0.048 0.096 0.19 0.38 0.76 1.54 3.07 6.14 12.28 24.58 49.15 98.30 mJy/beam.



Relative R.A. (marcsec)

Figure 8.1 (continued)

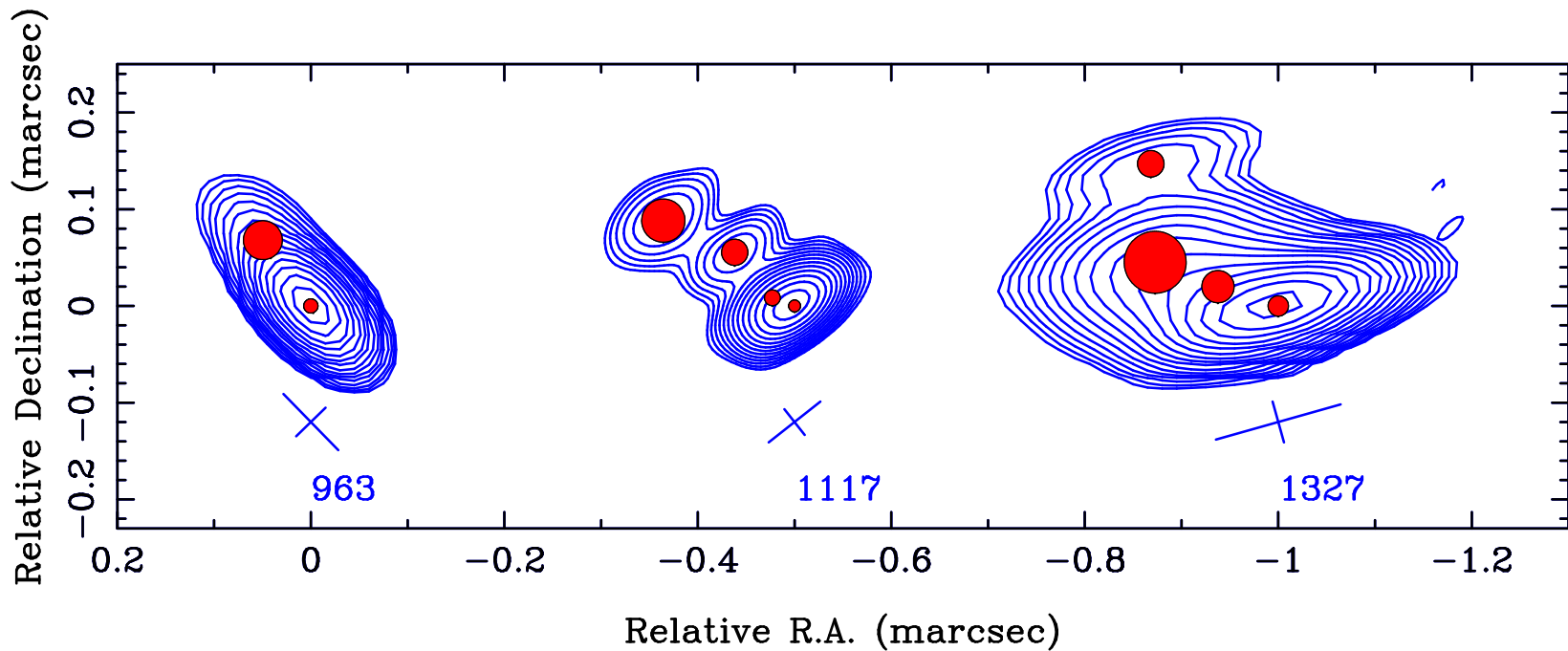


Figure 8.2: The inner jet structure of the BL Lac S5 0716+714 at 3 mm. The cross at the bottom of each map represents the FWHM of the restoring beam (0.07×0.04 (mas)). Contour levels are -0.004 0.004 0.008 0.016 0.032 0.064 0.12 0.25 0.51 1.02 2.04 4.09 8.19 16.38 32.77 65.54 mJy/beam.

Table 8.1: Results from Gaussian Model fitting and component parameters

Epoch (JD')	S_{peak} (Jy/beam)	r (mas)	θ ($^{\circ}$)	ϕ (mas)	Comp ^a
720	1.670±0.084	0.000±0.000	0.00±0	0.044±0.002	core
	0.139±0.007	0.098±0.005	39.90±2	0.034±0.002	A1
	0.023±0.001	0.714±0.036	13.28±0.66	0.427±0.021	C1
787	1.670±0.084	0.000±0.000	0.00±0	0.038±0.002	core
	0.188±0.009	0.103±0.005	29.29±1.46	0.071±0.004	A1
	0.022±0.001	1.516±0.076	12.33±0.62	0.487±0.024	C1
822	2.044±0.102	0.000±0.000	0.00±0	0.034±0.002	core
	0.082±0.004	0.139±0.007	26.83±1.34	0.101±0.005	NC1
	0.013±0.001	1.700±0.085	13.57±0.68	0.538±0.027	C1
856	2.167±0.108	0.000±0.000	0.00±0	0.034±0.002	core
	0.405±0.020	0.108±0.005	8.06±0.40	0.045±0.002	A1
	0.052±0.003	0.292±0.015	15.92±0.80	0.171±0.009	NC1
	0.025±0.001	1.572±0.079	11.01±0.55	0.879±0.044	C1
885	1.717±0.086	0.000±0.000	0±0	0.035±0.002	core
	0.420±0.021	0.125±0.006	6.64±0.33	0.051±0.003	A1
	0.053±0.003	0.383±0.019	9.89±0.49	0.201±0.010	NC1
	0.016±0.001	1.873±0.094	13.47±0.67	0.642±0.032	C1
924	1.038±0.052	0.000±0.000	0±0	0.018±0.001	core
	0.552±0.028	0.036±0.002	56.28±2.81	0.036±0.002	NC2
	0.187±0.009	0.150±0.008	13.26±0.66	0.062±0.003	A1
	0.051±0.003	0.460±0.023	7.60±0.38	0.163±0.008	NC1
	0.020±0.001	1.672±0.084	8.84±0.44	0.692±0.035	C1
963	0.354±0.018	0.000±0.000	0±0	0.011±0.001	core
	0.104±0.005	0.028±0.001	73.33±3.67	0.012±0.001	NC3
	0.043±0.002	0.084±0.004	47.52±2.38	0.025±0.001	NC2
	0.048±0.002	0.159±0.008	54.57±2.73	0.030±0.001	A1
	0.030±0.001	0.441±0.022	16.93±0.85	0.047±0.002	K1
	0.019±0.001	0.628±0.031	39.92±2.00	0.044±0.002	NC1
982	0.482±0.024	0.000±0.000	0±0	0.038±0.002	core
	0.118±0.006	0.109±0.005	29.31±1.47	0.074±0.004	NC2
	0.035±0.002	0.525±0.026	5.61±0.28	0.192±0.010	K1
1004	0.548±0.027	0.000±0.000	0±0	0.039±0.002	core
	0.075±0.004	0.104±0.005	31.10±1.56	0.097±0.005	NC3
	0.022±0.001	0.594±0.030	8.26±0.41	0.148±0.007	K1
	0.564±0.028	0.000±0.000	0±0	0.035±0.002	core
1040	0.166±0.008	0.080±0.004	39.50±1.98	0.040±0.002	A2
	0.038±0.002	0.165±0.008	19.10±0.96	0.067±0.003	NC3
	0.010±0.001	0.690±0.035	11.10±0.56	0.187±0.009	K1

$$JD' = JD - 2454000$$

8.1 Multi-frequency VLBI data

Table 1 continued.

Epoch (JD')	S_{peak} (Jy/beam)	r (mas)	θ ($^{\circ}$)	ϕ (mas)	Comp ^a
1060	0.663±0.033	0.000±0.000	0±0	0.039±0.002	core
	0.125±0.006	0.079±0.004	56.40±2.82	0.040±0.002	A2
	0.030±0.002	0.188±0.009	23.50±1.18	0.066±0.003	NC3
	0.019±0.001	0.494±0.025	6.77±0.34	0.181±0.009	NC2
	0.006±0.000	1.098±0.055	2.52±0.13	0.104±0.005	NC1
1091	0.873±0.044	0.000±0.000	0±0	0.045±0.002	core
	0.172±0.009	0.112±0.006	48.70±2.44	0.044±0.002	NC4
	0.041±0.002	0.388±0.019	11.50±0.58	0.199±0.010	NC3
	0.015±0.001	0.764±0.038	9.97±0.50	0.147±0.007	NC2
1117	0.356±0.018	0.000±0.000	0±0	0.012±0.001	core
	0.110±0.005	0.029±0.001	73.71±3.69	0.015±0.001	NC6
	0.041±0.002	0.084±0.004	48.90±2.45	0.017±0.001	NC5
	0.042±0.002	0.158±0.008	53.49±2.67	0.024±0.001	NC4
	0.021±0.001	0.502±0.025	17.16±0.86	0.040±0.002	NC3
1119	0.835±0.042	0.000±0.000	0±0	0.039±0.002	core
	0.122±0.006	0.100±0.005	47.00±2.35	0.041±0.002	NC5
	0.025±0.001	0.563±0.028	11.50±0.58	0.197±0.010	NC3
	0.013±0.001	0.875±0.044	15.00±0.75	0.189±0.009	NC2
1121	1.142±0.057	0.000±0.000	0±0	0.040±0.002	core
	0.175±0.009	0.100±0.005	48.10±2.41	0.041±0.002	NC5
	0.038±0.002	0.607±0.030	10.30±0.52	0.248±0.012	NC3
	0.007±0.000	1.201±0.060	20.30±1.02	0.352±0.018	NC1
1125	1.204±0.060	0.000±0.000	0±0	0.039±0.002	core
	0.243±0.012	0.103±0.005	43.20±2.16	0.052±0.003	NC5
	0.036±0.002	0.648±0.032	9.79±0.49	0.238±0.012	NC3
	0.010±0.001	1.177±0.059	9.19±0.46	0.391±0.020	NC1
1131	1.446±0.072	0.000±0.000	0±0	0.035±0.002	core
	0.262±0.013	0.115±0.006	40.70±2.04	0.052±0.003	NC5
	0.029±0.001	0.675±0.034	10.90±0.55	0.224±0.011	NC3
	0.013±0.001	1.256±0.063	14.30±0.72	0.227±0.011	NC1
1152	4.144±0.207	0.000±0.000	0±0	0.032±0.002	core
	0.397±0.020	0.075±0.004	31.60±1.58	0.064±0.003	NC6
	0.077±0.004	0.254±0.013	27.30±1.37	0.099±0.005	NC4
	0.018±0.001	0.736±0.037	10.70±0.54	0.214±0.011	NC3
1207	1.880±0.094	0.000±0.000	0±0	0.043±0.002	core
	0.206±0.010	0.108±0.005	20.30±1.02	0.060±0.003	NC6
	0.025±0.001	0.380±0.019	17.20±0.86	0.224±0.011	NC4
	0.015±0.001	0.817±0.041	9.89±0.49	0.271±0.014	NC3

Table 1 continued.

Epoch (JD')	S_{peak} (Jy/beam)	r (mas)	θ ($^{\circ}$)	ϕ (mas)	Comp ^a
1239	1.503±0.075	0.000±0.000	0±0	0.035±0.002	core
	0.219±0.011	0.046±0.002	48.90±2.45	0.041±0.002	NC7
	0.064±0.003	0.138±0.007	15.50±0.78	0.072±0.004	NC6
	0.031±0.002	0.355±0.018	11.90±0.60	0.280±0.014	NC5
	0.007±0.000	0.951±0.048	12.07±0.60	0.152±0.008	NC3
1262	1.453±0.073	0.000±0.000	0±0	0.035±0.002	core
	0.477±0.024	0.082±0.004	38.90±1.94	0.041±0.002	NC7
	0.050±0.002	0.198±0.010	6.09±0.30	0.072±0.004	NC6
	0.016±0.001	0.550±0.027	12.60±0.63	0.254±0.013	NC4
	0.011±0.001	1.464±0.073	7.88±0.39	0.374±0.019	NC3
1327	0.902±0.045	0.000±0.000	0±0	0.020±0.001	core
	0.194±0.010	0.065±0.003	71.62±3.58	0.032±0.002	A3
	0.019±0.001	0.560±0.028	14.54±0.73	0.024±0.001	NC7
	0.213±0.011	0.134±0.007	70.29±3.51	0.063±0.003	X
	0.023±0.001	0.200±0.010	45.00±2.25	0.021±0.001	NC5
1336	1.543±0.077	0.000±0.000	0±0	0.041±0.002	core
	0.359±0.018	0.109±0.005	58.30±2.92	0.062±0.003	A3
	0.043±0.002	0.435±0.022	12.40±0.62	0.232±0.012	NC6
	0.009±0.000	1.624±0.081	15.20±0.76	0.323±0.016	X
1362	0.783±0.039	0.000±0.000	0±0	0.041±0.002	core
	0.261±0.013	0.110±0.005	49.50±2.48	0.075±0.004	A3
	0.020±0.001	0.687±0.034	12.00±0.60	0.251±0.013	NC6
	0.005±0.000	1.781±0.089	15.60±0.78	0.171±0.009	X
1410	1.389±0.069	0.000±0.000	0±0	0.040±0.002	core
	0.438±0.022	0.070±0.003	70.20±3.51	0.053±0.003	A3
	0.080±0.004	0.250±0.013	29.70±1.49	0.173±0.009	NC7
	0.014±0.001	0.620±0.031	8.66±0.43	0.181±0.009	NC6
1458	2.974±0.149	0.000±0.000	0±0	0.033±0.002	core
	0.535±0.027	0.081±0.004	73.60±3.68	0.040±0.002	A3
	0.030±0.002	0.185±0.009	50.50±2.53	0.050±0.003	X
	0.022±0.001	0.324±0.016	29.80±1.49	0.176±0.009	NC7
	0.032±0.002	0.693±0.035	10.90±0.55	0.235±0.012	NC6

^a : Identification of the individual components. If a component appeared only in a single epoch, it is labeled as X.

defined as the line connecting adjacent jet components. Finally, I search for correlations between the jet kinematics and the broad-band flux variations.

8.2 Jet kinematics

8.2.1 Evolution of the jet ridge line

The jet ridge line connects the bright features in the jet, therefore its evolution does not require any component identification. Figure 8.3 shows the evolution of the jet ridge line during different epochs. The variation in the component paths during different epochs is larger than the positional uncertainties of the individual components. This implies that the jet ridge line evolves significantly during different epochs, and the ridge line swinging is more pronounced in the inner core region (within 0.1 mas). Moreover, during the phases of maximum source brightness, the jet is more pointed towards the East (larger position angles). Therefore, I investigate the position angle variations as a function of time.

8.2.2 Position angle variations

The position angle (PA) variations as a function of time are shown in Fig. 8.4 (top). The visual inspection of PA of the innermost portion of the jet indicates an apparent variation. In order to quantify this, a straight line is fitted between the core and the secondary jet component (i.e. component next to the core). The PA of this line provides a reasonably good estimate of the direction of the inner portion of the jet. The PA variations are investigated at three different radial distances from the core i.e. at $r = 0.02$ mas, 0.05 mas, and 0.1 mas.

To quantify the strength of variability and to extract the time scale of variability, the structure function analysis method is used. The details of the structure function method are given in Section 3.2.1.1. The PA structure function curves are shown in Fig. 8.4 (bottom). I found that the $PA_{r=0.05 \text{ mas}}$ structure function curve shows faster variations compared to the $PA_{r=0.1 \text{ mas}}$ structure function curve. The former follows a continuous rising trend showing the first peak at ~ 40 days and another peak at ~ 230 days that are followed by dips at ~ 65 and 369 days, respectively. The variability features at ~ 200 days are also observed for $PA_{r=0.1 \text{ mas}}$ structure function curve; however, the faster

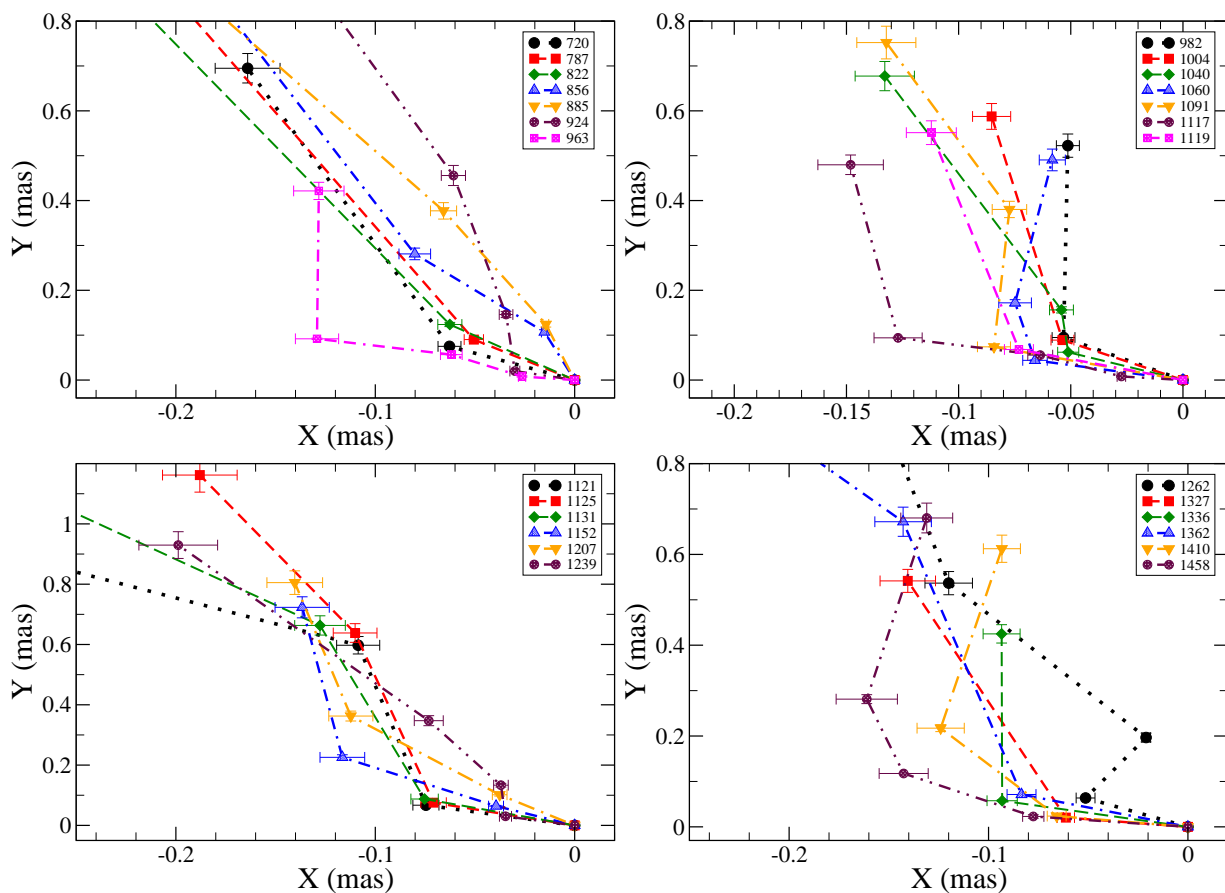


Figure 8.3: Evolution of the jet ridge line of the source during different epochs. At a given epoch, positions of the adjacent components are plotted relative to the stationary assumed core.

variability (~ 40 days) is not apparent in the PA variations at larger core separation ($r=0.1$ mas). The dips in the structure function curves at ~ 65 and 369 days represent the possible time scale of periodic variations. However, the data sampling is not dense enough to quantify the significance of the presence of the harmonics.

8.2.3 Component motion

For the kinematic study of the individual components, the VLBI core was chosen as a reference point and is fixed to $(0,0)$. This follows the physical assumption that the VLBI core position is not moving with time and therefore can be regarded as a stationary reference point. It is a reasonable assumption as the VLBI core is found to be rather stationary in phase-referencing measurements (see [Bartel et al., 2012](#), and references

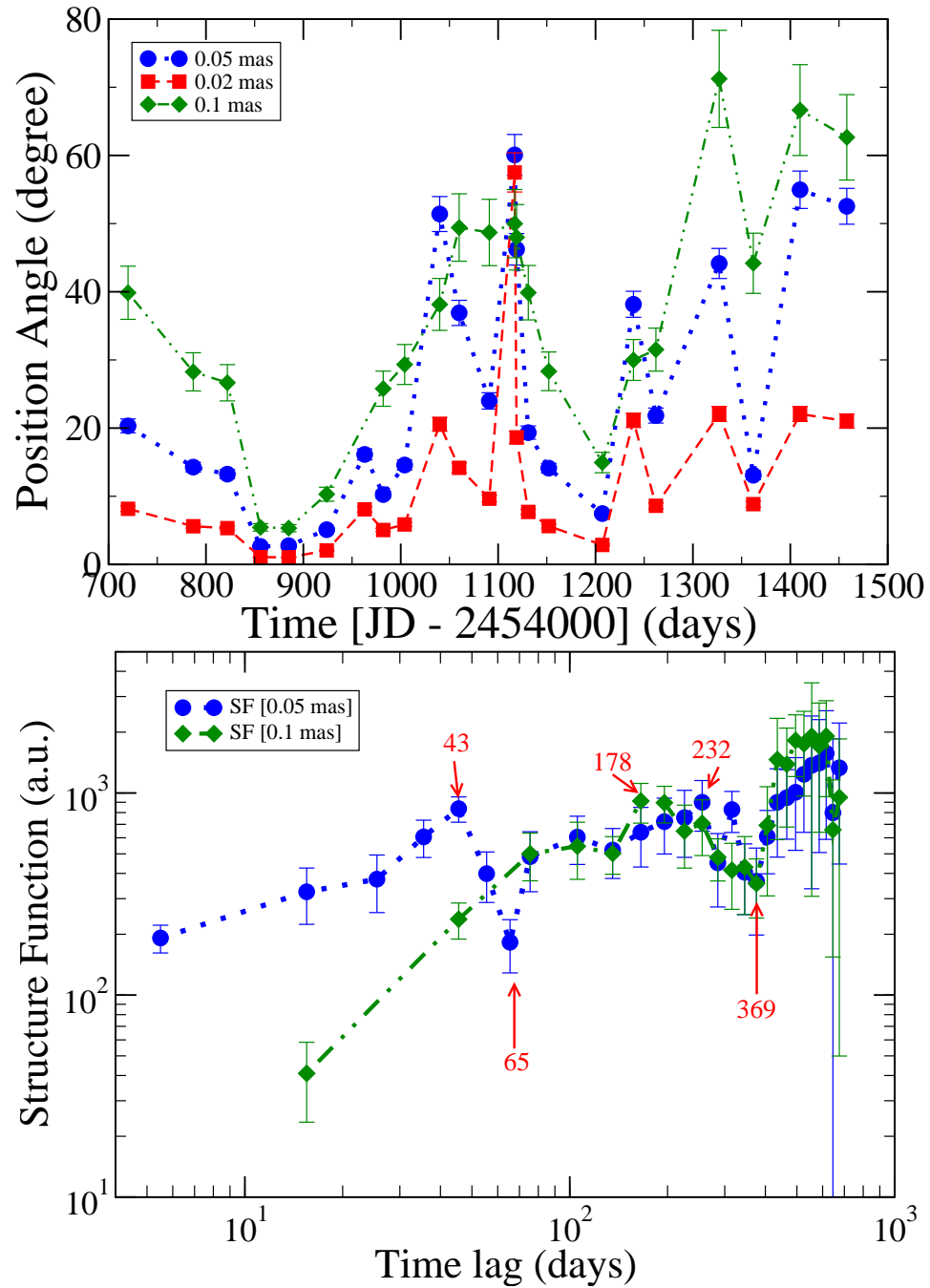


Figure 8.4: Top : Position angle variations versus time in the central region of the jet. Different colors represent different radial separations from the core. Bottom : The structure function analysis curve of the PA variations. The peaks in the structure function curve represent the timescale of variability and the local minima indicate possible timescales of periodicity.

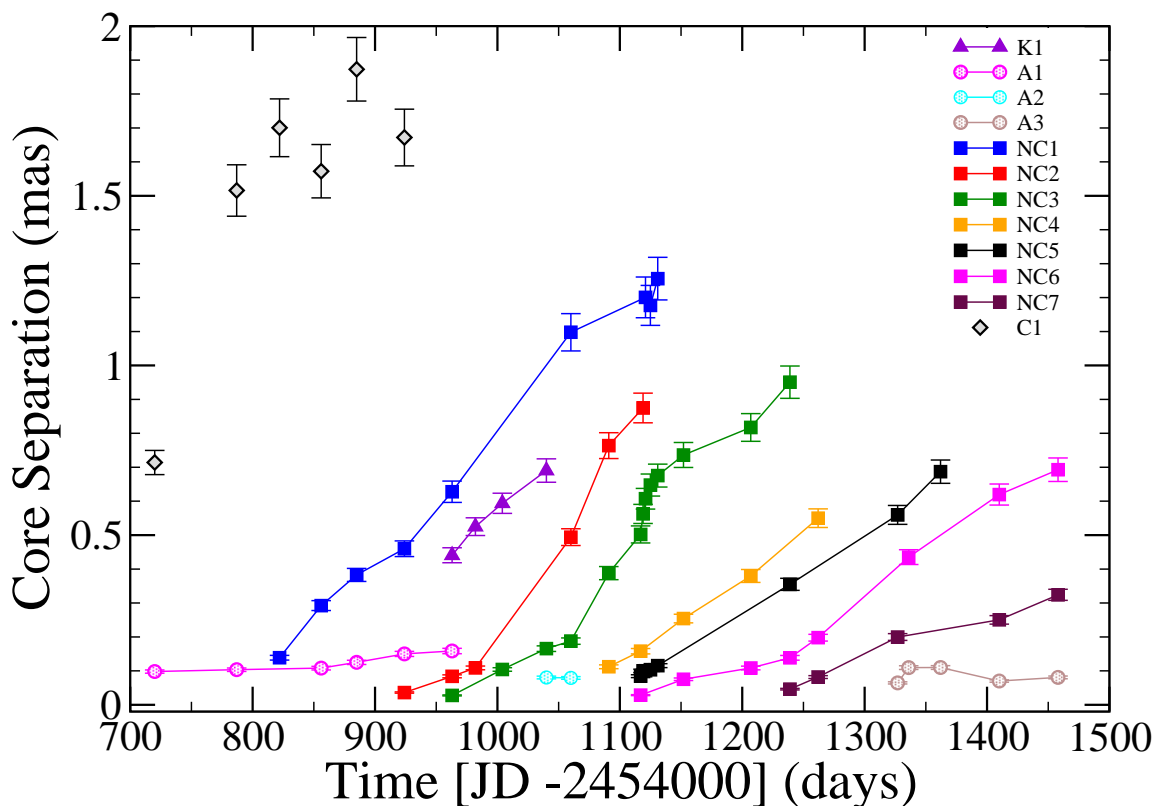


Figure 8.5: The core separation of individual components as a function of time.

therein). The motion of the individual components was measured relative to the core component. The VLBI data of the source were fitted by different number of components during different activity stages for a time period between September 2008 and October 2010. During this period, a total of 12 components C1, K1, A1, A2, A3, NC1, NC2, NC3, NC4, NC5, NC6, and NC7, are identified in addition to the core, C0. Figure 8.5 shows the evolution of the core separation for the individual components, and Fig. 8.6 shows their trajectories in XY-plane projected on the sky.

The sequence of the VLBI images allow us to investigate the component motion along the jet as a function of time. Apparently, most of the components exhibit significant motion down the jet except A1, A2, and A3, which are rather stable in distance with respect to the core; although, they exhibit significant scattering in position angle that exceeds the uncertainties (see Fig. 8.6). But as far as their radial motion is concerned, they remain stationary at ~ 0.10 – 0.15 mas distance from the core. Stationary features are a common characteristic of the AGN jets (Fromm et al., 2013a; Jorstad

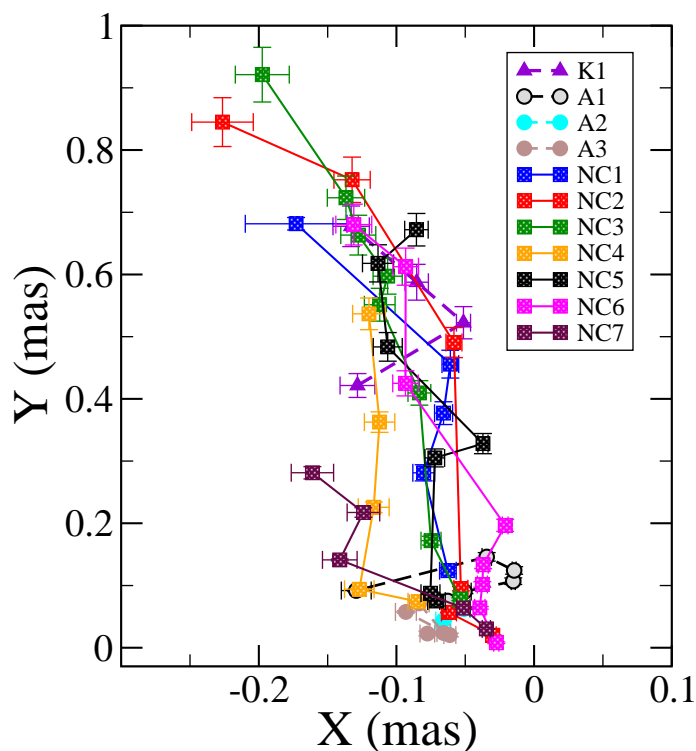


Figure 8.6: Trajectories of the jet knots in the X-Y plane, where $X = r \cdot \cos(\theta + 90)$ and $Y = r \cdot \sin(\theta + 90)$ (r is the radial separation from the core and θ is the position angle with respect to an imaginary line drawn vertically through the map center).

et al., 2001; Schinzel, 2011). In straight jets, these can be produced by recollimation shocks, instabilities, and/or magnetic-pinch (see Hardee, 2006; Marscher, 2009; Meier et al., 2001, for details). Bends in the jet can also cause quasi-stationary features, either because the jet turns more into the line of sight or due to the formation of a shock (Alberdi et al., 1993). It has been shown via simulations that a moving knot passes through a standing re-collimation shock, the components blend into a single feature and split up after the collision with no changes in proper motion of the moving knot (Fromm et al., 2012; Gomez et al., 1997). I found that the kinematics of three new components NC2, NC3, and NC6, is significantly different before and after the re-collimation. The components move slower ($\beta_{app} \leq 10c$) when they approach the stationary feature and later they move faster ($\beta_{app} \geq 20c$). Such a behavior can be expected if the stationary feature is produced at a bend in the jet (Alberdi et al., 1993). Therefore, it is likely that the standing features are stationary oblique shocks.

All the other components, C1, K1, and NC1 to NC7, exhibit significant motion in

Table 8.2: Physical parameters of the radio emission

Component	T_0	μ (mas/yr)	$\beta_{app}(c)$	δ_{var}
NC1	783_{-13}^{+8}	1.30 ± 0.04	24.88 ± 0.88	7.030 ± 0.35
NC2 _l	900_{-16}^{+10}	0.45 ± 0.00	8.71 ± 0.13	13.84 ± 0.69
NC2 _u		1.93 ± 0.14	37.06 ± 2.75	
NC3 _l	933_{-12}^{+16}	0.61 ± 0.03	11.69 ± 0.64	6.02 ± 0.30
NC3 _u		1.87 ± 0.17	35.78 ± 3.29	
NC4	1047_{-9}^{+10}	0.87 ± 0.04	16.81 ± 0.95	6.91 ± 0.34
NC5	1079_{-4}^{+5}	0.85 ± 0.03	16.30 ± 0.59	11.72 ± 0.58
NC6 _l	1092_{-17}^{+26}	0.34 ± 0.04	6.53 ± 0.77	15.33 ± 0.76
NC6 _u		0.99 ± 0.04	19.05 ± 0.92	
NC7	1203_{-7}^{+9}	0.48 ± 0.04	9.20 ± 0.84	20.96 ± 1.04

l and u stands for the lower and upper limits for the component speeds.

radial direction (see Table 8.2). The component C1 represents a very faint emission at a core separation of ≥ 1 mas. It may trace a component ejected in earlier epochs. The bright feature K1 could be a trailing component that forms behind a strong shock (Agudo et al., 2001) because it is identified at four epochs after the ejection of a new component NC1.

All components tend to follow curved trajectories in the rectangular coordinates on the plane of sky (XY-plane). The wiggling trajectories of the components along the jet axis are shown in Fig. 8.6. One can parametrize these trajectories by fitting different order polynomials. It is found that for most of the components a single order polynomial well describes their motion. The resulting fitted radial separation, $r(t) = \sqrt{x(t)^2 + y(t)^2}$, is shown in Fig. 8.7. I found that a linear function is sufficient to fit the trajectories of components NC1, NC4, NC5, and NC7. However, a second order polynomial is required to fit the trajectories of components NC2, NC3, and NC6, which indicates an apparent acceleration. Two different linear fits shown by solid lines in Fig. 8.6 provide a clear indication of a change in the slope of linear fit. Therefore a quadratic function is used to fit the component trajectories. In Fig. 8.6, the solid lines represent the fitted linear function, while the dashed curves are the quadratic fits.

For each component, the fits yield average proper motion and mean speed. The back-extrapolation of the fitted radial separation allows to estimate the time of zero separation from the core (i.e. ejection time, T_0). The calculated ejection times for

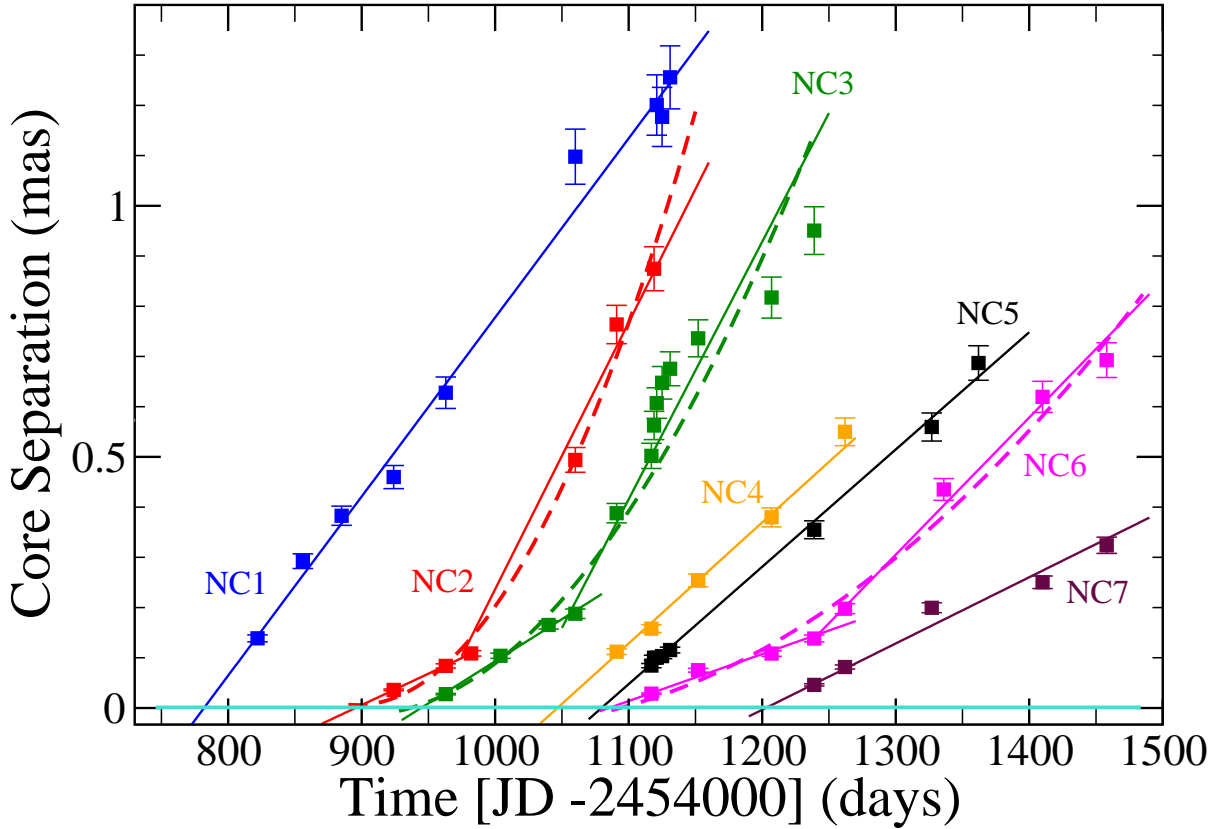


Figure 8.7: Evolution of radial separation of different components from the core. The solid lines represent the fitted linear function, while the dashed curves are quadratic fits.

the individual components are listed in Table 8.2. Using the estimated angular speed μ , I compute the kinematic parameters of the jet, e.g. apparent speed, β_{app} , and the Doppler factor, δ . The apparent speed of the components, β_{app} , is derived from the angular speed, μ :

$$\beta_{app} = \frac{\mu d_L}{c(1+z)} \quad (8.1)$$

where d_L is the luminosity distance and z the redshift of the source. The luminosity distance d_L corresponding to $z=0.31$ is $d_L = 1600$ Mpc for a Λ CDM cosmology with $\Omega_m = 0.27$, $\Omega_\lambda = 0.73$, and $H_0 = 71$ km s $^{-1}$ Mpc $^{-1}$ (Spergel et al., 2003). The angular and apparent speed of the individual components are given in Table 8.2¹. The jet components move with relatively high apparent speeds of $6c - 37c$. For the accelerating components NC2, NC3, and NC6, I estimate the lower and upper values of the apparent

¹1 mas yr $^{-1}$ = 19.13c

speeds. A significant acceleration is found for these components along the jet axis. The estimated values are $\dot{\mu} = 4.90 \pm 1.55 \text{ mas yr}^{-2}$ for NC2, $\dot{\mu} = 2.45 \pm 0.80 \text{ mas yr}^{-2}$ for NC3, and $\dot{\mu} = 0.94 \pm 0.36 \text{ mas yr}^{-2}$ for NC6.

The variability Doppler factor (Jorstad et al., 2005) can be derived using

$$\delta_{var} = \frac{sd_L}{c\Delta t_{var}(1+z)} \quad (8.2)$$

where s is the angular size of the component defined as $1.69 \times a$ for a Gaussian with $\text{FWHM} = a$ measured at the epoch of maximum flux and d_L is the luminosity distance (Jorstad et al., 2005). The timescale of variability is defined as $\Delta t_{var} = dt / \ln(S_{max}/S_{min})$ (Burbidge et al., 1974), where dt is the time separation in years between maximum (S_{max}) and minimum (S_{min}) flux densities. The estimated δ_{var} values for the individual components are listed in Table 8.2.

8.2.4 Brightness temperature gradient in the jet

The redshift-corrected observed brightness temperature ($T_{B,obs}$) of the bright emission features can be approximated using the following relation (Jorstad et al., 2005),

$$T_{B,obs} = 1.22 \times 10^{12} \frac{S_{comp}}{(1+z) d_{comp}^2 \nu^2} \text{ K} \quad (8.3)$$

where S_{comp} is the component flux density in Jy, d_{comp} is the FWHM of the circular Gaussian component in mas, and ν is the observing frequency in GHz. The calculated brightness temperature ($T_{B,obs}$) for all the components shows a general decay trend as a function of radial separation from the core (see Fig. 8.8). The decay trend can be approximated by a power law, $T_{B,obs} \sim r^c$, with $c = 2.36 \pm 0.41$. The solid line in Fig. 8.8 represents the fitted power law.

The observed brightness temperature gradient is investigated in the context of the shock-in-jet model (Marscher & Gear, 1985). In the common picture of the shock-in-jet model, a relativistic shock propagates down a conical jet slowly expanding and maintaining the shock conditions during propagation. While the shock propagates down the jet, it undergoes three major evolutionary stages dominated by Compton, synchrotron, and adiabatic energy losses. As a result, the observed brightness temperature decays as a power law, $T_{B,obs} \propto r_{jet}^{-c}$, where r_{jet} is the radial distance along the jet axis. The pa-

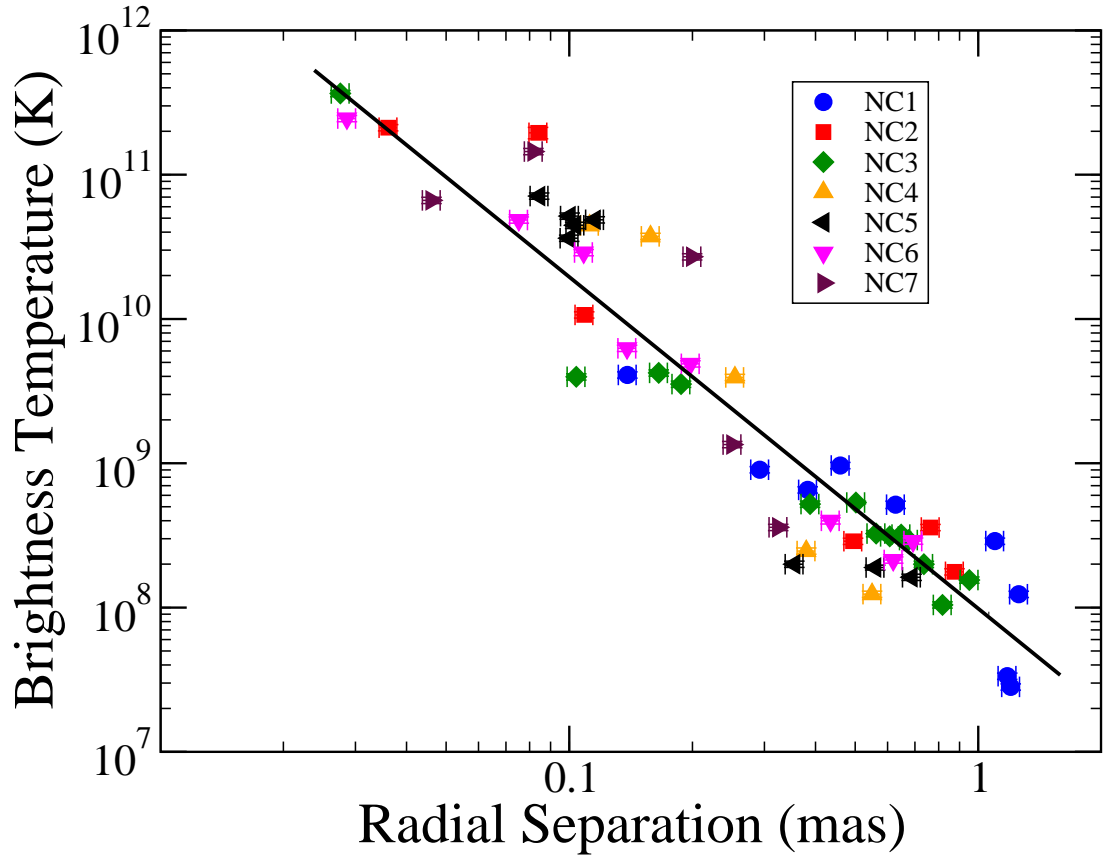


Figure 8.8: Component brightness temperature as a function of radial separation from the core. The solid line represents the fitted power law with index equal to 2.36 ± 0.41 .

parameter ϵ can be derived from the spectral evolution of the radio emission (Fromm et al., 2013b; Lobanov & Zensus, 1999). Following $T_b \propto S_\nu / r_{jet}^2 \nu^2$ and $S(\nu) \propto r_{jet}^\xi \nu^\zeta \delta^{(s+3)/2}$ (Lobanov & Zensus, 1999), ϵ is defined for the three stages as :

$$\epsilon_{Compton} = \frac{11 - s - a(s + 1)}{8} + \frac{b(s + 3)}{2} - 2 \quad (8.4)$$

$$\epsilon_{synchrotron} = \frac{-[4(s - 1) + 3a(s + 1)]}{6} + \frac{b(s + 3)}{2} - 2 \quad (8.5)$$

$$\epsilon_{adiabatic} = \frac{2(5 - 2s) - 3a(s + 1)}{6} + \frac{b(s + 3)}{2} - 2 \quad (8.6)$$

where a , s , and b parametrize the variations of Doppler factor $\delta \propto r_{jet}^b$, magnetic field $B \propto r_{jet}^{-a}$, and power law distribution of energy of electrons $N(\gamma) \propto \gamma^{-s}$ along the jet axis. Assuming a constant Doppler factor i.e. $b = 0$, and using a typical value of $s = 2$

(corresponding to an optically thin synchrotron spectral index = -0.5), and $a = 1$ to 2 , the estimated parameter ranges are $\epsilon_{Compton} = 1.3$ to 1.6 , $\epsilon_{synchrotron} = 4.2$ to 5.7 , and $\epsilon_{adiabatic} = 3.2$ to 4.7 . A change in the Doppler factor can be inferred for the ϵ values, which are inconsistent with these slopes.

The observed brightness temperature gradient in S5 0716+714 (Fig. 8.8) has a slope equal to 2.36 ± 0.41 . The observed intensity gradient slope thus rules out the simple assumptions of a constant Doppler factor. Therefore, I consider a variable Doppler along the jet axis. It is found that the observed ϵ value is consistent with the adiabatic loss if $\delta \propto r_{jet}^{-0.4}$, which infer a moderate variation in the Doppler factor. However, with relatively larger variations in the Doppler factor $\delta \propto r_{jet}^{-0.7}$, the observed ϵ value can be interpreted as synchrotron loss also.

The evolution of radio flares in turnover flux density – turnover frequency ($S_m - \nu_m$) plane, discussed in chapter 6 (Section 6.1.2), also suggests a variation of δ along the jet axis. For the two flares, I found that δ changes as $R^{0.7}$ during the rise and as $R^{2.6}$ during the decay of the first radio flare (R6). The evolution of the second flare (R8) is governed by $\delta \propto R^{0.4}$ during the rising phase and $\delta \propto R^{-2.0}$ during the decay phase. Therefore, it is evident that the two flares suggest a different dependence of δ on R , which is also inconsistent with what I obtain for the brightness temperature gradient ($\delta \propto R^{-0.4}$ to $R^{-0.7}$). It can be anticipated in two ways. First, the single dish radio flux correlates well with the VLBI core flux (see Section 8.3 for details). This implies that the radio flares are originating within the core. The core is more compact than the individual components with a comparatively high brightness temperature, and can follow a different dependence of δ on R . The individual components trace the intensity gradient further downstream of the jet, and therefore can have a different $\delta - R$ dependence. There is an equal possibility that in the brightness temperature gradient plot what we are seeing is an averaged behavior of the two flares.

8.3 Correlation: Jet kinematics and broad-band flares

8.3.1 Position angle versus flux variations

As noticed in Section 8.2.2, the PA of the inner jet region exhibits significant variations with two different timescales of variability (40 and 180 days). The optical/ γ -ray flux light curves of the source exhibit similar variability following a superposition of fast

8.3 Correlation: Jet kinematics and broad-band flares

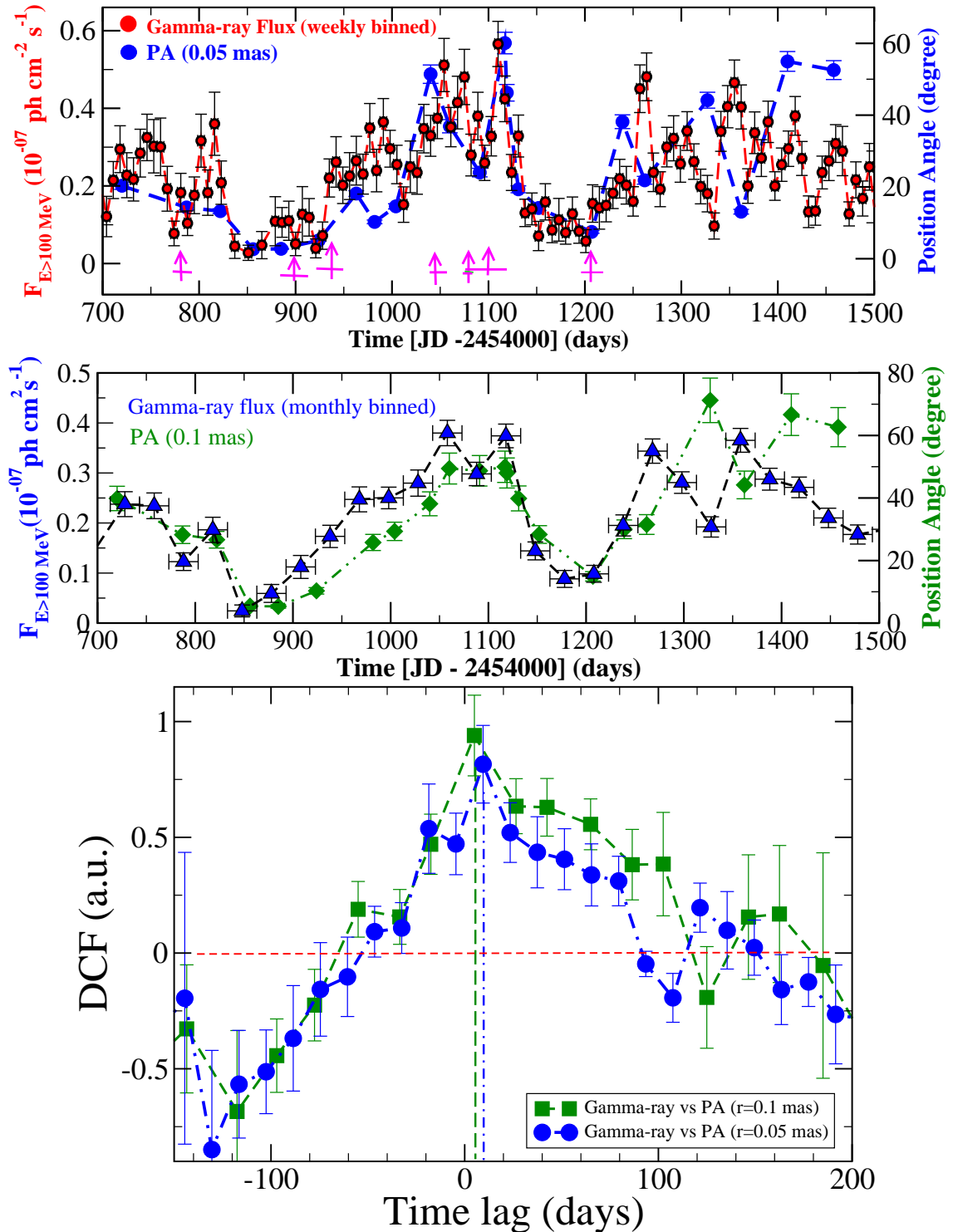


Figure 8.9: The weekly-averaged (top) and monthly-averaged (middle) γ -ray flux light curves superimposed with the inner $r=0.05 \text{ mas}$ and $r=0.1 \text{ mas}$ PA light curves, respectively. The arrows in the top panel mark the ejection epochs of new components. Bottom : The DCF curve of γ -ray flux versus PA at $r=0.05 \text{ mas}$ and $r=0.1 \text{ mas}$ radial separations using a time binning of 10 and 15 days, respectively.

repetitive flares ($t_{var} \sim 30$ day) on top of a long term variability trend ($t_{var} \sim 180$ day). Moreover, the timescales of nearly periodic variations, 60 and 360 days, are also common in the broad-band flux and PA variations. This suggests a possible correlation of the PA and the broad-band flux variations.

To compare the broad-band flares with the PA variations, the $PA_{r=0.05 \text{ mas}}$ are over-plotted with the weekly averaged γ -ray light curve (see Fig. 8.9 top). The arrows in the figure mark the ejection epochs of the new components. The monthly averaged γ -ray flux variations are compared with the $PA_{r=0.1 \text{ mas}}$ variations (Fig. 8.9 middle). Concurrent variations can be seen in the two curves.

To quantify the apparent correlation of the PA and γ -ray flux variations, I employed the discrete cross-correlation function (DCF) method (Edelson & Krolik, 1988; Rani et al., 2009). Figure 8.9 (bottom) shows the DCF analysis results of the weekly averaged γ -ray flux versus $PA_{r=0.05 \text{ mas}}$ (in blue) and the monthly averaged γ -ray flux versus $PA_{r=0.1 \text{ mas}}$ (in green). The DCF analysis of the weekly averaged γ -ray flux versus $PA_{r=0.05 \text{ mas}}$ has a peak value of (0.82 ± 0.16) at a time lag of (9.5 ± 5.0) days. The monthly averaged γ -ray flux versus $PA_{r=0.1 \text{ mas}}$ DCF analysis curve has a peak (0.94 ± 0.17) at (5.0 ± 7.5) day time lag. **Therefore, the DCF analysis confirms a correlated variation between the γ -ray flux and the PA variations of the innermost jet region.** The former correlation indicates a positive time lag with γ -ray leading PA variations by (9.5 ± 5.0) days. However, such a time lag can not be claimed in monthly averaged data sampling of the VLBI observations. In conclusion, the γ -ray flux and the PA variations are significantly correlated with each other with no time lag longer than one month.

8.3.2 Connection with broad-band flares

Figure 8.10 shows the radio (single dish) and γ -ray flux light curves superimposed on top of the 43 GHz VLBI core flux light curve. Although, the VLBI observations of the source are missing at the peak of the two major radio flares (see Fig. 8.10), still there seems to be an apparent one-to-one correlation between the core flux and single dish radio flux measurements. Concurrent variations in the single dish and VLBI core flux have been observed for many other sources as well (e.g. Agudo et al., 2011; Bach et al., 2006; Wehrle et al., 2001, and references therein). The γ -ray flux on the other hand seems to have an anti-correlation with the core flux variations. The broad-band flux

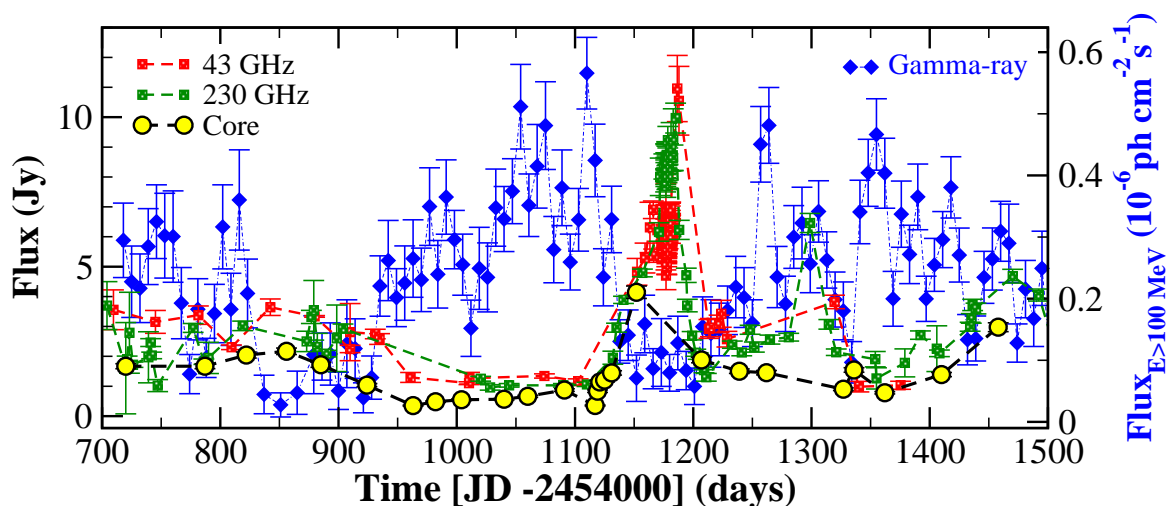


Figure 8.10: The radio (single dish) and γ -ray flux light curves superimposed on the 43 GHz VLBI core flux light curve.

cross-correlations (Chapter 5) indicate that the flux variations at γ -ray (optical too) and radio frequencies are correlated such that γ -ray lead radio by a two month time period. This suggests that the γ -ray flux is leading the VLBI core flux by a time period of two months. Moreover, the new jet components are either ejected in the beginning or at the peak of the γ -ray flares. Interestingly, no new component was found to be ejected during the quiescent period of the γ -ray flaring activity.

8.4 Discussion

The monthly sampled high frequency VLBI monitoring of the source allows to study the inner jet kinematics and to investigate its relation to the broad-band flux variability of the BL Lac S5 0716+714. The study reveals a significant variation in the jet ridge line of the source. Apparently, the components tend to move along curved trajectories. In radial directions, the individual components exhibit quite fast speeds as high as $\sim 38c$. However, an apparent speed of $\sim 20c$ seems to be more common in the parsec scale jet of 0716+714. Recently, [Lister et al. \(2013\)](#) reported an apparent speed of up to $43.6 \pm 1.3c$, even higher than for typical quasars. Therefore, the source exhibit exceptionally high superluminal motion. Since the jets of BL Lac objects, on average, have slower component speeds than the quasars ([Lister et al., 2009](#)), the high speed in S5 0716+714 is quite exceptional.

I propose that the observed variations in the jet ridge line, the wiggling trajectories of the component motion, the observed correlation between the optical/ γ -ray flux, and the inner jet PA variations can be explained by adopting an interpretation via helical jet models (e.g. as discussed by [Blandford & Payne, 1982](#); [Blandford & Znajek, 1977](#); [Camenzind & Krockenberger, 1992](#); [Hardee, 2006](#); [Meier et al., 2001](#), and references therein). Magnetohydrodynamic instabilities, prominently Kelvin-Helmholtz instabilities ([Hardee, 2006](#); [Perucho et al., 2006](#)) can explain the bending and helical structures in jets. Such an instability may also explain the wiggles observed in parsec-scale radio jets and can potentially account for the jet collimation and acceleration as well. In the magnetohydrodynamic models ([Blandford & Payne, 1982](#); [Blandford & Znajek, 1977](#); [Camenzind & Krockenberger, 1992](#); [Meier et al., 2001](#)), the out flowing jet plasma in a magnetized jet carries away angular momentum; as a result, the moving component also rotates because of the conservation of the total angular momentum along the given magnetic flux tube. Therefore, the observed flux variability is just a consequence of the temporal variation of the angle between the line-of-sight and the velocity vector of the moving component. Since each component does not necessarily follow the same path, a variation in the jet ridge line can also be expected.

The core flux significantly correlates with the radio flux light curves. However, I do not find any significant correlation between the core flux and γ -ray flux variations. The correlation analysis suggests that the major optical/ γ -ray flares lead the radio flares by a time lag of 65 days. Consequently, a significant correlation of radio and core flux variations implies that the optical/ γ -ray emission is leading the emission by a time period of ~ 65 days. *This suggests that the high-energy emission is coming further upstream the core. A time lag of 65 days corresponds to a separation of 0.27 parsec (or 0.06 mas) between the two emission regions.*

Chapter 9

Summary and Future Perspectives

The origin of high-energy emission has always been a key question in AGN physics. Since its launch in June 2008, the Fermi-Large Area Telescope (LAT) has opened a new era in high-energy astrophysics. The γ -ray bright blazars therefore constitute a unique laboratory to probe jet formation and its relation to radio-to- γ -ray variability. Investigation of the temporal characteristics is a unique way to probe into the location and physical processes related to emission mechanism in the vicinity of super massive black holes. A study of the fine scale structures is required for a better understanding of the acceleration and collimation processes involved. High-resolution Very Long Baseline Interferometry (VLBI) observations offer the unique possibility of studying the structural and spectral evolution in blazars on parsec to sub-parsec scales. These observations provide a tool to test different jet models and to probe if and how variations within the first few parsecs contribute to the high-energy emission.

This thesis is an attempt to explore the emission mechanisms at the base of relativistic jets in blazars. The aim is to obtain a more detailed understanding of the relation between flux density outbursts seen in optical and γ -ray frequencies and the subsequent structural variability as seen by high frequency VLBI. To do so, the densely sampled multi-frequency observations of the **BL Lac object S5 0716+714** are investigated during the past 5 years. A combination of high-resolution VLBI images associated with densely time sampled multi-frequency flux measurements of the source allows to study its broad-band variability and to probe the jet acceleration zone, with emphasis on the location and size of the emitting regions and the evolution with time. This thesis presents the characteristics of prominent mm-/ γ -ray flares in the context of (1) the shock-in-jet model, (2) broad-band spectral modeling, (3) and jet kinematics,

to probe the location and the origin of the high-energy emission region. The aim of the broad-band variability study reported in this thesis is to provide a general physical scenario which allows to put the observed variation of the source across several decades of frequencies in a coherent context.

A simultaneous multi-wavelength monitoring was carried out for a time period between April 2007 and April 2012. During this period, a sequence of flares were observed in the source at optical and higher frequencies. Two major radio outbursts were also observed during this high activity period. From the rapid rise and decay, the derived variability brightness temperatures exceeds the IC limit (10^{12} K) not only at cm-wavelengths, but also at mm-radio bands, which is a very unique behavior. A long-term variability trend (~ 360 days timescale) is visible in the optical light curves which is superimposed with repetitive variations on shorter time scales (~ 60 – 70 days). A comparison of the various flaring episodes of S5 0716+714 strongly indicates a one-to-one correlation between the strength of the γ -ray emission and the strength of the optical emission. *A quadratic dependence of the amplitude of the γ -ray variability with respect to that of the optical favors a synchrotron self-Compton (SSC) explanation.*

The high-energy (optical/ γ -ray) flares propagate down to radio frequencies with a time delay of ~ 65 days following **a power-law dependence on frequency with a slope ~ 0.3** . This indicates that **opacity** plays a key role in producing time delays among light curves at optically thin and thick wavelengths. Since the radio outbursts are low-peaking flares, such a long time lag is only possible in the case of optical flares being the precursors of radio ones. An orphan X-ray flare is observed ~ 50 days after the major optical/ γ -ray flares. The detection of an isolated X-ray flare challenges simple one-zone emission models, rendering them too simple. *The spectral analysis shows that the X-ray flare has equal contributions from both the synchrotron and the inverse-Compton emission mechanisms (in a leptonic model interpretation).*

A simplistic approach of a one-zone leptonic model is used to fit the observed broad-band spectral energy distribution (SED) of the source during different brightness phases. Interestingly, the low activity states of the source are well described by a pure synchrotron self-Compton (SSC) model, while an external Compton (EC) contribution is required to reproduce the SEDs for bright phases. The SSC+EC model returns a magnetic field parameter value close to equipartition ($e_B \sim 1$), with the external radiation field dominated by Ly- α emission from the broad-line region (BLR). A detailed investigation of the high-energy spectrum supports the view that the BLR has a significant

impact on the observed γ -ray spectral breaks at a few GeVs, due to $\gamma\gamma$ absorption. *The radiation field energy density of this external field varies between 10^{-6} to 10^{-5} erg cm^{-3} , which is a factor of ~ 1000 lower than what is expected for a typical quasar and is a reasonable value for a gas poor BL Lac object like S5 0716+714.*

The evolution of the radio flares is in agreement with the generalized 3-stage shock-in-jet model proposed by Marscher & Gear (1985). The evolution of the flare in the turnover flux density – turnover frequency ($S_m - \nu_m$) plane shows a very steep rise and decay over the Compton and adiabatic stages with a slope too high to be expected from intrinsic variations, requiring an additional Doppler factor variation along the jet. It is found that δ changes as $R^{0.7}$ during the rise and as $R^{2.6}$ during the decay of the first radio flare (R6). The evolution of the second flare (R8) is governed by $\delta \propto R^{0.4}$ during the rising phase and $\delta \propto R^{-2.0}$ during the decay phase of the flare. The change in δ can be easily interpreted as a few degree variation in the viewing angle, or a more noticeable change of the bulk Lorentz factor (jet intrinsic acceleration). *A correlation of the high-energy flux with the inner jet position angle variations argues in favor of a geometric interpretation.*

Different methods yield robust and self-consistent lower limits of Doppler factor, $\delta \geq 20$ and equipartition magnetic field, $B_{eq} \geq 0.36$ G in the source. Causality arguments constrain the size of emission region $\theta \leq 0.004$ mas, which is much smaller than the size of mm-VLBI core (~ 0.04 mas). *The estimated value of k parameter, which is defined as the energy ratio between electrons and heavy particles, is ~ 5 . A small value of k implies that the jet is mainly composed of electron-positron plasma.*

Quasi-simultaneous high frequency VLBI observations were used to investigate the parsec scale jet kinematics of the source. Patterns in the jet flow revealed a standing oscillating pattern observed at ~ 0.1 mas separation from the core. The long-term fits to the component trajectories manifest acceleration in the sub-mas region of the jet. The instability pattern found in the source, if being a result of Kelvin-Helmholtz instabilities, paired with numerical simulations, can be used to obtain a measure for the jet particle densities and matter composition of the jet. The jet composition is one of the major remaining questions about relativistic extragalactic jets and an important ingredient of the high-energy emission models.

In radial directions the individual components move as fast as $\sim 38c$ which is exceptionally high for BL Lac objects. Curved trajectories in the component motion, variations in the jet ridge line, and the position angle swings at the base of the jet

are all consistent with a **helical jet model** (Blandford & Payne, 1982; Camenzind & Krockenberger, 1992; Meier et al., 2001). As a result, the out flowing jet plasma in a magnetized jet carries away angular momentum; and hence, the moving components also rotate because of the conservation of the total angular momentum along a given magnetic flux tube. **A significant correlation of the core flux with the single dish radio flux, and the concurrent inner jet position angle and optical/ γ -ray flux variations suggests that the high-energy emission is coming from a region, which is located inside the mm-VLBI core, i.e. upstream to the $\tau=1$ surface on scales <0.06 mas (0.27 parsec) towards the central black hole.**

The results presented in this thesis are based on a single source. Further investigations need to show to which extent our findings can be generalized and applied also to other BL Lac objects. There is still an ongoing controversy about the location and origin of high-energy emission in these objects. The literature is biased towards leptonic models; however, hadronic processes remain a viable alternative. The existence and detailed form of multi-zone emission models are again an open issue, which require further investigation. Global observing campaigns are underway studying multi-wavelength emission from a variety of objects, and will very likely provide a better understanding of the acceleration processes at the base of relativistic jets.

The main question about launching and collimation of jets still persists. There is a fair agreement that magnetic fields play an important role, but what that role exactly is, is still under debate. The ongoing high frequency VLBI observations provide the direct view into sub-pc scale regions and the energy extraction from the super-massive black holes which ultimately will shed more light on jet formation and acceleration. New dimensions will be added to this study by the planned inclusion of the Atacama Large Millimeter Array (ALMA) to VLBI observations at 1 mm, which will offer an angular resolution up to a few ten micro-arcsecond scales (\leq few hundred R_S).

The database will be continued, broadened and enhanced by current and future observation facilities. A number of ground based telescopes are available in order to cover optical, infra-red, and radio bands. In the high-energy range (X-ray and γ -ray) recent advances have been made possible by satellites such as XMM-Newton, Chandra, RXTE, Swift, and Fermi etc. A range of major planned upgrades to these facilities, plus additional facilities planned and under construction are also there (e.g. NuSTAR, ECLAIRS, ASTROSAT etc.). To understand the radiation processes and the emission

mechanisms which are dominating in various bands, it is required to do simultaneous multi-frequency observations of blazars with a as complete as possible wavelength coverage of the EM spectrum over a longer span of time. The high-energy end of the synchrotron branch and the Compton scattered emission are of special importance. Long term simultaneous observations of blazars are required to investigate correlated variability and time lags at different wavelengths.

The combination of the multi-frequency flux measurements with kinematical studies is the most direct method to study (i) the launching of jets and (ii) the related production of high-energy emission. Such studies help to answer the question on the exact location of the γ -ray emission site (SSC, EC in core or by interacting shocks downstream the jet), and on the role of geometrical effects (Doppler boosting, jet curvature) against variations in intrinsic properties (jet speed, magnetic energy).

References

- Abdo, A. A., et al. 2009, ApJS, 183, 46 [113](#)
- Abdo, A. A., et al. 2010a, ApJ, 710, 1271 [23](#)
- Abdo, A. A., et al. 2010b, ApJ, 708, 1310 [31](#)
- Abdo, A. A., et al. 2010c, Nature, 463, 919 [83](#)
- Ackermann, M., et al. 2012, ApJS, 203, 4 [34](#)
- Ackermann, M., et al. 2011, ApJ, 743, 171 [33](#), [34](#)
- Agudo, I., Gómez, J.-L., Martí, J.-M., Ibáñez, J.-M., Marscher, A. P., Alberdi, A., Aloy, M.-A., & Hardee, P. E. 2001, ApJ, 549, L183 [17](#), [137](#)
- Agudo, I., Marscher, A. P., Jorstad, S. G., Gómez, J. L., Perucho, M., Piner, B. G., Rioja, M., & Dodson, R. 2012, ApJ, 747, 63 [19](#)
- Agudo, I., et al. 2011, ApJ, 735, L10 [82](#), [143](#)
- Alberdi, A., Marcaide, J. M., Marscher, A. P., Zhang, Y. F., Elosegui, P., Gomez, J. L., & Shaffer, D. B. 1993, ApJ, 402, 160 [17](#), [136](#)
- Aller, H. D., Aller, M. F., Latimer, G. E., & Hodge, P. E. 1985, ApJS, 59, 513 [26](#)
- Anderhub, H., et al. 2009, ApJ, 704, L129 [23](#), [102](#), [114](#)
- Anderson, B., Donaldson, W., Palmer, H. P., & Rowson, B. 1965, Nature, 205, 375 [42](#)
- Andreyanov, V. V. 1999, Experimental Astronomy, 9, 103 [42](#)

¹ [The number at the end of each reference is the page number of its citation.](#)

- Angelakis, E., Fuhrmann, L., Marchili, N., Krichbaum, T. P., & Zensus, J. A. 2008, *Mem. Soc. Astron. Italiana*, 79, 1042 [26](#)
- Atwood, W. B., et al. 2009, *ApJ*, 697, 1071 [30](#), [31](#)
- Baade, W., & Minkowski, R. 1954, *ApJ*, 119, 206 [2](#)
- Bach, U., Krichbaum, T. P., Ros, E., Britzen, S., Tian, W. W., Kraus, A., Witzel, A., & Zensus, J. A. 2005, *A&A*, 433, 815 [21](#), [104](#)
- Bach, U., et al. 2006, *A&A*, 456, 105 [104](#), [105](#), [143](#)
- Bartel, N., Bietenholz, M. F., Lebach, D. E., Lederman, J. I., Petrov, L., Ransom, R. R., Ratner, M. I., & Shapiro, I. I. 2012, *ApJS*, 201, 3 [133](#)
- Barthel, P. D. 1989, *ApJ*, 336, 606 [7](#)
- Biermann, P., et al. 1981, *ApJ*, 247, L53 [20](#)
- Biermann, P. L., Schaaf, R., Pietsch, W., Schmutzler, T., Witzel, A., & Kuehr, H. 1992, *A&AS*, 96, 339 [23](#)
- Björnsson, C.-I., & Aslaksen, T. 2000, *ApJ*, 533, 787 [94](#)
- Blandford, R. D. 1990, in *Active Galactic Nuclei*, ed. R. D. Blandford, H. Netzer, L. Woltjer, T. J.-L. Courvoisier, & M. Mayor, 161 [13](#)
- Blandford, R. D., & Königl, A. 1979, *ApJ*, 232, 34 [2](#), [3](#), [4](#), [18](#), [93](#)
- Blandford, R. D., & Payne, D. G. 1982, *MNRAS*, 199, 883 [3](#), [145](#), [149](#)
- Blandford, R. D., & Rees, M. J. 1978, in *BL Lac Objects*, ed. A. M. Wolfe, 328 [7](#), [9](#), [15](#)
- Blandford, R. D., & Znajek, R. L. 1977, *MNRAS*, 179, 433 [9](#), [145](#)
- Böttcher, M., et al. 2007, *ApJ*, 670, 968 [14](#)
- Böttcher, M., & Bloom, S. D. 2000, *AJ*, 119, 469 [11](#)
- Böttcher, M., & Chiang, J. 2002, *ApJ*, 581, 127 [117](#)
- Böttcher, M., Harris, D. E., & Krawczynski, H. 2012, *Relativistic Jets from Active Galactic Nuclei* [115](#)

- Brecher, K., & Burbidge, G. R. 1972, *ApJ*, 174, 253 [9](#)
- Britzen, S., et al. 2009, *A&A*, 508, 1205 [21](#)
- Burbidge, G. R., Jones, T. W., & Odell, S. L. 1974, *ApJ*, 193, 43 [139](#)
- Burrows, D. N., et al. 2005, *Space Sci. Rev.*, 120, 165 [28](#)
- Burrows, D. N., et al. 2000, in *Society of Photo-Optical Instrumentation Engineers (SPIE) Conference Series*, Vol. 4140, *Society of Photo-Optical Instrumentation Engineers (SPIE) Conference Series*, ed. K. A. Flanagan & O. H. Siegmund, 64 [28](#)
- Camenzind, M., & Krockenberger, M. 1992, *A&A*, 255, 59 [19](#), [145](#), [149](#)
- Cappi, M., Comastri, A., Molendi, S., Palumbo, G. G. C., Della Ceca, R., & Maccacaro, T. 1994, *MNRAS*, 271, 438 [23](#)
- Carini, M. T., & Miller, H. R. 1992, *ApJ*, 385, 146 [45](#)
- Chiaberge M., Ghisellini G., 1999, *MNRAS*, 306, 551 [81](#)
- Chen, A. W., et al. 2008, *A&A*, 489, L37 [23](#), [24](#), [81](#)
- Ciprini, S., Tosti, G., Raiteri, C. M., Villata, M., Ibrahimov, M. A., Nucciarelli, G., & Lanteri, L. 2003, *A&A*, 400, 487 [36](#)
- Clements, S. D., Smith, A. G., Aller, H. D., & Aller, M. F. 1995, *AJ*, 110, 529 [82](#)
- Danforth, C. W., Nalewajko, K., France, K., & Keeney, B. A. 2013, *ApJ*, 764, 57 [20](#)
- Dondi, L., & Ghisellini, G. 1995, *MNRAS*, 273, 583 [102](#)
- Eckart, A., Witzel, A., Biermann, P., Johnston, K. J., Simon, R., Schalinski, C., & Kuhr, H. 1986, *A&A*, 168, 17 [21](#)
- Eckart, A., Witzel, A., Biermann, P., Johnston, K. J., Simon, R., Schalinski, C., & Kuhr, H. 1987, *A&AS*, 67, 121 [21](#)
- Edelson, R. A., & Krolik, J. H. 1988, *ApJ*, 333, 646 [37](#), [143](#)
- Fan, J. H., Cheng, K. S., Zhang, L., & Liu, C. H. 1997, *A&A*, 327, 947 [8](#), [22](#)

- Fanaroff, B. L., & Riley, J. M. 1974, MNRAS, 167, 31P [5](#)
- Ferrero, E., Wagner, S. J., Emmanoulopoulos, D., & Ostorero, L. 2006, A&A, 457, 133
[20](#), [23](#), [24](#)
- Finke, J. D., & Dermer, C. D. 2010, ApJ, 714, L303 [112](#), [113](#)
- Finke, J. D., Dermer, C. D., & Böttcher, M. 2008, ApJ, 686, 181 [102](#)
- Foschini, L., et al. 2006, A&A, 455, 871 [20](#), [24](#)
- Fossati, G., Maraschi, L., Celotti, A., Comastri, A., & Ghisellini, G. 1998, MNRAS, 299, 433 [8](#)
- Fromm, C. M., Perucho, M., Ros, E., Mimica, P., Savolainen, T., Lobanov, A. P., & Zensus, J. A. 2012, International Journal of Modern Physics Conference Series, 8, 323 [136](#)
- Fromm, C. M., et al. 2011, A&A, 531, A95 [15](#), [89](#), [94](#), [95](#)
- Fromm, C. M., et al. 2013a, A&A, 551, A32 [16](#), [135](#)
- Fromm, C. M., et al. 2013b, A&A, 551, A32 [140](#)
- Fromm, C. M., 2013, Ph.D. thesis, Max-Planck-Institut für Radioastronomie [17](#)
- Fuhrmann, L., et al. 2008, A&A, 490, 1019 [21](#), [99](#), [102](#), [104](#), [105](#)
- Fuhrmann, L., Zensus, J. A., Krichbaum, T. P., Angelakis, E., & Readhead, A. C. S. 2007, in American Institute of Physics Conference Series, Vol. 921, The First GLAST Symposium, ed. S. Ritz, P. Michelson, & C. A. Meegan, 249 [26](#)
- Gehrels, N., et al. 2004, ApJ, 611, 1005 [28](#)
- Ghisellini, G., Padovani, P., Celotti, A., & Maraschi, L. 1993, ApJ, 407, 65 [101](#)
- Ghisellini, G., et al. 1997, A&A, 327, 61 [8](#), [22](#)
- Gierliński, M., Middleton, M., Ward, M., & Done, C. 2008, Nature, 455, 369 [41](#)
- Giommi, P., Ansari, S. G., & Micol, A. 1995, A&AS, 109, 267 [8](#)

- Giommi, P., et al. 2008, *A&A*, 487, L49 [24](#)
- Giommi, P., et al. 1999, *A&A*, 351, 59 [20](#)
- Glynn, F., E., Chen, J., & Mushegian, R., A. 2006, *Bioinformatics*, 22, 310 [38](#)
- Gomez, J. L., Marti, J. M. A., Marscher, A. P., Ibanez, J. M. A., & Alberdi, A. 1997, *ApJ*, 482, L33 [136](#)
- Gupta, A. C., Srivastava, A. K., & Wiita, P. J. 2009, *ApJ*, 690, 216 [22](#)
- Gurwell, M. A., Peck, A. B., Hostler, S. R., Darrah, M. R., & Katz, C. A. 2007, in *Astronomical Society of the Pacific Conference Series*, Vol. 375, *From Z-Machines to ALMA: (Sub)Millimeter Spectroscopy of Galaxies*, ed. A. J. Baker, J. Glenn, A. I. Harris, J. G. Mangum, & M. S. Yun, 234 [27](#)
- Hardee, P. E. 1987, *ApJ*, 318, 78 [19](#)
- Hardee, P. E. 2006, in *American Institute of Physics Conference Series*, Vol. 856, *Relativistic Jets: The Common Physics of AGN, Microquasars, and Gamma-Ray Bursts*, ed. P. A. Hughes & J. N. Bregman, 57 [136](#), [145](#)
- Hartman, R. C., et al. 1999, *ApJS*, 123, 79 [23](#)
- Hayashida, M., et al. 2012, *ApJ*, 754, 114 [83](#)
- Heavens, A. F., & Meisenheimer, K. 1987, *MNRAS*, 225, 335 [99](#)
- Heeschen, D. S., Krichbaum, T., Schalinski, C. J., & Witzel, A. 1987, *AJ*, 94, 1493 [21](#)
- Heidt, J., & Wagner, S. J. 1996, *A&A*, 305, 42 [8](#), [22](#)
- Högbom, J. A. 1974, *A&AS*, 15, 417 [43](#)
- Hovatta, T., Tornikoski, M., Lainela, M., Lehto, H. J., Valtaoja, E., Tornainen, I., Aller, M. F., & Aller, H. D. 2007, *A&A*, 469, 899 [35](#), [36](#), [37](#), [38](#)
- Hufnagel, B. R., & Bregman, J. N. 1992, *ApJ*, 386, 473 [37](#)
- Hughes, P. A., Aller, H. D., & Aller, M. F. 1992, *ApJ*, 396, 469 [35](#), [36](#)
- Impey, C. D., Brand, P. W. J. L., & Tapia, S. 1982, *MNRAS*, 198, 1 [8](#)

- Jorstad, S. G., et al. 2010, *ApJ*, 715, 362 [82](#)
- Jorstad, S. G., et al. 2005, *AJ*, 130, 1418 [139](#)
- Jorstad, S. G., Marscher, A. P., Mattox, J. R., Aller, M. F., Aller, H. D., Wehrle, A. E., & Bloom, S. D. 2001, *ApJ*, 556, 738 [16](#), [43](#), [135](#)
- Kalberla, P. M. W., Burton, W. B., Hartmann, D., Arnal, E. M., Bajaja, E., Morras, R., & Pöppel, W. G. L. 2005, *A&A*, 440, 775 [29](#)
- Kardashev, N. S. 1962, *Soviet Ast.*, 6, 317 [98](#)
- Kawabata, K. S., et al. 2008, in *Society of Photo-Optical Instrumentation Engineers (SPIE) Conference Series*, Vol. 7014, *Society of Photo-Optical Instrumentation Engineers (SPIE) Conference Series* [27](#)
- Kellermann, K. I., & Pauliny-Toth, I. I. K. 1969, *ApJ*, 155, L71 [100](#)
- Kellermann, K. I., Sramek, R., Schmidt, M., Shaffer, D. B., & Green, R. 1989, *AJ*, 98, 1195 [4](#)
- Kumbhavi A. K., Narlikar J. V., 1999, *Quasars and active galactic nuclei : an introduction*, ed. Kembhavi, A. K. & Narlikar, J. V. Cambridge Univ. Press, Cambridge [92](#)
- Kirk, J. G., Guthmann, A. W., Gallant, Y. A., & Achterberg, A. 2000, *ApJ*, 542, 235 [13](#)
- Komissarov, S. S. 2011, *Mem. Soc. Astron. Italiana*, 82, 95 [9](#)
- Königl, A. 1981, *ApJ*, 243, 700 [82](#)
- Königl, A., & Choudhuri, A. R. 1985, *ApJ*, 289, 188 [19](#)
- Kraus, A., et al. 2003, *A&A*, 401, 161 [21](#)
- Krawczynski, H. 2004, *New A Rev.*, 48, 367 [14](#)
- Krichbaum, T. P., Agudo, I., Bach, U., Witzel, A., & Zensus, J. A. 2006, in *Proceedings of the 8th European VLBI Network Symposium* [43](#)

- Krichbaum, T. P., et al. 2008, ArXiv:0812.4211 [43](#)
- Krichbaum, T. P., et al. 2013, arXiv:1305.2811 [42](#)
- Krichbaum, T. P., et al. 1992, A&A, 260, 33 [43](#), [125](#)
- Krolik, J. H. 1999, ApJ, 515, L73 [12](#)
- Kudryavtseva, N. A., Gabuzda, D. C., Aller, M. F., & Aller, H. D. 2011, MNRAS, 415, 1631 [82](#)
- Kühr, H., Pauliny-Toth, I. I. K., Witzel, A., & Schmidt, J. 1981, AJ, 86, 854 [20](#)
- Lin, Y. C., et al. 1995, ApJ, 442, 96 [23](#)
- Lister, M. L., et al. 2013, AJ, 146, 120 [144](#)
- Lister, M. L., et al. 2009, AJ, 138, 1874 [16](#), [144](#)
- Liu, X., Song, H.-G., Marchili, N., Liu, B.-R., Liu, J., Krichbaum, T. P., Fuhrmann, L., & Zensus, J. A. 2012, A&A, 543, A78 [21](#)
- Lobanov, A. P., & Zensus, J. A. 1999, ApJ, 521, 509 [95](#), [96](#), [140](#)
- Lobanov, A. P., & Zensus, J. A. 2001, Science, 294, 128 [19](#)
- Lomb, N. R. 1976, Ap&SS, 39, 447 [38](#)
- Lott, B., Escande, L., Larsson, S., & Ballet, J. 2012, A&A, 544, A6 [60](#)
- Ly, C., Walker, R. C., & Junor, W. 2007, ApJ, 660, 200 [19](#)
- Malkan, M. A., & Sargent, W. L. W. 1982, ApJ, 254, 22 [12](#)
- Marscher, A. P. 1987, in Superluminal Radio Sources, ed. J. A. Zensus & T. J. Pearson, 280 [103](#)
- Marscher, A. P. 1996, in Astronomical Society of the Pacific Conference Series, Vol. 110, Blazar Continuum Variability, ed. H. R. Miller, J. R. Webb, & J. C. Noble, 248 [10](#), [15](#), [16](#), [64](#), [81](#)
- Marscher, A. P. 2009, ArXiv e-prints [17](#), [136](#)

- Marscher, A. P., & Gear, W. K. 1985, *ApJ*, 298, 114 [15](#), [16](#), [82](#), [87](#), [93](#), [94](#), [139](#), [148](#)
- Marscher, A. P., et al. 2008, *Nature*, 452, 966 [124](#)
- Mattox, J. R., et al. 1996, *ApJ*, 461, 396 [34](#)
- Meegan, C., et al. 2007, in *American Institute of Physics Conference Series*, Vol. 921, *The First GLAST Symposium*, ed. S. Ritz, P. Michelson, & C. A. Meegan, 13 [30](#)
- Meier, D. L., Koide, S., & Uchida, Y. 2001, *Science*, 291, 84 [2](#), [3](#), [9](#), [136](#), [145](#), [149](#)
- Miller, H. R., Carini, M. T., & Goodrich, B. D. 1989, *Nature*, 337, 627 [45](#)
- Montagni, F., Maselli, A., Massaro, E., Nesci, R., Sclavi, S., & Maesano, M. 2006, *A&A*, 451, 435 [22](#)
- Nieppola, E., Tornikoski, M., & Valtaoja, E. 2006, *A&A*, 445, 441 [9](#)
- Nilsson, K., Pursimo, T., Sillanpää, A., Takalo, L. O., & Lindfors, E. 2008, *A&A*, 487, L29 [20](#), [99](#)
- Nolan, P. L., et al. 2012, *ApJS*, 199, 31 [34](#)
- Orr, M. J. L., & Browne, I. W. A. 1982, *MNRAS*, 200, 1067 [7](#)
- Ostorero, L., et al. 2006, *A&A*, 451, 797 [24](#), [99](#)
- Padovani, P., & Giommi, P. 1995, *MNRAS*, 277, 1477 [8](#)
- Padovani, P., & Urry, C. M. 1992, *ApJ*, 387, 449 [7](#)
- Perucho, M., Lobanov, A. P., Martí, J.-M., & Hardee, P. E. 2006, *A&A*, 456, 493 [145](#)
- Pier, E. A., & Krolik, J. H. 1992, *ApJ*, 399, L23 [7](#)
- Pier, E. A., & Krolik, J. H. 1993, *ApJ*, 418, 673 [7](#)
- Piner, B. G., Pant, N., Edwards, P. G., & Wiik, K. 2009, *ApJ*, 690, L31 [19](#)
- Porcas, R. 2010, in *10th European VLBI Network Symposium and EVN Users Meeting: VLBI and the New Generation of Radio Arrays* [42](#)
- Poutanen, J., & Stern, B. 2010, *ApJ*, 717, L118 [112](#), [122](#)

- Press, W. H., & Rybicki, G. B. 1989, *ApJ*, 338, 277 [38](#), [39](#), [40](#)
- Qian, S., Witzel, A., Krichbaum, T. P., Kraus, A., Zensus, J. A., & Zhang, X. 1999, in *Astronomical Society of the Pacific Conference Series*, Vol. 159, BL Lac Phenomenon, ed. L. O. Takalo & A. Sillanpää, 443 [95](#)
- Qian, S. J., Krichbaum, T. P., Zensus, J. A., Steffen, W., & Witzel, A. 1996, *A&A*, 308, 395 [95](#)
- Quirrenbach, A., et al. 1991, *ApJ*, 372, L71 [22](#), [82](#)
- Raiteri, C. M., et al. 2003, *A&A*, 402, 151 [22](#), [37](#), [53](#), [63](#), [80](#), [81](#), [82](#)
- Rani, B., Gupta, A. C., Joshi, U. C., Ganesh, S., & Wiita, P. J. 2010a, *ApJ*, 719, L153 [22](#)
- Rani, B., Gupta, A. C., Joshi, U. C., Ganesh, S., & Wiita, P. J. 2011, *MNRAS*, 413, 2157 [22](#)
- Rani, B., et al. 2010b, *MNRAS*, 404, 1992 [8](#), [22](#), [41](#)
- Rani, B., et al. 2013a, *A&A*, 552, A11 [8](#), [45](#), [101](#), [115](#)
- Rani, B., Krichbaum, T. P., Lott, B., Fuhrmann, L., & Zensus, J. A. 2013b, *Advances in Space Research*, 51, 2358 [45](#), [112](#)
- Rani, B., Lott, B., Krichbaum, T. P., Fuhrmann, L., & Zensus, J. A. 2013c, *A&A*, 557, A71 [112](#), [122](#), [124](#)
- Rani, B., Wiita, P. J., & Gupta, A. C. 2009, *ApJ*, 696, 2170 [35](#), [45](#), [143](#)
- Readhead, A. C. S. 1994, *ApJ*, 426, 51 [101](#)
- Reynolds, S. P. 2009, *ApJ*, 703, 662 [98](#), [99](#)
- Rowan-Robinson, M. 1977, *ApJ*, 213, 635 [7](#)
- Sahayanathan, S., & Godambe, S. 2012, *MNRAS*, 419, 1660 [114](#)
- Sambruna, R. M., Maraschi, L., & Urry, C. M. 1996, *ApJ*, 463, 444 [8](#)

- Sanders, D. B., Phinney, E. S., Neugebauer, G., Soifer, B. T., & Matthews, K. 1989, *ApJ*, 347, 29 [7](#)
- Scargle, J. D. 1982, *ApJ*, 263, 835 [38](#), [39](#), [40](#), [41](#)
- Scheuer, P. A. G., & Readhead, A. C. S. 1979, *Nature*, 277, 182 [7](#)
- Schinzel, F. K. 2011, Ph.D. thesis, Max-Planck-Institut für Radioastronomie [136](#)
- Schinzel, F. K., Lobanov, A. P., Taylor, G. B., Jorstad, S. G., Marscher, A. P., & Zensus, J. A. 2012, *A&A*, 537, A70 [124](#)
- Schmidt, M. 1963, *Nature*, 197, 1040 [2](#)
- Schmidt, M. 1968, *ApJ*, 151, 393 [2](#)
- Schwadron, N. A., Lee, M. A., & McComas, D. J. 2008, *ApJ*, 675, 1584 [15](#)
- Scott, M. A., & Readhead, A. C. S. 1977, *MNRAS*, 180, 539 [101](#)
- Senturk, G. D., Errando, M., Boettcher, M., Coppi, P., Mukherjee, R., & Roustazadeh, P. 2011, *ArXiv:1111.0378* [23](#), [112](#), [122](#)
- Seyfert, C. K. 1943, *ApJ*, 97, 28 [1](#)
- Shakura, N. I., & Sunyaev, R. A. 1973, *A&A*, 24, 337 [11](#)
- Shepherd, M. C., Pearson, T. J., & Taylor, G. B. 1994, in *Bulletin of the American Astronomical Society*, Vol. 26, *Bulletin of the American Astronomical Society*, 987 [43](#)
- Sikora, M., Begelman, M. C., Madejski, G. M., & Lasota, J.-P. 2005, *ApJ*, 625, 72 [9](#)
- Sikora, M., & Madejski, G. 2001, in *American Institute of Physics Conference Series*, Vol. 558, *American Institute of Physics Conference Series*, ed. F. A. Aharonian & H. J. Völk, 275 [14](#)
- Simonetti, J. H., Cordes, J. M., & Heeschen, D. S. 1985, *ApJ*, 296, 46 [35](#)
- Smith J. E., Robinson A., Alexander D. M., Young S., Axon D. J., Corbett E. A., 2004, *MNRAS*, 350, 140 [6](#)

- Sokolovsky, K. V. e. a. 2013, ArXiv:1303.5451 [42](#)
- Spergel, D. N., et al. 2003, ApJS, 148, 175 [99](#), [138](#)
- Spruit, H. C. 2010, in Lecture Notes in Physics, Berlin Springer Verlag, Vol. 794, Lecture Notes in Physics, Berlin Springer Verlag, ed. T. Belloni, 233 [3](#)
- Stickel, M., Fried, J. W., & Kuehr, H. 1993, A&AS, 98, 393 [20](#)
- Stroh, M. C., & Falcone, A. D. 2013, ApJS, 207, 28 [29](#)
- Svensson, R. 1987, MNRAS, 227, 403 [102](#)
- Takalo, L. O., Sillanpaae, A., & Nilsson, K. 1994, A&AS, 107, 497 [8](#), [22](#)
- Takalo, L. O., et al. 1996, A&AS, 120, 313 [45](#)
- Tanaka, Y. T., et al. 2011, ApJ, 733, 19 [112](#), [122](#)
- Tavecchio, F., & Ghisellini, G. 2012, ArXiv:1209.2291 [114](#)
- Taylor, G. B., Carilli, C. L., & Perley, R. A., ed. 1999, Astronomical Society of the Pacific Conference Series, Vol. 180, Synthesis Imaging in Radio Astronomy II [43](#)
- Teräsraanta, H., et al. 2004, A&A, 427, 769 [26](#), [45](#)
- Teräsraanta, H., et al. 1998, A&AS, 132, 305 [26](#)
- Tornikoski, M., Valtaoja, E., Terasraanta, H., & Okyudo, M. 1994, A&A, 286, 80 [22](#), [82](#)
- Türler, M. 2011, Mem. Soc. Astron. Italiana, 82, 104 [15](#), [16](#)
- Türler, M., Courvoisier, T. J.-L., & Paltani, S. 2000, A&A, 361, 850 [89](#)
- Urry, C. M., & Padovani, P. 1995, PASP, 107, 803 [2](#), [3](#), [7](#), [8](#)
- Urry, C. M., Sambruna, R. M., Worrall, D. M., Kollgaard, R. I., Feigelson, E. D., Perlman, E. S., & Stocke, J. T. 1996, ApJ, 463, 424 [23](#)
- Valtaoja, E., Terasraanta, H., Urpo, S., Nesterov, N. S., Lainela, M., & Valtonen, M. 1992, A&A, 254, 71 [82](#), [97](#)

- Vaughan, S. 2005, *A&A*, 431, 391 [40](#), [41](#)
- Vaughan, S., Edelson, R., Warwick, R. S., & Uttley, P. 2003, *MNRAS*, 345, 1271 [40](#)
- Villata, M., et al. 2004, *A&A*, 424, 497 [37](#)
- Villata, M., et al. 2007, *A&A*, 464, L5 [22](#), [82](#)
- Villata, M., et al. 2008, *A&A*, 481, L79 [22](#), [24](#), [82](#)
- Vittorini, V., et al. 2009, *ApJ*, 706, 1433 [24](#)
- Wagner, S. J. 1992, in *X-ray Emission from Active Galactic Nuclei and the Cosmic X-ray Background*, ed. W. Brinkmann & J. Truemper, 97 [23](#)
- Wagner, S. J., et al. 1996, *AJ*, 111, 2187 [8](#), [20](#), [21](#), [22](#), [23](#)
- Watanabe, M., et al. 2005, *PASP*, 117, 870 [27](#)
- Wehrle, A. E., Piner, B. G., Unwin, S. C., Zook, A. C., Xu, W., Marscher, A. P., Teräsanta, H., & Valtaoja, E. 2001, *ApJS*, 133, 297 [143](#)
- Witzel, A., Heeschen, D. S., Schalinski, C., & Krichbaum, T. 1986, *Mitteilungen der Astronomischen Gesellschaft Hamburg*, 65, 239 [21](#)
- Witzel, A., Schalinski, C. J., Johnston, K. J., Biermann, P. L., Krichbaum, T. P., Hummel, C. A., & Eckart, A. 1988, *A&A*, 206, 245 [21](#)

Acknowledgements

I avail this opportunity to express my profound gratitude to my thesis supervisor Dr. Thomas P. Krichbaum for his guidance, inspiration and keen interest in this work. My knowledge of AGNs, my streams of thought about time variability, my scientific writing and a part of my scientific philosophy will always be largely influenced by him. Whenever I go to him for scientific as well as non-scientific discussion he was always there to help me. I am very thankful for all the wisdoms, knowledge and advise that were passed on to me. I express my deepest gratitude to Prof. Anton Zensus for the support, resources, and encouragement I have received from him. I owe my sincere thanks to Prof. Andreas Eckart for all his help and support over the past years.

I am happy to acknowledge Prof. Benoit Lott for teaching me several aspects of Gamma-ray astronomy. We worked together on several research papers during my thesis. His suggestions and comments were always fruitful for me. I am very thankful to Lars Fuhrmann for his motivation and valuable suggestions at the various stages of my Ph.D. work. It has been a great experience working with the *Fermi*/LAT collaboration. I owe my sincere thanks to Dave Thompson, Seth Digel, Marco Ajello, and Justin Finke. I sincerely thank Markus Böttcher for sharing his knowledge on high energy spectral modeling. He help me in understanding the theoretical aspects of AGN Physics.

It has always been a pleasure to work at MPIfR, Bonn. It is difficult to summarize all the support I have received over the past years from so many people. I especially thank Manolis Angelakis and Simone Pott for their help and support. It has always been a pleasure to discuss with the people in the VLBI group. I would like to particularly thank Silke Britzen, Stefanie Komossa, Richard Porcas, Tuomas Savolainen, and Mohammed Zamaninasab.

I acknowledge the support of Alan Marscher and Svetlana Jorstad, who provided many helpful comments and shared calibrated data-sets of their observation campaigns with me. I would like to thank FGAMMA team for allowing me to use the unpublished light curves of their monitoring.

I thank Pankaj for his very pleasant company that I experienced over the last several years. He always comes up with suggestions, consolation and encouragement, whichever is needed in academic and personal matters during good as well as hard times. I am very grateful for the company of Florent, Jeff, Ioannis, Vassilis, Bia, Eric, Moritz, and Christian, which I value very much, may it be the occasional chat during the day, having a good time together.

Most of all I express my gratitude to my parents for their blessings, love and affection. They have always given me the strength and wisdom to be sincere in my work and always motivated me time to time. They let me to follow the ways I prefer, help me in stepping the peaks, save me from the hurdles on the ways, strengthen me when I was disappointed, love me when I feel lonely and company me when I need it. I am happy to acknowledge my brothers Varun and Tarun, for their true love and affection. They are my love, my strength, my charm, my beauty, my affection and my dreams and I have no existence without them.

Erklärung

Ich versichere, dass ich die von mir vorgelegte Dissertation selbständig angefertigt, die benutzten Quellen und Hilfsmittel vollständig angegeben und die Stellen der Arbeit, einschließlich Tabellen, Karten und Abbildungen, die anderen Werken im Wortlaut oder dem Sinn nach entnommen sind, in jedem Einzelfall als Entlehnung kenntlich gemacht habe; dass diese Dissertation noch keiner anderen Fakultät oder Universität zur Prüfung vorgelegen hat; dass sie, abgesehen von unten angegebenen Teilpublikationen – noch nicht veröffentlicht worden ist sowie, dass ich eine solche Veröffentlichung vor Abschluss des Promotionsverfahrens nicht vornehmen werde. Die Bestimmungen der Promotionsordnung sind mir bekannt. Die von mir vorgelegte Dissertation ist von Prof. Dr. J. Anton Zensus und Prof. Dr. Andreas Eckart betreut worden.

Köln, den 14.11.2013

Teilpublikationen

Rani, B.; Krichbaum, T. P.; Marscher, A. P.; Jorstad, S. J.; Hodgson, J. A.; Fuhrmann, L.; Angelakis, E.; and J.A. Zensus. : “*S5 0716+714 : Inner jet kinematics and the origin of high energy emission*”, A&A, 2013 (in preparation).

Rani, B.; Krichbaum, T. P.; Lott, B.; Fuhrmann, L.; and Zensus, J. A. : “*S5 0716+714: GeV variability study*”, AdSpR 2013, Vol. 51, 2358.

Rani, B.; Krichbaum, T. P.; Fuhrmann, L.; Böttcher, M.; Lott, B.; Aller, H. D.; Aller, M. F.; Angelakis, E.; Bach, U.; Bastieri, D.; Falcone, A. D.; Fukazawa, Y.; Gabanyi, K. E.; Gupta, A. C.; Gurwell, M.; Itoh, R.; Kawabata, K. S.; Krips, M.; Lhteenmki, A. A.; Liu, X.; Marchili, N.; Max-Moerbeck, W.; Nestoras, I.; Nieppola, E.; Quintana-Lacaci, G.; Readhead, A. C. S.; Richards, J. L.; Sasada, M.; Sievers, A.; Sokolovsky, K.; Stroh, M.; Tammi, J.; Tornikoski, M.; Uemura, M.; Ungerechts, H.; Urano, T.; and Zensus, J. A. : “*Radio to gamma-ray variability study of blazar S5 0716+714*”, A&A 2013, Vol. 552, A11.

Rani, B.; Krichbaum, T. P.; Fuhrmann, L.; Lott, B.; Boettcher, M.; and Zensus, J. A. : “*Rapid Variability: What do we learn from correlated mm-/gamma-ray variability in jets ?*”, Proceedings of the Nuclei of Seyfert galaxies and QSOs - Central engine conditions of star formation, Bonn (Germany), November 6-8, 2012 [[arXiv:1302.3084](https://arxiv.org/abs/1302.3084)].

Curriculum Vitae

PERSONAL INFORMATION

Name : Ms. Bindu Rani
Address : Max-Planck-Institut für Radioastronomie
Auf dem Hügel 69, 53121 Bonn, Germany
Phone : +49 (228) 525-358
E-mail : brani@mpifr-bonn.mpg.de
Birth date and place : 08.09.1984, Mukandpur Jhajjar Haryana, India

ACADEMIC HISTORY

2012-continue Ph.D. student at University of Köln and
Max-Planck-Institut für Radioastronomie Bonn, Germany
Scientific Advisors: Dr. Thomas P. Krichbaum and Prof. Dr. J. Anton Zensus
Title: *Broad-band study of selected Gamma-ray active blazars*

2007-2011 Research Fellow at Aryabhata Research Institute of Observational Sciences
Manora Peak, Nainital 263129, India.

2005-2007 Master of Science in Physics at Department of Physics and Astrophysics,
University of Delhi, India.

2002-2005 Bachelor of Science Maharashi Dayanand University, Rohtak
Haryana, India.

2000-2002 Senior Secondary School, Board of School Education, Haryana (India)

AWARDS AND FELLOWSHIPS

1. Fellowship from the International Max Planck Research School for Astronomy and Astrophysics, 2012-2013.
2. COSPAR capacity building fellowship, December 2011.
3. Council of Scientific and Industrial Research (CSIR) fellowship through the JRF/National Eligibility Test (NET) conducted by University Grants Commission (UGC), Government of India in December 2006 and June 2007.
4. Joint Entrance Screening Test (JEST), 2007.
5. National scholarships for Higher secondary (2002) and graduation (2005) examinations, Government of India.

LIST OF PUBLICATIONS

23. G. Bhatta, J. R. Webb, H. Hollingsworth, ..., **B. Rani** et al.
The 72-h WEBT microvariability observation of blazar S5 0716+714 in 2009,
A&A, 558, A92 (2013).
22. **B. Rani**, B. Lott, T. P. Krichbaum, L. Fuhrmann, J.A. Zensus
Constraining the location of rapid gamma-ray ares in the FSRQ 3C 273,
A&A, 557, A71 (2013).
21. **B. Rani**, T. P. Krichbaum, B. Lott, L. Fuhrmann, J.A. Zensus
S5 0716+714: GeV variability study,
AdSpR, 51, 2358 (2013).
20. **B. Rani**, T. P. Krichbaum, L. Fuhrmann, et al.
Radio to gamma-ray variability study of blazar S5 0716+714,
A&A, 552, A11 (2013).
19. **B. Rani**, T. P. Krichbaum, L. Fuhrmann, et al.
Rapid Variability: What do we learn from correlated mm-/gamma-ray variability in jets ?
Proceedings of the Nuclei of Seyfert galaxies and QSOs - Central engine conditions of star formation, Bonn (Germany), November 6-8, 2012 [arXiv:1302.3084].

-
18. Alok C. Gupta, T. P. Krichbaum, P. J. Wiita, **B. Rani**, et al.
Multiwavelength intraday variability of the BL Lacertae S5 0716+714,
MNRAS, 425, 1357 (2012).
 17. **B. Rani**, T. P. Krichbaum
S5 0716+714 : GeV variability study,
39th COSPAR Scientific Assembly, E2.1, 1572 (2012).
 16. S. P. Gupta, U. S. Pandey, K. Singh, **B. Rani**, et al.
Optical Intra-day Variability Timescales and Black Hole Mass of the Blazars,
New Astronomy, 17, 8–17 (2012).
 15. **B. Rani**, A. C. Gupta, R. Bachev, et al.
Comparative study of Spectral Energy Distribution variation in BL Lacs and FS-RQs,
MNRAS, 417, 1881-1890 (2011).
 14. **B. Rani**, Alok C. Gupta, Paul J. Wiita
Variability of the Spectral Energy Distribution of the Blazar S5 0716+714,
JAA, 32, 217-222 (2011).
 13. **B. Rani**, A. C. Gupta, U. C. Joshi, S. Ganesh, P. J. Wiita,
Optical Intraday Variability of Ten Low Energy Peaked Blazars,
Monthly Notices of the Royal Astronomical Society (MNRAS), 413,
2157-2172 (2011).
 12. **B. Rani**, A. C. Gupta, U. C. Joshi, S. Ganesh, P. J. Wiita,
Optical quasi-periodic oscillations of ~ 15 minutes in the Optical Light Curve of the BL Lac S5 0716+714,
ApJL, 719, L153–L157 (2010).
 11. **B. Rani**, A. C. Gupta, A. Strigachev, et al.
Short-term ux and colour variations in low-energy peaked blazars,
MNRAS, 404, 1992–2017 (2010).
 10. A. K. Srivastava, D. Kuridze, T. V. Zaqarashvili, B. N. Dwivedi, **B. Rani**,
Network Loop Oscillations with EIS/Hinode,
Astrophysics and Space Science Proceedings (ASSP), 437–439 (2010).

-
9. A. C. Gupta, P. J. Wiita, H. Gaur, P. Lachowicz, **B. Rani**, A. K. Srivastava,
Quasi periodic oscillations (QPOs) in blazars on diverse timescales,
38th COSPAR Scientific Assembly, 38, 2294 (2010).
 8. H. Gaur, **B. Rani**, A. C. Gupta,
Rapid optical intra-day variability in blazars,
38th COSPAR Scientific Assembly, 38, 2287 (2010).
 7. **B. Rani**, H. Gaur, A. C. Gupta,
Simultaneous Multi-wavelength Correlated Variability of the Blazar S5 0716+714,
38th COSPAR Scientific Assembly, 38, 2280 (2010)
 6. E. Semkov, R. Bachev, A. Strigachev, ..., **B. Rani**, et al.
*Short term optical variability of blazars: first results from joint international col-
laborations,*
Bulgarian Astronomical Journal, 14, 1–5 (2010).
 5. Alok C. Gupta, **B. Rani**, Haritma Gaur, T. Krichbaum, L. Fuhrmann, N. Mar-
chili, I. Agudo, M. Boettcher, N. Palma, K. Hawkins,
Blazar S5 0716+714 is in the Optical Outburst State ?
ATEL, 2353 (2009).
 4. Alok C. Gupta, Haritma Gaur, **B. Rani**,
*Strong Optical Flaring after Super Gamma-Ray Flare detected in the Blazar 3C
454.3,*
ATEL, 2352 (2009).
 3. Alok C. Gupta, Haritma Gaur, **B. Rani**,
Optical flaring in the blazar OJ 287,
ATEL, 2314 (2009).
 2. **B. Rani**, P. J. Wiita & A. C. Gupta,
*Nearly Periodic Fluctuations in the Long Term X-ray Light Curves of the Blazars
AO 0235+164 and 1ES 2321+419,*
ApJ, 696, 2170–2178 (2009).

-
1. P. J. Wiita, A. C. Gupta, **B. Rani** & A. K. Srivastava,
*Nearly periodic variability in both optical and X-ray emission from the blazar S5
0716+714,*
American Astronomical Society (AAS), Meeting, 213, 326.04 (2009).